

University of St Andrews

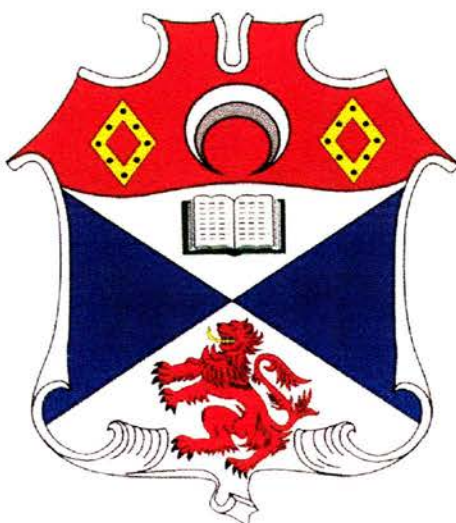


Full metadata for this thesis is available in
St Andrews Research Repository
at:

<http://research-repository.st-andrews.ac.uk/>

This thesis is protected by original copyright

A μ SR Study of Unconventional Superconductors.



A thesis submitted for the degree of Doctor of Philosophy

by

Adrian Hillier

September 1998.



I, Adrian Hillier, hereby certify that this thesis, which is approximately 30,000 words in length, has been written by me, that it is a record of work carried out by me and that it has not been submitted in any previous application for a higher degree.

Date 4 Sept 98 Signature of Candidate

I was admitted as a research student in October 1994 and as a candidate for the degree of Doctor of Philosophy in October 1995; The higher study for which this is a record was carried in the University of St. Andrews between 1994 and 1998.

Date 4 Sept 98 Signature of Candidate

I hereby certify that the candidate has fulfilled the conditions of the Resolution and Regulations appropriate for the degree of Doctor of Philosophy in the University of St. Andrews and that the candidate is qualified to submit this thesis in application for that degree.

Date Signature of Supervisor

In submitting this thesis to the University of St. Andrews I understand that I am giving permission for it to be made available for the use in accordance with the regulations of the University Library for the time being in force, subject to any copyright vested in the work not being affected thereby. I also understand that the title and abstract will be published, and that a copy of the work maybe made and supplied to any bona fide library or research worker.

Date 4 Sept 98 Signature of Candidate

ABSTRACT.

In this thesis a wide range of intermetallic superconducting compounds has been studied using principally, muon spin rotation, neutron scattering and magnetisation techniques. In particular those compounds which are close to a magnetic instability, and in which magnetic spin fluctuations are expected to play a role in defining the superconductivity and magnetic properties, have been selected. These include the RNi_2B_2C compounds (where R is a Rare earth, a combination of rare earth elements or Y), the yttrium hexaboride compound, the C16 compounds with stoichiometry Zr_2TM (where TM is Fe, Co, Ni or Rh), the C15 Laves phase compounds based upon ZrV_2 with transition metal substitution of V.

From the muon experiments accurate values for the London penetration depth, λ , and its variation with temperature have been extracted. These measurements of λ have been coupled with values for the Sommerfeld constant obtained from the published measurements of the heat capacity of the respective compounds, to provide an estimation of the so-called Fermi temperature, T_F .

The resulting ratio of the superconducting transition temperature, T_c , to T_F have been analysed within the framework of the classification scheme suggested by Uemura for the so-called 'exotic' superconductors. It is found that within this scheme the superconducting compounds generally fall outside, yet close to the limits for exotic superconductivity. In this respect they may represent an intermediate class of superconductor mid-way between conventional Bardeen-Cooper-Schrieffer phonon mediated superconductivity and more exotic local pairing Bose condensate superconductivity. On the basis of recent theoretical predictions based on the Self-Consistent-Renormalisation theory of itinerant magnetism, it is argued that spin fluctuation may indeed play a role in mediating superconducting in these systems.

ACKNOWLEDGEMENTS.

I am greatly indebted to my supervisor, Prof. Bob Cywinski, without his help, guidance and patience I would have been unable to submit this thesis. I am also grateful to Rob Bewley, Mark Telling, Sue Kilcoyne, Ross Stewart, Paz Manuel and Jude Dann, the members of the Magnetism and Superconductivity at St. Andrews, both past and present, who have made my time here both happy and enjoyable. Also, I would like to thank Steve Lee and Christof Aegerter for some very useful discussions. In addition, I am grateful for the technical support of Reg Gavine, Fritz Akerboom and the control room staff at both ISIS and the ILL. I also acknowledge the support and advice of the staff at ISIS, Drs. C. Scott, S Cottrell, and Phillip King and at the ILL Dr Clemens Ritter.

I would also like to thank EPSRC and the University of St. Andrews for the PhD studentship.

Finally, it leaves me to thank my father, mother and my little brother, Tony, who for the past four years have forced me to keep my feet on the ground and my sanity.

To my family.

'I have no data yet. It is a capital mistake to theorise before one has data. Insensibly one begins to twist the facts to suit theories, instead of theories to suit facts'

*A Scandal in Bohemia, from The Adventures of Sherlock Holmes, by Sir A. Conan
Doyle.*

CONTENTS

1. INTRODUCTION

2. SUPERCONDUCTIVITY.

2.1 Introduction.

2.2 The Meissner-Ochsenfeld effect.

2.3 The Two-fluid model.

2.4 The London equations.

2.5 A type I superconductor.

2.6 A type II superconductor.

2.6.1 The Bean model.

2.6.2 Flux pinning and instabilities.

2.7 The Macroscopic Theory- Ginzburg Landau Theory.

2.8 The Microscopic Theory- BCS Theory.

2.9 Local pairing superconductivity.

3. EXPERIMENTAL TECHNIQUES.

3.1 Introduction.

3.2 Sample preparation.

3.3 Structural characterisation.

3.3.1 Theory of diffraction.

3.3.2 X-ray diffraction.

3.3.2.1 Experimental set-up for x-ray diffraction.

3.3.3 Neutron diffraction.

3.3.3.1 The experimental set-up for D1B at the ILL.

3.3.3.2 The experimental set-up for POLARIS at ISIS.

3.3.4 Analysis of diffraction spectra- Rietveld analysis.

3.4 Magnetic Characterisation.

3.5 References.

4. MUON SPIN ROTATION.

4.1 Introduction.

4.2 Properties of a muon.

4.3 Muon production at ISIS.

4.4 The muon spectrometers at ISIS.

4.4.1 The muon beam lines at ISIS.

4.4.2 The spectrometers.

4.5 The muon spin rotation technique.

4.5.1 Sample mounting.

4.5.2 The time evolution of the muon spin direction.

4.6 Data analysis.

4.6.1 Time domain analysis.

4.6.2 Field domain analysis.

4.7 References.

5. THE NICKEL BOROCARBIDES.

5.1 Introduction.

5.1.1 The superconducting properties of the nickel borocarbides.

5.1.2 The magnetic properties of the nickel borocarbides.

5.2 Sample preparation and structural characterisation.

5.3 The structural determination of the nickel borocarbides.

5.4 $\text{LuNi}_2\text{B}_2\text{C}$.

5.5 $Y(Ni_{1-x}Co_x)_2B_2C$.

5.6 $(Y_{1-x}La_x)Ni_2B_2C$.

5.7 $(Er_{1-x}Tb_x)Ni_2B_2C$.

5.7.1 DC magnetisation study of the $(Er_{1-x}Tb_x)Ni_2B_2C$ alloys.

5.7.2 Neutron diffraction study of $(Er_{1-x}Tb_x)Ni_2B_2C$.

5.8 Conclusions.

5.9 References.

6. YTTRIUM HEXABORIDE.

6.1 Introduction.

6.2 Initial characterisation.

6.2.1 Sample preparation.

6.2.2 Magnetic characterisation.

6.3 Muon spin rotation.

6.4 Conclusions.

6.5 References.

7. THE Zr_2TM ALLOYS.

7.1 Introduction.

7.2 Initial characterisation.

7.2.1 Sample preparation and x-ray diffraction.

7.2.2 DC magnetisation.

7.2.2.1 The superconducting properties of Zr_2TM
($TM = Rh$ and Co).

7.2.2.2 Magnetic hysteresis and flux jumps in Zr_2Rh .

7.3 Muon spin rotation.

7.4 Conclusions.

7.5 References.

8. $\text{ZrV}_{2-x}\text{TM}_x$.

8.1 Introduction.

8.2 Initial Characterisation.

8.2.1 Sample preparation.

8.2.2 Magnetic characterisation.

8.3 Muon spin rotation.

8.4 Conclusions.

8.5 References.

9. Discussion and conclusions.

9.1 Classification of superconductors within the Uemura scheme.

9.2 The role of spin fluctuations.

9.3 Future work.

1. Introduction.

The problem of finding an appropriate classification scheme for the remarkably diverse range of known superconducting materials is a long standing one. Nevertheless the literature abounds with claims of discoveries of “new classes” of superconductors, although the nature of the “class” is rarely defined explicitly. In cases where the structural, electronic or magnetic properties of the new superconductor are particularly unusual it is tempting to accept such claims: heavy fermions, high T_C cuprates, organic superconductors and buckminsterfullerenes are all examples of superconducting materials which superficially have little in common either with each other or with the more conventional superconducting elements and compounds and might therefore be considered as genuinely belonging to different classes. However the underlying uniformity of the superconducting ground state and its general conformity with the predictions of BCS theory continues to unite an extraordinarily disparate group of superconducting materials. Consequently over the last few decades there have been numerous attempts to provide an empirical framework, based upon the fundamental parameters of the superconducting state, within which superconducting materials can be compared and contrasted, thus enabling classes of superconductor to be unambiguously identified. For example, until the early 1980s a correlation between the superconducting transition temperature, T_C , and the Sommerfeld constant, i.e. the coefficient of the linear electronic specific heat γ , was frequently invoked. A plot of $\log T_C$ versus $\log \gamma$ was found to yield an approximately universal curve (see figure 1.1)¹. However, first the heavy fermion compounds, with enormous γ s yet low transition temperatures and then, later, the cuprates with modest γ s but remarkably high T_C s proved to be marked exceptions to this universality, apparently confirming their status as members of new, exotic classes of superconductors.

More recently a rather surprising universal scaling relationship has emerged from systematic transverse field muon spin rotation (μ SR) measurements of flux penetration in superconducting systems. Uemura and co-workers² were the first to recognise the new

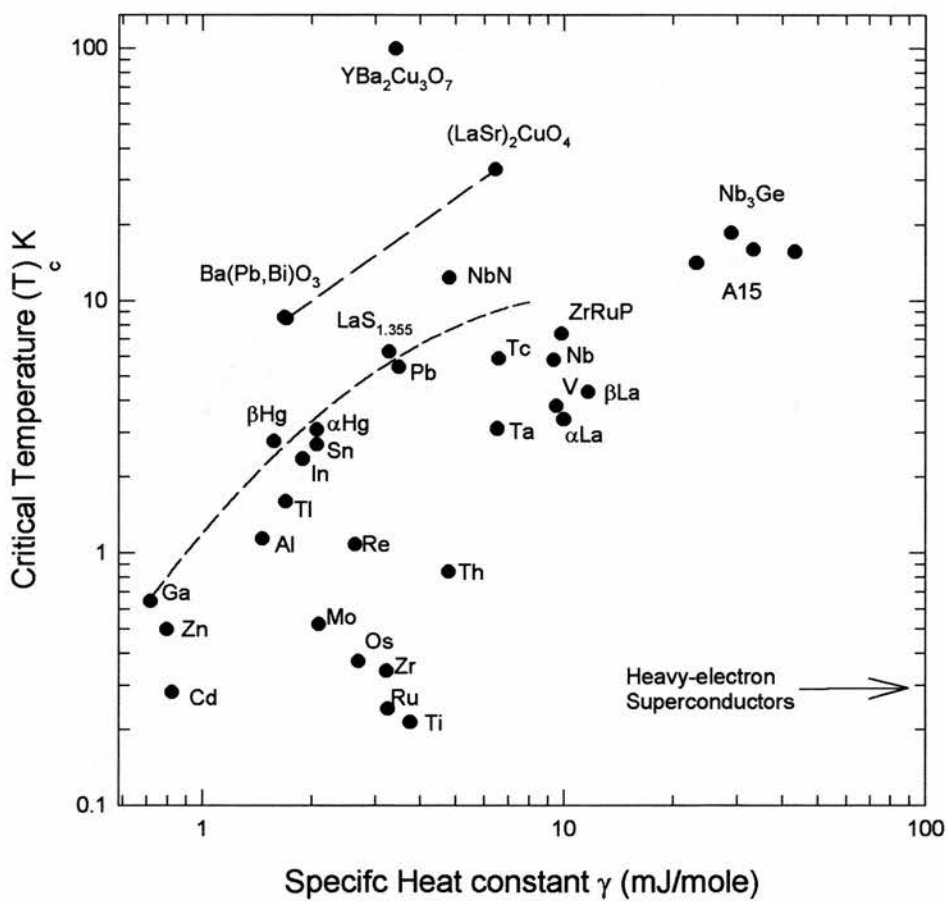


Figure 1.1 A 'universal' scaling relationship between the superconducting transition temperature and the coefficient of the electronic specific heat, γ .

scaling relationship, observing that for several different members of the family of high temperature cuprate superconductors an initial increase in carrier doping leads to precisely the same linear increase of T_C with the muon spin depolarisation rate, σ . Deviations from linearity, first appearing as a saturation and then a suppression of T_C , only appears at high levels of doping. Remarkably, several Chevrel phase superconductors were also found to follow the same linear relationship, while bismuthates, fullerenes, organic superconductors and heavy fermion compounds exhibit a similar scaling behaviour^{3,4}.

The correlation between T_C and σ observed in μ SR studies has suggested a new empirical framework for classifying superconducting materials. In this thesis I shall briefly review the role played by μ SR in establishing this new classification scheme, and discuss the underlying physical phenomena responsible for the observed correlations. I shall present some μ SR measurements on a range of superconducting families and attempt to interpret the results of these measurements within the proposed classification scheme.

UEMURA CLASSIFICATION SCHEME.

The superconducting penetration depth, λ , is related directly to two of the principal parameters of the electronic ground state of a material, namely the effective mass of the electron, m^* , and the carrier density, n_s . Also, $\lambda(\text{nm})$ is related to $\sigma(\mu\text{s}^{-1})$ by the relation

$$\sigma = \frac{75780}{\lambda^2}. \quad 1.1$$

The general London formula for the zero temperature limit of the penetration depth, $\lambda(0)$ for an isotropic superconductor gives

$$\lambda(0) = \left[\frac{m^*/m_e}{4\pi n_s r_e} \left(1 + \frac{\xi}{l_e} \right) \right]^{1/2} \quad 1.2$$

where n_s is the superconducting electron density, r_e ($=2.82 \times 10^{-15} \text{m}$) is the classical radius of the electron, l_e is the electron mean free path, and ξ is the superconducting coherence

length. ξ/l_e defines the dirty limit correction. Correspondingly we can see from equations 1.1 and 1.2 that, within the clean limit, ie for $\xi/l_e \ll 1$,

$$\sigma(0) \propto \frac{n_s(0)}{m^*} \quad 1.3$$

The linear dependence of T_C upon $\sigma(0)$ observed by Uemura et al ^{2,3,4} therefore implies a direct correlation between T_C and $n_s(0)/m^*$. Such a linear correlation is not consistent with the conventional weak coupling limit of BCS theory, in which the electron pairing mechanism is phononic in origin and the Debye frequency, ω_D , defines the energy scale of the pairing such that $T_C \propto \hbar \omega_D$. Usually the electronic density of states is structureless on the scale of $\hbar \omega_D$ and so T_C is not expected to be directly related to n_s . However, recognising the quasi-two dimensional character of both the high T_C cuprates and the organic superconductors, and also noting that the Fermi energy, E_F , of a non-interacting 2d electron gas is proportional to n_e/m^* , Uemura et al inferred ^{3,4} that, for these systems at least, the linear correlation may imply $T_C \propto E_F$. Such a relationship is expected if the energy scale of the electron pairing in the superconducting state is comparable to, or exceeds, E_F ⁵. The possible correlation between T_C and E_F was further demonstrated by considering the variation of the superconducting transition temperature with the effective Fermi temperature, $T_F = E_F/k_B$. For the quasi-2d systems T_F may be estimated directly from the muon depolarisation rate $\sigma(0)$ via the relation

$$k_B T_F = (\hbar^2 \pi) n_{s2d} / m^* \quad 1.4$$

n_{s2d} is the carrier concentration within the superconducting planes calculated from the volume carrier density using $n_s d$, where d is the interplanar spacing. For a 3d system, however, the Fermi temperature is given by

$$k_B T_F = (\hbar^2 / 2) (3\pi^2)^{2/3} n_s^{2/3} / m^* \quad 1.5$$

To determine T_F the measured muon depolarisation rate must therefore be coupled with, for example, the Sommerfeld constant, γ ,

$$\gamma = \left(\frac{\pi}{3}\right)^{2/3} \frac{k_B^2 m^* n_e^{1/3}}{\hbar^2} \quad 1.6$$

where n_e is the carrier density. Assuming that n_s at $T=0$ is equivalent to n_e above T_C we may combine equations 1.4 and 1.5 to obtain

$$k_B T_F \propto \sigma(0)^{3/4} \gamma^{-1/4}. \quad 1.7$$

Using this parameterisation Uemura et al^{3,4} were able to confirm a close correlation between T_C and T_F . The cuprate, heavy fermion, organic, fullerene and Chevrel phase superconductors all follow a similar linear trend with $1/100 < T_C/T_F < 1/10$, in contrast to the conventional BCS superconductors (Nb, Sn, Al etc) for which $T_C/T_F < 1/1000$. The ‘‘Uemura plot’’ of $\log(T_C)$ against $\log(T_F)$, shown in a stylised form in figure 1.2, thus appears to discriminate dramatically between the ‘‘exotic’’ and ‘‘conventional’’ superconductors. Indeed, on the basis of the Uemura plot it is tempting to place all of the ‘‘exotic’’ superconductors in a single ‘‘class’’ which is quite distinct from the class of conventional BCS superconductors.

The Uemura plot has been taken as an indication that the strongly coupled ‘‘exotic’’ superconductors may, in a thermodynamic sense, be close to Bose-Einstein condensation. The condensation temperature of an ideal boson gas is defined only by n_s and m^* , and is independent of the scale of the pairing interaction, providing that $\hbar \omega_B \gg kT_B$ ⁶ The BE condensation temperature, T_B , represented graphically by the dashed line in the Uemura plot of figure 1.2, has been estimated using the expression for an ideal 3d boson gas, i.e.

$$k_B T_B = (1.04 \hbar^2) n_B^{2/3} / m_B \quad 1.8$$

together with a boson density of $n_B = n_s/2$ and boson mass of $m_B = 2m^*$. (Although there can be no Bose-Einstein condensation in an perfect 2d system this value of T_B nevertheless provides an estimate of the maximum condensation temperature for the quasi-2d systems discussed here). Intriguingly, all the exotic superconductors are found to have values of T_C/T_B in the range 1/3 to 1/30, thereby emphasising the proximity of these systems to BE-like condensation.

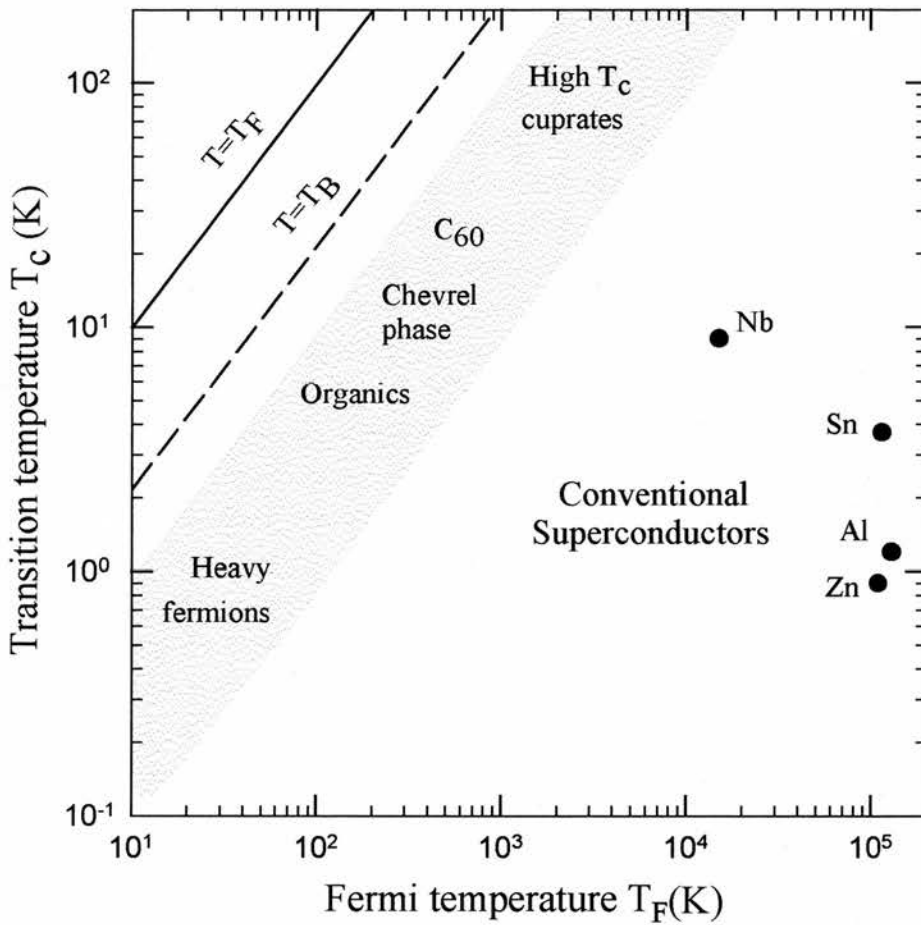


Figure 1.2 A schematic representation of the “Uemura plot” of superconducting transition temperature T_C against effective Fermi temperature T_F . The “exotic” superconductors fall within a common band for which $1/100 < T_C/T_F < 1/10$, indicated by the shaded region in the figure. The dashed line correspond to the Bose-Einstein condensation temperature, T_B , calculated according to equation (1.8).

To summarise, the Uemura formalism has provided a classification scheme which not only discriminates effectively between conventional BCS superconductors and strongly coupled exotic, and perhaps BE-like, superconductors, but also highlights the fundamental similarities between a rather diverse group of exotic superconductors.

In this thesis I have conducted a detailed study of a wide range of superconductors that could be considered as unusual because of their close proximity to magnetic order. I have chosen to examine the nickel borocarbides, YB_6 , Zr_2TM and ZrV_2 , using principally the muon spin rotation technique, and examined their behaviour within the context of the Uemura scheme.

REFERENCES.

¹ Physics Today **40**, 23 April 1987

² Y. J. Uemura, G. M. Luke, B. J. Sternlieb, J. H. Brewer, J. F. Carolan, W. N. Hardy, R. Kadono, J. R. Kempton, R. F. Kiefl, S. R. Kreitzman, P. Mulhern, T. M. Riseman, D. L. Williams, B. X. Yang, S. Uchida, H. Takagi, J. Gopalkrishnan, A. W. Sleight, M. A. Subramanian, C. L. Chien, M. Z. Cieplak, Gang Xiao, V. Y. Lee, B. W. Statt, C. E. Stronach, W. J. Kossler, X. H. Yu, Phys Rev Let **62**, 2317 (1989).

³ Y. J. Uemura, L. P. Le, G. M. Luke, B. J. Sternlieb, W. D. Wu, J. H. Brewer, T. M. Riseman, C. L. Seaman, M. B. Maple, M. Ishikawa, D. G. Hinks, J. D. Jorgensen, G. Saito, H. Yamochi, Phys Rev Let **66**, 2665 (1991).

⁴ Y. J. Uemura, Physica C **185-189**, 733 (1991).

⁵ V. J. Emery, G. Reiter, Phys Rev B **38**, 4547 (1988).

⁶ R. Mincus, J. Ranninger, S. Rabaszkiewicz, Rev Mod Phys **62**, 113 (1990).

2. Superconductivity.

2.1 INTRODUCTION.

Superconductivity was first discovered in 1911 by Kamerlingh Onnes¹ who found that the electrical resistivity of pure mercury dropped to zero, within experimental resolution, at a temperature of 4.2K. Shortly afterwards it was discovered that this zero resistance state could be destroyed by the application of an applied magnetic field. In 1933, Meissner and Ochsenfeld showed conclusively that superconductivity was an entirely new state of matter as a superconductor would expel a time invariant magnetic field from its interior when cooled through the superconducting transition temperature. Subsequently, superconductivity was found in many elements and compounds, and it was soon realised that two types of superconducting ground states were possible, known as type I and type II, which could be distinguished by the way in which the superconducting ground state was destroyed by a magnetic field. Considerable theoretical effort was devoted to explaining the nature of the superconducting ground state, culminating in the extremely successful Bardeen, Cooper and Schiffer theory in the 1950's. Since then there have been many refinements and developments to the theory. Alternative theoretical approaches have also been proposed in which, for example, Bose-Einstein-like local pairing or condensation mechanisms have been invoked to explain the anomalous behaviour of some unusual or unconventional superconductors. In this chapter I shall review some of the theoretical concepts of the superconducting ground state. A more detailed review of superconductivity can be found in references 2, 3 and 4.

2.2 THE MEISSNER-OCHSENFELD EFFECT.

In 1933, Meissner and Ochsenfeld⁵ measured the magnetisation of tin and lead below the superconducting transition temperature and found that if a superconductor is cooled below T_c in an applied field, the magnetic flux is excluded from the superconducting

sample. In this case the superconductor behaves as a perfect diamagnet and thus has a susceptibility of -1. This shows that $B=0$ inside a superconductor and that a superconductor is not just a perfect conductor. Since taking ohms law,

$$\underline{E} = \rho \underline{j}, \quad 2.1$$

if the resistivity, $\rho=0$ and the current, \underline{j} , is finite then $\underline{E}=0$. Using Maxwell's equations,

$$\text{curl } \underline{E} = -\frac{d\underline{B}}{dt}, \quad 2.2$$

then $d\underline{B}/dt=0$. This implies that the flux density does not change through the transition temperature. However, Meissner and Ochsenfeld observed that the flux was expelled and hence concluded that perfect diamagnetism is associated with a superconducting state must be quantum mechanical in origin.

2.3 THE TWO-FLUID MODEL.

In 1934 Gorter and Casimer⁶ suggested a phenomenological two fluid model to explain experimental results. The conduction electrons in the superconducting state can be separated into two groups. One group behaves as if the electrons are normal and hence experience resistance. The other group consists of superelectrons which do not interact with the lattice. If we consider the free energy of each group of electrons then the temperature dependence of the superconducting electron density can be determined. The free energy, F , is given by

$$F(x, T) = -\frac{x^{1/2}\gamma T^2}{2} - (1-x)\beta, \quad 2.3$$

where x is the ratio of normal electrons to the total number of electrons, $-\beta$ is the condensation energy and $\gamma T^2/2$ is the normal free electron energy. Minimising with respect to x and using the limits $F(0, T)=-\beta$ and $F(1, T)=-\gamma T^2/2$ then

$$x = \left[\frac{T}{T_c} \right]^4. \quad 2.4$$

This yields the temperature dependence of the superelectron density⁶

$$n_s(T) = n_s(0) \left(1 - \left(\frac{T}{T_c} \right)^4 \right). \quad 2.5$$

The two states of electrons are generally observed in both type I and type II superconductors.

2.4 THE LONDON EQUATIONS.

The Meissner effect has shown that the flux density inside a superconductor is always zero, i.e. both $\delta \underline{B} / \delta t$ and \underline{B} should reduce to zero close to the surface of a superconductor. F. and H. London suggested a phenomenological model⁷ for the magnetic properties of a superconductor in which

$$\nabla^2 \underline{\dot{B}} = \frac{1}{\alpha} \underline{\dot{B}} \quad 2.6$$

as in a perfect conductor with the additional condition

$$\nabla^2 \underline{B} = \frac{1}{\alpha} \underline{B} \quad 2.7$$

where

$$\alpha = \frac{m}{\mu_0 n_s e^2}. \quad 2.8$$

The solution to equations 2.7 and 2.8 is

$$B(x) = B_a \exp\left(\frac{-x}{\sqrt{\alpha}}\right). \quad 2.9$$

This shows that the field inside a superconductor exponentially decreases to zero. Equation 2.10 shows that the field density falls to 1/e of the applied field, B_a , at $x = \sqrt{\alpha}$. This distance is called the London magnetic penetration depth, λ_L , and is given by

$$\lambda_L = \sqrt{\frac{m}{\mu_0 n_s e^2}}. \quad 2.10$$

2.5 A TYPE I SUPERCONDUCTOR.

A type I superconductor has two possible magnetic states below the superconducting transition temperature, T_c . The first, below a critical field, H_c , in which all flux is excluded, is the Meissner-Ochsenfeld state (see §2.2). At a critical field, H_c , the magnetic field penetrates the interior of the sample. This has a destructive effect on the superconducting electron pairs and drives the superconductor into a normal state (see figure 2.1). However, it is possible for both the normal state and superconducting state to coexist. Consider a type I superconductor with a demagnetisation factor, for example: a long thin cylinder with the long axis perpendicular to the applied field or even a sphere. The internal field is related to the applied field and the magnetisation by the relation

$$H_{\text{int}} = H_{\text{app}} - nM \quad 2.11$$

where H_{int} is the internal field, H_{app} is the applied field, n is the demagnetisation factor of the sample and M is the magnetisation. Applying a field at the critical value, H_c , destroys the superconductivity and the sample returns to the normal state. However, in the normal state the magnetisation, M , is zero. In this case, the internal field is less than the critical field, and the sample should return to the superconducting state. This apparent contradiction can be resolved if both a normal state and superconducting state can coexist in equilibrium. In this case, the superconducting sample is partly normal and partly superconducting. The magnetic flux passes through the normal regions while being expelled from the superconducting regions. This state is called the intermediate state. For the intermediate state to exist, the Gibbs free energy of the intermediate state must be lower than the Gibbs free energy of either the superconducting state or the normal state. The Gibbs free energy is given by

$$G(H_a) = G(0) - \int_0^{H_a} \mu_0 M dH_a \quad 2.12$$

where $G(0) = Vg_s(0)$ at $H_a = 0$ and V is volume. There are three regions to be considered:

The superconducting state i.e. $0 < H_a < (1-n)H_c$.

In this region, the sample is fully superconducting therefore

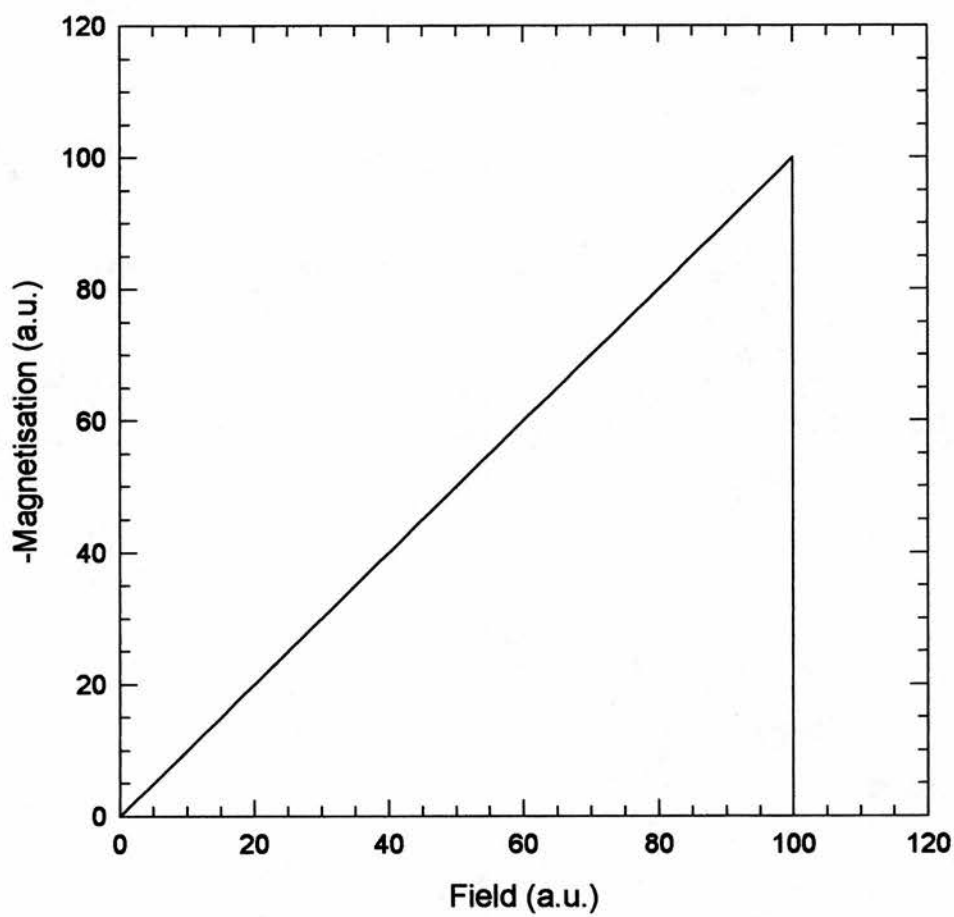


Figure 2.1 The virgin magnetisation curve for a type I superconductor.

$$G(H_a) = Vg_s + \frac{V\mu_0 H_a^2}{2(1-n)} \quad 2.13$$

The intermediate state i.e. $(1-n)H_c < H_a < H_c$.

In this region part of the sample is superconducting and part is normal therefore the magnetisation is given by

$$M = \frac{B}{\mu_0} - H_{int}. \quad 2.14$$

Clearly, the magnetisation, M , is related to the ratio of the normal to superconducting fraction, η

$$M = (\eta - 1)H_{int} = (\eta - 1)H_c. \quad 2.15$$

It therefore follows that in this region of applied fields the Gibbs free energy is

$$G(H_a) = Vg_s(0) + \frac{V\mu_0 H_c}{2n} \left[H_a \left(2 - \frac{H_a}{H_c} \right) - H_c(1-n) \right] \quad 2.16$$

The normal state i.e. $H_c < H_a$.

This is in the region of applied fields when the sample is completely normal ($M=0$) therefore

$$G(H_a) = Vg_s(0) + \frac{1}{2} V\mu_0 H_c^2 = Vg_n(0). \quad 2.17$$

This variation of the Gibbs free energy clearly shows that the intermediate state has a lower free energy than both the superconducting and normal state and therefore must be a stable ground state. This state was first shown experimental by Meshkovshy and Shalnikov⁸. A visual example of the intermediate state is given in figure 2.2⁹.

In order to determine the structure of the intermediate state an examination of the interface between the normal and superconducting states is required. In 1953, Pippard introduced the concept of a coherence length¹⁰. Pippard argued that the density of the superconducting electrons, n_s , could not change abruptly at the interface between the normal state and the superconducting state. Therefore there must be some characteristic length over which n_s can change. This distance was called the coherence length, ξ . The

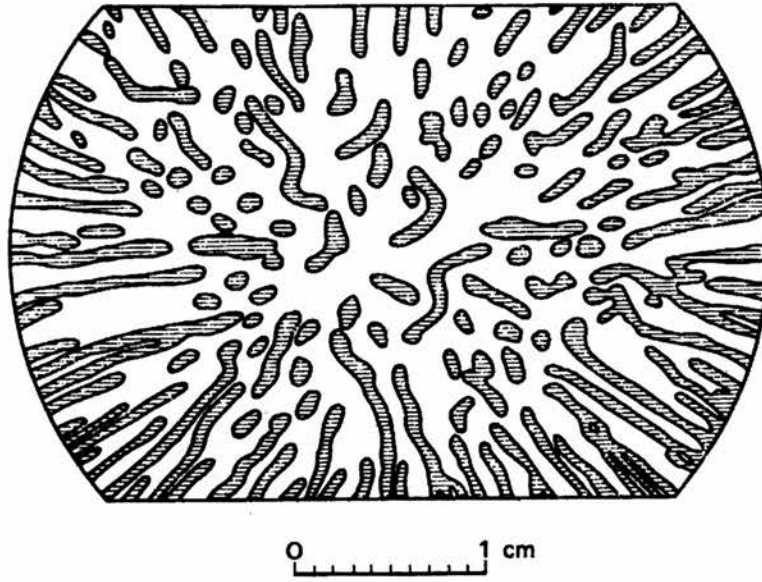


Figure 2.2 The intermediate state of aluminium plate with $H=0.65H_c$ and $T=0.92T_c$. The shaded areas are regions of non-superconducting aluminium whereas the clear areas are regions of the superconducting state.

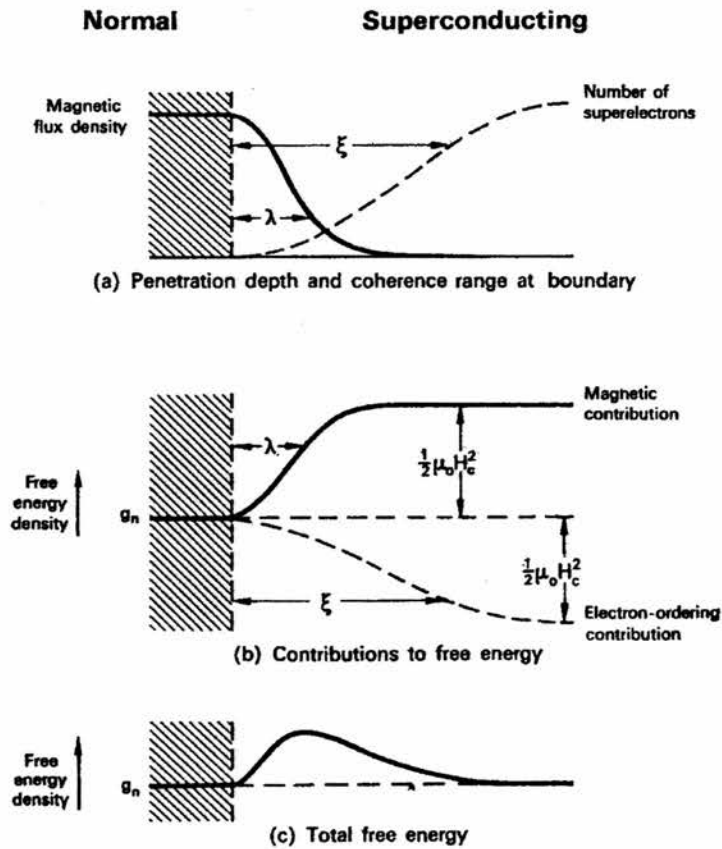


Figure 2.3 The surface energy of a type I superconductor.

free energy can be determined from the magnetic penetration and the superconducting electron density (see figure 2.3b¹¹) and therefore the surface energy can be resolved. If λ is shorter than ξ , as is the case for a type I superconductor, a positive surface energy results at the boundary between the normal and superconducting state (see figure 2.3c).

Clearly, in order to minimise the free energy of the intermediate state the boundaries between the superconducting state and the normal state have to be reduced. This can be achieved by having a few thick domains of normal or superconducting phases (for an example see figure 2.2).

2.6 A TYPE II SUPERCONDUCTOR.

A type II superconductor has the possibility of three magnetic states. The first state is the same as that of a type I superconductor, i.e. the Meissner-Ochsenfeld state, where the magnetic flux is expelled from the superconducting sample below a critical field, H_{c1} . When the applied field is increased beyond H_{c1} , the superconducting sample enters the so-called mixed state. The mixed state is magnetically stable and does not require the presence of a significant demagnetisation factor to exist. The final state is the normal state where the applied field is greater than the upper critical field, H_{c2} .

A type II superconductor has a coherence length shorter than the magnetic penetration depth. If the free energy from the magnetic field and electron-ordering contribution is considered then the surface energy is negative (see figure 2.4). A direct consequence of the surface energy being negative that it is energetically more favourable for the sample to split into small field domains i.e. to maximise the interface between the normal to superconducting areas. This leads to normal domains which are cylindrical in form, and which usually form a hexagonal lattice stabilised by magnetic forces. In the mixed state, the bulk of the sample is diamagnetic; the magnetic flux within the normal cylindrical cores are supported by screening currents or vortices. At each core the density of the superelectrons decreases to zero and each core contains a flux line which is quantised in single quanta given by

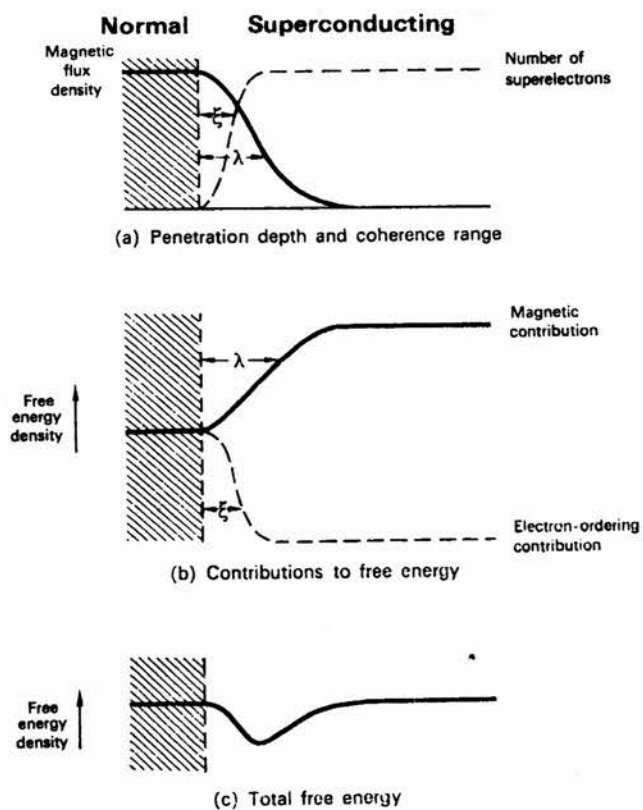


Figure 2.4 The surface energy for a type II superconductor.

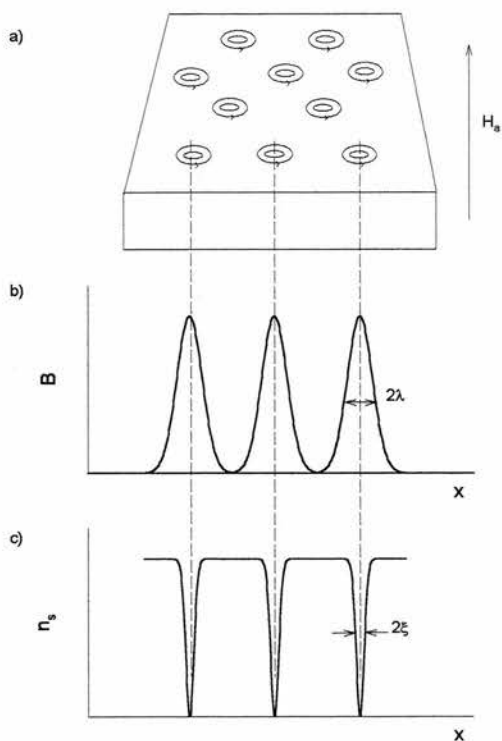


Figure 2.5 The mixed state of a type II superconductor with an applied field greater than H_{c1} .

$$\Phi_0 = \frac{h}{2e} = 2.07 \times 10^{-15} \text{ Wb} . \quad 2.18$$

The superelectron density and the magnetic penetration depth do not change abruptly at the domain boundaries. This leads to a periodic change in the superelectron density and magnetic penetration depth (see figure 2.5). The periodic change in field implies that any probe that can measure the internal field can directly determine the magnetic penetration depth and coherence length. Summing across the whole flux lattice will yield the probability distribution of the internal fields for the superconductor in the mixed state (see figure 2.6). The shape of this field distributions gives details of the exact structure and dynamics of the flux lattice. For the example given in figure 2.6 the flux lattice has the usual hexagonal structure.

It is possible to enter a mixed state below H_{c1} . If a type II superconductor is in a form in which the demagnetisation factor is important then a mixed state is found for applied field less than H_{c1} . On entering the mixed state, a reduction in magnetisation is observed. Decreasing the magnetisation leads to a reduction in the internal field causing the internal field to be lower than the critical field. In order to remove this instability the mixed state ensues. This is directly analogous to the formation of the intermediate state in a type I superconductor. An example of the magnetic response of a type II superconductor is given in figure 2.7 which shows the different magnetic states of a type II superconductor. Initially, the Meissner state is observed. On increasing the applied field, the magnetic flux is expelled from the sample and a perfect diamagnet with a susceptibility of -1 is observed. On increasing the field still further, the mixed state is formed. This allows flux into the superconducting state. Finally, when the magnetisation is zero the normal state results.

2.6.1 The Bean model.

The magnetisation measured in a magnetic hysteresis loop of a superconductor is dependent on the critical current. In 1962, Bean suggested a model to explain this relationship¹². The Bean model makes several basic assumptions, the first is that if a magnetic field is applied to a superconducting sample then the screening currents are

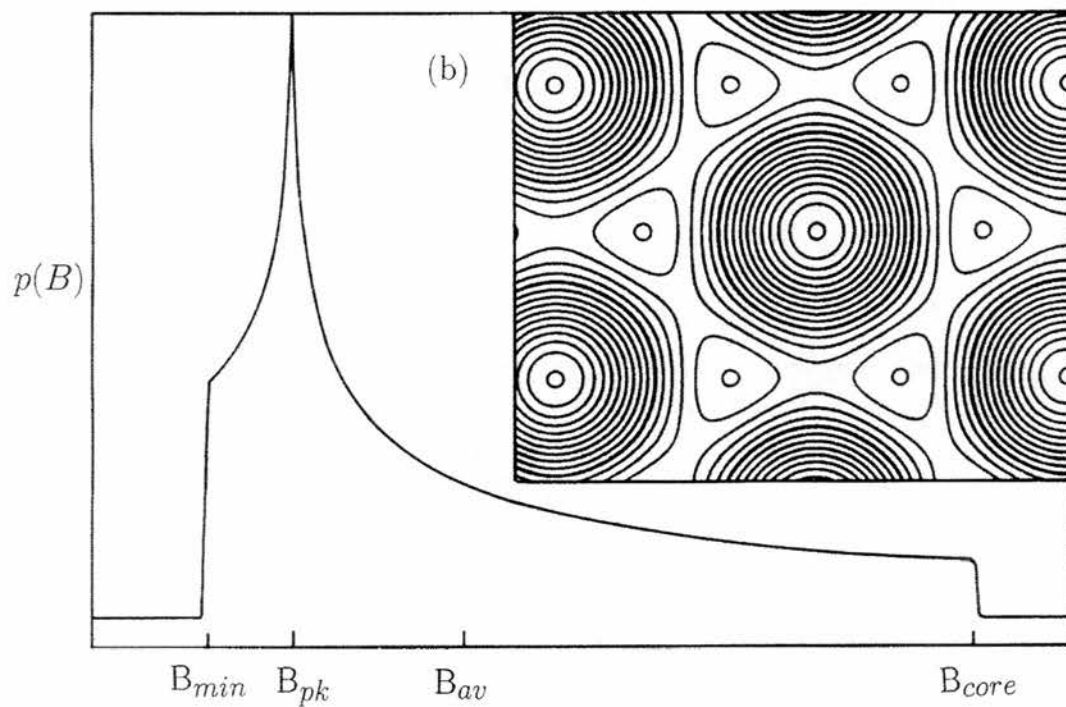


Figure 2.6 An example of the ideal hexagonal probability field distribution within a type II superconductor in the mixed state. The insert is a contour plot of the flux lattice.

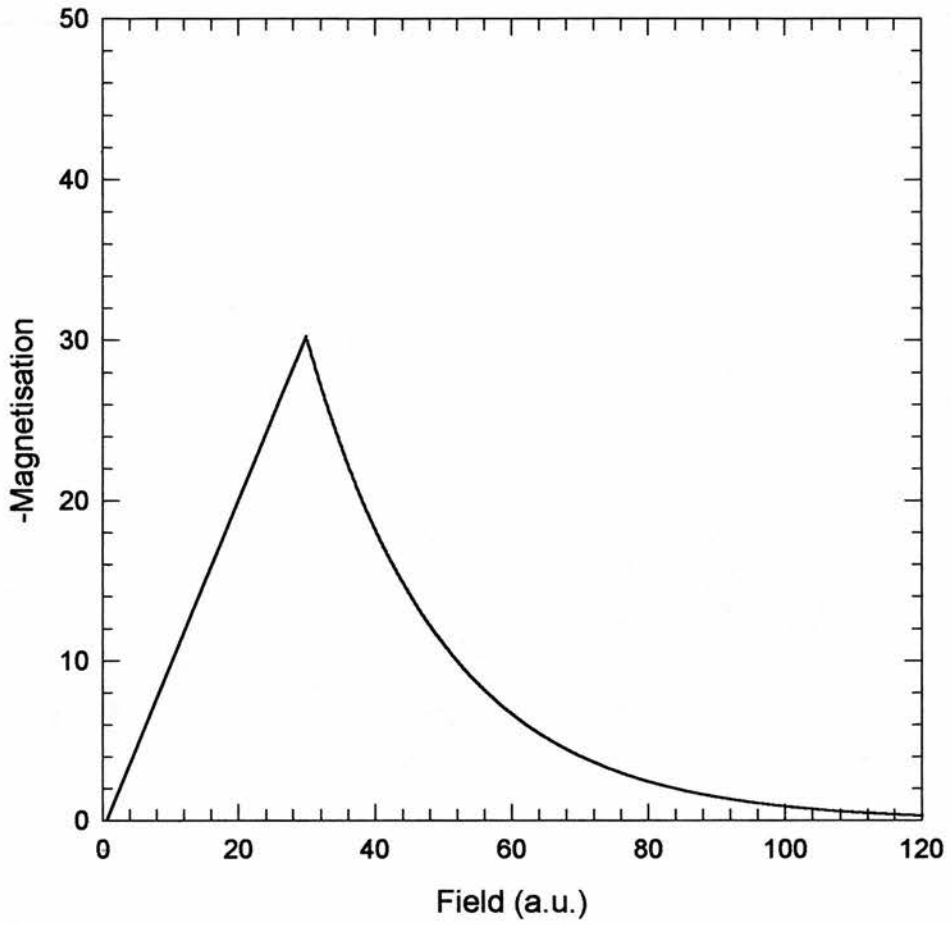


Figure 2.7 The virgin magnetisation curve for a type II superconductor.

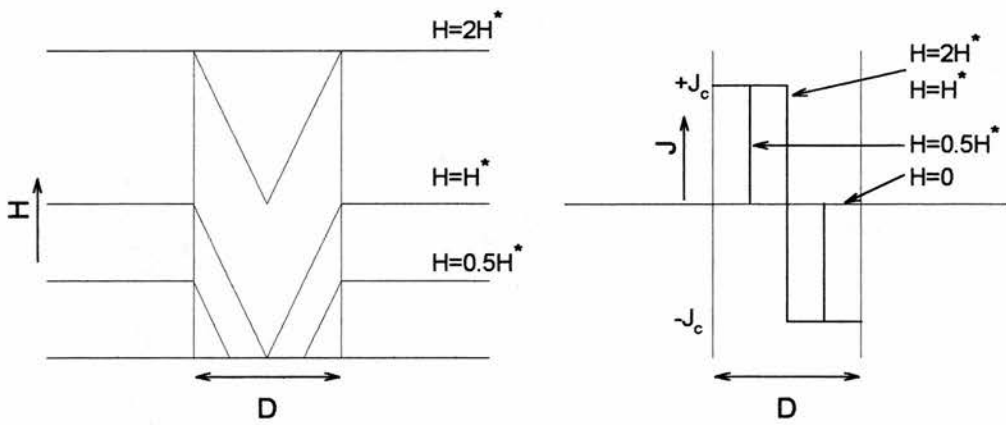


Figure 2.8 The field and critical current profile of a slab according to the Bean model.

either at a maximum value, J_c , or zero. Secondly, the maximum, or critical, current is independent of applied magnetic field. The resulting field and critical current profiles for a slab are shown in figure 2.8. When the applied field exceeds the lower critical field, H_{c1} , then the magnetic flux penetrates the sample. Because of pinning effects a uniform distribution through the sample is not observed. Instead it is assumed that the field gradient within the sample is constant at a value maintained by the value of the critical current. The Bean model was developed to allow a direct calculation of the critical current to be made.

Figure 2.9 shows the field profile within a superconducting sample at four points on the hysteresis curve. In figure 2.9a the applied field has reached a critical value in which the magnetic flux fully penetrates the sample. Increasing the applied field still further to a maximum value of $2H^*$ shows an increase in flux penetration (see figure 2.9b). Reducing the applied field by δH induces screening currents at the edge of the sample. In figure 2.9d, the external field has been reduced to zero but the flux remains in the sample shielded by the screening currents. As can be seen from figure 2.9d, the amount of trapped flux is dependent on the critical current. Moreover, the width of the magnetisation hysteresis can be used to calculate the critical current density. The internal field, B , of the sample is given as (in cgs units)

$$\underline{B} = \underline{H} + 4\pi\underline{M}. \quad 2.19$$

Rearranging and normalising for volume gives

$$4\pi\underline{M} = \frac{1}{V} \int_V (\underline{B} - \underline{H}) dV. \quad 2.20$$

Consider a cylindrical sample, i.e. a sample with a small demagnetisation factor, in which the magnetic field has fully penetrated the interior. This condition is illustrated in figure 2.9a. The Maxwell equation

$$\nabla \times \underline{B} = 4\pi \underline{J}_c \quad 2.21$$

can be simplified to

$$\underline{B} = B(r)\underline{k}. \quad 2.22$$

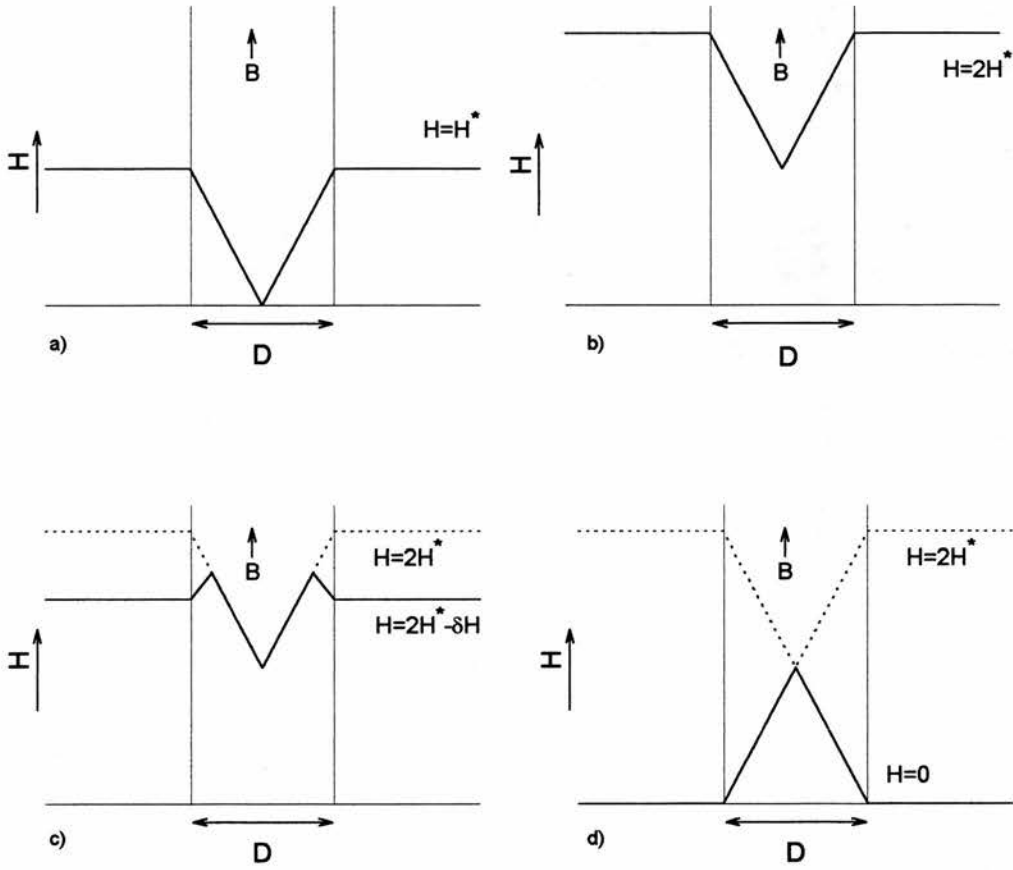


Figure 2.9 The field profile of a superconductor according to the Bean model at four points on a magnetic hysteresis curve. a) Complete flux penetration, b) the mixed state, c) reversing the applied magnetic field, thus showing the flux being trapped within the sample, d) the flux trapped when the applied field is returned to zero.

where r is the radial distance. Combining equations 2.21 and 2.22 and solving gives

$$B(r) = 4\pi J_c r + b \quad 2.23$$

where b is a constant of integration. The condition $B(R)=H$, where R is the radius of the cylinder gives

$$b = H - 4\pi J_c R. \quad 2.24$$

Therefore, it follows that

$$B(r) = 4\pi J_c (r - R) + H. \quad 2.25$$

Using equation 2.20 the magnetisation measured while increasing the field is given by

$$M_{\uparrow} = \frac{J_c}{\pi R^2} \int_0^R (r - R) 2\pi r \, dr = -\frac{J_c R}{3}. \quad 2.26$$

Similarly, the magnetisation on decreasing field is given by

$$M_{\downarrow} = +\frac{J_c R}{3}. \quad 2.27$$

Therefore, the critical current can be calculated from the difference in magnetisation, ΔM , where

$$\Delta M = M_{\downarrow} - M_{\uparrow}, \quad 2.28$$

and

$$J_c = \frac{3\Delta M}{2R}. \quad 2.29$$

However, for spherical samples

$$J_c = \frac{32}{1500} \frac{\Delta M}{\mu_0 d} \quad 2.30$$

where J_c is in A/m^2 , ΔM is in $m^3 kg^{-1}$.

2.6.2 Flux pinning and instabilities.

Flux pinning is caused by an interaction of the flux line lattice with the microstructure of the superconductor. Consider a region of normal state within the superconducting matrix and the flux line core. The flux line core is a normal region of volume $\pi\xi^2\ell$. If a region of normal state, for instance an inclusion, and flux line merge then the energy of the system is lower by

$$\Delta g = \pi\xi^2\ell \frac{B_c}{2\mu_0}. \quad 2.31$$

Therefore, the flux lines are likely to remain at the regions of normal state within the sample and are unlikely to move. The force on the vortices are the Lorentz force, F_L , viscous force, F_v , and pinning force and are given by

$$\underline{F}_L = \underline{J} \times \underline{\Phi}_0 \quad 2.32$$

$$\underline{F}_v = \eta \underline{v} \quad 2.33$$

$$\underline{F}_p = \underline{J}_c \times \underline{\Phi}_0 \quad 2.34$$

respectively. The flux pinning density is the critical Lorentz force and is given by

$$P_f = J_c B. \quad 2.35$$

At equilibrium the flux lattice is stationary if

$$\underline{F}_L + \underline{F}_v + \underline{F}_p = 0. \quad 2.36$$

However, as the field is increased the flux line lattice starts to break down. There are three mechanisms which can result in a breakdown of the flux line lattice; elastic interactions; plastic deformation; and shearing. A summary of these mechanisms is given in Table 2.1.

Elastic interactions	Plastic deformation	Shearing of the Flux line lattice
Weak interaction J_c small	J_c is determined by pair breaking	J_c is determined by pair avoidance
$b=B/B_{c2}$	$J_c \sim b(1-b)$	$J_c \sim b^{0.5}(1-b)^{0.5}$

Table 2.1 A summary of the stable breakdown mechanisms of the flux line lattice.

A superconductor with a very high J_c and therefore a high flux pinning strength can have an unstable flux line lattice. These magnetic instabilities are associated with magnetic flux

suddenly rushing into the sample^{13,14}. Surface shielding currents are created in a hard superconductor if the superconductor is exposed to a changing magnetic field¹². When the applied field exceeds the internal field by a critical amount, the surface shielding currents become unstable and the magnetic flux rushes into the sample. If the difference between the applied field and the shielding field exceeds approximately 0.1T then the flux jumps are generally complete and the magnetisation falls to zero. However, if the difference between the applied field and internal field is small, i.e. less than 0.1T, then the flux jumps are generally incomplete. In this case, the shielding currents are re-established and the magnetisation does not go to zero. Since a flux jump is an instability in the flux line lattice then the instability condition is generally not reproducible¹⁵. However, the difference in applied field between the flux jumps is generally approximately constant. The flux jumps are generally dependent upon temperature and ramp rate of the applied field.

Consider a superconductor cooled in a field such that the superconductor is in the mixed state. In addition, the applied field is isothermally increased by an amount, H_i . In this case the shielding currents have been established. Next, the superconductor receives a small increment in field, ΔH , in a short time. This time must be short relative to the thermal diffusion properties of the superconductor. If the total change in flux per unit volume is $\Delta\phi$ then $\Delta\phi/\Delta H$ is the adiabatic permeability. If the adiabatic permeability is infinite then a flux jump can occur. This is known as the adiabatic critical state model¹⁶. The physical picture is the pinning force on a flux line is reduced as the temperature is increased. Each time the applied field is increased the volume of superconductor exposed to the change in field receives locally an increase in temperature. This increase in temperature lowers the flux pinning force and gives rise to flux motion. This, in turn, can give rise to a further increase in temperature. Therefore, under certain conditions this can lead to a catastrophic breakdown in the flux line lattice. Using this adiabatic critical state model, the instability in the field limit as

$$H_{fj} = \left(-\pi^3 C J_c \left(\frac{\partial J_c}{\partial T} \right) \right)^{1/2} \quad 2.37$$

Assuming that the specific heat,

$$C = \beta T^3, \quad 2.38$$

and the temperature dependence of the critical current is

$$J_c(T) = J_c(0) \left(1 - \left(\frac{T}{T_c} \right) \right) \quad 2.39$$

then

$$H_{fj} = \left(\pi^3 \beta T_c T^3 \left(1 - \frac{T}{T_c} \right) \right)^{1/2}. \quad 2.40$$

If the non-adiabatic condition is considered and instead of thermal diffusion but magnetic diffusion then the dimensions of the sample become important¹⁷. This model yields the thickness condition,

$$d \leq \left(\frac{-10^2 \pi C}{4J_c \left(\frac{\partial J_c}{\partial T} \right)} \right)^{1/2}, \quad 2.41$$

where d is the thickness of the sample.

2.7 THE MACROSCOPIC THEORY- GINZBURG LANDAU THEORY.

The Ginzburg-Landau (GL) theory¹⁸ was developed before the more detailed BCS theory (see §2.8). However, the GL theory is not so restrictive as the BCS theory as it can easily be applied to a system that has an energy gap that is spatially inhomogeneous; for example, the intermediate state in a type I superconductor. The GL theory treats the macroscopic behaviour of the superconductor in which the overall free energy is important. This is in contrast to the BCS theory where a detailed spectrum of excitations is required.

In order to describe the superconducting state, a pseudowavefunction, $\psi(\mathbf{r})$, was introduced as a complex order parameter. $|\psi(\mathbf{r})|^2$ is used to represent the local superconducting electron density, n_s . This theory was developed by applying a variational method to an assumed expansion of the free energy density in powers of $|\psi|^2$ and $|\nabla\psi|^2$. This gives two complex differential equations for $\psi(\mathbf{r})$ and the vector potential $\mathbf{A}(\mathbf{r})$. The

result was a generalisation of the London theory and has dealt with situations in which n_s varies in space and to the non-linear response to fields strong enough to change n_s .

The free energy density, F_s , in the presence of a magnetic field is given by (in cgs)

$$F_s = F_N + \alpha|\psi|^2 + \beta|\psi|^4 + \frac{1}{2m^*} \left| \left(\frac{\hbar}{i} \nabla - \frac{e^*}{c} \underline{A} \right) \psi \right|^2 + \frac{B^2}{8\pi}. \quad 2.42$$

In a uniform external magnetic field, the Gibbs free energy function, G_s , is given by

$$\int G_s d^3x = \int \left(F_s - \frac{1}{4\pi} \underline{B} \cdot \underline{H} \right) d^3x \quad 2.43$$

The G_s must be stationary with respect to variations in the order parameter and the vector potential \underline{A} . The minimisation of G_s with respect to the order parameter, ψ^* gives the first GL equation

$$\alpha\psi + \beta|\psi|^2\psi + \frac{1}{2m^*} \left(\frac{\hbar}{i} \nabla - \frac{e^*}{c} \underline{A} \right)^2 \psi = 0 \quad 2.44$$

and the second GL equation is obtained by minimising G_s with respect to the vector potential, \underline{A}

$$\underline{J} = \frac{c}{4\pi} \text{curl } \underline{B} = \frac{e^* \hbar}{2m^* i} (\psi^* \nabla \psi - \psi \nabla \psi^*) - \frac{e^{*2}}{m^* c} \psi^* \psi \underline{A}. \quad 2.45$$

The study of these solutions in limiting cases (i.e. in zero applied field and in an applied field) has given the definition of the two fundamental parameters of the superconducting state.

In zero applied field, $\underline{A}=0$ and therefore $\nabla \underline{A}=0$. Using equation 2.42

$$F_s = F_N + \alpha|\psi|^2 + \beta|\psi|^4. \quad 2.46$$

If $\alpha > 0$ then $F_s - F_N$ has a minimum at $|\psi|^2 = 0$ i.e. the normal state. However, if $\alpha < 0$ then

$$|\psi|^2 = |\psi_\infty|^2 = -\frac{\alpha}{\beta}, \quad 2.47$$

i.e. the superconducting state. If the wavefunction is normalised, such that $f = \psi/\psi_\infty$, then in one dimension the first GL equation (equation 2.44) becomes

$$\frac{\hbar^2}{2m^*|\alpha|} \frac{d^2f}{dx^2} + f - f^3 = 0. \quad 2.48$$

Using this relation the coherence length, ξ_{GL} , for the variation of ψ is given by

$$\xi^2(T) = \frac{\hbar^2}{2m^*|\alpha(T)|}. \quad 2.49$$

It should be noted that this is not the same length as the coherence length introduced by Pippard, since ξ_{GL} diverges at T_c whereas Pippard's ξ is approximately temperature independent.

The second case to consider is when an external magnetic field is applied but the order parameter is constant, $\psi = \psi_\infty$. The second GL equation (equation 2.45) reduces to

$$\frac{c}{4\pi} \text{curl } \underline{B} = -\frac{e^*2}{m^*c} |\psi|^2 \underline{A}(\underline{x}) = \underline{J}(\underline{x}). \quad 2.50$$

Using this relation the magnetic penetration depth, λ , can be determined using the relation

$$\underline{B} = \text{curl } \underline{A}. \quad 2.51$$

It follows that

$$\text{curl curl } \underline{A} = -\frac{1}{\lambda^2} \underline{A}. \quad 2.52$$

As in the London treatment⁷ in section 2.1, the magnetic penetration depth is

$$\lambda^2 = \frac{m^*c^2}{4\pi|\psi|^2 e^{*2}} = \frac{m^*c^2}{4\pi n_s e^{*2}}. \quad 2.53$$

Since the classical electron radius, r_e , is given by

$$r_e = \frac{e^2}{4\pi\epsilon_0 mc^2} \quad 2.54$$

then it follows that the London magnetic penetration depth is given by

$$\lambda = \sqrt{\frac{m^*/m_e}{4\pi n_s r_e}}. \quad 2.55$$

The ratio of λ to ξ_{GL} can be used as an indicator to whether a superconductor is type I or type II. This indicator, κ , is the Ginzburg Landau constant and is defined as

$$\kappa = \frac{\lambda}{\xi_{GL}}. \quad 2.56$$

Indeed, Abrikosov showed in 1957¹⁹ that if $\kappa < 1/\sqrt{2}$ then the superconductor is type I, whereas a value of $\kappa > 1/\sqrt{2}$ indicates a type II superconductor. When considering the free energy in a type II superconductor the lower critical field, H_{c1} , defined as

$$H_{c1} = \frac{\Phi_0}{4\pi\lambda^2} (\ln(\kappa)). \quad 2.57$$

The upper critical field, H_{c2} , is defined as the field required to drive the superconductor normal, i.e. when the cores overlap, therefore

$$H_{c2} = \frac{\Phi_0}{2\pi\xi^2}. \quad 2.58$$

2.8 THE MICROSCOPIC THEORY- BCS THEORY.

In 1957, Bardeen, Cooper and Schrieffer introduced their microscopic theory of superconductor in that the effects of superconductivity could be explained²⁰. The basis of the BCS theory is the formation of superelectron pairs or Cooper pairs²¹. In 1950, Fröhlich²² had shown that it is possible to have an attraction between two electrons via a phonon interaction (see figure 2.10). During the interaction momentum must be conserved. However, between the initial and final states the energy need not be conserved. This is a result of the energy-time uncertainly principal. The interaction time of the phonon is small therefore there is a large energy uncertainty. Fröhlich showed that the process of an electron emitting a phonon is attractive if

$$E_1 - E_1' < h\nu_q \quad 2.59$$

where E_1 and E_1' are the energies before and after the emission of a phonon. This was suggested as a mechanism for superconductivity. This phonon mediated energy transfer can be used to explain the isotope effect²³.

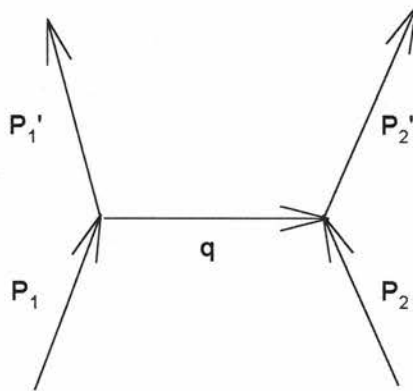


Figure 2.10 A schematic represent the Fröhlich interaction between two electrons (P_1 and P_2) via a phonon, q .

Cooper²¹, in 1956, considered the case of a metal at absolute zero with two additional electrons at the Fermi surface. The two additional electrons would occupy the same state and the momentum, P , would be greater than the Fermi momentum, P_f . Using detailed quantum mechanics, Cooper showed that there was an attraction between these two electrons and the bound state has an energy of less than $2E_f$. This attraction can be visualised by a thought experiment. Imagine an electron travelling through a positively charged lattice. The electrons attract a positive cloud due to the displacement of positive ions. This positive cloud attracts another electron. The net result is an overall attraction between electrons.

The model suggested by Cooper is not entirely realistic. Bardeen, Cooper and Schrieffer showed that Cooper's early work could be extended to a many electron system. If we consider a metal at absolute zero, the electrons at the Fermi energy or just below can lower the overall ground state energy by the formation of Cooper pairs. The interaction between the two electrons reduces the potential energy to a value less than twice the Fermi energy. This results in the formation of an energy gap, E_g , and is given by

$$E_g = 4\hbar\nu \exp\left(-\frac{1}{N(E_f)V}\right) = 3.5kT_c \quad 2.60$$

where ν is the average phonon frequency, V is the matrix element of the scattering interaction and $N(E_f)$ is the density of state at the Fermi energy. A consequence of the formation of an energy gap is the apparent maximum in T_c . If $N(E_f)V < 0.5$ then the maximum T_c is 35K. However, in order for superconductivity to exist there must be an increase in probability of finding an electron at a distance r with opposite momentum and spin. The probability of finding an electron in the same state, i.e. opposite momentum and spin, and within a distance r for a normal material is given by

$$\frac{1}{4}n^2 dv_1 dv_2 \quad 2.61$$

where n is the density of electrons. This is independent of r and hence there is no increase in spin correlations at small r . However using the results of the BCS theory, the

probability function increases at small r , thus indicating a correlation length or coherence length (see figure 2.11).

The BCS theory gives a good description of a wide range of superconductors. However, there are superconductors that show deviations from the BCS theory. For example: anomalous temperature dependence of the upper critical fields at temperatures close to T_c . In addition, the high temperature superconductors exhibit superconductivity at temperatures greater than the BCS limiting temperature, and also exhibit the possibility of d-wave rather than s-wave symmetry of the electron pairs. The possibility of local paired superconductivity has been introduced by some authors to explain this anomalous behaviour.

2.9 LOCAL PAIRING SUPERCONDUCTIVITY.

Local paired systems have been suggested to exist in a wide range of materials, not only in superconductors but also in heavy fermions, amorphous semiconductors, conducting polymers and in narrow band systems in which there is charge density wave formation. Of particular relevance to this thesis local pairing mechanisms have been used to explain some non-BCS behaviour in the so-called 'exotic' superconductors. Examples of superconductors that are suggested to exhibit non-BCS like behaviour include the A15, C15, Chevrel phase, carbides, nitrides and, of course, the high temperature superconducting cuprates^{24,25,26,27,28}. In general, these exotic superconductors have narrow electronic bands. There are several possible mechanisms responsible for local pairing.

1) *Strong electron-lattice coupling*: A strong electron-lattice coupling can cause an electron to locally deform the lattice. This local deformation causes the formation of a polaron. This leads to an attraction between electrons, if the coulomb repulsion can be overcome, via the lattice deformation.

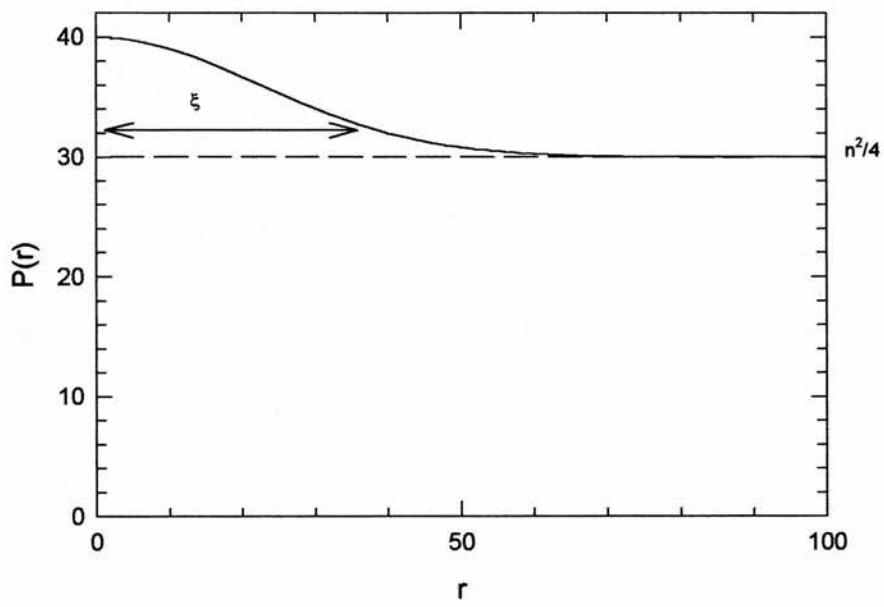


Figure 2.11 The probability distribution of finding an electron of opposite momentum and spin within a distance, r .

2) *Electron-quasibosonic coupling*: This is an attraction between the electron and quasibosonic excitations, such as excitons and plasmons. These excitations are electronic in nature.

3) *Electronic coupling*: An electronic coupling between electrons and electronic subsystems. Those which are not quasibosonic. This type of attraction is due to the overscreening of the coulomb repulsion term and hence an attraction is formed.

In contrast to a BCS superconductor, the electron pair in a local pair superconductor can exist above the transition temperature. The transition temperature increases when external or chemical pressure is applied to the local pairs. At some temperature greater than the superconducting transition temperature, the pairs finally break up and normal electrons are restored. Three distinct phases can be identified in a locally paired superconductor. The first is the low temperature phase in which the pairs are in a superconducting state. The second state is when the pairs are disordered and the superconductivity has been destroyed. The final state is when the pairs are dissociated and the system returns to a normal state. The transition between the first and second state can lead to the formation of a charge density wave. As the superelectron pairs are considered to exist above the transition then it follows that the energy gap must also appear above the superconducting transition temperature. This results in the energy gap being almost temperature independent below T_c and for temperatures well above T_c .

The major effect on the magnetic properties of a local paired superconductor is the effect on the upper critical field. The coupling between the local pair and the magnetic field leads to the upper critical field, H_{c2} , and the magnetic penetration depth being greatly enhanced. The enhancement of H_{c2} is a result of the short range coupling between the pairs. At temperatures close to T_c , H_{c2} deviates from the normal BCS model and two fluid model and follows a temperature dependence of the form

$$H_{c2} \propto \left(1 - \left(\frac{T}{T_c} \right)^{3/2} \right)^{3/2} . \quad 2.62$$

This results in a positive curvature of the H_{c2} at temperature close to T_c . The relationship between the magnetic penetration depth and temperature may also not be BCS-like. For $T \ll T_c$ the temperature dependence of the magnetic penetration depth is given by

$$\frac{\lambda_H(T)}{\lambda_H(0)} - 1 \cong \left(\frac{T}{T_c} \right)^{d+1} \quad 2.63$$

and approaching the transition temperature

$$\frac{\lambda_H(T)}{\lambda_H(0)} = \left(1 - \left(\frac{T}{T_c} \right)^{d/2} \right)^{1/2}. \quad 2.64$$

An overall comparison between BCS and local pair superconductors can be found in Table 2.2.

A more detailed explanation of the mechanisms for local paired superconductors can be found in references 29 and 30. However, it should be noted that similar temperature dependence of the critical fields and magnetic penetration depths have been noted in the barium bismuthate superconductors and this has been attributed to impurity effects. Clearly, a method for classifying these superconductors is required. This classification should be related to the fundamental superconducting parameters and the ‘conventional’ BCS and ‘exotic’ local pair superconductors need to be clearly distinguished.

Local pair superconductor	BCS superconductor
Real space pairing. All the electrons are paired via a short-range static attraction	Electrons near E_f participate in cooper pairing
Non ordered pairs can exist above T_c at T_c they undergo Bose condensation.	Cooper pairs are formed and condense at T_c .
E_g exists above T_c .	$E_g^{BCS}(0)$ decreases monotonically with increasing T.
Critical behaviour can deviate from the Ginzburg Landau type.	Classical Ginzburg Landau type critical behaviour.
Penetration depth for magnetic field	$\lambda_{LP} \geq (1 \text{ to } 100)\lambda_{BCS}$
$\kappa \gg 1$, extreme type II.	
Upper critical magnetic field. a) Paramagnetic effect ($T \ll T_c$), $k_B T_c \ll \mu_B H_{c2}$ b) $T \leq T_c$ orbital effect. Very large values of H_{c2} and positive curvature.	Clogston limit, $\mu_B H_{c2} \leq k_B T_c$
Effect of structural disorder is strong	Effect of structural disorder is weak.
Effect of magnetic impurities is weak	Effect of magnetic impurities is strong

Table 2.2 A comparison between the 'conventional' BCS superconductors and the 'exotic' local pair superconductors³⁰.

2.10 REFERENCES

- ¹ H. Kamerlingh Onnes, Leiden Comm. **120b**, **122b**, **124c** (1911).
- ² Superconductivity of metals and alloys. P.G. de Gennes. W.A. Benjamin, Inc. New York.
- ³ Introduction to superconductivity. M. Tinkham. McGraw Hill. London.
- ⁴ Superconductivity. R.D.Parks. Marcel Dekker, Inc. New York.
- ⁵ W. Meissner, R. Ochsenfeld, Naturwissenschaften, **21**, 787, (1933).
- ⁶ C.J. Gorter, H.B.G. Casimer, Physica, **1**, 306 (1934).
- ⁷ F. London and H. London, Proc. Roy. Soc. (London) **A155**, 71 (1935).
- ⁸ A.G. Meshkovsky, A.I. Shalnikov, Zh. Eksperim. I. Teor. Fiz. **17**, 851 (1947).
- ⁹ T.E. Faber, Proc. Roy. Soc. (London), **A248**, 460, (1958).
- ¹⁰ A.B. Pippard, Physica **19**, 765 (1953).
- ¹¹ Introduction to superconductivity. A.C. Rose-Innes and E.H. Rhoderick. Pergamon Press. Oxford
- ¹² C.P. Bean, Phys. Rev. Letters, **8**, 250 (1962).
- ¹³ B.B. Goodman, M. Wertheimer, Phys. Letters, **18**, 236 (1965).
- ¹⁴ P.S. Swartz, C.H. Rosner, J. Applied Phys. **33**, 2292, (1962).
- ¹⁵ J.M. Corsan, Phys. Letters, **12**, 85 (1964).
- ¹⁶ P.S. Swartz, C.P. Bean, Journal of Applied Physics, **39**, 4991 (1968).
- ¹⁷ S.L. Wipf, M.S. Lubell, Phys. Letters, **16**, 103 (1965).
- ¹⁸ V.L. Ginzburg, L.D. Landau, Zh. Eksperim. I. Teor. **20**, 1064 (1950).
- ¹⁹ A.A. Abrikosov Soviet Phys. JETP **5**, 1174 (1957).
- ²⁰ J. Bardeen, L.N. Cooper, J.R. Schrieffer, Phys. Rev. **108**, 1175 (1957)
- ²¹ L.N. Cooper, Phys. Rev. **104**, 1189 (1956).
- ²² Fröhlich, Phys. Rev. **79**, 845 (1950).
- ²³ E. Maxwell, Phys. Rev. **78**, 477 (1950).
- ²⁴ A.S. Alexandrov, Russ. J. Phys. Chem. **57**, 273 (1983).
- ²⁵ A.S. Alexandrov, JETP, **59**, 1125 (1984).
- ²⁶ S.P. Ionov, G.V. Ionova, V.S. Lubimov, E.F. Makai, Phys. Status Solidi B, **71**, 11 (1975).
- ²⁷ S.P. Ionov, G.V. Ionova, A.I. Maiybaev, L.A. Manakova, G.K. Semin, Akad. Nauk. SSSR. **45**, 589 (1981).
- ²⁸ B. Oh, K. Char, A.D. Kent, M. Naito, M.R. Beasley, T.H. Geballe, R.H. Hammond, A. Kapitulnik, J.M. Graybeal, Physical Review B. **37**, 7861 (1988).
- ²⁹ J.P. Carbotte, Reviews of modern physics. **62**, 1027 (1990).
- ³⁰ R. Micnas, J. Ranninger, S. Robaszkiewicz, Reviews of modern physics. **62**, 113 (1990).

3. Experimental Techniques

3.1 INTRODUCTION

In this chapter the sample preparation and the structural and magnetic characterisation procedures of the superconducting systems will be discussed. In order to conduct a successful muon spin rotation experiment the samples have to be carefully prepared and characterised. Using dc magnetometry, the critical temperatures and fields were determined. Room temperature x-ray diffraction and neutron diffraction were used for structural characterisation. Magnetic neutron diffraction was used to characterise the spin configuration in the magnetically ordered samples. The results obtained will be discussed in full in the relevant sample chapters.

3.2 SAMPLE PREPARATION.

All of the samples discussed in this thesis have been prepared by arc melting stoichiometric amounts of the constituent elements under an argon atmosphere. One exception is the YB_6 compound, which was purchased from Aldrich Chemicals. The spectrographically pure (>4N) constituent elements are placed together in the argon arc furnace on a water cooled copper hearth and then subjected to an electrical arc that heats the sample. The applied current is generally in the range between 0 and 400A giving a maximum temperature of approximately 3500°C. The atmosphere of the furnace is flushed with argon several times to insure no oxygen is present and the argon pressure is finally set to 600mbar. As a check of the purity of the argon atmosphere in the furnace and also to remove any existing gaseous impurities, a titanium getter is melted. On cooling, the titanium getter absorbs any reactive gaseous elements. Absorbing these impurities discolours the titanium getter thus giving a visible warning of a contaminated atmosphere. This ensures that the atmosphere is completely free of any impurities and that the sample can be melted without the risk of contamination.

Samples which require annealing are sealed in a quartz tube, which is flushed with argon three times with the final pressure adjusted to one third of an atmosphere. Argon is an inert gas and therefore does not react with the sample. However, samples in contact with the quartz tube may react with the silica at high temperatures thus contaminating the sample. In order, to reduce the risk of contamination the samples are loosely wrapped in tantalum foil.

3.3 STRUCTURAL CHARACTERISATION.

3.3.1 Theory of diffraction¹.

A beam with a wavelength, λ , comparable to the d-spacing of a crystal lattice can be diffracted by crystal planes. For structural analysis of crystals, the wavelengths are typically of the order of a few tenths of a nanometers. There are several beams that can be used, for example: electrons, neutrons and x-rays. The diffraction from a periodic crystal structure is given by Bragg's law

$$\lambda = 2d \sin \theta. \quad 3.1$$

This can be shown with simple geometry using figure 3.1. The amplitude of the resulting diffraction peaks is determined by the structure factor. If we consider the scattering amplitude given from A and B then the amplitude from A is

$$\text{Amp}_A = \frac{\phi}{r_A} f_A \exp(i(\underline{k}' \underline{r}_A - \omega t)) \quad 3.2$$

and from B is

$$\text{Amp}_B = \frac{\phi}{r_B} f_B \exp(i(\underline{k}' \underline{r}_B - \omega t + \delta)) \quad 3.3$$

where ϕ is the incident flux, f is the scattering power, r is the distance to the relevant detector, \underline{k}' is the momentum vector and δ is the phase shift. The phase shift is given by

$$\delta = \rho \cdot \Delta \underline{k} \quad 3.4$$

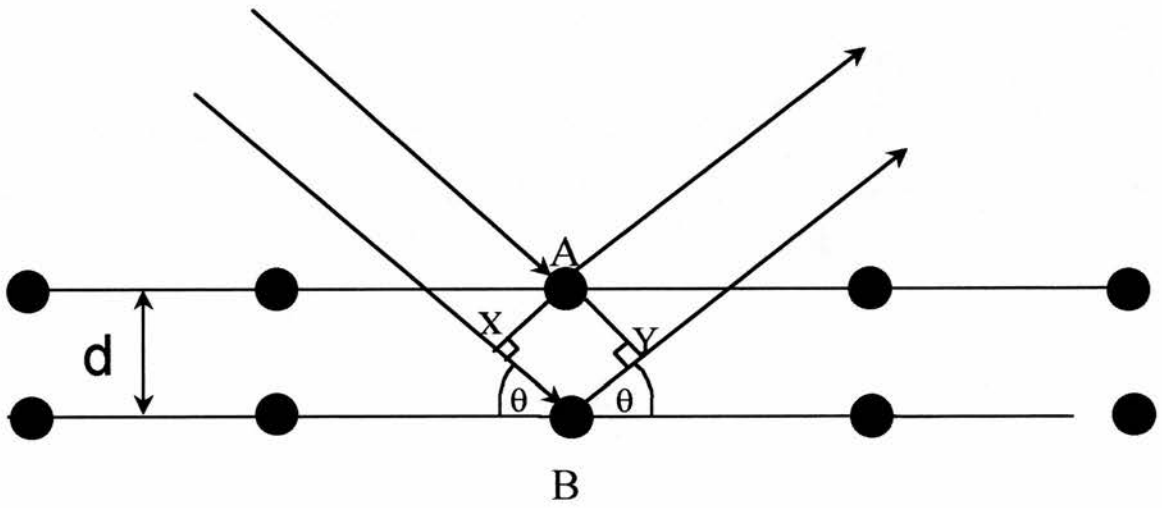


Figure 3.1 A schematic of the diffraction of a plane wave.

where ρ is the scattering vector. Therefore, the total amplitude at the detector is given by

$$D = \sum_{\substack{j=\text{all} \\ \text{atoms}}} \frac{\phi}{r_j} f_j \exp(i(\underline{k}' \cdot \underline{r}_j - \omega t)) \cdot \exp(i(\underline{\rho}_j \cdot \Delta \underline{k})) \quad 3.5$$

The distance to the detector from each atom, r_j , can be taken to be constant since the distance between the atoms will be the order of 0.1nm whereas the distance to the detector will be of the order of 1m. The relative amplitude at the detector is given by the parts that are only effected by j hence

$$A = \sum_{\substack{j=\text{all} \\ \text{atoms}}} f_j \exp(i(\underline{\rho}_j \cdot \Delta \underline{k})). \quad 3.6$$

The basis of a crystal is the simplest building block required to construct the crystal. Since ρ_j is determined by the basis of the crystal and $\Delta \underline{k}$ is the reciprocal lattice vector, G_{hkl} , for elastic scattering then the relative amplitude is given by the relation

$$A = \sum_{\substack{j=\text{all} \\ \text{atoms} \\ \text{in the} \\ \text{basis}}} f_j \exp(i(\underline{\rho}_j \cdot G_{hkl})) \quad 3.7$$

The structure of any sample can be reduced to a multiple number of unit cells, each constructed from a simple basis then the relative amplitude is redefined as the structure factor, S_{hkl} , and is given by the relation

$$S_{hkl} = \sum_{\substack{\text{all atoms} \\ \text{in basis } j}} f_j \exp(2\pi i(hu_j + kv_j + lw_j)) \quad 3.8$$

where h, k, l are the Miller indices. As the intensity of a reflection is the square of the scattering amplitude, the intensity of the Bragg peak is thus related to the basis of the unit cell and the Miller planes and is thus, effectively, the square of the Fourier transform of the structure under investigation.

The determination of the amplitude of the Bragg peaks by this method assumes that the atoms are stationary. However in a real sample this is not the case. The atomic positions vary due to their thermal motion. This leads to a mismatch in coherent scattering amplitude. Consequently the amplitude of the Bragg peaks is reduced by a factor known as the Debye Waller factor

$$\exp(-2W(\underline{\kappa})) \quad 3.9$$

where

$$W(\underline{\kappa}) = \langle \{\underline{\kappa} \cdot \hat{\underline{u}}(\ell)\} \rangle \quad 3.10$$

where $\underline{\kappa}$ is the scattering vector and $\hat{\underline{u}}(\ell)$ is the displacement of the atom at the ℓ th lattice site.

3.3.2 X-ray diffraction.

A beam of electrons with sufficient energy bombarding a target composed of a single element, can produce a x-ray spectrum. These x-rays have an energy of several keV (for Cu $K_{\alpha 1}$ the energy is 12.4keV). such x-rays have a relatively small penetration depth into the sample ($\sim 10\mu\text{m}$). However, their wavelengths are $\sim \text{nm}$, and thus they can be used for diffraction and structural determination. The x-rays are diffracted by the electron density of the atom, i.e. orbitals, rather than the nucleus. The scattering power of an atom is then dependent on the electron density and hence the scattering length of an x-ray is proportional to the atomic number. This may be a problem as elements close to each other in the periodic table have similar scattering lengths and therefore provide little contrast in x-ray diffraction.

3.3.2.1 *Experimental set-up for x-ray diffraction.*

The samples were initially characterised by the use of x-ray diffraction using Cu $K_{\alpha 1}$, $\lambda=0.147\text{nm}$, radiation. Two x-ray diffractometers have been used, dependent on the constituent elements of the sample and the resolution required.

Transmission geometry: The instrument used was a STOE Stadi P diffractometer (see figure 3.2). The x-rays pass first through a germanium monochromator which absorbs the Cu $K_{\alpha 2}$ emission and then through a thin layer of finely powdered sample (see figure 3.3). This set-up is optimised for samples that do not fluoresce. Fluorescence occurs when the incident x-rays excite the electrons of the constituent elements into a higher

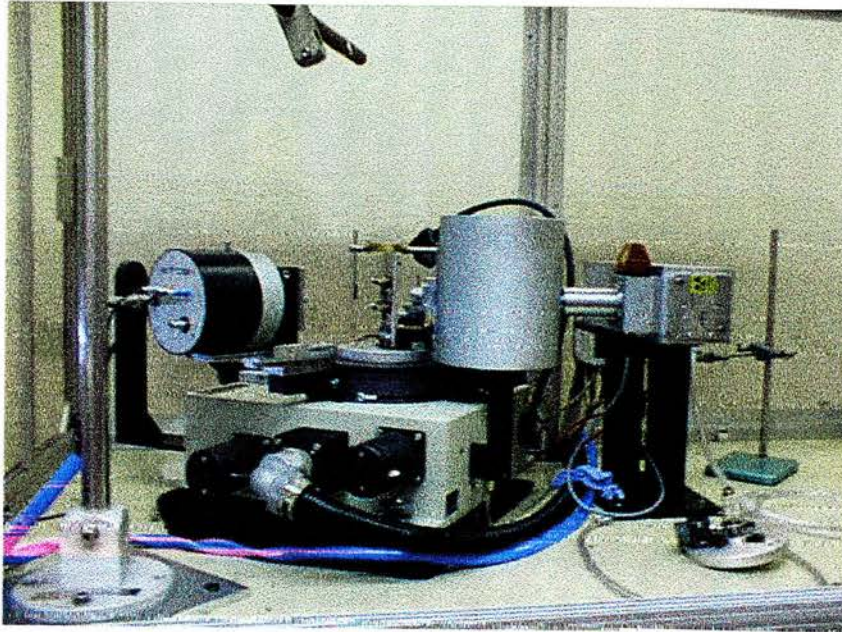


Figure 3.2 The STOE Stadi P diffractometer.

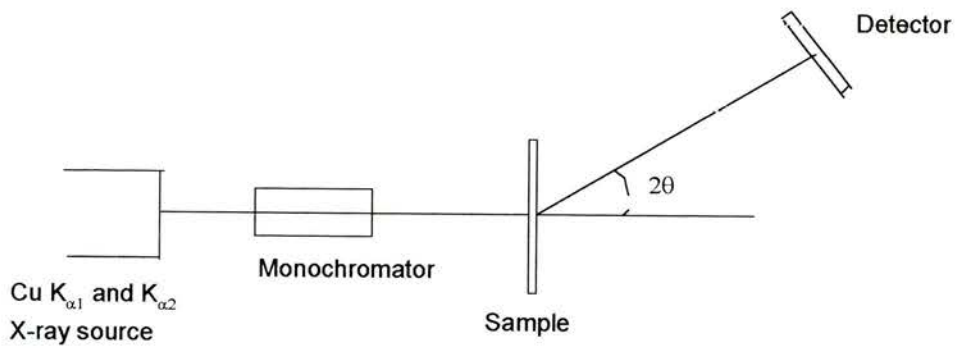


Figure 3.3 A schematic diagram of the x-ray diffraction apparatus in transmission geometry.

energy state. Once in this state the electrons return to the ground state, but in order to do so energy must be lost. This energy loss is achieved by the emission of an x-ray. The emission of x-rays from excited electrons is a random process, causing a large incoherent background thus losing the detail of the refinement. Elements that are likely to fluoresce in Cu $K_{\alpha 1}$ radiation are those close to copper in the periodic table, such as: Mn, Fe, Co and Ni. These elements have similar electronic configurations and therefore similar activation energies for the electrons. In addition, the x-rays have to pass through the mounted sample so only samples that are not strongly absorbing can be examined. However, this set-up does have the major advantage that the sample under investigation can be rotated as the diffraction pattern is collected and this reduces preferred orientation effects. The detector system attached to the transmission geometry instrument ensures a high resolution in 2θ (0.02°).

Reflection geometry: Again, the sample is finely powdered, in order to remove preferred orientation effects, and mounted onto a flat plate. The x-rays are emitted onto the surface of the sample and the diffracted x-rays pass through a monochromator. This monochromator is design to remove generally fluorescence from, for example Mn and Ni. However, this monochromator does not removed the Cu $K_{\alpha 2}$ x-ray. The sample plane moves along with the detector to increase resolution (see figure 3.4). The instrument used for reflection measurements was a Phillips diffractometer (see figure 3.5).

The results from both experimental set-ups are of the form 2θ verses intensity. This data was refined using the FULLPROF Rietveld refinement package². The results of the refinement have given the crystal structure, lattice parameters and atomic positions. A typical example of a refined x-ray diffraction pattern is shown in figure 3.6. The results from the x-ray diffraction will be discussed in the relevant sample chapters.

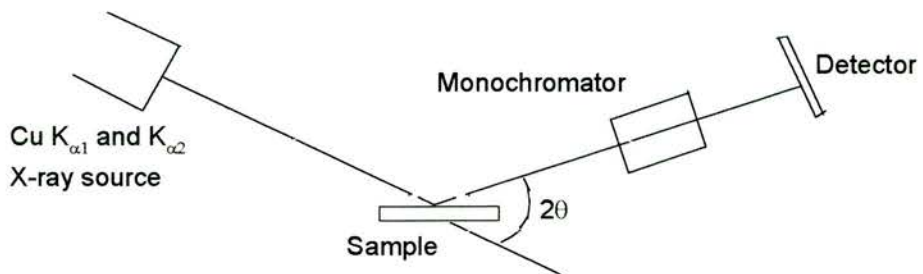


Figure 3.4 A schematic diagram of the x-ray diffraction apparatus in reflection geometry.

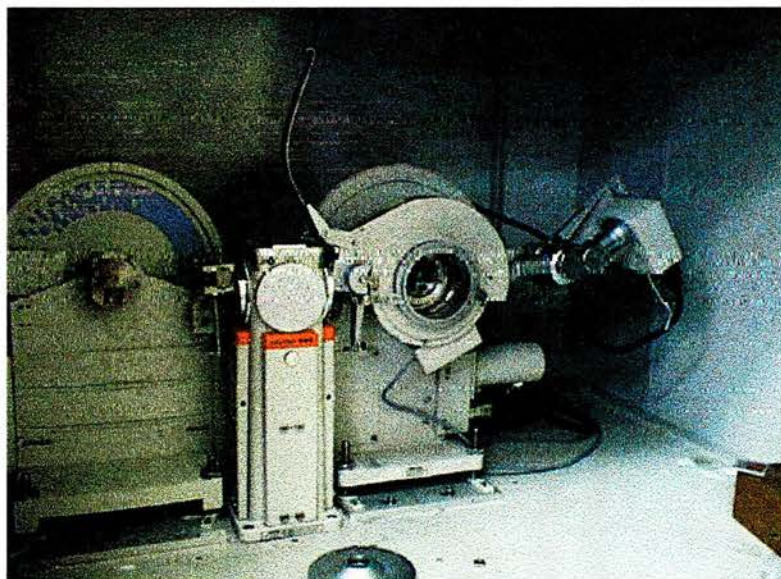


Figure 3.5 The Phillips diffractometers. These diffractometers are in reflection geometry.

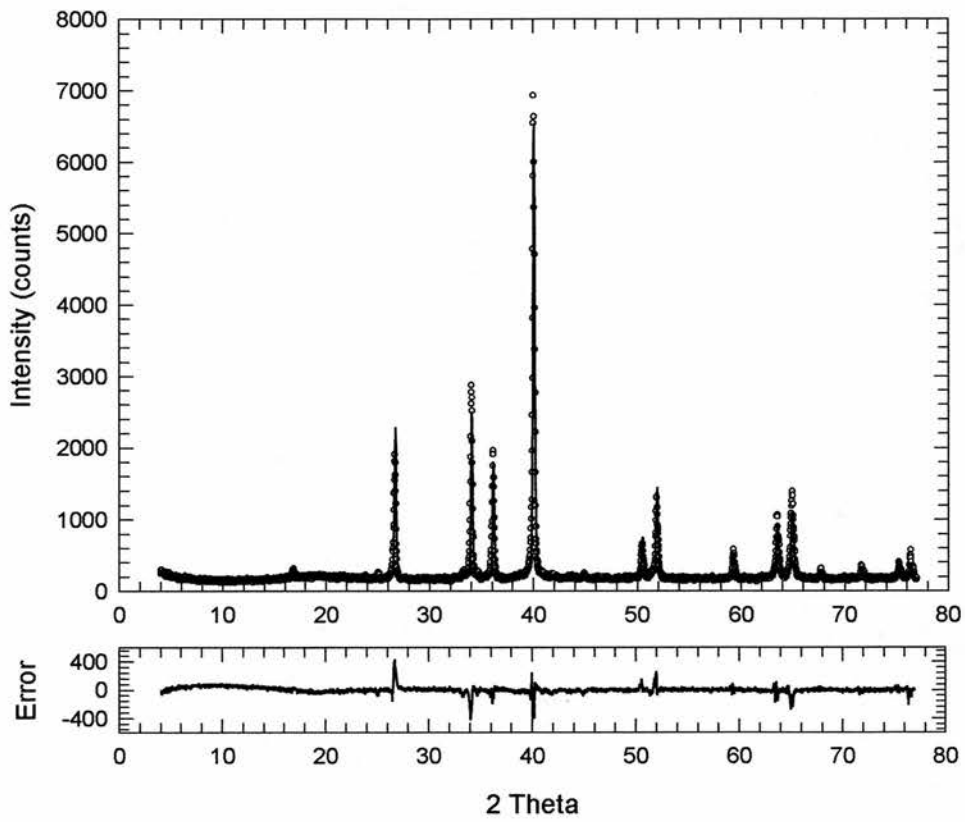


Figure 3.6 A room temperature x-ray diffraction pattern of $Y(Ni_{0.95}Co_{0.05})_2B_2C$. The line is the fit to the data.

3.3.3 Neutron diffraction¹.

The neutron is a particle consisting of one up quark and two down quarks with charges of $2/3$ and $-1/3$ respectively. Consequently the overall charge of a neutron is zero. However, the charge density has an internal structure. This leads to the neutron having a magnetic moment. A summary of the basic properties can be found in Table 3.1.

Mass	$m_n=1.008664924(14)\text{a.m.u.}$
Spin	$s=1/2$
Magnetic moment	$\mu_n=1.91304275(45)\mu_N$
Half life	$\tau=615(3)\text{s}$

Table 3.1 A summary of the basic properties of the neutron..

The neutron undergoes a β -decay into an electron, a positron and a neutrino. As the neutron has a finite lifetime of $\sim 615\text{s}$, they must be created for the specific experiment. There are two principal methods for the creation of neutrons: a nuclear reactor and by spallation processes.

A nuclear reactor relies upon a fission process using enriched uranium-235. In a fission reaction, a thermal neutron is absorbed by the uranium nucleus. This absorption of the neutron into the nucleus excites the uranium atom into an unstable state and causes the atom to split into a few fragments. Generally, these fragments are heavy elements and 2-5 neutrons. This is the process used at the 59MW high flux research reactor at the Institut Laue Langevin (ILL) in Grenoble, France.

At ISIS, at the Rutherford Appleton Laboratory (RAL), Oxfordshire the neutron production technique is based upon the spallation process. A proton with energy 800MeV collides with a uranium or tantalum target. This results in a wide range of particles including protons, pions, muons and neutrinos being produced. Most importantly about 10-20 neutrons per proton are produced from a 200 μA proton beam.

Both these methods produce neutrons in the MeV energy range. However, most neutron experiments require an incident energy of 25meV since the wavelength of a neutron with 25meV is of the order of the atomic spacing,

$$E = \frac{h^2}{2m\lambda^2}. \quad 3.11$$

In order to reduce the energy of the neutrons a moderation process is required. The high-energy neutrons produced by fission and spallation are brought into thermal equilibrium with the moderator through inelastic collisions. The moderators at ISIS consist of H₂O and CH₄ and at the ILL, the moderation process uses deuterium and graphite.

The interaction between the neutron and matter is a weak interaction. Similarly, the magnetic dipole interaction between the neutron and any unpaired electrons is also a weak interaction. Since the neutron does not undergo any long-range interactions, such as Coulomb interactions, the penetration depth into most materials is large. This differs from the penetration depth of charged particles, such as x-rays or electrons, where only a surface layer is generally probed. The neutron interacts only with the nucleus whereas x-rays interact with the electron clouds, thus neutrons and x-rays provide complementary information. As the neutron interacts with the nucleus, the scattering length varies from atom to atom, and even isotope to isotope. For example: hydrogen has a negative coherent scattering length whereas deuterium has a positive coherent scattering length. In addition, the magnetic moment of the neutron interacts with the magnetic field arising from the atomic electrons. This enables the magnetic structure and magnetic excitations to be examined in a material. If the material under investigation is paramagnetic then the magnetic moments are randomly orientated and hence an incoherent magnetic background is observed. However, once the sample orders magnetically then coherent magnetic scattering from the aligned magnetic moments is observed. For elastic magnetic diffraction the scattering length, p , is given by

$$p = \left(\frac{e^2 \mu_N}{2mc} \right) gJf \quad 3.12$$

where e is the electronic charge, μ_N is the magnetic moment, m is the electron mass, c is the speed of light, gJ is the effective magnetic moment and f is the form factor. The magnetic scattering lengths are of the same order of magnitude as nuclear scattering lengths.

3.3.3.1 *The experimental set-up for D1B at the ILL³.*

The experimental set-up for a neutron diffraction instrument at the ILL is similar to that of an x-ray diffractometer. A white beam of thermal neutrons is produced by the nuclear reactor. A single wavelength is selected from this beam using a pyrolytic graphite (002) or germanium (311) crystal. Graphite and germanium are used to enable range a choice of wavelengths (e.g. graphite, $\lambda=0.252\text{nm}$, germanium, $\lambda=0.128\text{nm}$). However, the graphite crystal gives a higher flux ($6.5 \times 10^6 \text{ncm}^{-2}\text{s}^{-1}$). The monochromatic beam is then collimated to the sample position (see figure 3.7⁴). A variety of sample environment equipment is available at the sample position. For the experiments conducted in this thesis an ‘orange’ cryostat with a temperature range of 1.5K to 300K was used.

For the neutron diffraction measurements the sample is finely powdered, in order to limit preferred orientation effects, and placed into a vanadium can. Vanadium is used because the coherent scattering length is almost zero and therefore no Bragg peaks are observed. The diffracted neutrons are collected as a function of angle 2θ , as in the case of x-rays. A typical diffraction pattern can be collected in 10 minutes. A picture of D1B can be seen in figure 3.8. The large green ‘banana’ shaped area in figure 3.8 is the detector bank. There are 400 ^3He detectors that cover a 2θ range of 80° . The detector bank can be rotated to give a range of angles from 2° to 160° . If large d spacing are to be measured then small scattering angles are required. Small d-spacings require large diffraction angles. However, increasing the angle of diffraction reduces the resolution of the instrument. This is shown from the partial differential of Bragg’s law which, assuming that the errors are uncorrelated, gives

$$\frac{\Delta d}{d} = \left[\left(\frac{\Delta \lambda}{\lambda} \right)^2 + \Delta \theta^2 \cot^2 \theta \right]^{1/2} \quad 3.13$$

For D1B, at angles of 10° the resolution is 0.2° and for angles of 70° the resolution is 1.2° , for an incident wavelength of 0.252nm .

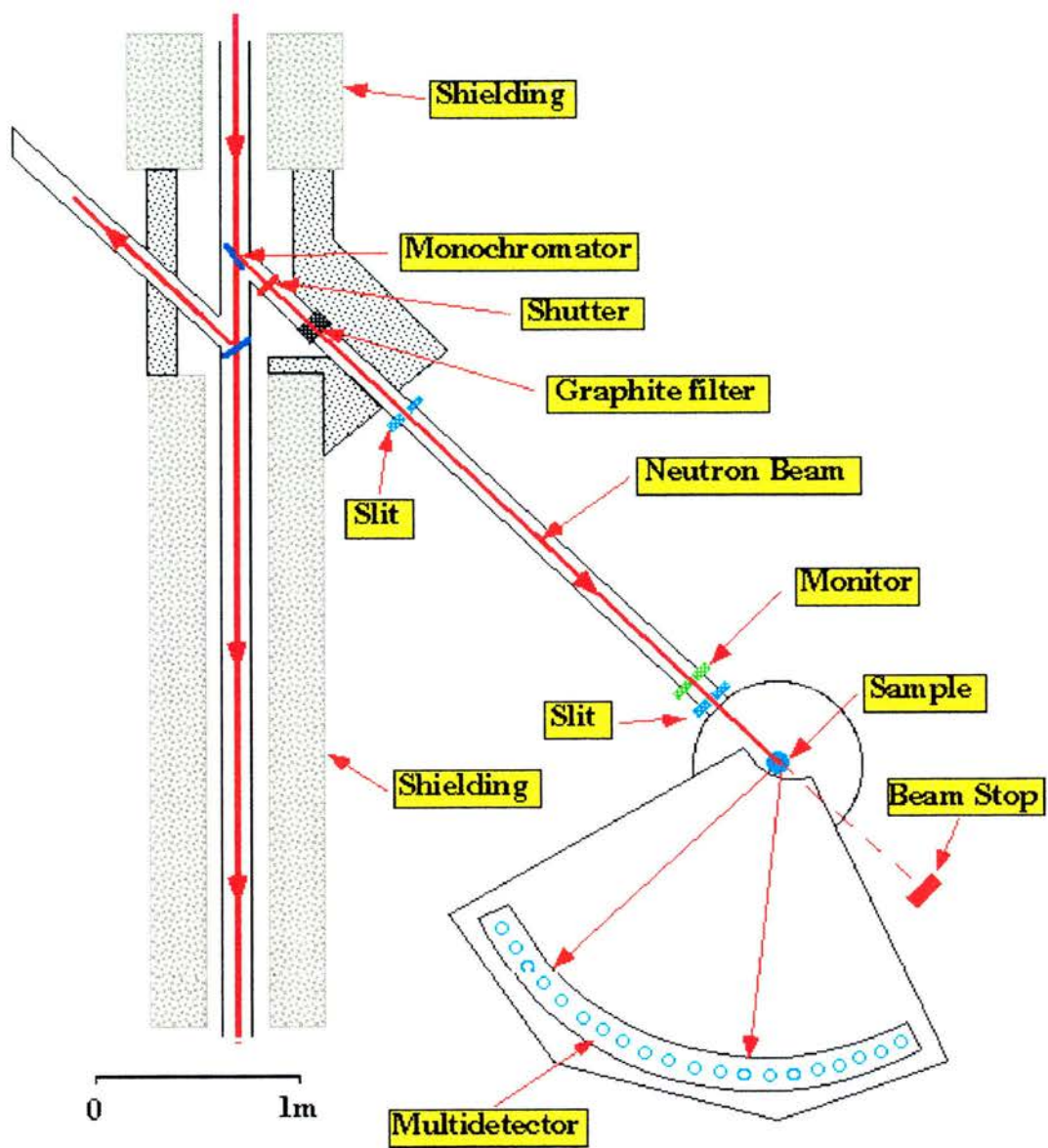


Figure 3.7 A schematic of D1B at the ILL.



Figure 3.8 A picture of the D1B instrument at the ILL.

3.3.3.2 The experimental set-up for POLARIS at ISIS^{5,6}.

The POLARIS powder diffractometer at ISIS is built on a 316K H₂O moderator with gadolinium foil at 2cm. Using this moderator the incident neutrons have wavelengths between 0.01nm and 0.6nm. This corresponds to incident energies of 8eV and 2meV. The sample is placed 12 metres from the tantalum target. The neutrons travel along an evacuated collimated tube to the sample. POLARIS has a number of detector banks in which the neutrons are counted and time sorted according to their time of arrival. Depending upon the position of the detectors, measured d spacing is defined by

$$d = \frac{ht}{mL \sin \theta}, \quad 3.14$$

where L is the path length of the neutron, h is Planck's constant. For measurements of large d spacing a low angle detector bank is used for which the detectors are between 14° and 30°. For short d spacing the backscattering detector bank is used (130° to 158°). However, the resolution is also dependent on the angular position of the detectors. This can be seen from the partial derivative of equation 3.12

$$\frac{\Delta d}{d} = \left[\Delta \theta^2 \cot^2 \theta + \left(\frac{\Delta t}{t} \right)^2 + \left(\frac{\Delta L}{L} \right)^2 \right]^{1/2}. \quad 3.15$$

Using this equation, it can be seen that the backscattering detectors have a much higher resolution than the low angle detector bank as the cotθ term approaches zero at 2θ=180°. There is also another detector bank on POLARIS, at 90°. This is to provide a region between the high resolution, back scattering bank, and long d-spacing, low angle bank (see figure 3.9⁷). As with D1B, POLARIS has a range of sample environments.

3.3.4 Analysis of diffraction spectra- Rietveld analysis⁸.

The unit cell parameters and atomic positions can be determined from the Bragg diffraction peaks and diffraction peak intensity. However, this technique is suitable for a diffraction pattern with well-defined Bragg peaks that are not overlapping. In most crystallographic studies this is not the case as in powder diffraction patterns the Bragg

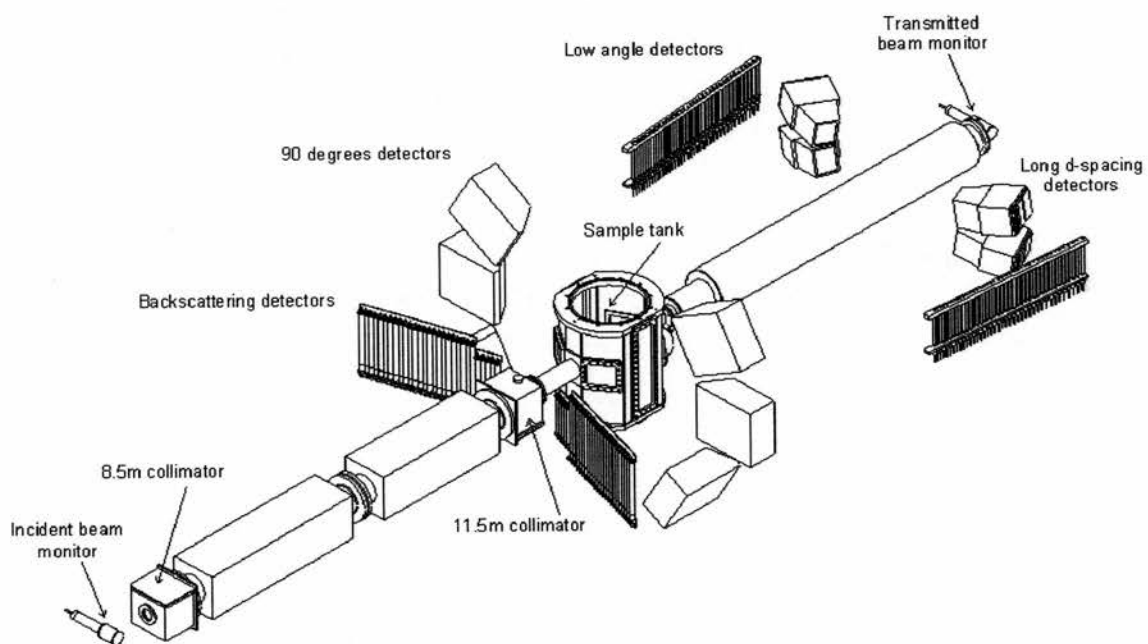


Figure 3.9 A schematic of the POLARIS instrument at ISIS.

peaks often overlap. Rietveld refinement was developed for solving such a problem. Using this method the crystal structure, lattice parameters, atomic positions and even the temperature factor can be determined from a powder diffraction pattern. The refinement procedure is based on a model of the unit cell from which a calculated pattern is obtained. This calculated pattern is then compared to the whole of the experimental diffraction pattern. Using a number of variables, such as the crystal symmetry, lattice parameters, atomic positions, temperature factor, resolution and line shape, the calculated pattern is least squares fitted to the experimental diffraction pattern, minimising χ^2 . There are a number of measures of the 'goodness' of the fit to the data, these are known as the R-factors. These factors provide more information than just the χ^2 alone. The definitions of the R-factors are given below.

The profile R-factor: This R-factor is associated with the whole pattern and is a measure of the goodness of the fit, it is defined as

$$R_p = 100 \frac{\sum_i |Y_{\text{obs}_i} - Y_{\text{calc}_i}|}{\sum_i |Y_{\text{obs}_i}|} \quad 3.16$$

where Y_{obs} and Y_{calc} are the observed and calculated intensities at a given point.

The Weighted R-factor: This also measures the goodness of the fit, taking into consideration the error associated with the number of counts and is defined as

$$R_{\text{wp}} = 100 \left[\frac{\sum_i w_i |Y_{\text{obs}_i} - Y_{\text{calc}_i}|^2}{\sum_i w_i |Y_{\text{obs}_i}|^2} \right]^{1/2} \quad 3.17$$

where the weighting factor is given by $w=1/Y_{\text{obs}}$.

The Bragg R-factor: This is associated only with the error in the peak intensities and is defined as

$$R_B = 100 \frac{\sum_k |I_{\text{obs}_k} - I_{\text{calc}_k}|}{\sum_k |I_{\text{obs}_k}|} \quad 3.18$$

where I is the intensity at a Bragg peak.

The expected R-factor: This, in an ideal case, is the expected value for the weighted R factor and is defined as

$$R_{\text{exp}} = 100 \left[\frac{N - P}{\sum_i w_i y_{\text{obs}_i}^2} \right]^{1/2} \quad 3.19$$

where N is the number of points in the refinement and P is the number of refined parameters.

χ^2 : This is a measure of the overall goodness of the fit and is defined as

$$\chi^2 = \left[\frac{R_{\text{wp}}}{R_{\text{exp}}} \right]^2 \quad 3.20$$

This method uses all the data rather than using just the structure factors and therefore increases the accuracy of the determined values.

3.4 MAGNETIC CHARACTERISATION.

The magnetic characterisation was undertaken using an Oxford Instruments Vibrating Sample Magnetometer (VSM) with a 12 Tesla magnet. The basic principle of operation is as follows: The sample is subjected to a DC field and then vibrated at a constant and known frequency, in our case 66.6Hz. Two pickup coils are placed above and below the sample. The voltage pickup in the sense coils is then directly proportional to the magnetic moment, μ , vibration amplitude, a_v , and vibration frequency, f_v ,

$$V = \text{Const} \cdot \mu \cdot a_v \cdot f_v \quad 3.21$$

Since the vibration frequency and vibration amplitude are known, the voltage pickup is then directly proportional to the magnetic moment. This induced voltage is calibrated against a small sphere of nickel of known mass and hence known magnetic moment. A schematic of the VSM is shown in figure 3.10.

The VSM is computer controlled with a standard RS232 computer connection. The magnet's power supply is a high current, low voltage power source and drives a NbSn wound superconducting wire. This is capable of producing fields of up to 12 Tesla. The sample is situated in a continuous flow He cryostat, allowing access to a temperature range of 3.8-311K. The temperature controller is a standard Oxford Instruments ITC4 with a Au-Fe/Chromel thermocouple. The sample is inserted from above mounted at the end of a carbon fibre rod in a delrin sample holder. Delrin is used since it is diamagnetic and its magnetic response is negligible compared to the signals observed from typical samples. A picture of the VSM used is shown in figure 3.11.

The VSM is an extremely powerful tool in the study of magnetic and superconducting materials. For the superconducting materials discussed in this thesis, superconducting transition temperatures, critical fields and full hysteresis curve can be measured. All the results obtained from the VSM will be discussed in the relevant sample chapter, but the experimental techniques shall be discussed in detail here.

The superconducting transition temperature, T_c , of a sample is determined by first cooling the sample in zero field to just below T_c and then applying a small dc field, usually of 6mT. The magnetisation is then measured as a function of temperature. T_c is the temperature at which the diamagnetic signal disappears (for example see figure 3.12). The lower critical field, H_{c1} , of the sample under investigation is determined by applying a slowly increasing field (0.5mT/s) after first zero field cooling the sample below the superconducting temperature. The lower critical field is defined as the field at which the magnetic flux first penetrates the sample, and the initial susceptibility first shows a deviation from linearity (see figure 3.13). This definition must be used with caution; if the sample is a powder then a random orientation of the grains within the sample may exist. This may lead to a distribution of demagnetisation factors and hence lead to the formation of an intermediate state in those grains with a high demagnetisation factor even below H_{c1} ⁹. The formation of the

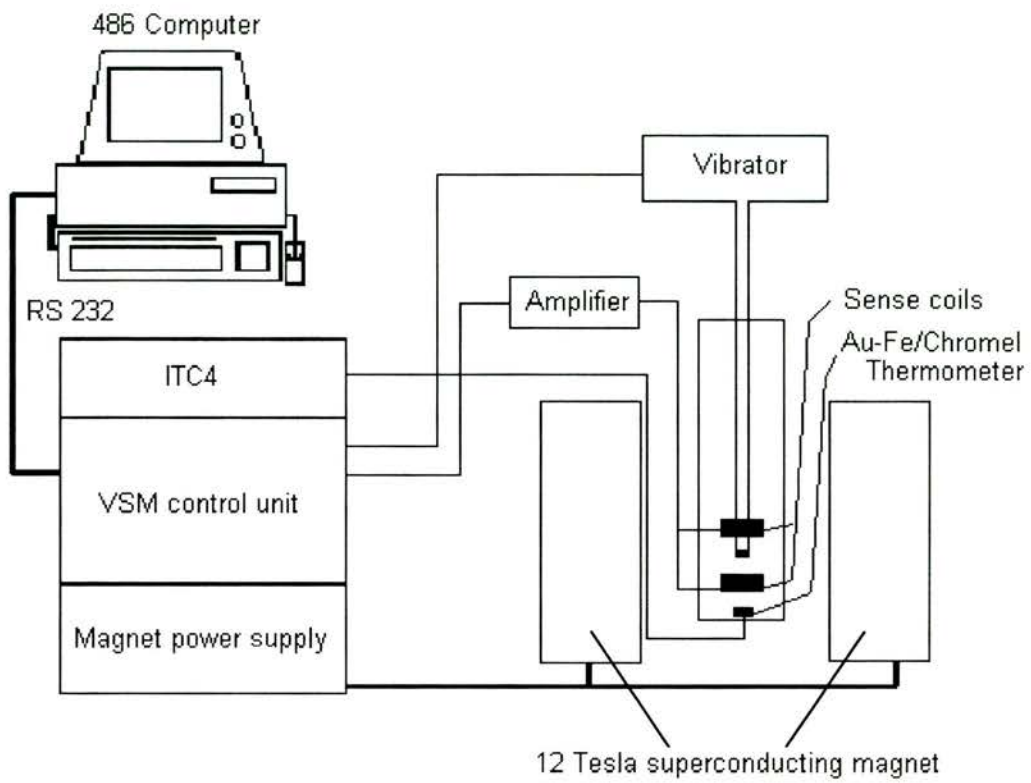


Figure 3.10 A schematic of the VSM



Figure 3.11 The Oxford Instruments Vibrating Sample Magnetometer.

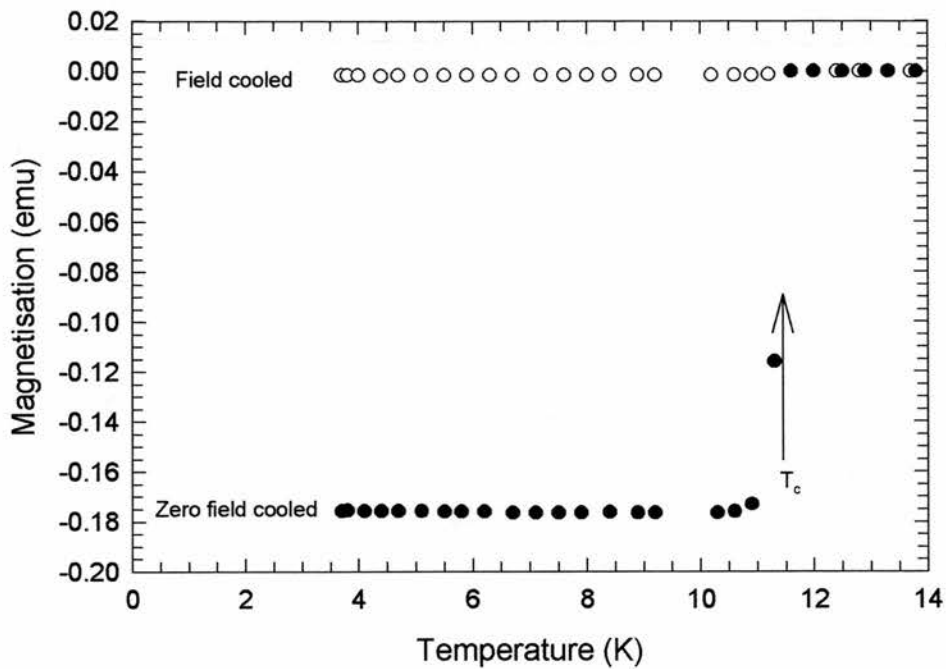


Figure 3.12 The temperature dependence of the magnetisation for Zr_2Rh . Using this graph T_c has been determined to be 11.2K.

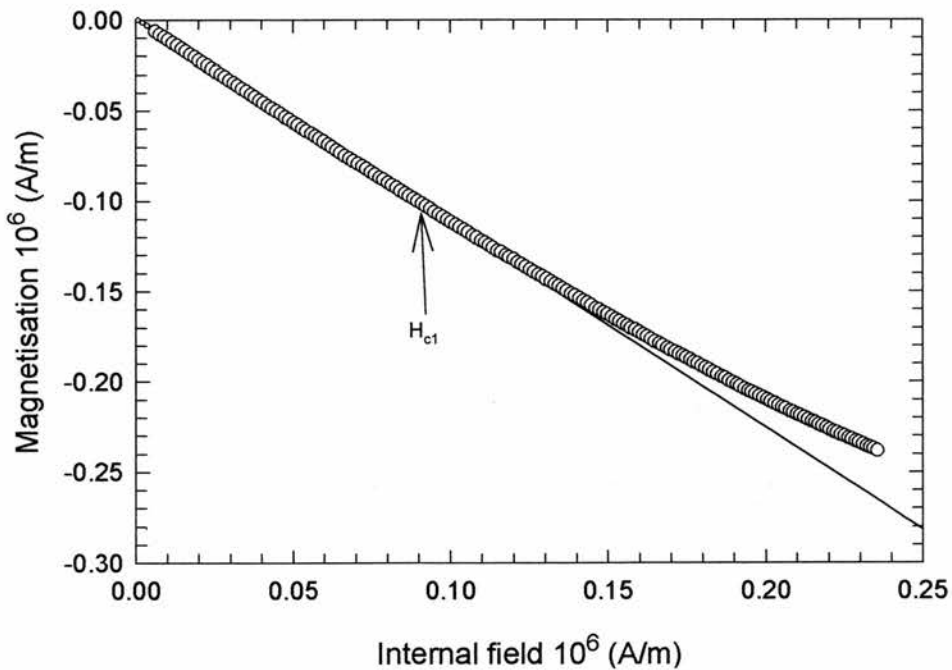


Figure 3.13 The virgin magnetisation curve for Zr_2Rh at 4K. The lower critical field, H_{c1} , is defined as the point at which a deviation from linearity is first observed..

intermediate state allows flux to enter the sample so a deviation from linearity is observed. However, if the sample is a solid sphere then a correction can be made for the demagnetisation factor.

The upper critical field, H_{c2} , is defined as the field at which the superconducting sample first becomes normal. This is also the point at which the magnetic hysteresis loop first closes (see figure 3.14). For the magnetic hysteresis measurements the applied field is swept at a rate of 5mT/s in order to reduce the error of the ramp rate dependence of the width of the hysteresis loop, i.e.

$$\frac{\Delta M}{\Delta M^*} = \ln\left(\frac{2\beta}{\beta^*}\right), \quad 3.22$$

where $\beta=dH/dt$, ΔM is the width of the hysteresis loop at a constant field and the asterisk is to distinguish between the measurements at different applied field ramp rates. This ramp rate dependence can be caused by strong flux pinning as a result of an impurity phase or crystal defects.

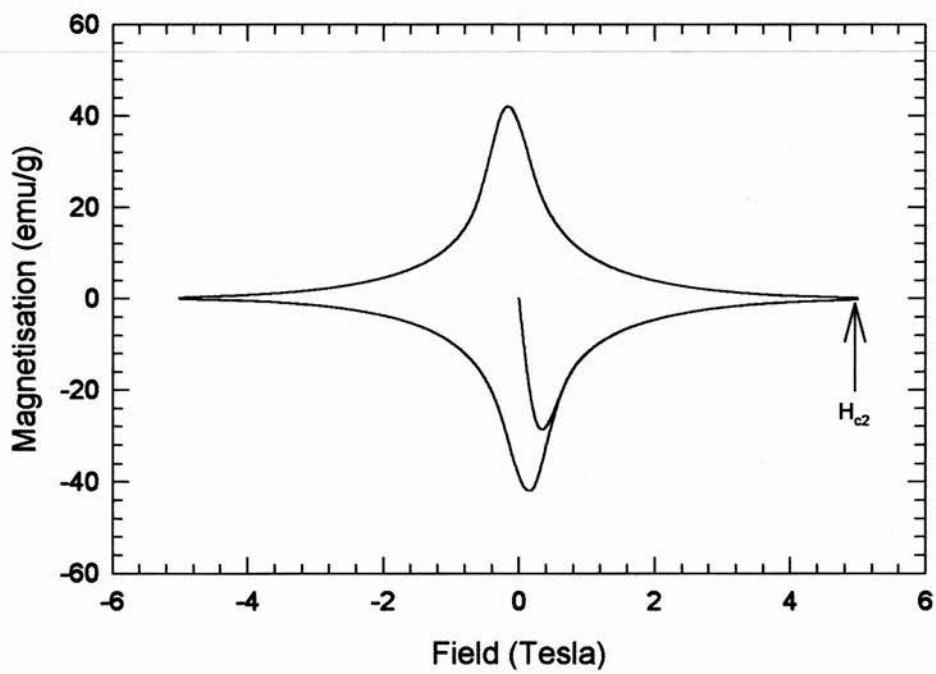


Figure 3.14 The magnetic hysteresis loop for Zr_2Rh at 4K. The upper critical field, H_{c2} , is defined as the field at which the loop first closes..

3.5 REFERENCES

- ¹ Neutron diffraction, G.E. Bacon, Clarendon Press, Oxford (1975).
- ² J. Rodriguez-Carajal. FULLPROF refinement program, LLB.
- ³ Guide to neutron research facilities at the ILL, ed. H. Blank and B. Maier, Imprimerie Poncet, France (1988).
- ⁴ <http://www.ill.fr/YellowBook/D1B/>
- ⁵ User guide for the POLARIS diffractometer at ISIS, S. Hull and J. Mayers, Rutherford Appleton Report, RAL-89-118 (1989).
- ⁶ Pulsed Neutron scattering, C.G. Windsor, Taylor and Francis Ltd, London (1981).
- ⁷ <http://www.isis.rl.ac.uk/Crystallography/POLguide.htm>
- ⁸ The Rietveld Method, ed. R .A. Young, International Union of Crystallography Monographs on Crystallography, Oxford University Press (1993).
- ⁹ Introduction to Superconductivity. Tickham. McGraw Hill Kogakusha Ltd. Tokyo.

4. Muon spin rotation.

4.1 INTRODUCTION.

μ SR is an extremely sensitive probe of the local magnetic environment of the implanted muon. There are three main experimental methods in muon spectroscopy: muon spin rotation, muon spin relaxation and muon spin resonance. These techniques are sensitive to both static, dynamic, nuclear, atomic or applied fields.

Muon spin rotation: For muon spin rotation the applied field at the sample is perpendicular to the muon momentum and spin direction. Implanted muon then precesses at a rate depending on the resultant of the internal field and the applied field. This is also known as transverse geometry.

Muon spin relaxation: For muon spin relaxation the applied field is generally zero and the detectors are placed forward and backward of the sample with respect to the direction of the muon beam and consequently the muon spin direction. Applied fields may also be applied parallel to the incident muon spin direction. This is also known as longitudinal geometry.

Muon spin resonance: This technique is similar to pulsed NMR. A static field is applied to the sample parallel to the initial muon spin direction and a radio frequency pulse is applied perpendicular to the initial muon polarisation direction. Muon spin resonance will not be discussed any further in this thesis.

In this chapter the basic principles of muon production, beam lines and muon spin rotation at the ISIS, Rutherford Appleton Laboratories, Chilton, Oxford, UK are discussed.

4.2 PROPERTIES OF A MUON.

The muon is classified as a weakly and electromagnetically interacting particle and belongs to the lepton family of fundamental particles, along with electrons and neutrons. Some of the fundamental properties of the muon are listed in Table 4.1

Mass	206.8m _e 0.113m _p
Spin	1/2ħ
Charge	+e,-e
Magnetic moment	3.183μ _p
Gryomagnetic ratio	135.5MHzT ⁻¹
Life time	2.197μs

Table 4.1 The fundamental properties of the muon.

The muon has a magnetic moment and a spin. The muons can be produced in one of two charged states: positive and negative. The spin and the magnetic moment of a positive muon are parallel and for a negative muon are anti-parallel. Negative muons are attracted to the nucleus of the constituent elements of the sample and form muonium, whereas the positive muon is either implanted at an interstitial lattice site, for a metal, or it may form muonium, for a semiconductor or insulator. Only positive muons have been used for this work. The muon has a mass approximately 1/9 of a proton and approximately 200 times an electron mass. The muon has a lifetime of approximately 2.2μs and decays into a positron and 2 neutrinos, to conserve parity.

$$\mu^+ = e^+ + \nu_e + \bar{\nu}_\mu \quad 4.1$$

The direction of the positron emission is preferentially along the muon spin direction. The positron emission direction is given by the relation

$$P(\theta) = 1 + a_0 \cos(\theta). \quad 4.2$$

where a_0 depends on the energy range of the positron. For example, $a_0=1$ if only positrons with the maximum energies are considered (see figure 4.1a) and $a_0=1/3$ if all energies are considered (see figure 4.1b).

4.3 MUON PRODUCTION AT ISIS.

At ISIS muons are produced from pions which in turn have been produced by protons of sufficient energy bombarding a carbon target.



The pion decays into a muon and a neutrino



Each pion has an average lifetime of 26ns. A spin-polarised beam can be produced by using the low energy pions, which have stopped near to the surface of the target. The positive pions will then decay according to equation 4.4. The positive muons emerging will be 100% spin polarised. Any negative pions will be captured by the target nuclei and the decay will not be observed. This type of muon generation is called surface μ^+ beam production. At ISIS the positive muon beam is produced by placing a water cooled graphite target into the path of the 200 μ A proton beam. This target is 7mm thick and at 45° to the incident beam. The extracted muon beam has the same time structure as the incident proton beam and consists of two pulses, each pulse having a full width half maximum of 80ns, separated by 340ns. The repetition rate for these two pulses is 50Hz.

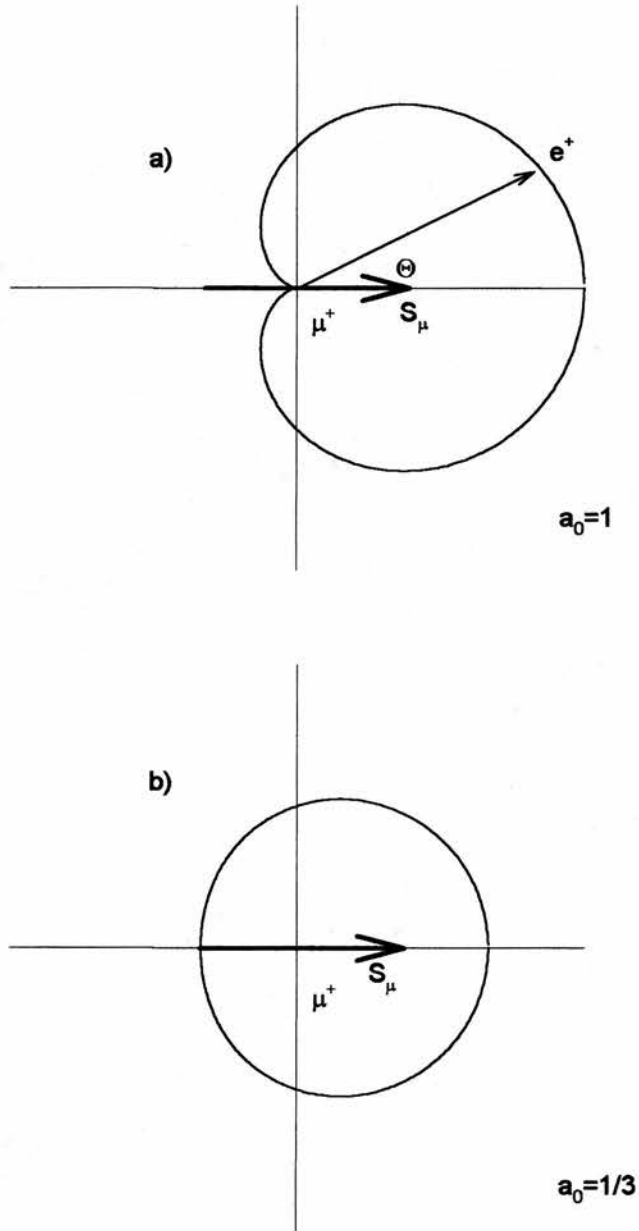


Figure 4.1 The angular distribution of the positron emission considering a muon with, a) maximum energy only, b) all energies.

4.4 THE MUON SPECTROMETERS AT ISIS.

4.4.1 The muon beam lines at ISIS.

The EC muon beams at ISIS consist of quadrupole focusing magnets and bending magnets along with a separator and an electrostatic kicker which take the muon beam into three independent spectrometers, DEVa, MuSR and EMu. A schematic of the muon beam is shown in figure 4.2.

The quadrupole magnets focus the beam whereas the bending magnets select the required momentum, 26.5MeV/c. However, selecting the momentum of the muon beam does not eliminate contamination of the beam from positrons of the same momentum. In order to remove these positrons, which are generated by in-beam decay, an electrostatic separator is used. This separator consists of a vertical electric field and a horizontal magnetic field. The force on the muon can be balanced so that the muon is unaffected, in theory. In practice the muon spin direction is shifted by, approximately, 7° from the momentum axis and should be corrected for in any data analysis. The in-beam positrons have the same momentum but greater velocities. Therefore, the positrons are deflected out of the muon beamline. The proton beam produces two muon pulses every 50Hz. The first pulse is split between DEVa and EMu whereas the second pulse continues towards MuSR without being affected. The beam is split by using the electrostatic kicker. This kicker consists of two grounded outer electrodes and a thin central anode. The first pulse is equally split between the EMu and DEVa by applying 32KV across the anode. In 100ns, the voltage is reduced to zero and the second pulse passes without deviation (see figure 4.3).

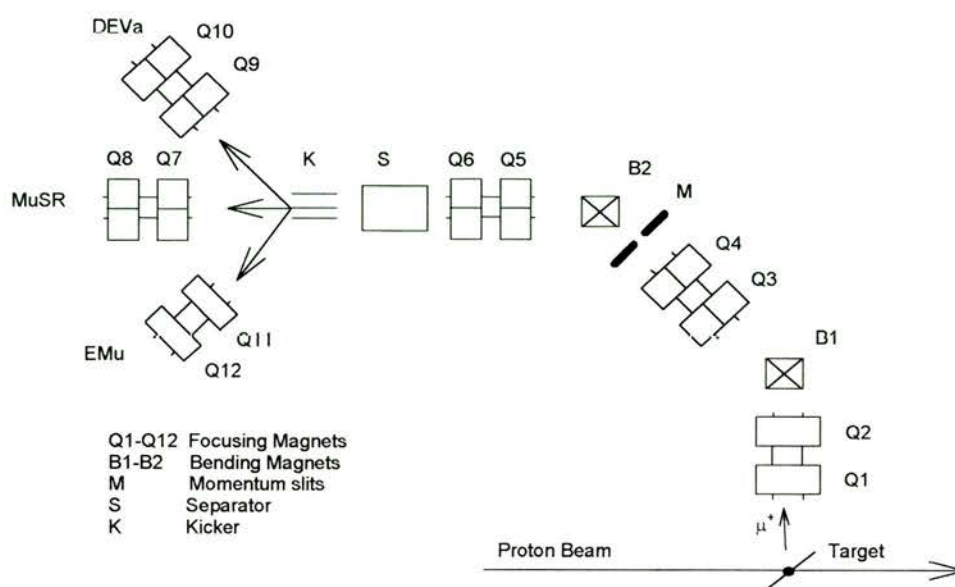


Figure 4.2 A schematic of the EC muon beams at ISIS.

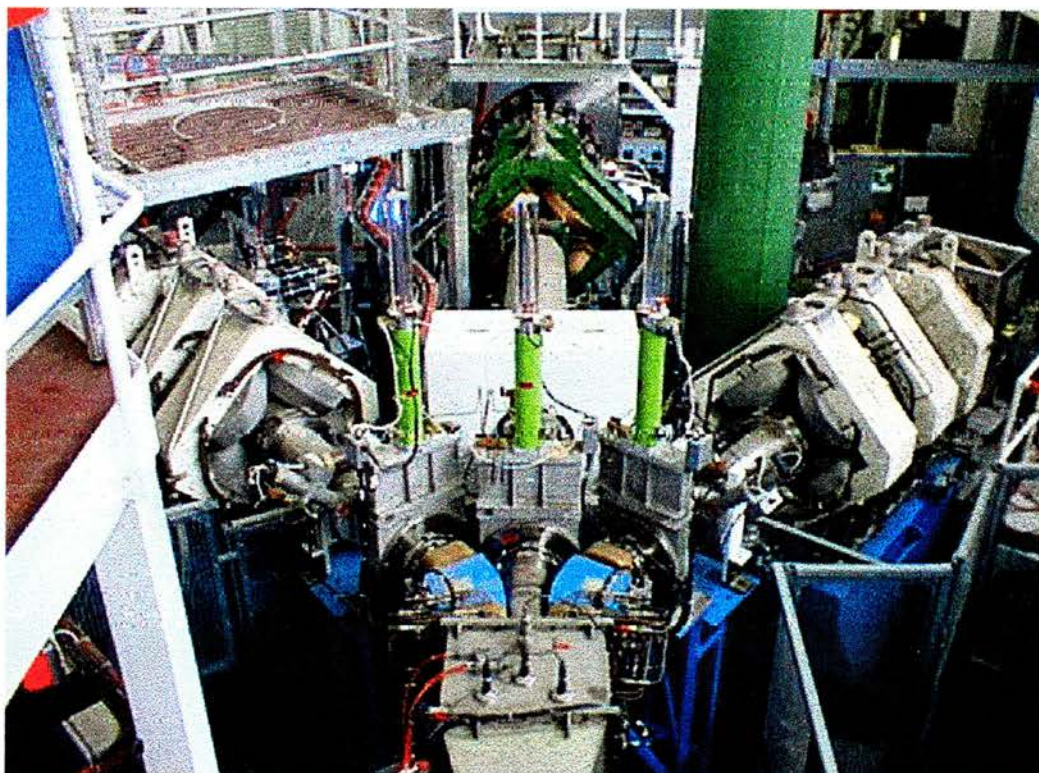


Figure 4.3 The electrostatic kicker separating the muon pulse into the three muon instruments at the end of the beam line.

4.4.2 The spectrometers.

At ISIS, there are two spectrometers available to users, i.e. EMu and MuSR. The third beam line is a development instrument, DEVa, which is devoted to the development of such techniques as muon resonance and slow muons. The EMu beamline instrument can only be used in a longitudinal geometry; i.e. the detectors and applied field are parallel to the muon spin and momentum directions. However, the MuSR instrument can be used in either transverse or longitudinal geometries. In transverse geometry, the muon spin is perpendicular to the applied field direction. In the longitudinal set-up, the difference between EMu and MuSR is the maximum applied field. For EMu, the maximum field is 0.4T from a set of water-cooled Helmholtz coils whereas on MuSR it is only 0.2T from a set of Helmholtz coils. Also, there is another important consideration. Since the muons for EMu have been ‘kicked’ down the beamline a larger beam spot and hence a larger background results. Each instrument has a set of compensation coils to ensure zero field. These are used to set the field at the sample position to less than 5×10^{-7} T in any given direction.

Each user instrument consists of 32 positron scintillator detectors. These detectors group into two sets. Each set of detectors consists of 16 lightguides and photomultiplier tubes and are divided into either forward or backwards detectors, for longitudinal geometry, or left and right detectors, for transverse geometry. Figure 4.4 shows the MuSR instrument in transverse geometry.

The positrons are detected by the emission of light from a scintillator down a light guide and into a photomultiplier. The photomultiplier converts the light pulse into an electrical signal, which is collected by the data acquisition electronics (TDC’s). Each electrical pulse is placed into a time bin. Each instrument has a maximum of 2000 time bins and a range of time bins widths (8, 16, 24, 32ns).

Both instruments have a variety of sample environments to ensure that a wide range of temperatures can be obtained. For MuSR, temperatures from 40mK-5K can be achieved in a dilution refrigerator; temperatures from 1.5K to 320K are available in an orange

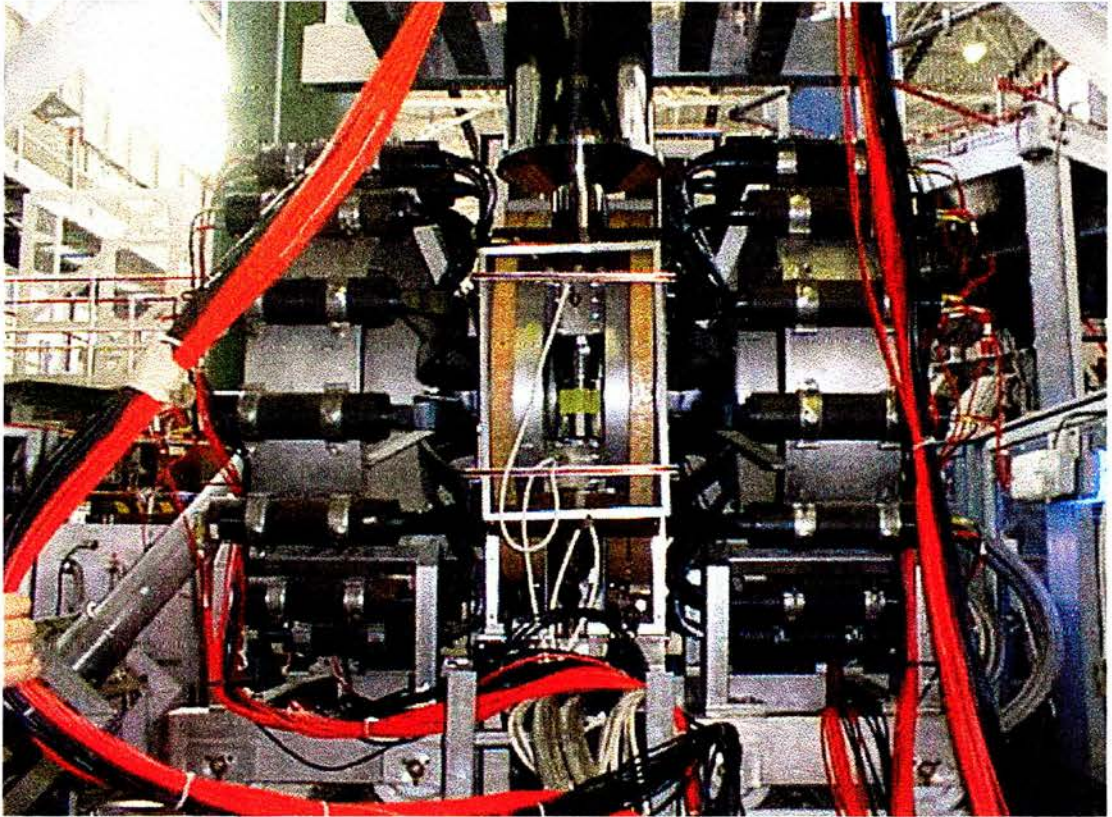


Figure 4.4 The MuSR instrument in transverse geometry with the dilution fridge inserted.

cryostat. The closed cycle refrigerator can provide temperatures between 10K and 350K. The EMu instrument has a similar range of sample environments except that the dilution refrigerator is replaced by a sorption cryostat which has a temperature range of 300mK to 50K. All sample environments have thin aluminised Mylar windows to ensure that the low energy muons are implanted into the sample and not into the surrounding sample environment.

4.5 THE MUON SPIN ROTATION TECHNIQUE.

4.5.1 Sample mounting.

The sample under investigation is generally coarsely powdered and mounted onto a sample plate using GE varnish. GE varnish has a high thermal conductivity, which reduces thermal gradients across the sample. The samples inserted into the orange cryostat are mounted onto an aluminium sample holder (40mmx40mmx0.5mm) while for the dilution refrigerator samples, a silver plate (40mmx40mmx0.5mm) is used, because aluminium has a superconducting transition at 1.1K. Moreover, since the dilution refrigerator relies upon a cold finger attachment to the cryogen a superconductor, such as Al, does not provide a sufficiently high thermal conductivity. Also, should any muons pass through the sample will land in the silver which has small nuclear moments and therefore will not contribute a significant time dependent background. Around the outside of the sample any exposed silver or aluminium is covered with dried Fe_2O_3 mixed with Bostick glue. Any muons implanted into the Fe_2O_3 precess at 210MHz^1 . This frequency is well above the highest observable frequency on MuSR (approximately 8MHz) and results in the muons being completely depolarised within the MuSR time window. To ensure ideal performance the Fe_2O_3 powder is dried by heating in air at 900°C for 1 week.

4.5.2 The time evolution of the muon spin direction.

A magnetic moment placed in a field experiences a torque which acts to align the magnetic moment with the field,

$$\underline{\tau} = \underline{\mu} \wedge \underline{B}. \quad 4.5$$

However, if the initial magnetic moment is not parallel to the field then the moment precesses around the field. The torque is also related to the rate of change of angular momentum and using classical mechanics,

$$\underline{\tau} = \frac{d\underline{S}}{dt}. \quad 4.6$$

The magnetic moment is proportional to the spin,

$$\underline{\mu} = \gamma \underline{S} \quad 4.7$$

where γ is the gyromagnetic ratio, for our case the muon. Combining equations 4.5, 4.6 and 4.7 gives

$$\frac{d\underline{S}}{dt} = \gamma \underline{S} \wedge \underline{B}. \quad 4.8$$

This equation defines the equation of motion for the spin (see figure 4.5).

Using simple vector analysis, for small angles

$$|d\underline{S}| = |\underline{S}| \sin \theta d\phi \quad 4.9$$

and using the definition of a cross product equation 4.8 becomes

$$|\underline{S}| \sin \theta \frac{d\phi}{dt} = \gamma |\underline{S}| |\underline{B}| \sin \theta \quad 4.10$$

therefore

$$\frac{d\phi}{dt} = \gamma |\underline{B}| \quad 4.11$$

and since the rate of change of the angle ϕ is the frequency, ω , then

$$\omega = \gamma |\underline{B}|. \quad 4.12$$

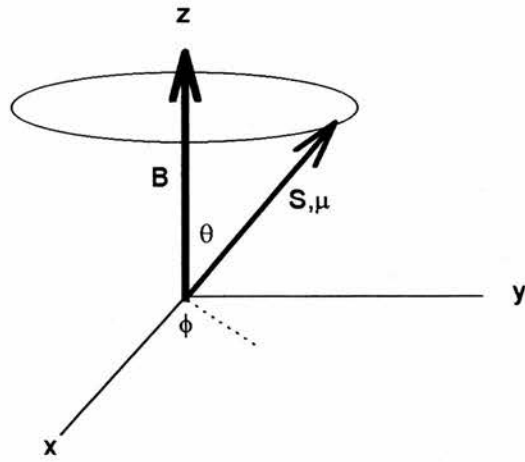


Figure 4.5 The motion of the spin because of the torque being induced from the field.

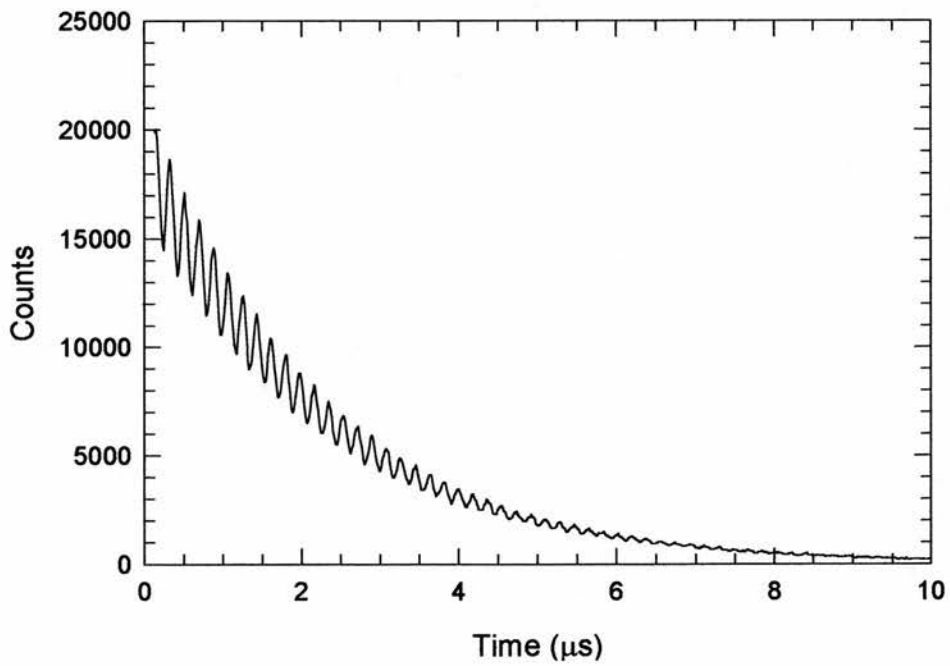


Figure 4.6 The muon counts as a function of time in the top detector.

The behaviour of the spin polarised muon in an applied field is directly analogous to this classical result and using relation 4.12 it can be seen that the frequency of the muon precession is directly proportional to the field within the sample.

The muon (or in reality the decay positron) spectrum in each detector consists of the muon decay spectrum modulated by the muon spin rotational motion (see figure 4.6) and can be described by

$$N(t) = N_0 \exp\left(-\frac{t}{\tau_\mu}\right) \cdot (1 + R(t)). \quad 4.13$$

In order to analyse the muon spin rotation data the muon exponential decay is removed from the counts to obtain the asymmetry function,

$$R(t) = A_\perp G_\perp \cos(\omega t + \phi) \quad 4.14$$

where ω is the precession frequency and ϕ is the phase. This leaves an oscillating function around $R(t)=0$ (see figure 4.7). The asymmetry function, $R(t)$, is the Fourier transform of the probability distribution of the internal fields within the sample. For a superconducting sample in the mixed state the dimensions of the flux lattice are far greater than those of the unit cell. Therefore, the muons will sample all possible values of the internal field distribution and the resulting rotation spectrum will directly reflect the field profile within the sample. This field profile is dependent on the magnetic penetration depth and coherence length.

4.6 DATA ANALYSIS.

4.6.1 Time domain analysis.

The MuSR instrument has 16 detectors on either side of the muon beam. Each detector has a solid angle of approximately 0.01 steradians. In order to improve statistics the counts from each individual detector are collated with three neighbouring detectors and with the equivalent detectors on the opposite side of the beam. The detectors are summed into four groups: top, bottom, forward and backwards (see figure 4.8).

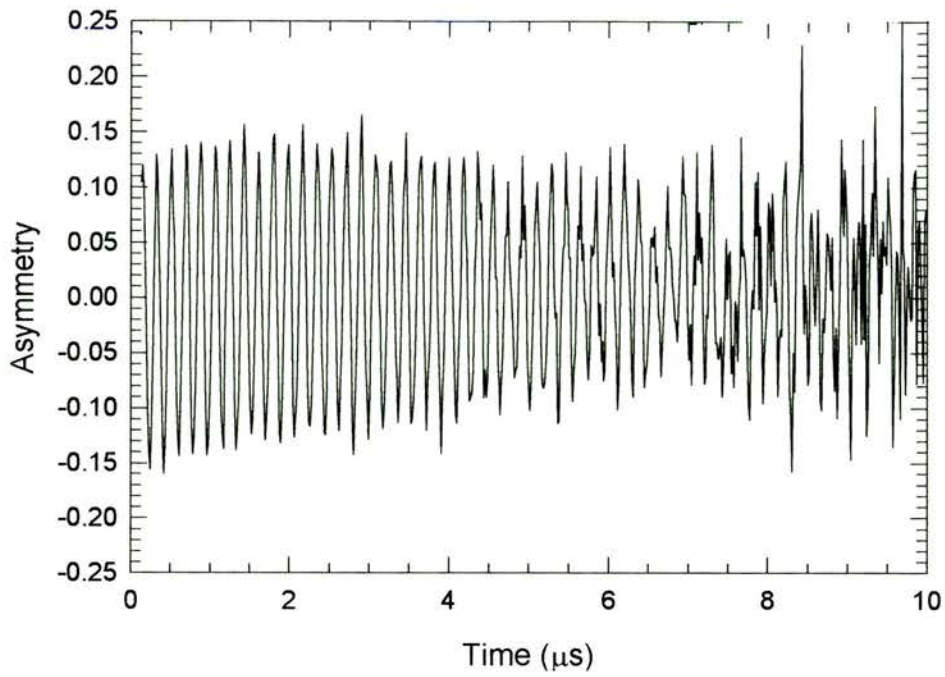


Figure 4.7 The muon spin depolarisation for the top detector with the exponential decay removed.

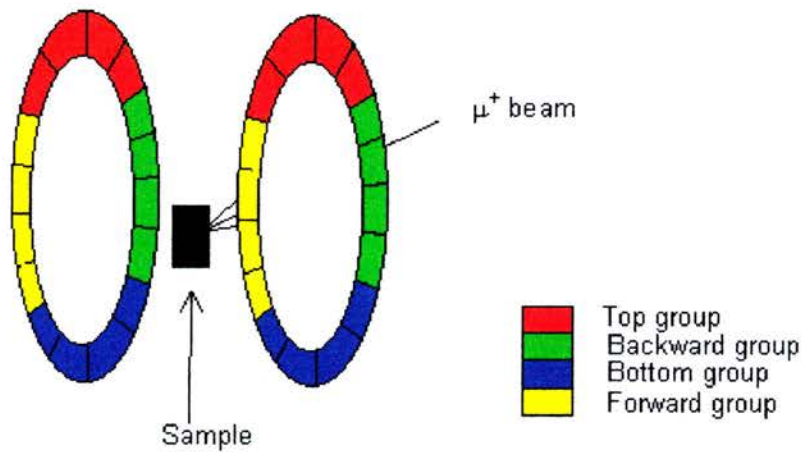


Figure 4.8 A schematic of the detector grouping for the MuSR instrument.

However, before the detectors can be grouped and the asymmetry function, $R(t)$, can be analysed, the individual detectors must be corrected for deadtimes. When each positron is counted, due to electronics and photomultiplier delays, the detector will be unable to count another event for a certain time, τ_D . This can be corrected by using a high statistic zero field measurement in longitudinal geometry. The sample used should have a very small depolarisation rate, such as high purity silver. Deadtime effects reduce the number of measured events below the true count rate and hence distort the asymmetry function. In a time bin of width, t_b , the true, N_t , and measured, N_m , counts are

$$N_t = n_t t_b \quad 4.15$$

and

$$N_m = n_m t_b \quad 4.16$$

respectively, where n_m and n_t are the respective count rates. The correction to the data is

$$N_{\text{corr}} = N_t - N_m. \quad 4.17$$

This is a direct result of the deadtime. Therefore, within this time bin the detector is dead for $N_m t_D$ and hence the difference in the counts is

$$N_{\text{corr}} = n_t N_m t_D. \quad 4.18$$

Therefore combining equations 4.17 and 4.18

$$\begin{aligned} N_t - N_m &= n_t N_m t_D \\ N_t - N_m &= N_t N_m \left(\frac{t_D}{t_b}\right) \\ \Rightarrow N_t &= \frac{N_m}{1 - N_m \left(\frac{t_D}{t_b}\right)}. \end{aligned} \quad 4.19$$

Using this relation, the true count rate can be determined so long as t_D is known.

For a material with zero depolarisation such as silver at room temperature then t_D can be calculated. In each detector $N(t) = N_0 \exp(-t/\tau_\mu)$ and substituting this into equation 4.19 a linear graph can be obtained,

$$N_m \exp\left(-\frac{t}{\tau_\mu}\right) = -N_0 \left(\frac{t_D}{t_b}\right) N_m + N_0, \quad 4.20$$

and hence from the gradient the detector deadtime can be determined. This is usually done for each individual photomultiplier tube before grouping the data. The effects of deadtimes can be clearly seen in figure 4.9. The dip at the beginning of the spectrum is the effect of deadtime. After deadtime corrections, the individual spectra can be grouped and fitted. Each group of detectors is fitted individually and an average of the results taken. The muon spectra are described by equation 4.14. The phase ϕ is determined from a slowly depolarising muon spectrum. For a superconductor this is done above the superconducting transition. The phase is dependent on the exact sample position and is determined for each sample.

For polycrystalline superconducting samples, it is generally assumed that the internal field distribution can be approximated to a Gaussian²³. This Gaussian profile is a result of an orientational average over a polycrystalline sample and broadening from a range of demagnetisation factors and random pinning processes. Even if the distribution is not precisely Gaussian, the second moment of a Gaussian fit often provides a reasonable estimate of the second moment of the actual field profile. The major disadvantage of this technique is that the spectra can only be fitted assuming a predetermined (Gaussian) model. Assuming such a model can lead to a loss of information on the precise nature of the form of the flux lattice.

4.6.2 Field domain analysis.

The internal field profile in a superconductor can be determined directly either by direct Fourier transforms or by Maximum Entropy Fourier transform. Direct Fourier transformation of the data introduces unacceptable noise into field profile. However, the maximum entropy technique determines the most probable field distribution for the data set and is less susceptible to the increase in counting errors at times which are long compared to the muon lifetime. The major advantage of these techniques is they are model independent. The maximum entropy program was initially written by Prof. B.D. Rainford and Dr. G.J. Daniell⁴ and modified by Dr. R. Cubitt and Prof. E.M. Forgan⁵. An example of direct Fourier transform and Maximum Entropy Fourier transform are shown in figures 4.9 and 4.10.

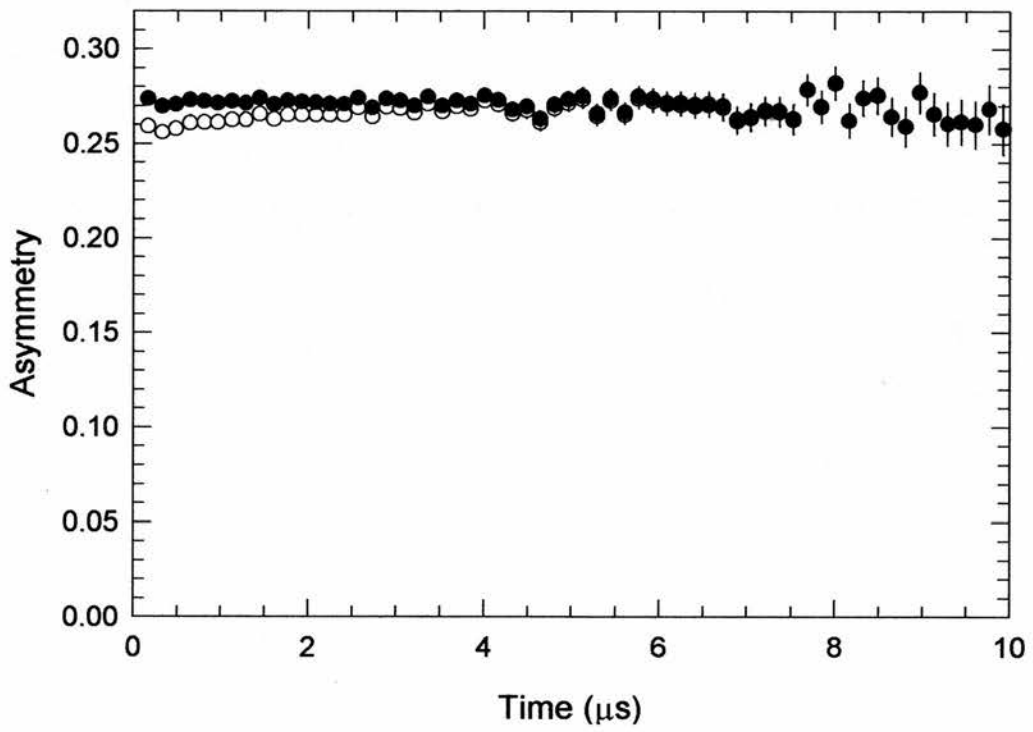


Figure 4.9 The longitudinal muon spin relaxation of silver before (o) and after (\bullet) deadtime correction.

The maximum entropy technique determines the field distribution, as the name suggests, by maximising the entropy of the probable field distribution, $p(B)$. The entropy of the system is given by

$$S = \sum_i \frac{p(B_i) \ln(p(B_i))}{d_i} \quad 4.21$$

where d_i are the initial default values. The probable field distribution, as determined by maximising the entropy, is then compared to the data by determining the error of the fit in the time domain using the relation

$$\chi^2 = \sum_i \frac{(R_i - \mathfrak{F}(p(B_i)))^2}{\sigma_i^2} \quad 4.22$$

where R_i is the muon spin rotation data after deadtime correction and removal of the muon radioactive decay exponential, $\mathfrak{F}(p(B_i))$ is the Fourier transform of the probable field distribution and σ_i are the experimental errors. The resulting field distribution is then obtained from minimising

$$L = S - \lambda \chi^2 \quad 4.23$$

where λ is the Lagrange multiplier. Using this technique the most probable, but not necessarily the smoothest distribution is determined. As the field width is the required result then this can be determined by the second moment of the distribution,

$$\sqrt{\Delta B^2} = \sqrt{\frac{\sum_i p(B_i)(B_i - \bar{B})^2}{\sum_i p(B_i)}} \quad 4.24$$

4.7 REFERENCES.

- ¹ K. Rugg, C. Boekema, W. Kundig, P.F. Meier, B.D. Patterson. *Hyperfine Interactions*. **8**. 547. (1981).
- ² B. Pumpin, *Phys Rev. B*, **42**, 8019, (1990)
- ³ M. Weber *Phys. Rev. B*, **48**, 13022 (1993).
- ⁴ B.D. Rainford, G.J. Daniell. *Hyperfine Interactions*, **87**, 1129 (1994).
- ⁵ R.Cubitt Thesis, University of Birmingham, 1994.

5. The nickel borocarbides.

5.1 INTRODUCTION.

The coexistence of magnetic order and superconductivity has received extensive investigation for many years. In 1971, the Chevrel phase superconductors were discovered and were one of the first families of superconductors to exhibit the coexistence of magnetic order and superconductivity¹. Later in 1986, the discovery of the cuprate superconductors rekindled interest in superconductivity research², not only because of their extremely high superconducting transition temperature but also because they exhibit magnetic order and superconductivity simultaneously. The magnetic ordering temperatures of the high T_c cuprates are usually of the order of 1K, i.e. within the temperature range where dipolar interactions rather than exchange interactions are important. However, the borocarbide superconductors have aroused considerable interest since their discovery³ not only because they exhibit the normally exclusive phenomena of magnetic order and superconductivity but they also have the highest recorded superconducting transition temperature, T_c , for an intermetallic alloy (YPd_2B_2C , $T_c=23K$)⁴. Moreover, the magnetic ordering temperatures are much higher than those observed high T_c superconductors and are similar to those observed in the Chevrel phase superconductors. These magnetic ordering temperatures, like those of the Chevrel phase superconductors, indicate the presence of relatively strong indirect exchange mechanisms operating in a temperature regime within which the associated conduction electrons might be expected to be involved in the superconducting state.

5.1.1 The superconducting properties of the nickel borocarbides.

The RNi_2B_2C (R=rare earth or yttrium) composition crystallises with a modified $ThCr_2Si_2$ structure⁵ (see figure 5.1). The assumed modification to the $ThCr_2Si_2$ structure is the insertion of carbon between the B/Si layers. This assumption is stoichiometrically correct although no experiments have yet conclusively proven the ordering between

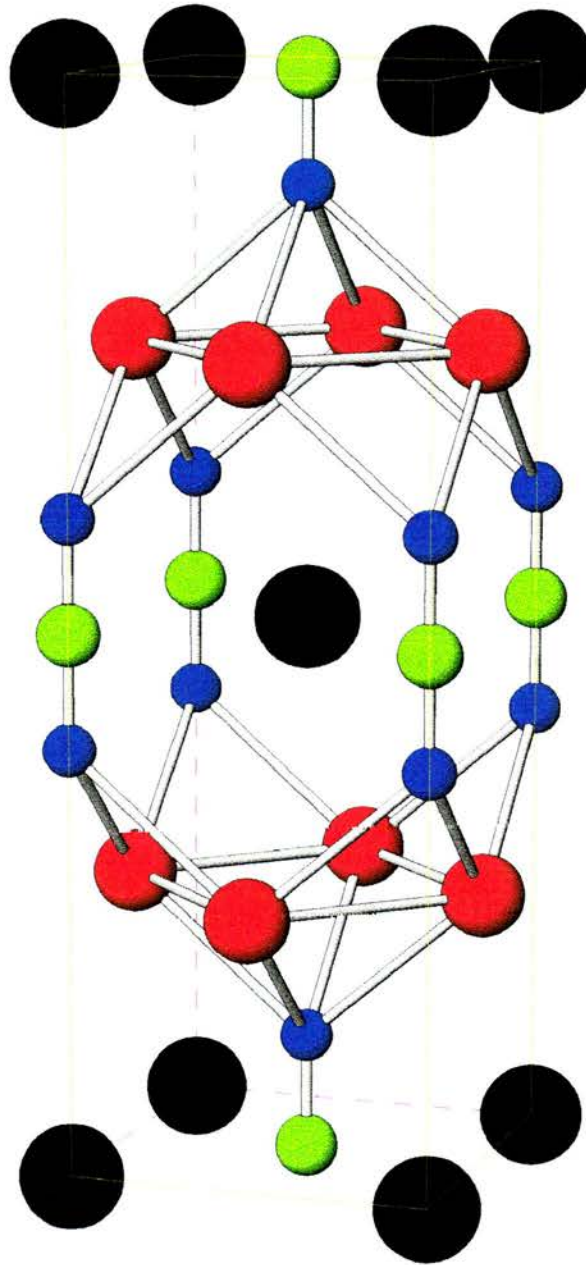


Figure 5.1 The crystal structure of RNi_2B_2C . This shows the modified $ThCr_2Si_2$ ($I4/mmm$) structure. The black spheres are the rare earths or yttrium atoms and the red, blue and green spheres are nickel, boron and carbon atoms respectively.

boron and carbon positions. The layered tetragonal and highly anisotropic structure has led to many suggestions that the borocarbides have similarities to the cuprate family⁵. However, most experimental and theoretical studies have concluded that the borocarbides are conventional BCS superconductors. Band structure calculations have suggested a 3D isotropic electronic structure with a van-Hove like peak in the density of states at the Fermi energy. This peak is associated with the relatively high superconducting transition⁶. Experimental evidence in support of the presence of this peak has been provided by partial substitution of 3d transition metals for nickel in $\text{YNi}_2\text{B}_2\text{C}$ ^{7,8}. Within a rigid band model, such a substitution moves the Fermi energy away from the peak and hence reduces T_c . However, antiferromagnetic spin fluctuations have also been invoked to explain the unusual temperature dependence of the ^{11}B spin lattice relaxation and Knight shift in $\text{YNi}_2\text{B}_2\text{C}$ and $\text{LuNi}_2\text{B}_2\text{C}$. In order to answer the question whether the borocarbides are conventional BCS superconductors or exotic superconductors, a detailed study of the superconducting ground state is required.

A μSR study of the superconducting ground state of the parent compound, $\text{YNi}_2\text{B}_2\text{C}$, has yielded an inconclusive result⁹. Within the Uemura classification scheme¹⁰, $\text{YNi}_2\text{B}_2\text{C}$ appears to be midway between the conventional and exotic superconductors. However, the temperature dependence of the magnetic penetration depth for $\text{YNi}_2\text{B}_2\text{C}$ is BCS-like. Further work is therefore required in order to clarify the nature of the superconducting ground state in the borocarbides family.

5.1.2 The magnetic properties of the nickel borocarbides.

The magnetic ground state of the $\text{RNi}_2\text{B}_2\text{C}$ alloys is very sensitive to the rare earth, R. For example, $\text{TbNi}_2\text{B}_2\text{C}$ is an incommensurate antiferromagnet at 15K¹¹ with a longitudinal spin wave along the a-axis ($q=0.545a^{12}$) and no superconductivity has been observed. Both magnetisation measurements¹¹ and neutron diffraction measurements¹² have indicated a small ferromagnetic component developing at 8K. $\text{GdNi}_2\text{B}_2\text{C}$ is also an incommensurate antiferromagnet with $T_N=21\text{K}$ ^{13,14,15}. A spin reorientation transition is observed at $\sim 14\text{K}$. For temperatures between 14K and 21K a transverse spin wave along the a-axis with a wave vector of 0.55b is observed. Below 14K, a component in the c-

axis is observed. Again, no superconductivity is observed in the $\text{GdNi}_2\text{B}_2\text{C}$ alloys. However, $\text{DyNi}_2\text{B}_2\text{C}$ is an antiferromagnet, $T_N=10\text{K}$ ¹⁶, but on cooling below 6K superconductivity is observed^{17,18}. A commensurate antiferromagnetic structure was observed with the moments aligned in the a-b plane¹⁹. In this case, both magnetic order and superconductivity coexist. $\text{HoNi}_2\text{B}_2\text{C}$ exhibits superconductivity at 6.5K but at the onset of an incommensurate antiferromagnetic ground state, at 5.5K, the superconductivity is lost²⁰. On decreasing the temperature still further, the superconductivity is recovered with a subtle change in magnetic order to a collinear antiferromagnet²¹. This is the same magnetic structure as found for $\text{DyNi}_2\text{B}_2\text{C}$. Between 4.7K and 5.5K the magnetic structure of $\text{HoNi}_2\text{B}_2\text{C}$ is characterised by two incommensurate wave vectors ($q=0.585,0,0$ and $q=0,0,0.915$)^{21,22,23,24}. For $\text{ErNi}_2\text{B}_2\text{C}$, superconductivity is observed at 10.5K. The coexistence of an antiferromagnetic ground state and superconductivity appears at 5K²⁵. The magnetic ground state is an incommensurate antiferromagnetic structure with a transverse modulation with $q=(0.553,0,0)$ and with the erbium moment along the b-axis^{26,27}. However, for $\text{LuNi}_2\text{B}_2\text{C}$ and $\text{YNi}_2\text{B}_2\text{C}$ only superconductivity is observed with $T_c=17\text{K}$ ²⁸ and 15K ²⁹ respectively.

Sample	T_c (K)	T_N (K)	de Gennes factor (g_J-1) ² J(J+1)
$\text{GdNi}_2\text{B}_2\text{C}$	0	21	15.7
$\text{TbNi}_2\text{B}_2\text{C}$	0	15	10.5
$\text{DyNi}_2\text{B}_2\text{C}$	6	10.5	7.08
$\text{HoNi}_2\text{B}_2\text{C}$	6.5	5.5	4.5
$\text{ErNi}_2\text{B}_2\text{C}$	10.5	5	2.55
$\text{TmNi}_2\text{B}_2\text{C}$	10.8	1.5	1.17
$\text{LuNi}_2\text{B}_2\text{C}$	17	-	0
$\text{YNi}_2\text{B}_2\text{C}$	15	-	0

Table 5.1 A summary of the magnetic and superconducting transition temperatures.

It has been shown that the superconducting transition temperature in the parent $\text{RNi}_2\text{B}_2\text{C}$ compounds scales approximately with the de Gennes factor³⁰ (see figure 5.2). This indicates a weak coupling between the local moments of the rare earth and the

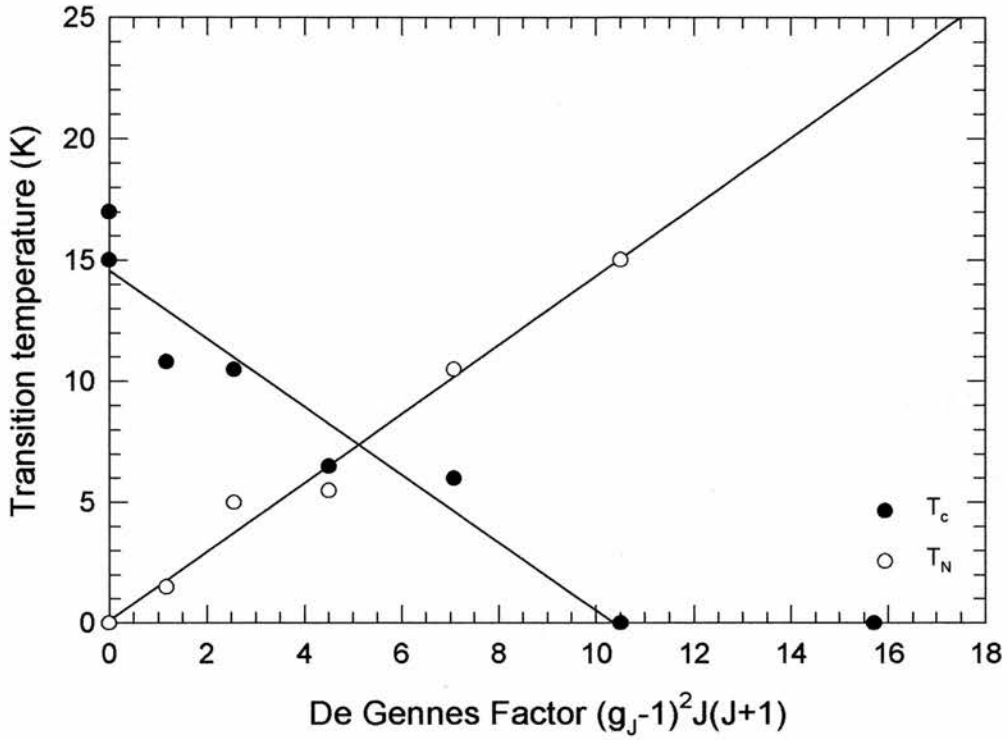


Figure 5.2 The de Gennes scaling of the magnetic and superconducting transition temperatures for $RNi_2B_2C^{31}$.

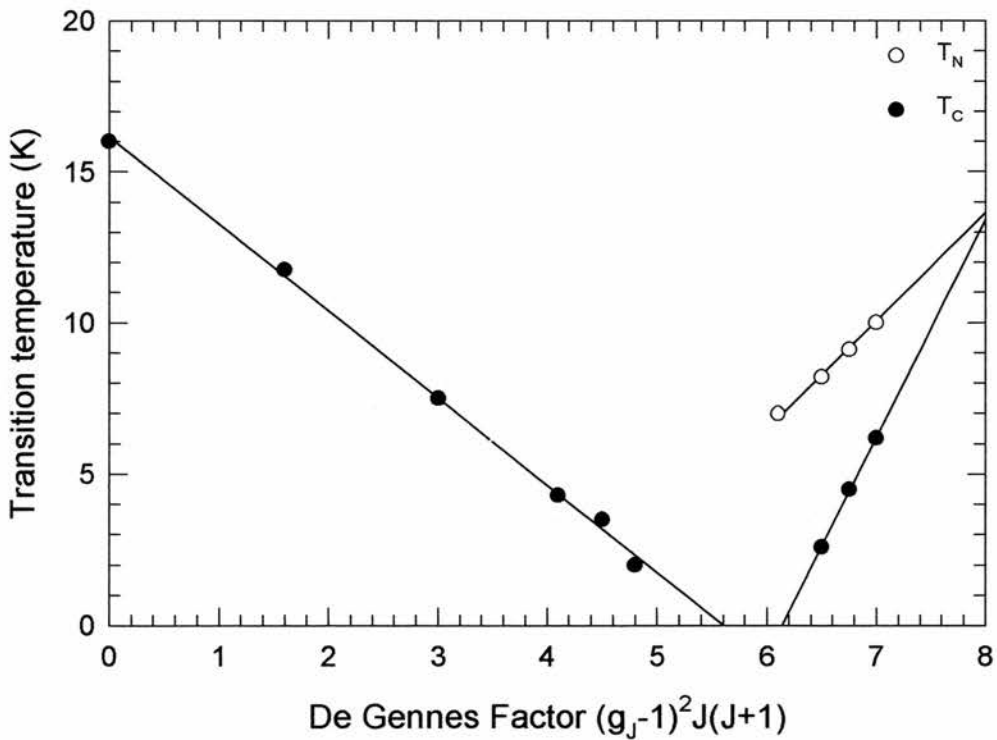


Figure 5.3 The breakdown of the de Gennes scaling for $R'_{1-x}R_xNi_2B_2C$ ($R'=Lu$ and $R=Dy$)³².

conduction electrons at the Fermi surface. However, this scaling is only observed for RNi_2B_2C . For some $(R'_{1-x}R_x)Ni_2B_2C$ ($R'=Lu$ and $R=Dy$) the de Gennes scaling breaks down³¹ (see figure 5.3).

For these systems, the magnetic phase diagram can be considered as two regions. Firstly when $T_c > T_N$, slight deviations in the de Gennes scaling is observed and attributed to crystalline electric fields. Secondly when $T_N > T_c$ the de Gennes scaling breaks down completely. It has been suggested that the breakdown arise from a softening of the magnon spectra in the ordered state.

As part of this study, and in order to investigate further the nature of magnetic order and deGennes scaling in the pseudoquaternary compounds, a survey of the magnetic and superconducting properties of $Er_{1-x}Tb_xNi_2B_2C$ has been conducted. In varying x it is expected that the magnetic and superconducting properties will change from $T_c > T_N$ through to $T_c < T_N$ and then into an antiferromagnet with no superconductivity being observed down to the lowest temperatures.

5.2 SAMPLE PREPARATION AND STRUCTURAL CHARACTERISATION.

Samples of $LuNi_2B_2C$, $Y(Ni_{1-x}Co_x)_2B_2C$, $Y_{1-x}La_xNi_2B_2C$, $(Er_{1-x}Tb_x)Ni_2B_2C$ and $YNi_2^{10}B_2C$ alloys were prepared by initially melting together stoichiometric amounts of the yttrium, rare earth, nickel, cobalt and boron pieces in an argon arc furnace. Upon heating the boron with an argon arc the boron pieces explode because of gaseous impurities. This results in a loss in a mass causing a deviation from stoichiometry. In order to reduce the problem the boron, yttrium and rare earth metal are wrapped in nickel foil. As nickel and yttrium melt before the boron explosion a protective liquid alloy forms around the boron and hence limits the spread, and loss, of boron. A stoichiometric amount of carbon was subsequently added to the YNi_2B_2 ingot. For all the prepared samples the total mass loss was not greater than 0.6%. Annealing the sample for between 1 and 7 days at $1000^\circ C$ removes the presence of any impurity phases. However, this annealing process does not effect the superconducting parameters³². The $YNi_2^{10}B_2C$ sample was annealed for 4 days.

The nickel borocarbide samples were initially characterised using x-ray diffraction. These measurements were collected in reflection geometry in order to reduce fluorescence (see §3.3). The x-ray diffraction patterns confirmed that the $Y(Ni_{1-x}Co_x)_2B_2C$ and $LuNi_2B_2C$ alloys crystallise with a modified $ThCr_2Si_2$ structure directly from the melt (see figure 5.4), in agreement with the literature⁴.

However, doping lanthanum for yttrium in YNi_2B_2C introduced a significant second phase for concentration of La greater than 10% (see figure 5.5). As yet this second phase is unidentified. The presence of a second phase should be taken into account when considering the results obtained later since this may introduce an error in determining the lanthanum concentration. Initial refinements of the x-ray diffraction pattern for $(Y_{1-x}La_x)Ni_2B_2C$ have shown that the lattice parameter, a , remains approximately constant whereas the lattice parameter, c , decreases with increasing lanthanum concentration, suggesting a contraction of the unit cell volume.

5.3 THE STRUCTURAL DETERMINATION OF THE NICKEL BOROCARBIDES.

The basic crystallographic structure of the nickel borocarbides was reported soon after their discovery⁴. The structural determination and all subsequent experiments have assumed that boron and carbon have quite independent sites, with the boron site at $(0,0,z)$ and the carbon at $(0,0,1/2)$. Natural boron, boron-11 and carbon have similar scattering lengths for both x-rays and neutrons. However, the isotope boron-10 has a scattering length quite different to that of natural boron since natural boron is 80% boron-11 (see Table 5.1). In principle, enrichment of the sample with boron-10 should enable the site occupancy of the boron carbon sublattice to be determined with neutron diffraction. Unfortunately boron-10 has one of the highest absorption cross sections in the periodic table (3835 barns at neutron energy of 25.30 meV, $\lambda=1.798\text{\AA}$).

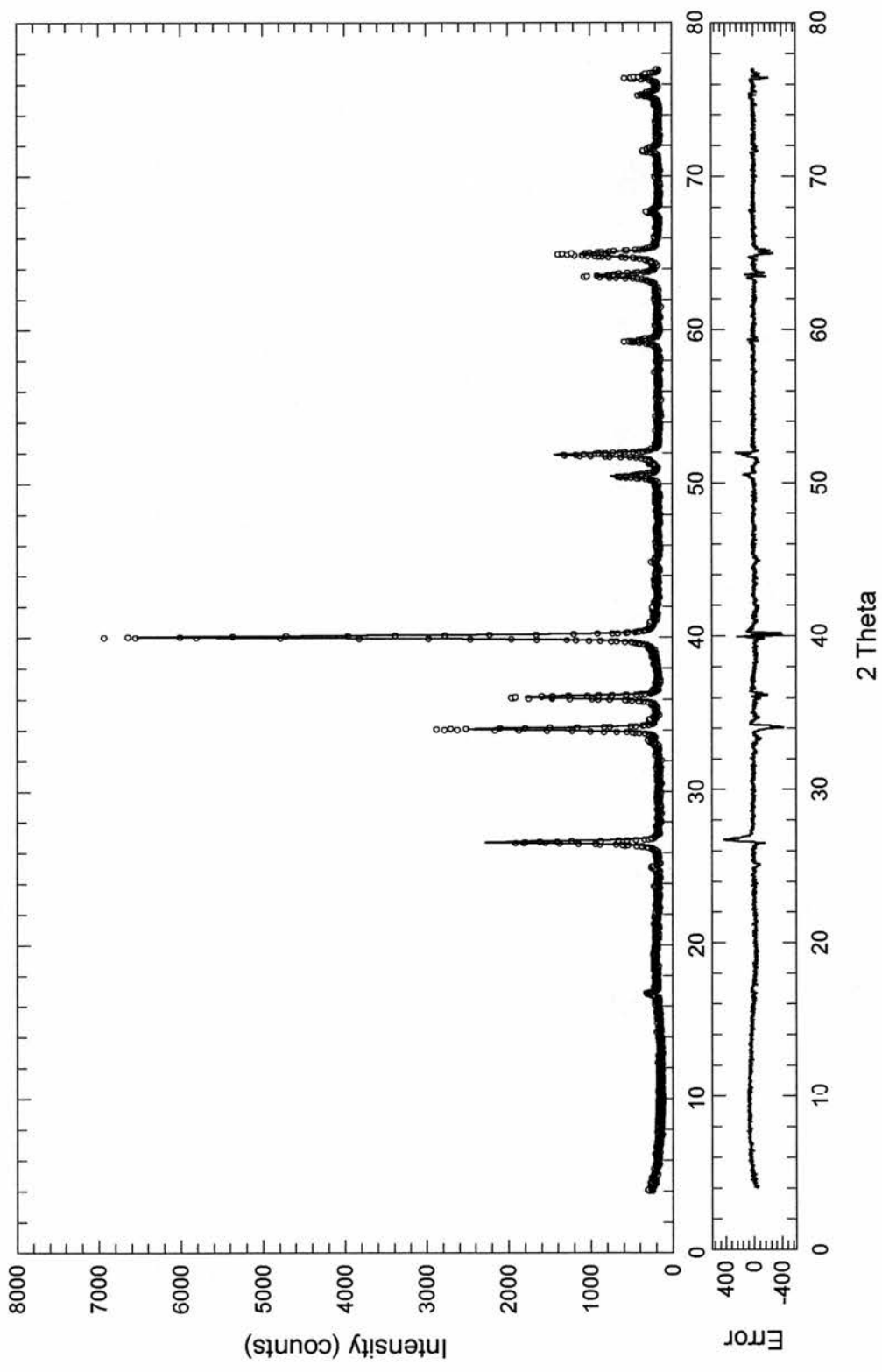


Figure 5.4 The x-ray diffraction pattern for $Y(Ni_{0.95}Co_{0.05})_2B_2C$. The line is a Rietveld refinement to the data. The difference of the fit to the data is given in the lower graph.

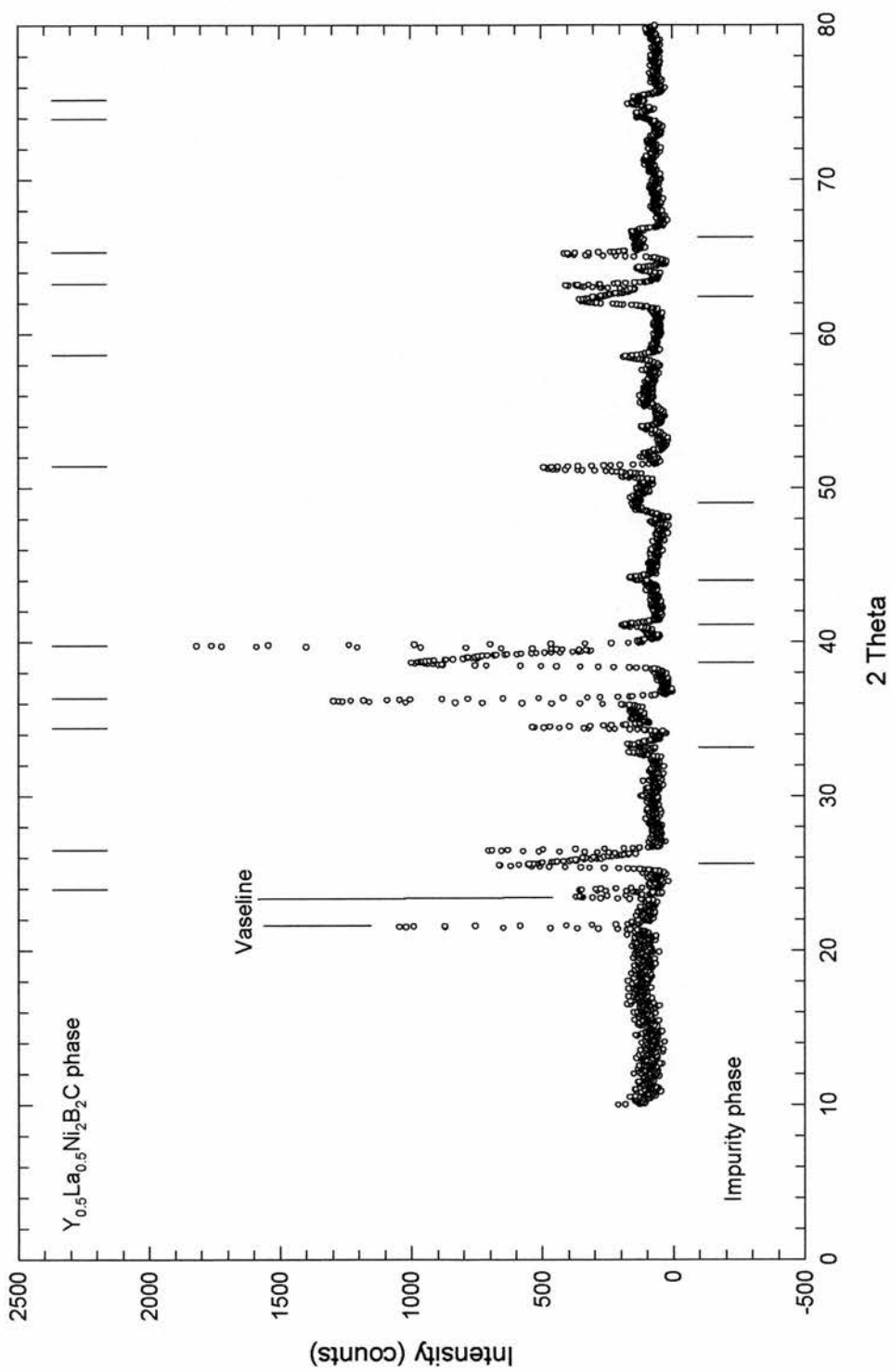


Figure 5.5 The x-ray diffraction pattern showing the presence of a significant impurity phase for the $(Y_{0.5}La_{0.5})Ni_2B_2C$ sample.

	Neutron coherent scattering length, b_c , fm ² .	Neutron absorption ($\lambda=1.798\text{\AA}$) cross section, σ_a , barns.
carbon	6.6460(12)	0.00350(7)
boron	5.30(4) -0.213(2)i	767(8)
¹¹ boron	6.65(4)	0.0055(33)
¹⁰ boron	-0.1(3) -1.066(3)i	3835(9)

Table 5.1 A table of the neutron coherent scattering lengths and absorption cross section for boron and carbon..

Nevertheless we attempted a neutron diffraction study of $\text{YNi}_2^{10}\text{B}_2\text{C}$ on the POLARIS time of flight neutron diffractometer at ISIS, RAL. As the POLARIS instrument is a time of flight diffractometer backscattering geometry is available. In this geometry, the neutrons do not have to pass through the sample and hence the absorption is minimised. The sample was mounted in a vanadium can. Vanadium is used since it has a low coherent scattering length (0.01838barns). However, $\text{YNi}_2^{10}\text{B}_2\text{C}$ has such a high absorption that the diffraction peaks from the vanadium in backscattering are also observed. The contribution to the diffraction pattern from the vanadium can was refined independently. The vanadium refinement was then subtracted from the diffraction pattern. The resulting corrected diffraction pattern was finally refined using the CCSL Rietveld refinement package³³ (see figure 5.6).

The refinement has confirmed the expected modified ThCr_2Si_2 structure with lattice parameters of $3.52582(4)\text{\AA}$ and $10.53537(21)\text{\AA}$ for a and c respectively. This result agrees with the literature³⁴. However, we find that the boron and carbon atoms are not entirely confined to the $(0,0,z)$ and $(0,0,1/2)$ sites respectively. Some site disorder does occur with the site occupancy for the boron on the boron site being refined to be 0.913(4) with a fractional occupancy of 0.086(4) for the carbon on the boron site. No evidence of any vacancies either on the $(0,0,z)$ or $(0,0,1/2)$ sites is observed. A summary of the results can be found in Table 5.2.

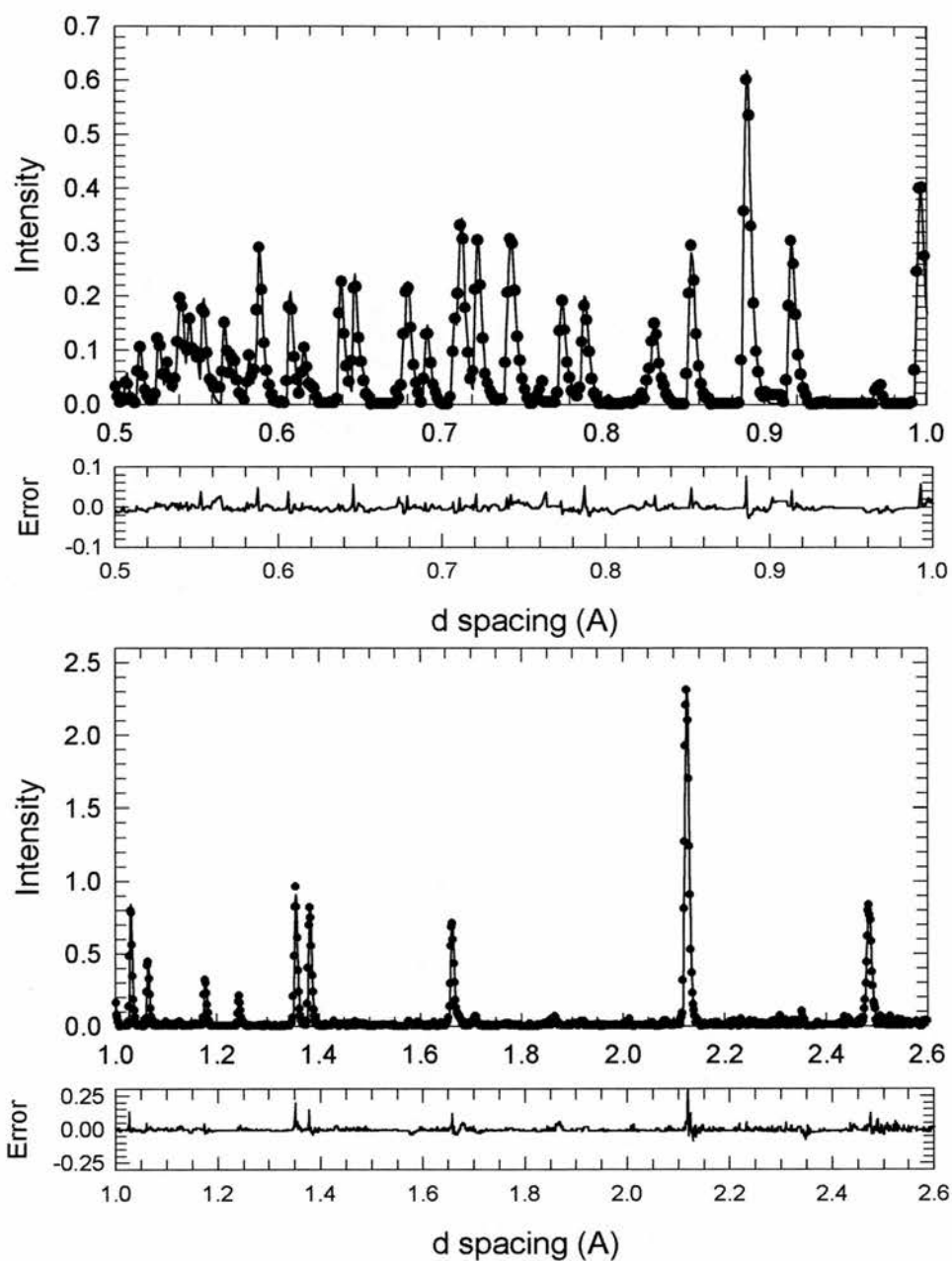


Figure 5.6 The neutron diffraction pattern of $YNi_2^{10}B_2C$ at room temperature after the subtraction of the vanadium refinement. The line is a Rietveld refinement to the diffraction pattern. The upper graph is the low d -spacing diffraction pattern whereas the lower is the longer d -spacing.

	x	y	z	U (Å ²)	Site occupancy
yttrium	0	0	0	0.204	1.0*
nickel	0.5	0	0.25	0.437	1.0*
boron1	0	0	0.3503(13)	0.514	0.913(4)
carbon1	0	0	0.3503(13)	0.514	0.086(4)
carbon2	0.5	0.5	0	0.673	0.913(4)
boron2	0.5	0.5	0	0.673	0.086(4)

Space group I4/mmm,

a=0.35258(1)nm, c=1.05354(2)nm,

R=19.56%, R_w=11.41%, R_{exp}=10.87%, $\chi^2=1.11$.

* These values are fixed.

Table 5.2 A summary of the results obtained from the neutron diffraction pattern of YNi₂¹⁰B₂C.

It is interesting to note that although the boron carbon site occupancies are similar to those generally assumed we have found evidence of a small but significant disorder between the two sites.

5.4 LuNi₂B₂C.

The superconducting transition temperature, T_c, and the upper critical fields, H_{c2}, of a sample of LuNi₂B₂C have been determined by dc magnetisation using the techniques described in §3.4. A known mass (325mg) of LuNi₂B₂C powder was mixed with an epoxy resin to provide a sample for the VSM measurements. An applied of 6mT was used to determine T_c, and a value of 17K was observed in agreement with the literature⁴ (see figure 5.7).

An attempt was made to determine H_{c1} by increasing the applied field slowly (0.5mT/s) after zero field cooling the sample below T_c. However, the VSM sample of LuNi₂B₂C is a powder and therefore a range of demagnetisation factors exist for the individual grains within the powder. Usually, H_{c1} is determined at the field at which the magnetisation first

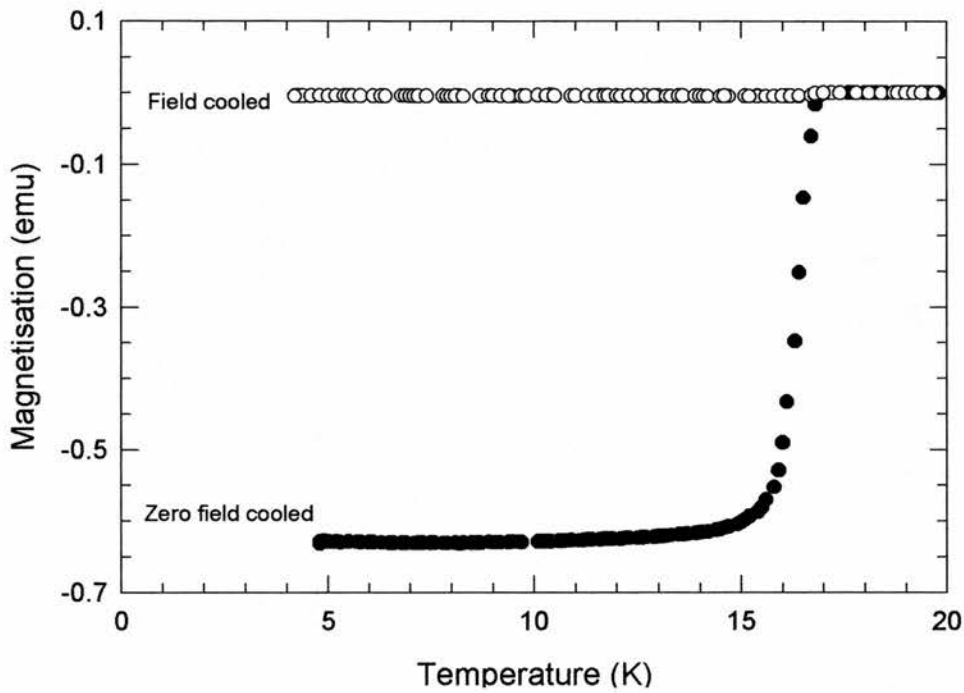


Figure 5.7 The temperature dependence of the magnetisation for $\text{LuNi}_2\text{B}_2\text{C}$ in an applied field of 6mT . The superconducting transition temperature is 17K .

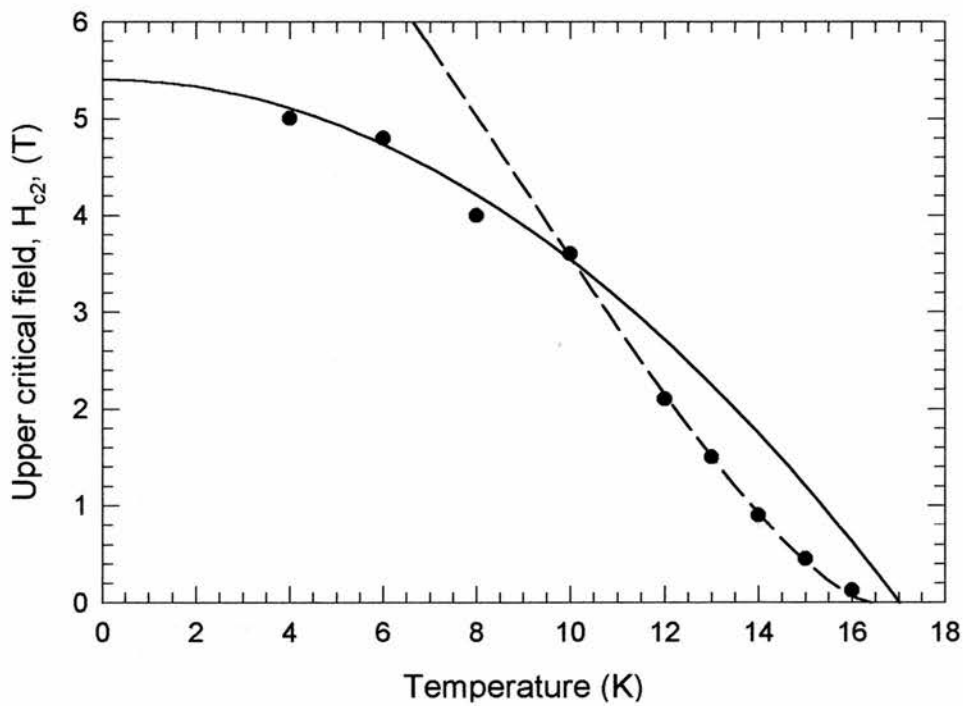


Figure 5.8 The temperature dependence of H_{c2} for $\text{LuNi}_2\text{B}_2\text{C}$. The solid line is the two fluid model fit and the dashed line is the local pairing fit to the data.

deviates from linearity, i.e. the field at which flux first penetrates the superconducting state. In a powder sample, the magnetisation deviates from linearity at fields lower than H_{c1} because of those grains with high demagnetisation factors. A precise determination of H_{c1} is consequently difficult. Magnetic measurements reported by Takagi *et al.* have determined $H_{c1}(0)$ to be 80mT ³⁵.

A combination of the two fluid model and local pairing model has been used to fit the temperature dependence of H_{c2} for the $\text{LuNi}_2\text{B}_2\text{C}$ sample (see figure 5.8). Using the two fluid model the extrapolation of H_{c2} to $T=0\text{K}$ has given $H_{c2}(0)=5.41(5)\text{T}$. However, at temperatures greater than 10K the two fluid model fit breaks down. The local pairing model³⁶,

$$H_{c2} \propto \left(1 - \left(\frac{T}{T_c} \right)^{3/2} \right)^{3/2} \quad 5.1$$

has been fitted to the data above 10K . The quality of this fit in the vicinity of T_c suggests the possibility of non-BCS behaviour in $\text{LuNi}_2\text{B}_2\text{C}$.

The critical fields are directly related to the fundamental superconducting parameters, the penetration depth, λ , and the coherence length, ξ , by the relations

$$H_{c2}(T) = \frac{\phi_0}{2\pi} \frac{1}{\xi^2(T)} \quad 5.2$$

and

$$H_{c1}(T) = \frac{\phi_0}{4\pi} \frac{1}{\lambda^2(T)} \ln(\kappa). \quad 5.3$$

Using these relations, $\lambda=68\text{nm}$ (determined from the H_{c1} value given by reference 35) and $\xi_{\text{GL}}=7.8\text{nm}$ and hence $\kappa=9.1$ ($\kappa=\lambda/\xi_{\text{GL}}$).

In order to determine the magnetic penetration depth without the problems associated with dc magnetisation a muon spin rotation experiment was conducted using the MuSR instrument at ISIS, RAL, Oxford, UK. All the μSR spectra are best described by a single Gaussian damped oscillating function (see figure 5.9),

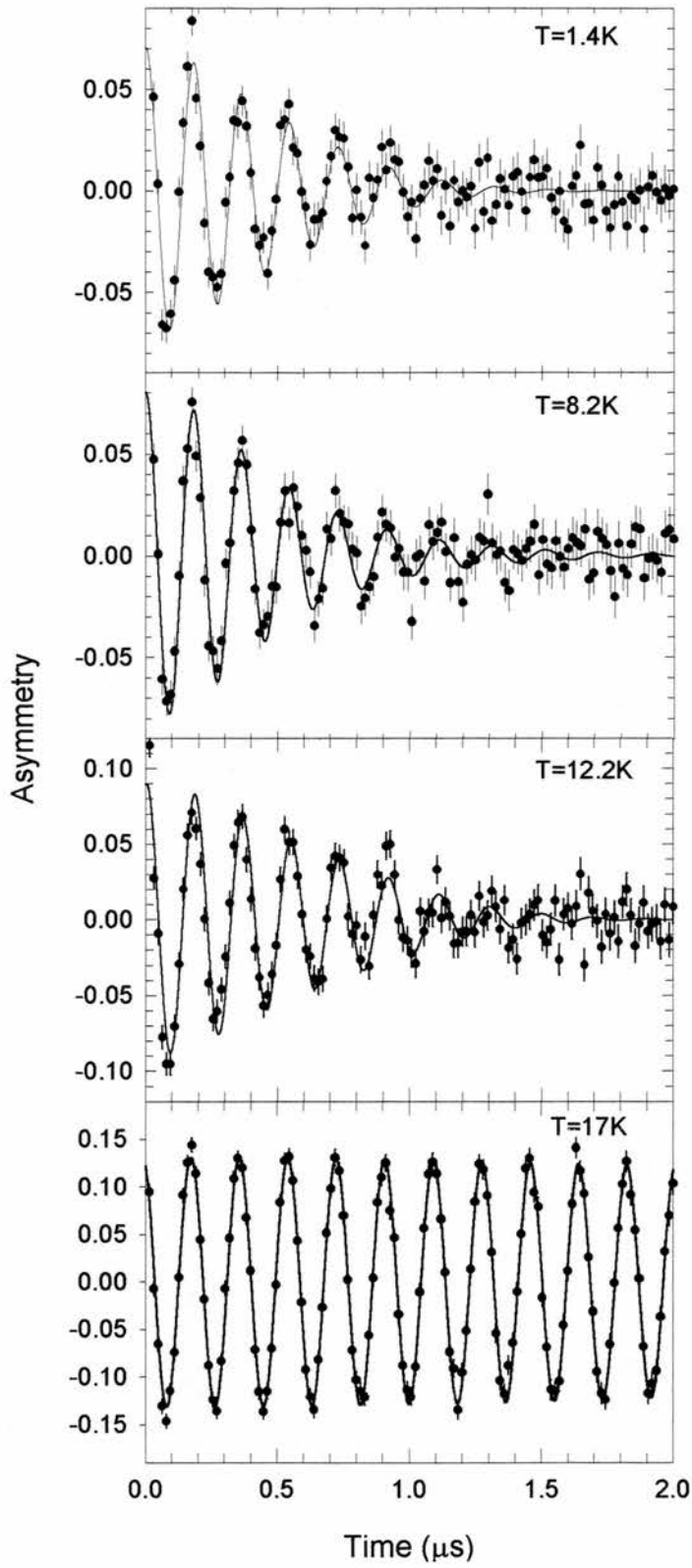


Figure 5.9 The muon spectra for $\text{LuNi}_2\text{B}_2\text{C}$ at a range of temperatures. The line is a least squares fit to the data.

$$G_z(t) = A_0 \exp(-\sigma^2 t^2) \cos(\omega t + \phi), \quad 5.4$$

where

$$\langle \Delta B^2 \rangle = \frac{2\sigma^2}{\gamma_\mu}. \quad 5.5$$

Equation 5.4 implies that a Gaussian distribution of internal fields is appropriate. For a polycrystalline powder sample such a Gaussian distribution of internal fields can be justified³⁷. To confirm the assumption for this particular case the field distribution was calculated directly from the μ SR spectra by using the maximum entropy Fourier transform technique^{38, 4.6.2} (see figure 5.10).

The field profile has sharp oscillating features overlying the peaks. This is a recognised artefact in the current maximum entropy software, which appears to be associated with the time window, in a manner similar to a conventional Fourier transform. A Gaussian field distribution has been fitted to the envelope of the field profile obtained from the muon depolarisation spectrum. As can be seen in figure 5.10 this Gaussian provides a reasonable description of the data, if the sharp oscillations are ignored.

The muon depolarisation rate was measured as function of temperature in an applied field of 40mT. It should be noted that the muons also depolarise as a result of the random nuclear dipolar fields at the muon site within the sample. The measured depolarisation rate in the superconducting state, σ_s , must therefore be corrected for this nuclear depolarisation, σ_N . Using the normal state depolarisation rate as a measure of σ_N and assuming this depolarisation rate does not change with temperature once below T_c , the depolarisation rate can be corrected using the relation

$$\sigma_{\text{corr}} = \sqrt{\sigma_s^2 - \sigma_N^2}, \quad 5.6$$

which assumes that σ_s and σ_N are entirely independent and are therefore combined in quadrature. The temperature dependence of the corrected superconducting depolarisation rate was fitted using the N-Fluid model (see figure 5.11),

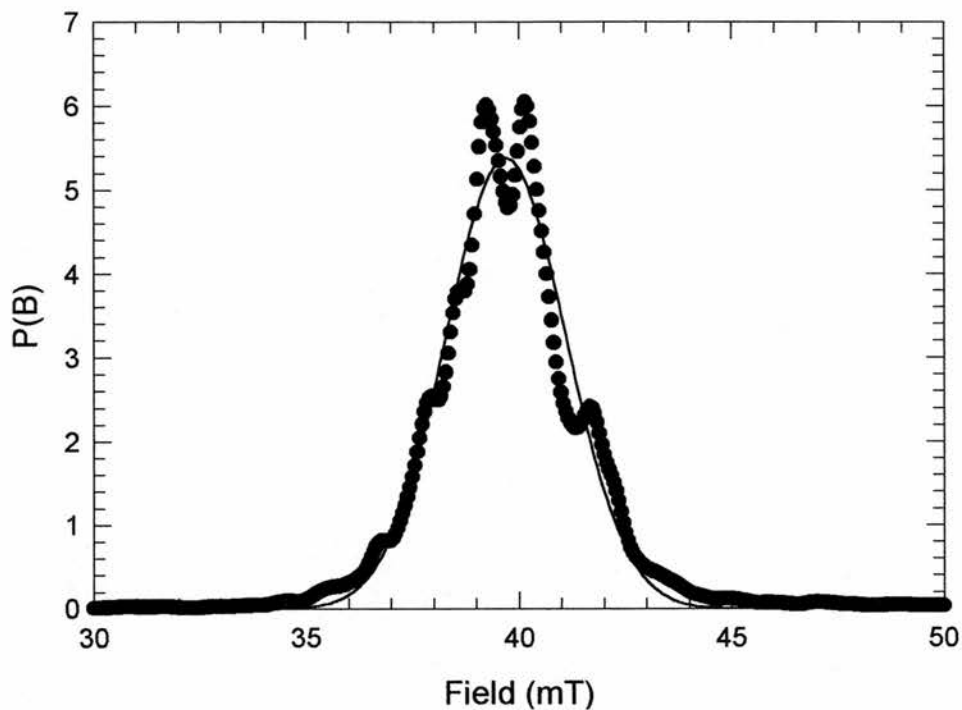


Figure 5.10 The field distribution of $\text{LuNi}_2\text{B}_2\text{C}$ at 1.5K after being field cooled in a field of 40mT. The line is a Gaussian fit to the data.

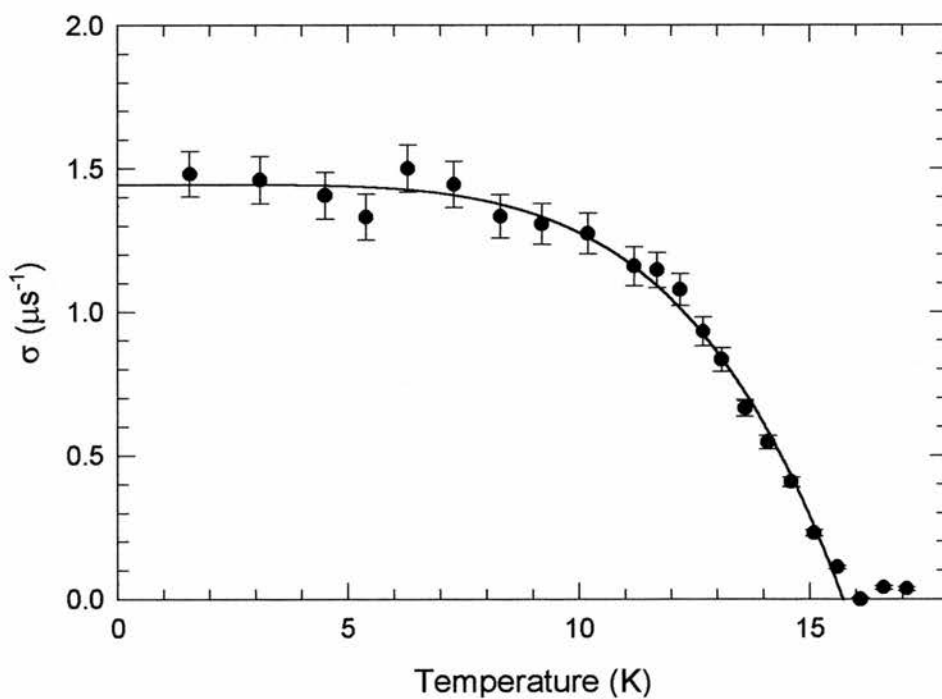


Figure 5.11 The temperature dependence of the muon depolarisation rate for $\text{LuNi}_2\text{B}_2\text{C}$. The line is a least squares fit to the data using the N-fluid model (see equation 5.3).

$$\sigma_{\text{corr}}(T) = \sigma(0)\left(1 - \left(\frac{T}{T_c}\right)^N\right). \quad 5.7$$

The fit provides a value of T_c of 15.7K. This slight suppression of T_c from the reported value of 17K is a result of field cooling the sample in a field greater than H_{c1} . The value of N obtained from the fit is 4.7. This value of N is slightly higher than the value of 4 obtained for $\text{YNi}_2\text{B}_2\text{C}$ ⁹. The extrapolated value of σ at $T=0\text{K}$ is $1.45\mu\text{s}^{-1}$.

The flux lattice for $\text{LuNi}_2\text{B}_2\text{C}$ has been reported to have a square³⁹ rather than the more commonly observed triangular symmetry. Our numerical simulations suggest that the second moment of the field distribution is relatively insensitive to the precise geometry of the flux lattice. A small correction of 2% in λ is required. As ξ_{GL} is relatively short ($\sim 7\text{nm}$) the muon depolarisation rate is directly related to the magnetic penetration depth by the relation

$$\sigma_0 = \frac{0.06219\Phi_0}{\lambda^2} \quad 5.8$$

for a square lattice. This provides a value for $\lambda(0)$ of 224nm for $\text{LuNi}_2\text{B}_2\text{C}$. This value is much larger than that expected from a direct calculation based on the lower critical field and is approximately double the value obtained for $\text{YNi}_2\text{B}_2\text{C}$ ⁹.

5.5 $\text{Y}(\text{Ni}_{1-x}\text{Co}_x)_2\text{B}_2\text{C}$.

The samples of $\text{Y}(\text{Ni}_{1-x}\text{Co}_x)_2\text{B}_2\text{C}$ ($x=0.05$ and 0.1) used for the dc magnetisation measurements were in the form of solid spheres formed directly from the melt in the argon arc furnace. A sphere has a known demagnetisation factor (1/3) and hence appropriate corrections can be made. The superconducting transition temperatures for $\text{Y}(\text{Ni}_{0.95}\text{Co}_{0.05})_2\text{B}_2\text{C}$ and $\text{Y}(\text{Ni}_{0.9}\text{Co}_{0.1})_2\text{B}_2\text{C}$ were determined by dc magnetisation and were found to be 10.3K and 5.4K respectively (see figure 5.12). These values agree with the literature^{7,8}.

The temperature dependence of the lower critical field of $\text{Y}(\text{Ni}_{0.95}\text{Co}_{0.05})_2\text{B}_2\text{C}$ and $\text{Y}(\text{Ni}_{0.9}\text{Co}_{0.1})_2\text{B}_2\text{C}$ have been determined and the two-fluid model has been fitted to the resulting data (see figure 5.13). The extrapolated values of H_{c1} at $T=0\text{K}$ were found to

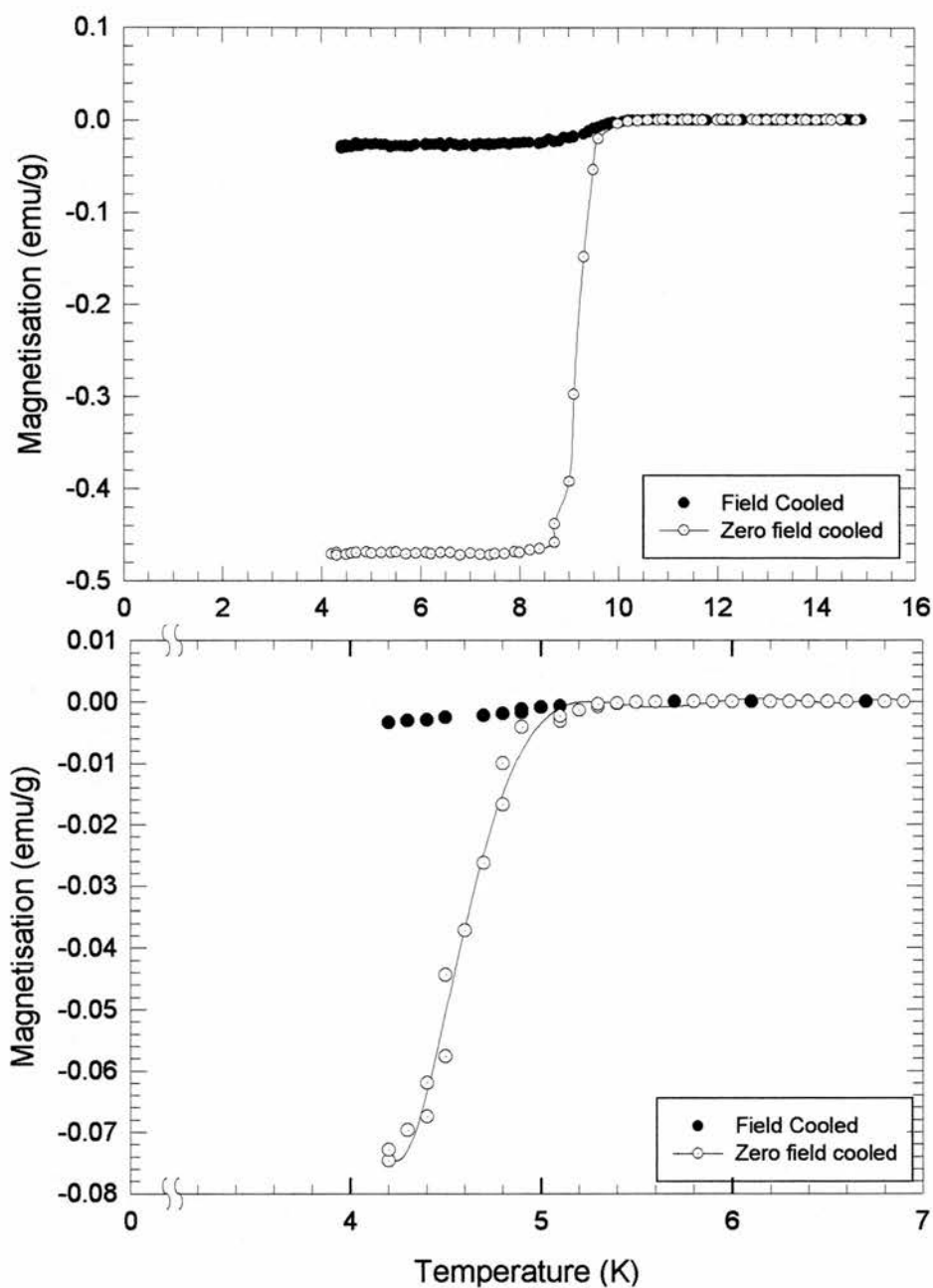


Figure 5.12 The temperature dependence of the magnetisation for $Y(Ni_{1-x}Co_x)_2B_2C$ in a field of 6mT and the lines are guides to the eye. The upper graph is the data for $Y(Ni_{0.95}Co_{0.05})_2B_2C$ and the lower is the data for $Y(Ni_{0.9}Co_{0.1})_2B_2C$. The superconducting transition temperatures are 10.3K and 5.4K for $Y(Ni_{0.95}Co_{0.05})_2B_2C$ and $Y(Ni_{0.9}Co_{0.1})_2B_2C$ respectively.

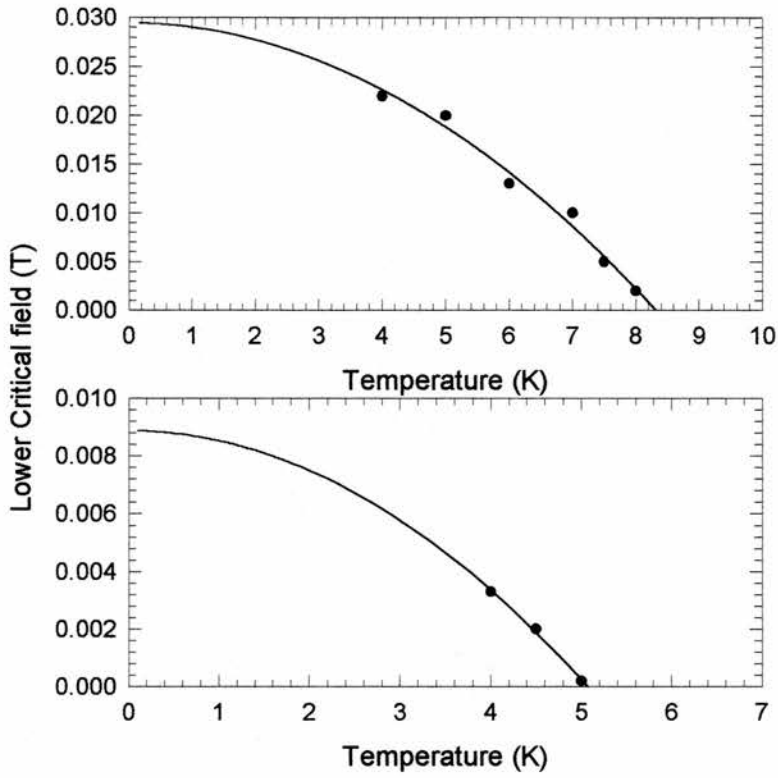


Figure 5.13 The temperature dependence of H_{c1} for $Y(Ni_{0.95}Co_{0.05})_2B_2C$ (upper graph) and $Y(Ni_{0.9}Co_{0.1})_2B_2C$ (lower graph). The lines are the two fluid model fits to the data.

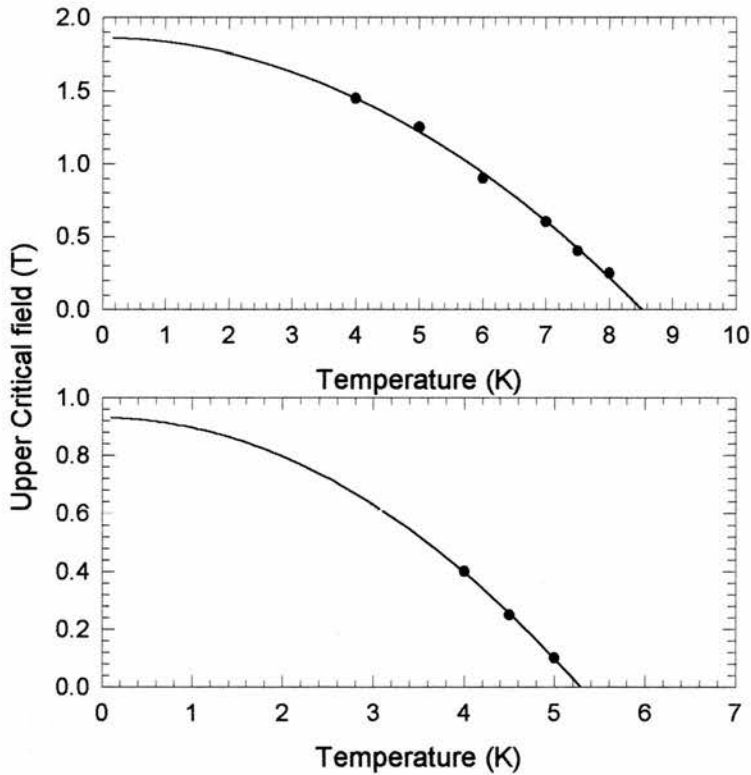


Figure 5.14 The temperature dependence of H_{c2} for $Y(Ni_{0.95}Co_{0.05})_2B_2C$ (upper graph) and $Y(Ni_{0.9}Co_{0.1})_2B_2C$ (lower graph). The lines are the two fluid model fits to the data.

be 29.4(12)mT and 8.9(4)mT for $Y(Ni_{0.95}Co_{0.05})_2B_2C$ and $Y(Ni_{0.9}Co_{0.1})_2B_2C$ respectively. These extrapolations should be treated with caution since only a few points close to T_c are available.

The upper critical fields, H_{c2} , have been obtained from the magnetic hysteresis loops and the two fluid model has been fitted to the $H_{c2}(T)$ data (see figure 5.14). The extrapolation of H_{c2} to $T=0K$ has given $H_{c2}(0)$ of 1.86T and 0.93T for $Y(Ni_{0.95}Co_{0.05})_2B_2C$ and $Y(Ni_{0.9}Co_{0.1})_2B_2C$ respectively. In all cases, the relatively high value of H_{c2} indicates these superconductors are extreme type II.

The magnetic penetration depth, λ , and coherence length, ξ_{GL} , are related to the critical fields H_{c1} and H_{c2} by equations 5.3 and 5.2 respectively. Using these relations, $\lambda=113nm$ and $\xi_{GL}=13nm$ for $Y(Ni_{0.95}Co_{0.05})_2B_2C$ and for $Y(Ni_{0.9}Co_{0.1})_2B_2C$, $\lambda=206nm$ and $\xi_{GL}=19nm$.

The penetration depth measurements on $Y(Ni_{0.95}Co_{0.05})_2B_2C$ and $Y(Ni_{0.9}Co_{0.1})_2B_2C$ were also performed using muon spin rotation at ISIS. The muon spectra were collected on warming after first field cooling the sample below the superconducting transition temperature. Above the superconducting transition the muon spectra were well described by a single Gaussian damped oscillating function representing the depolarisation due to the nuclear fields at the muon site. However, below T_c the muon depolarisation spectra for $Y(Ni_{1-x}Co_x)_2B_2C$ were best described by (see figure 5.15)

$$G_z(t) = A_{0_s} \exp(-\sigma_s^2 t^2) \cos(\omega_s t + \phi) + A_{0_B} \exp(-\sigma_B^2 t^2) \cos(\omega_B t + \phi) \quad 5.9$$

where A_0 is the initial asymmetry, σ is the muon depolarisation rate, ω is the muon precession frequency and ϕ is the phase.

The first term in equation 5.9 represents the contribution from the superconductor in the mixed state and the second term is a ‘background’ contribution arising from those muons being implanted into the cryostat. Equation 5.9 assumes that the internal field distributions associated both with the superconducting state and the ‘background’ are Gaussian in form. This can again be shown to be the case by Fourier transforming the

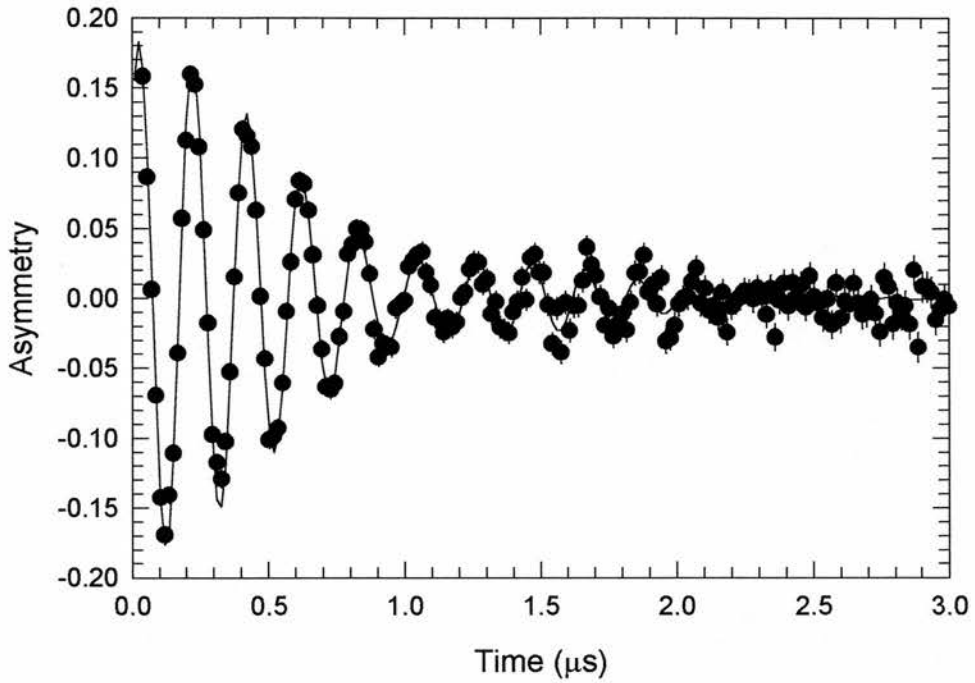


Figure 5.15 The transverse field muon depolarisation spectra for $Y(Ni_{0.9}Co_{0.1})_2B_2C$ at 1.5K. The line is a fit to the data using equation 5.8.

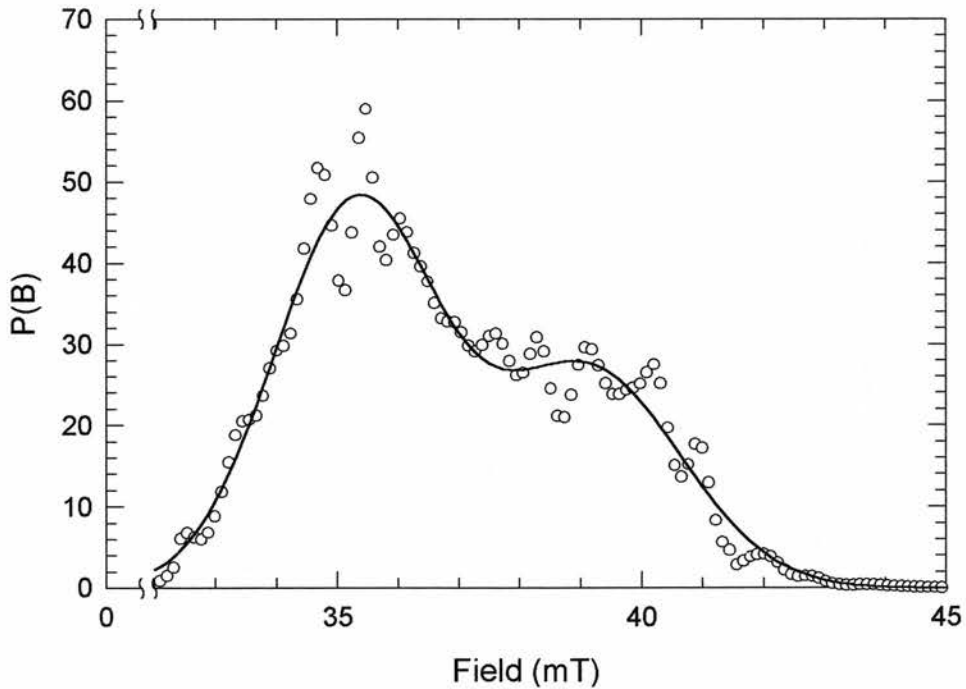


Figure 5.16 An example of the field distribution of a superconductor in the mixed state, $Y(Ni_{0.1}Co_{0.1})_2B_2C$ at 1.5K. The two Gaussian components are a result from a superconducting term and a background term. Using two Gaussian field profiles, the line is a fit to the data.

μ SR spectra using maximum entropy methods (see figure 5.16). In figure 5.16 the solid line is a fit to the data using two Gaussian profiles, one at the applied field, i.e. the ‘background’ contribution, and the other at a slightly lower field which can be associated with the superconducting mixed state of the sample.

The temperature dependence of the muon depolarisation rate was measured in an applied field of 40mT. The measured depolarisation rate, corrected for the nuclear contribution, was fitted using the N-Fluid model (see figure 5.17). Using the results from the fits, T_c was determined to be 8.6K and 5.8K for $Y(Ni_{0.95}Co_{0.05})_2B_2C$ and $Y(Ni_{0.9}Co_{0.1})_2B_2C$ respectively. The slight suppression of T_c is again a result of field-cooling the sample in a field greater than H_{c1} . The exponent N was found to be 3.1 and 2.1 for $Y(Ni_{0.95}Co_{0.05})_2B_2C$ and $Y(Ni_{0.9}Co_{0.1})_2B_2C$ respectively.

If the effect of the coherence lengths are ignored and we assume that the muon depolarisation rate is directly related to λ by the relation

$$\sigma = \frac{0.0609\Phi_0}{\lambda^2}. \quad 5.10$$

We obtain values of λ of 150nm and 250nm for $Y(Ni_{0.95}Co_{0.05})_2B_2C$ and $Y(Ni_{0.9}Co_{0.1})_2B_2C$ respectively. However, the muon depolarisation rate decreases if the flux line lattice becomes more compact and the flux lines start to overlap. The overlapping of the flux lines thus narrows the field distribution. Simulations using the modified London model⁴⁰ with a coherence length obtained from the previous magnetisation results have given values of λ of 130nm and 205nm for $Y(Ni_{0.95}Co_{0.05})_2B_2C$ and $Y(Ni_{0.9}Co_{0.1})_2B_2C$ respectively (see figure 5.18 and figure 5.19). The magnetic penetration depth obtained from the muon measurements with the appropriate coherence length corrections are in remarkable agreement with the results obtained from dc magnetisation.

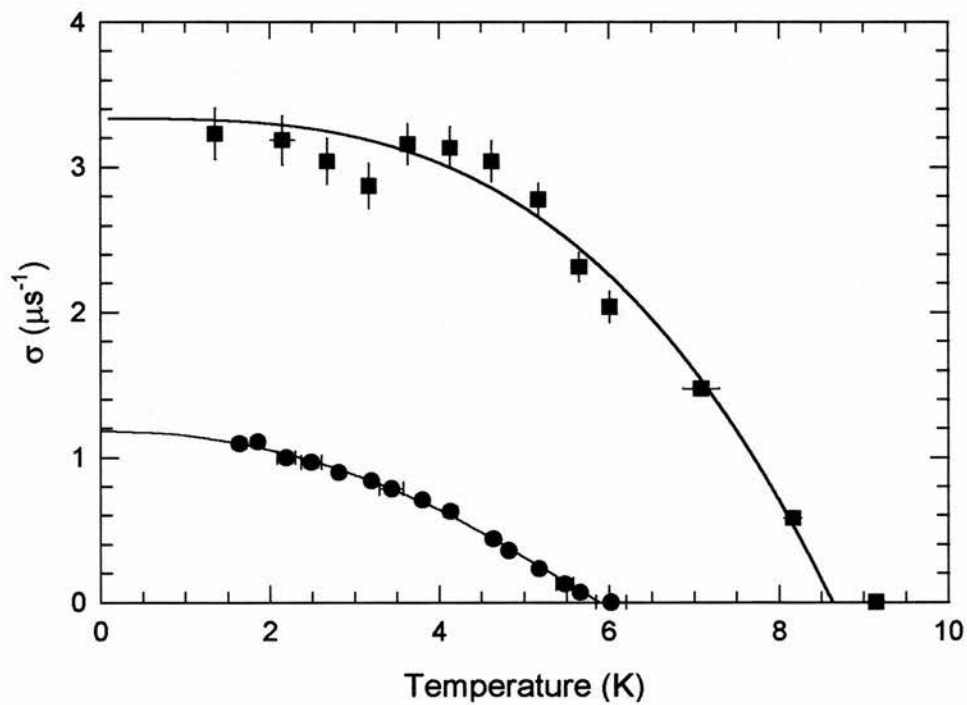


Figure 5.17 The temperature dependence of the muon depolarisation rate for $Y(Ni_{0.95}Co_{0.05})_2B_2C$ and $Y(Ni_{0.9}Co_{0.1})_2B_2C$. The line is a fit to the data using the N-fluid model (see equation 5.7).

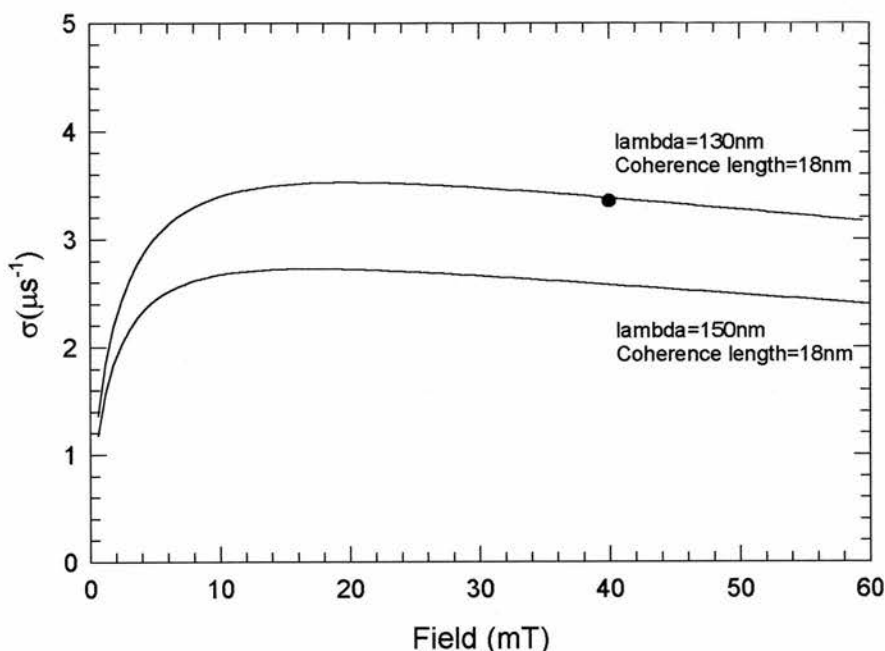


Figure 5.18 A simulation of the muon depolarisation rate field dependence with different magnetic penetration depths for $Y(Ni_{0.95}Co_{0.05})_2B_2C$. The simulation with $\lambda=150nm$ assumes a negligible effect of the coherence length. However, as can be seen the combination of the muon depolarisation and the magnetisation data gives $\lambda=130nm$. The coherence length was determined by dc magnetisation.

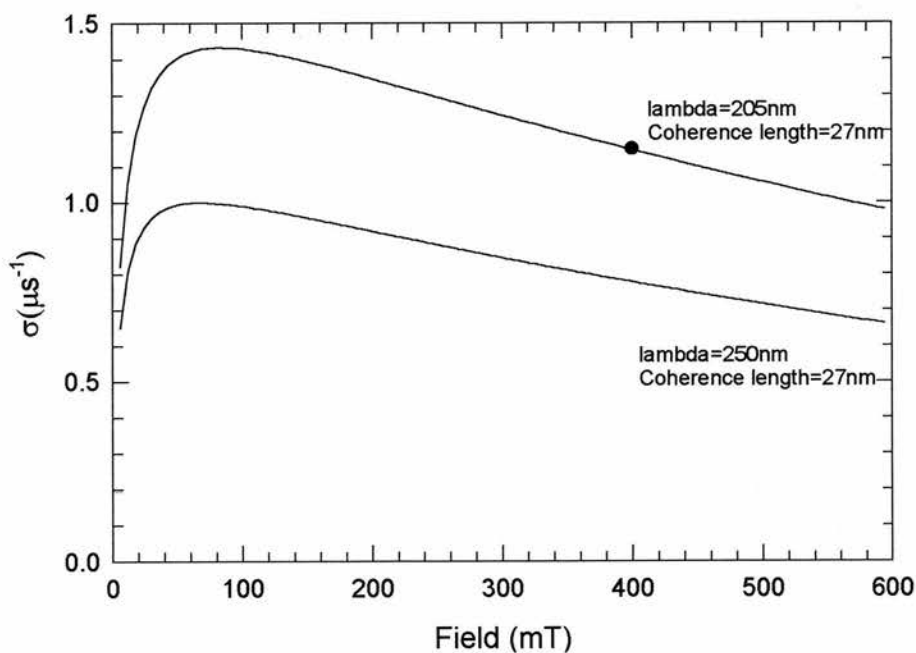


Figure 5.19 A simulation of the muon depolarisation rate field dependence with different magnetic penetration depths for $Y(Ni_{0.9}Co_{0.1})_2B_2C$. The simulation with $\lambda=250nm$ assumes a negligible effect of the coherence length. However, as can be seen the combination of the muon depolarisation and the magnetisation data gives $\lambda=205nm$. The coherence length was determined by dc magnetisation.

5.6 $(Y_{1-x}La_x)Ni_2B_2C$.

The $(Y_{1-x}La_x)Ni_2B_2C$ samples have been characterised by dc magnetisation. The samples used in these measurements were solid spheres formed directly from the melt in an argon arc furnace. Again, the temperature dependence of the magnetisation was used to determine T_c . However, no such literature exists for $(Y_{1-x}La_x)Ni_2B_2C$. The superconducting transition temperatures for $(Y_{0.95}La_{0.05})Ni_2B_2C$, $(Y_{0.8}La_{0.2})Ni_2B_2C$ and $(Y_{0.5}La_{0.5})Ni_2B_2C$ were found to be 14.2K, 13.3K and 6.2K (see figure 5.20). A summary of these results can be found in Table 5.3.

The lower, H_{c1} , and upper, H_{c2} , critical fields have been determined for $(Y_{0.95}La_{0.05})Ni_2B_2C$ and $(Y_{0.8}La_{0.2})Ni_2B_2C$ in the same way as for $LuNi_2B_2C$ and $Y(Ni_{1-x}Co_x)_2B_2C$. H_{c1} has been measured as a function of temperature only for $(Y_{0.95}La_{0.05})Ni_2B_2C$ and $(Y_{0.8}La_{0.2})Ni_2B_2C$ and not for $(Y_{0.5}La_{0.5})Ni_2B_2C$ since T_c is close to the lowest available temperature for our VSM. The two-fluid model has been fitted to H_{c1} (see figure 5.21). Extrapolating H_{c1} back to $T=0K$ gives $H_{c1}(0)$ for $(Y_{0.95}La_{0.05})Ni_2B_2C$ as 18.5mT and for $(Y_{0.8}La_{0.2})Ni_2B_2C$ as 12.1mT.

H_{c2} is determined as a function of temperature. The two fluid model has been fitted to H_{c2} for $(Y_{0.95}La_{0.05})Ni_2B_2C$ and $(Y_{0.8}La_{0.2})Ni_2B_2C$ (see figure 5.22). At temperatures close to T_c a positive curvature in H_{c2} is observed. This curvature is well described by the temperature dependence associated with local paired superconducting electrons. As with $LuNi_2B_2C$, the positive curvature of H_{c2} close to T_c may indicate non BCS superconductivity. The extrapolation to $H_{c2}=0$ gives a superconducting transition temperature equal to the value as determined by zero field cooling the sample.

The extrapolation of H_{c2} to $T=0K$ has given $H_{c2}(0)$ of 2.71T and 2.03T for $(Y_{0.95}La_{0.05})Ni_2B_2C$ and $(Y_{0.8}La_{0.2})Ni_2B_2C$ respectively. In all cases the relatively high value of H_{c2} and low values of H_{c1} indicates these superconductors are extreme type II (i.e. $\kappa > 10$).

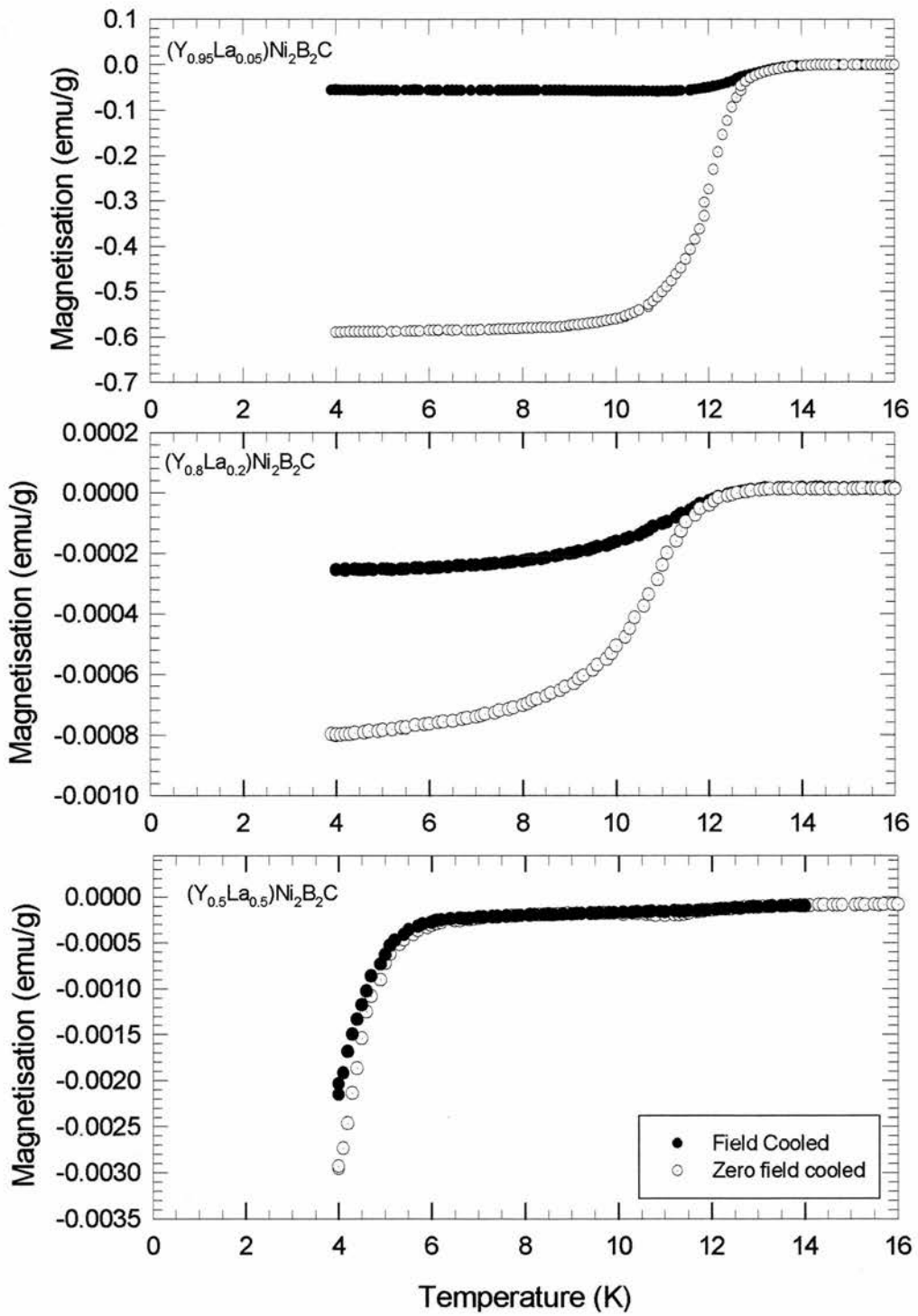


Figure 5.20 The temperature dependence of the magnetisation for $(Y_{1-x}La_x)Ni_2B_2C$ ($x=0.05, 0.2$ and 0.5) in a field of $6mT$.

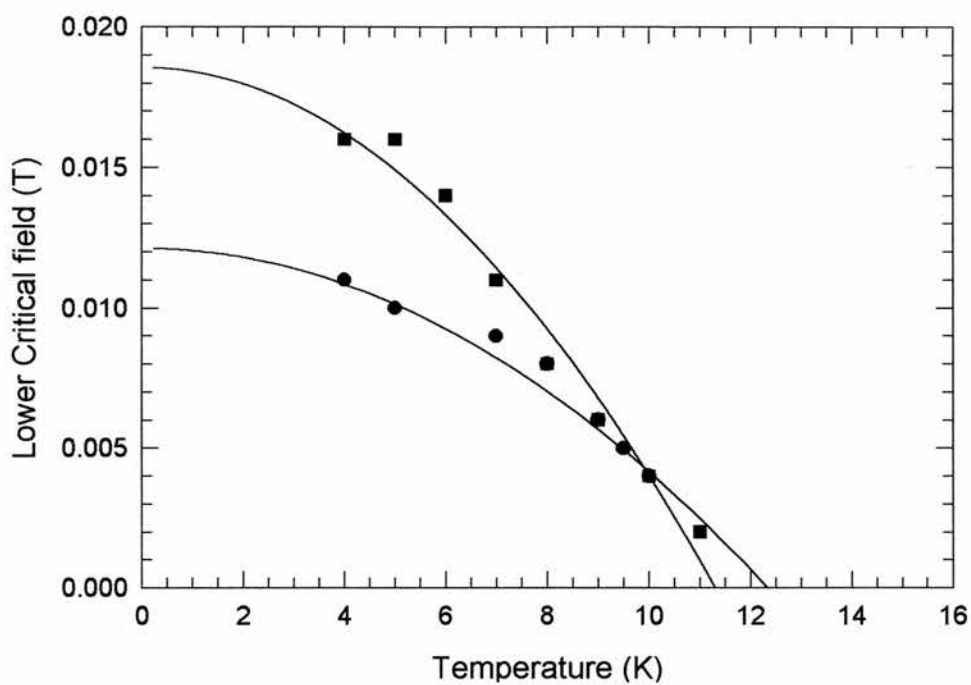


Figure 5.21 The temperature dependence of H_{c1} for $(Y_{1-x}La_x)Ni_2B_2C$ ($x=0.05$ {■} and 0.2 {●}). The line is the two fluid model fit to the data.

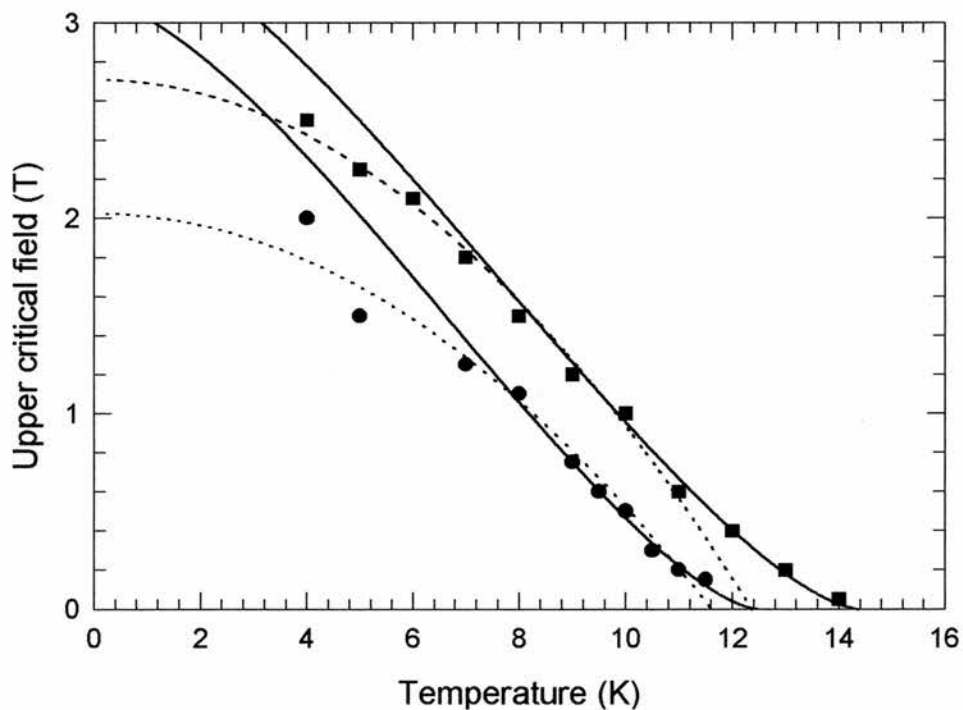


Figure 5.22 The temperature dependence of H_{c2} for $(Y_{1-x}La_x)Ni_2B_2C$ ($x=0.05$ {■} and 0.2 {●}). The dashed line is the two fluid model fit to the data and the solid line is a fit to the data using the local pairing model.

Using the value of H_{c1} and H_{c2} at zero temperature the magnetic penetration depth and coherence length can be determined using equations 5.2 and 5.3, producing the values summarised in Table 5.3.

	T_c (K)	H_{c1} (mT)	H_{c2} (T)	λ (nm)	ξ (nm)
$Y_{0.95}La_{0.05}Ni_2B_2C$	14.2	18.5	2.71	143	12
$Y_{0.8}La_{0.2}Ni_2B_2C$	13.1	12.1	2.03	177	13
$Y_{0.5}La_{0.5}Ni_2B_2C$	6.2				

Table 5.3 A summary of the results obtained from dc magnetisation.

$(Y_{1-x}La_x)Ni_2B_2C$ ($x=0.05, 0.2$ and 0.5) have been examined by μ SR. The muon spectra were fitted assuming a Gaussian distribution of internal fields. For $(Y_{0.95}La_{0.05})Ni_2B_2C$ and $(Y_{0.8}La_{0.2})Ni_2B_2C$ the coherence length is short enough as not to affect the muon depolarisation rate in fields accessible from the MuSR instrument. Therefore the muon depolarisation rate is directly related to λ . The N-fluid model (see equation 5.7) has been fitted to the muon depolarisation rate, which has been corrected for the nuclear dipole field contribution (see figure 5.23).

The determined values of T_c are 11.6K for both $(Y_{0.95}La_{0.05})Ni_2B_2C$ and $(Y_{0.8}La_{0.2})Ni_2B_2C$. The N-value remains constant at 4.6. The extrapolated value of $\sigma(0)$ is $4.8\mu s^{-1}$ and $1.4\mu s^{-1}$ for $(Y_{0.95}La_{0.05})Ni_2B_2C$ and $(Y_{0.8}La_{0.2})Ni_2B_2C$. Using the relation for a triangular flux lattice which relates the muon depolarisation rate, σ , with λ , i.e.,

$$\sigma = \frac{0.0609\Phi_0}{\lambda^2}, \quad 5.11$$

we find λ to be 125nm and 232nm for $(Y_{0.95}La_{0.05})Ni_2B_2C$ and $(Y_{0.8}La_{0.2})Ni_2B_2C$ respectively. However, for $(Y_{0.5}La_{0.5})Ni_2B_2C$ the field dependence of the muon spin depolarisation rate was measured in order to eliminate an error in the determination of λ resulting from a long ξ_{GL} . The muon depolarisation rate was measured as a function of temperature for a number of fields (10mT, 20mT and 40mT). At each field the N-fluid model was fitted to the muon depolarisation rate and the extrapolated value at $T=0K$ was found (see figure 5.24).

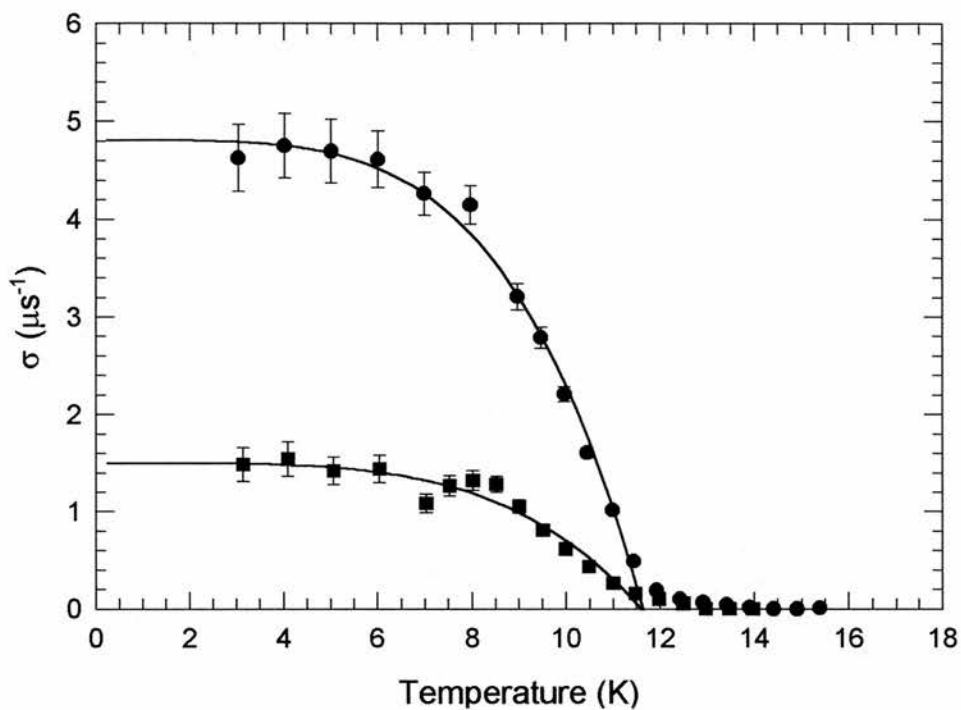


Figure 5.23 The temperature dependence of the muon depolarisation rate for $(Y_{1-x}La_x)Ni_2B_2C$ ($x=0.05$ (●) and 0.2 (■)). The line is a least squares fit using the two fluid model.

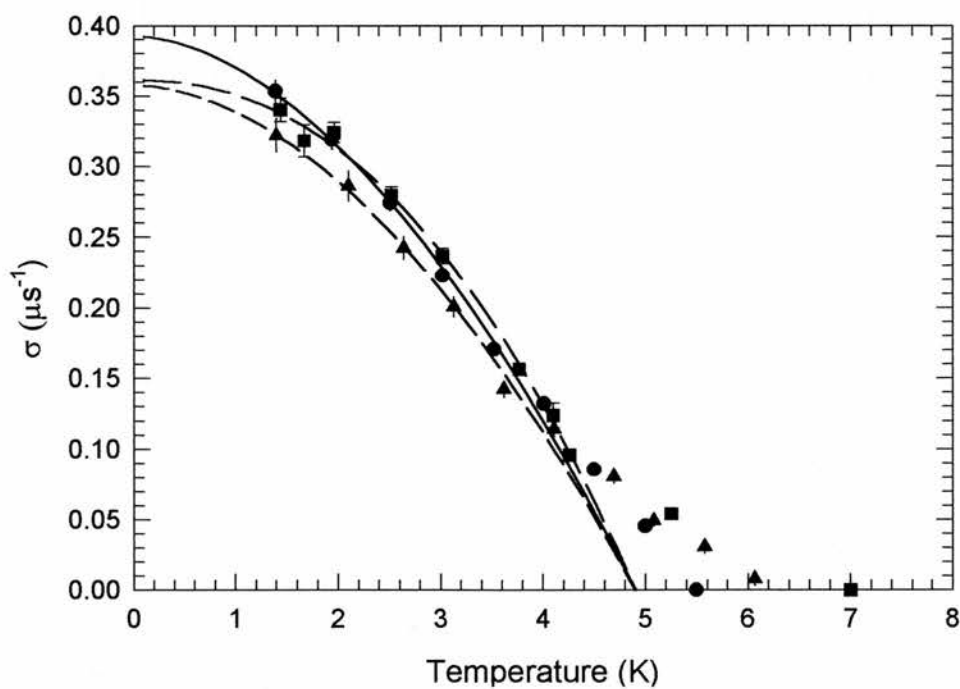


Figure 5.24 The temperature dependence of the muon depolarisation rate for $(Y_{0.5}La_{0.5})Ni_2B_2C$ at $10mT$ (●), $20mT$ (■) and $40mT$ (▲). The line is a least squares fit using the N fluid model

It is possible that the breakdown of the N-fluid model at temperatures close to T_c could be further evidence of local pairing superconductivity in these system. However, this conclusion must be treated with caution since the impurity phase observed by x-ray diffraction may also be responsible. The field dependence of $(Y_{0.5}La_{0.5})Ni_2B_2C$ has also been measured. The extrapolated value of the muon depolarisation rate at $T=0K$ remains approximately constant, within experimental error, at $0.36\mu s^{-1}$. Assuming a triangular lattice, the muon depolarisation rate is related to λ by equation 5.8. λ was determined as 460nm. The constant value of $\sigma(0)$ implies that ξ_{GL} is shorter than 15nm and cannot be determined using the MuSR instrument. The exponent N decreases from 2.2 to 1.9 to 1.8 for applied fields of 10mT, 20mT and 40mT respectively.

5.7 $(Er_{1-x}Tb_x)Ni_2B_2C$.

The large 4f moments in the $(Er_{1-x}Tb_x)Ni_2B_2C$ series lead to significant magnetic depolarisation of the muons at low temperatures. This has prevented penetration depth measurements being carried out at ISIS. Instead we have examined the interplay of magnetic and superconducting ground state in this series of alloys using magnetisation and neutron diffraction techniques.

5.7.1 DC magnetisation study of the $(Er_{1-x}Tb_x)Ni_2B_2C$ alloys.

The superconducting transition temperature has been determined using dc magnetisation described in chapter 3, using an applied field of 6mT (see figure 5.25). It should be noted that as the samples under investigation have large local moments, the resulting magnetisation has components arising from both the magnetic and superconducting response. Therefore, even at the onset of superconductivity the magnetisation signal remains positive. A summary of the determined T_c s can be found in Table 5.4.

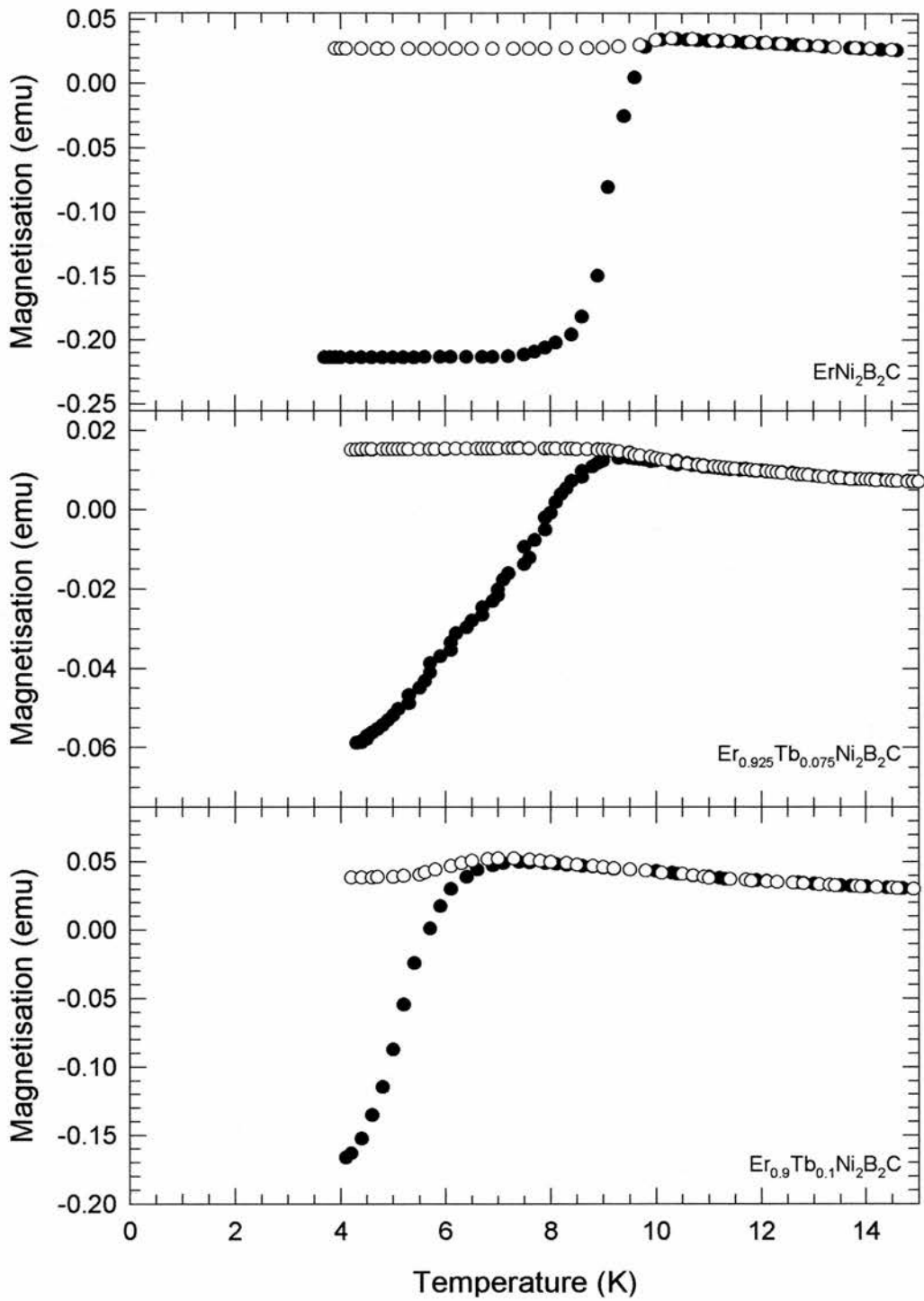


Figure 5.25 The magnetisation as a function of temperature for $\text{Er}_{1-x}\text{Tb}_x\text{Ni}_2\text{B}_2\text{C}$ ($x=0, 0.075$ and 0.1). Using this data T_c has been determined as 10.5K, 9.2K and 7.3K respectively.

Sample	T_c (K)
x=0.0	10.5
x=0.075	9.5
x=0.1	7.3
x=0.2	4.5

Table 5.4 A list of the superconducting transition temperatures for $Er_{1-x}Tb_xNi_2B_2C$.

The magnetic ordering temperature for each sample has been obtained by applying a field greater than H_{c2} at 3.8K and measuring the temperature dependence of the magnetisation. The magnetic ordering temperature is defined as peak in the magnetisation (see figure 5.26). These peaks are also characteristic of antiferromagnetic transitions. At temperatures below 8K, there is some evidence of a weak ferromagnetic component in $TbNi_2B_2C$ ^{41,42}. This ferromagnetic component is suggested as the reason for the suppression of the superconductivity. It is interesting that the weaker second magnetic transitions, below T_N , only occurs in samples that, or are predicted to, exhibit no superconductivity, i.e. $x > 0.35$, (see figure 5.26).

All our measured magnetic and superconducting transition temperatures are summarised in figure 5.27. On substituting terbium for erbium, the superconducting transition temperature decreases almost linearly. An extrapolation of this trend leads to a loss of superconductivity at a concentration of 35%Tb. As T_c could not be measured beyond 20%Tb because the transition temperatures are below 3.8K our data in this region is limited. However, this linear decrease is fully consistent with de Gennes scaling with no apparent breakdown for $T_c < T_N$. Therefore, terbium acts as a good magnetic pair breaker when substituted into $ErNi_2B_2C$.

The Neel temperature remains approximately constant for values of $x=0$ up to 0.5. After $x=0.5$, the Neel temperature rapidly increases with concentration up to a maximum of 15K for $TbNi_2B_2C$. Clearly for $x < 0.5$ there is no de Gennes scaling of T_N but approximate scaling is resumed for $x > 0.5$.

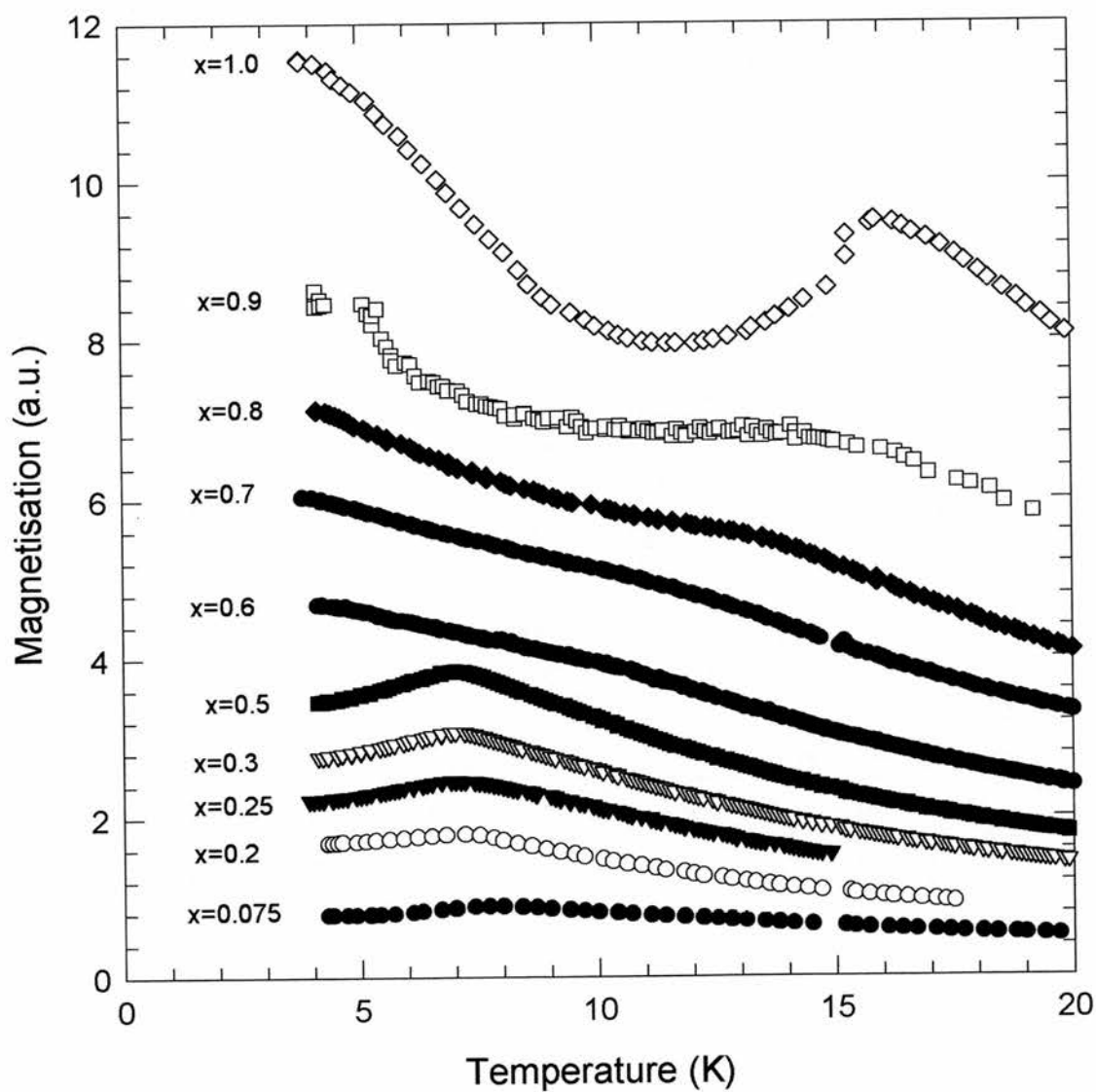


Figure 5.26 The temperature dependence of the magnetisation of $Er_{1-x}Tb_xNi_2B_2C$, measured in an applied field of 0.3 T.

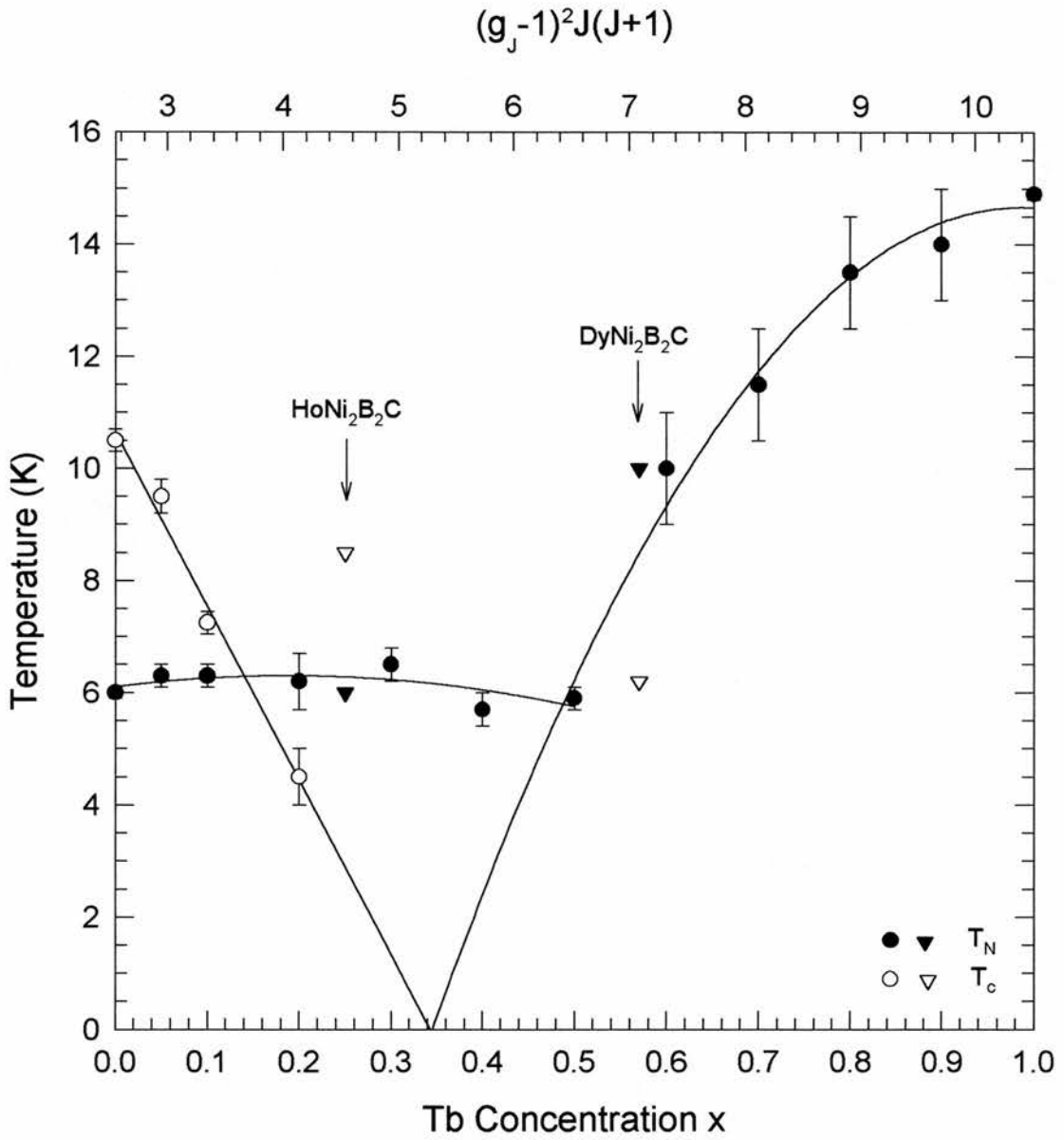


Figure 5.27 The magnetic and superconducting phase diagram for $(Er_x Tb_{1-x})Ni_2B_2C$. T_c and T_N have been plotted for $HoNi_2B_2C$ and $DyNi_2B_2C$ at the appropriate de Gennes factor. The lines are guides to the eye.

Interestingly, as can be seen for figure 5.27, the values T_N for $\text{HoNi}_2\text{B}_2\text{C}$ and $\text{DyNi}_2\text{B}_2\text{C}$ correspond closely to the values for the appropriate $(\text{Er}_x\text{Tb}_{1-x})\text{Ni}_2\text{B}_2\text{C}$ sample with the same de Gennes factor.

5.7.2 Neutron diffraction study of $(\text{Er}_{1-x}\text{Tb}_x)\text{Ni}_2\text{B}_2\text{C}$.

The crystal and magnetic structures of $(\text{Er}_{1-x}\text{Tb}_x)\text{Ni}_2\text{B}_2\text{C}$ have been determined by neutron diffraction. The diffraction patterns were collected on the D1B spectrometer at the ILL reactor in Grenoble. The D1B spectrometer uses a single monochromatic neutron wavelength of 2.15\AA and measures the diffracted intensity as a function of angle. The instrumental set-up is described in more detail in chapter 3. The samples were crushed into a fine powder and inserted into a vanadium can since vanadium has a low coherent neutron scattering length and therefore contributes only a flat background. A pumped helium orange cryostat provided access to temperatures as low as 1.5K. The diffraction patterns from the non-magnetically ordered samples were collected above the respective Neel temperatures and also in the magnetic ordered state at 1.5K. Each diffraction pattern was collected in 10mins and was refined using the FULLPROF Rietveld refinement package⁴³ (for examples see figure 5.28 and figure 5.29). For the two examples shown the diffraction patterns from the non-magnetically ordered state were obtained at 10K. The high temperature diffraction pattern yields information on the lattice parameters, site position and phase purity. The line is a Rietveld refinement to the data and the extra peaks not fitted are impurity peaks. The two diffraction patterns taken at 1.5K represent the samples in the magnetically ordered state. The additional peaks observed in these low temperature patterns spectra are magnetic in origin. A summary of the results of the analysis of the diffraction data is shown in Table 5.5 and figure 5.30.

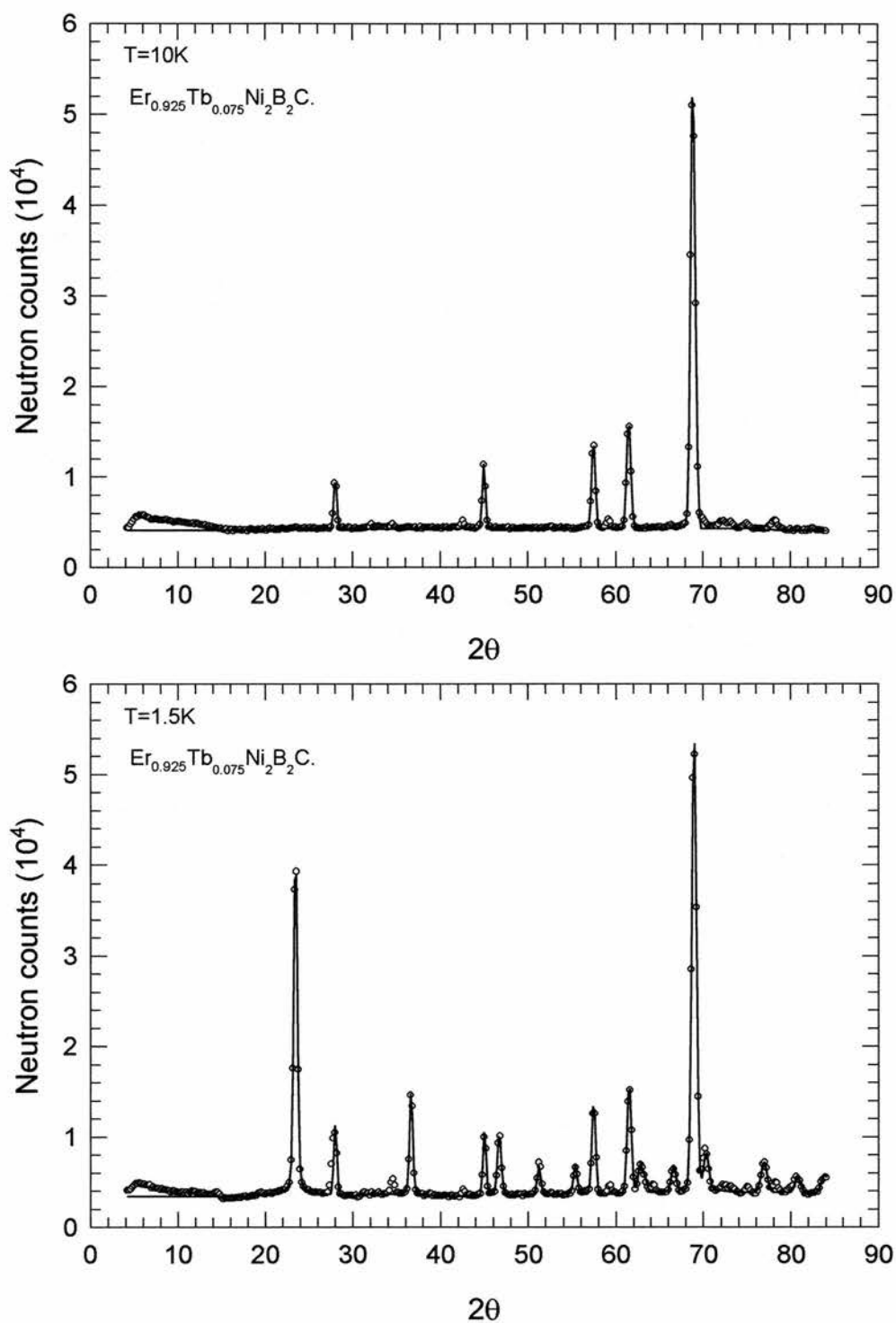


Figure 5.28 The diffraction patterns for $(\text{Er}_{0.925}\text{Tb}_{0.075})\text{Ni}_2\text{B}_2\text{C}$ above and below the magnetic ordering temperature ($T_N=6.3\text{K}$). The upper graph shows the nuclear diffraction peaks. The extra peaks in the lower graph are associated with the magnetic structure.

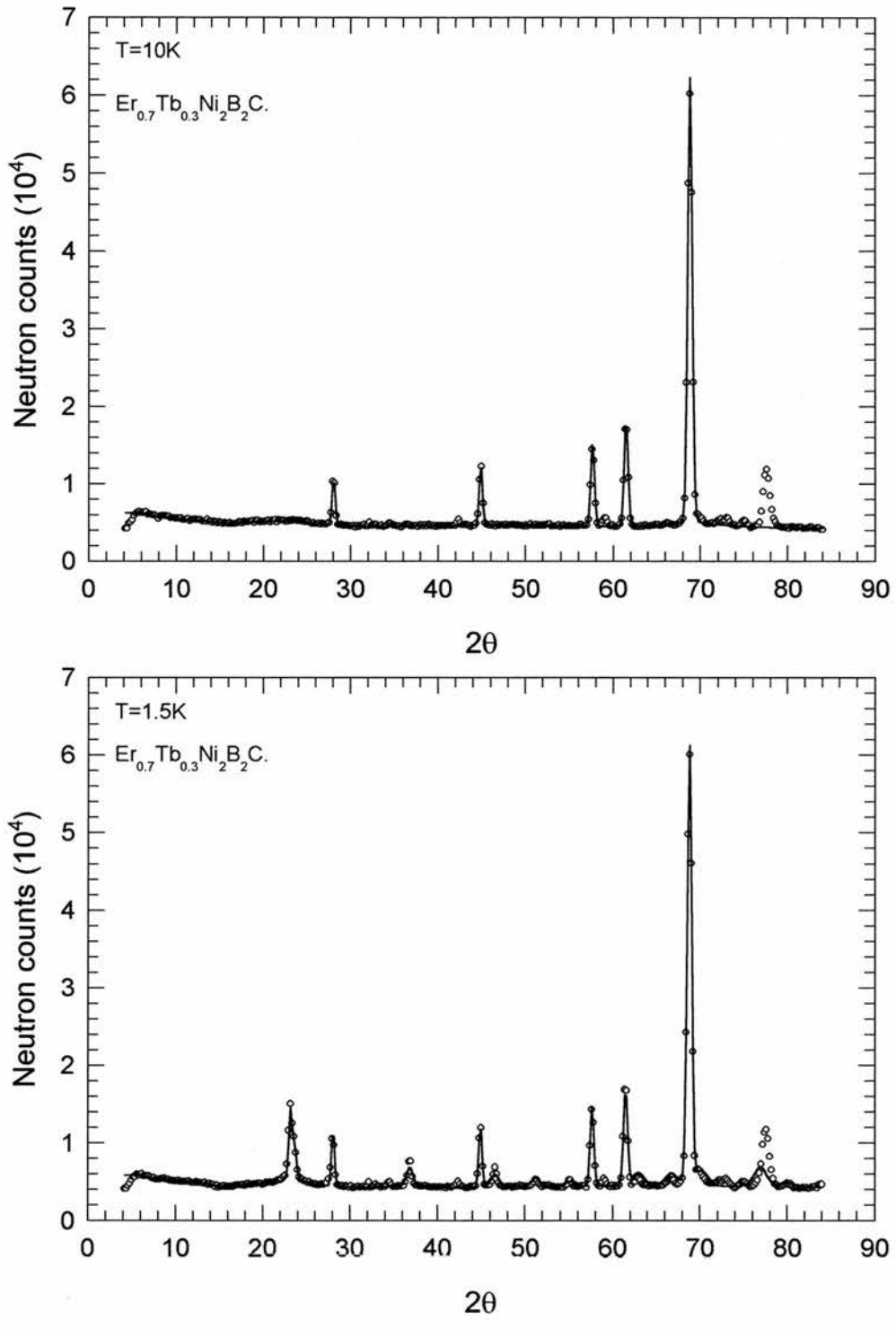


Figure 5.29 The diffraction patterns for $(Er_{0.7}Tb_{0.3})Ni_2B_2C$ above and below the magnetic ordering temperature ($T_N=6.5K$). The upper graph shows the nuclear diffraction peaks. The extra peaks in the lower graph are associated with the magnetic structure.

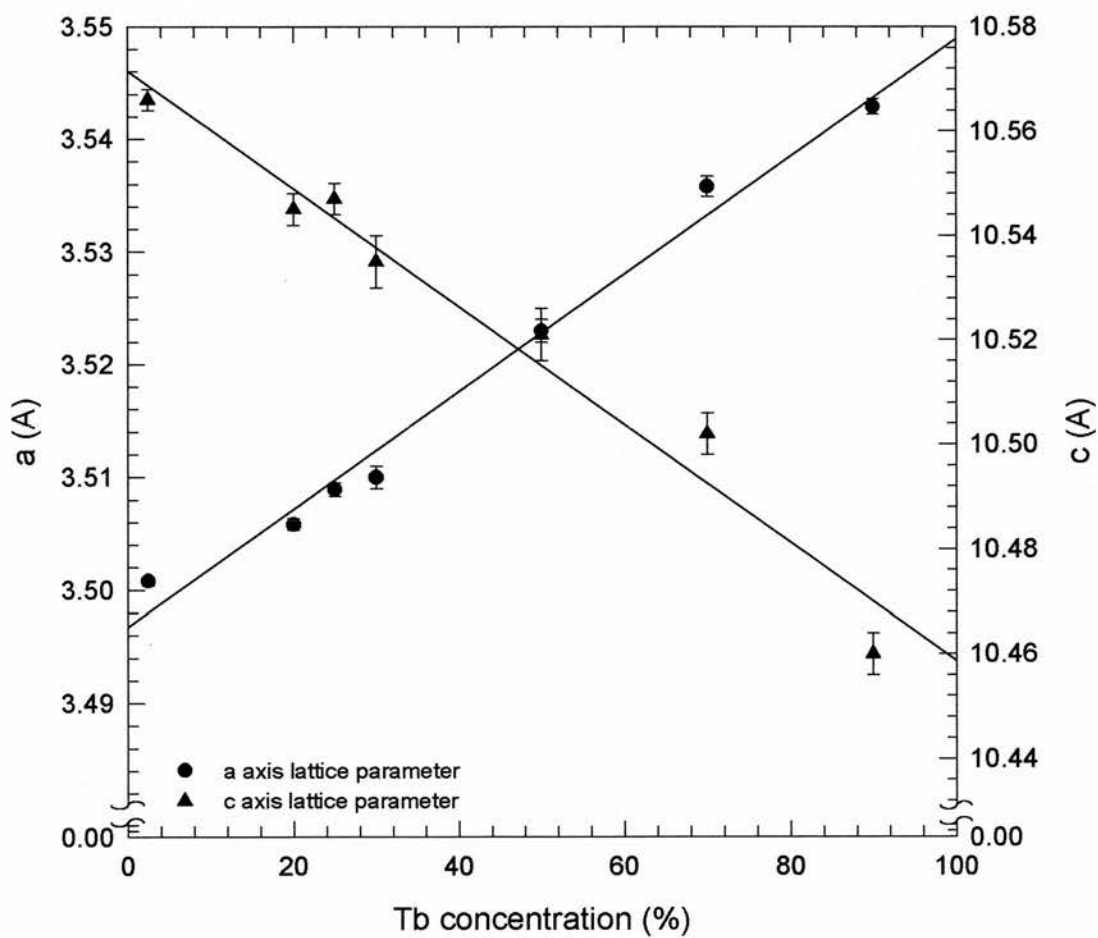


Figure 5.30 The lattice parameters as a function of terbium concentration in $(Er_{1-x}Tb_x)Ni_2B_2C$. The lines are guides for the eye.

%Tb in (Er _{1-x} Tb _x)Ni ₂ B ₂ C	a lattice parameter (Å)	c lattice parameter (Å)	Volume (Å ³)	boron position, z
2.5	3.5008(4)	10.566(2)	129.49(3)	0.352(2)
20	3.5058(5)	10.545(3)	129.60(4)	0.355(2)
25	3.5089(6)	10.547(3)	129.85(4)	0.355(1)
30	3.510(1)	10.535(5)	129.79(8)	0.355(2)
50	3.523(1)	10.521(5)	130.58(8)	0.356(2)
70	3.5358(9)	10.502(4)	131.29(7)	0.354(1)
90	3.5429(7)	10.460(4)	131.29(6)	0.355(2)

Table 5.5 A summary of the results obtained from the nuclear diffraction spectra.

This increase in the a lattice parameter and decrease in the c lattice parameter is unexpected since the terbium ion has a greater ionic radius, and therefore terbium doping might be expected to uniformly expand the lattice. Interestingly, the volume does not follow a uniform change with concentration (see figure 5.31). For x=0 to 20% the volume remains approximately constant. On increasing the concentration still further the unit cell volume increases linearly until reaching a plateau at x=70%. It is noteworthy that the lattice expansion occurs at a concentration close to that at which the superconductivity is suppressed although it has previously been shown that there is no volume dependence of the superconducting transition temperature in the RNi₂B₂C alloys⁴.

The magnetic structure of the RNi₂B₂C compounds has been discussed briefly in section 5.1.2. The addition of Tb for Er in the parent compound ErNi₂B₂C has shown that the magnetic transition temperatures are similar to those for HoNi₂B₂C and DyNi₂B₂C with the same de Gennes value. One might therefore expect that a similar magnetic structure might exist for the (Er_{1-x}Tb_x)Ni₂B₂C as the HoNi₂B₂C and DyNi₂B₂C (see figure 5.32). ErNi₂B₂C is an incommensurate antiferromagnet with a modulation vector, q, along the a-axis and the magnetic moment along the b-axis, a transverse modulation¹². TbNi₂B₂C has a similar antiferromagnetic magnetic ground state and modulation vector, q, but the

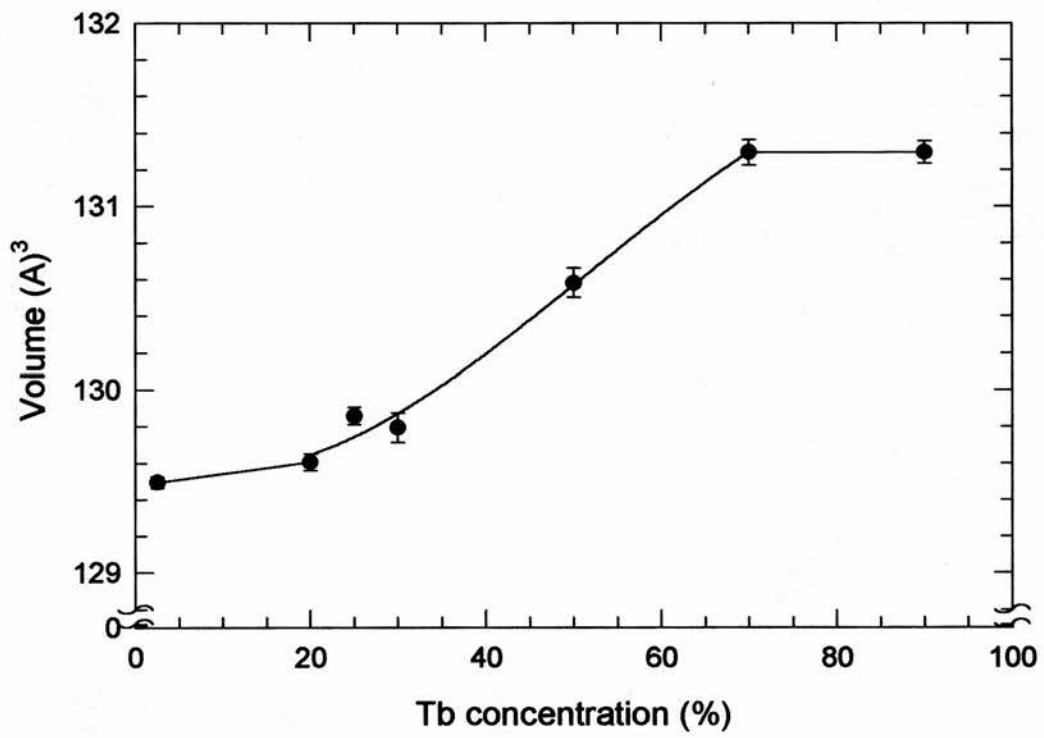
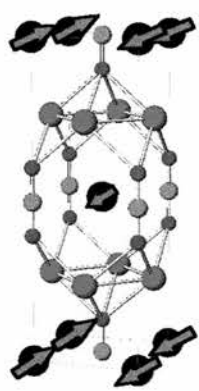
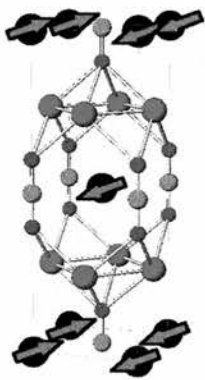
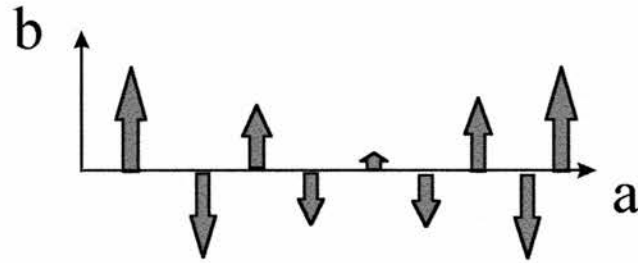


Figure 5.31 The volume as a function of terbium concentration in $(Er_{1-x}Tb_x)Ni_2B_2C$. The line is a guide to the eye.



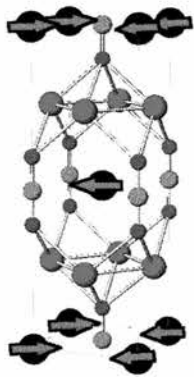
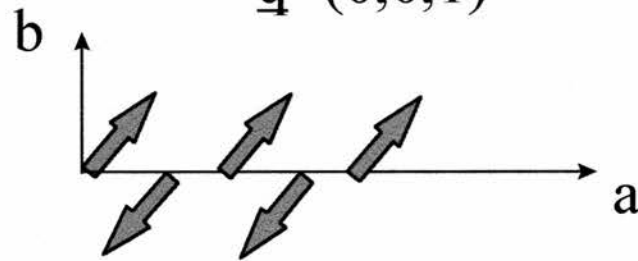
$\text{ErNi}_2\text{B}_2\text{C}$

$$\mathbf{q}=(0.5526,0,0)$$



$\text{HoNi}_2\text{B}_2\text{C}$

$$\mathbf{q}=(0,0,1)$$



$\text{TbNi}_2\text{B}_2\text{C}$

$$\mathbf{q}=(0.555,0,0)$$

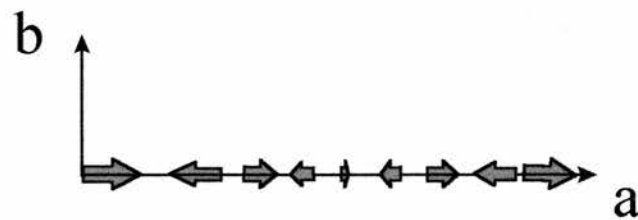


Figure 5.32 The magnetic structures observed for $\text{ErNi}_2\text{B}_2\text{C}$, $\text{HoNi}_2\text{B}_2\text{C}$ and $\text{TbNi}_2\text{B}_2\text{C}$. $\text{ErNi}_2\text{B}_2\text{C}$ has a transversely polarised spin density wave along the a axis. $\text{HoNi}_2\text{B}_2\text{C}$ consists of ferromagnetic sheets of spins in the a - b plane which are antiferromagnetically coupled. $\text{TbNi}_2\text{B}_2\text{C}$ has a longitudinally polarised spin density wave.

magnetic moment is now along the a-axis and longitudinally modulated (see figure 5.32). Our Rietveld refinements of the magnetic structure have shown that the magnetic moment turns from the a axis to the b axis with increasing terbium concentration (see figure 5.33). However, this rotation is not monotonic. Between the concentrations of 25%Tb and 30%Tb the rotation has a distinct discontinuity. It is interesting to note that it is at this concentration that the superconductivity is suppressed. A summary of the magnetic diffraction results is shown Table 5.6.

%Tb in (Er _{1-x} Tb _x)Ni ₂ B ₂ C	μ_a	μ_b	modulation vector, q
2.5	.02(69)	10.4(8)	.5531(3),0,0
20	.7(8)	8.9(2)	.5597(3),0,0
25	.97(91)	8.8(2)	.5604(3),0,0
30	2.6(6)	5.4(3)	.5617(6),0,0
50	3.9(6)	6.7(3)	.5626(9),0,0
70	4.3(4)	2.5(3)	.5528(8),0,0
90	8.8(4)	2.6(3)	.5529(4),0,0

Table 5.6 A summary of the results obtained from the magnetic neutron refinements.

The neutron diffraction data from the ErNi₂B₂C and TbNi₂B₂C have reported the observation of magnetic satellite peaks. Unfortunately, the resolution of our data is not good enough to see the higher harmonic diffraction peaks resulting from the squaring up of the sinusoidal spin waves.

5.8 CONCLUSIONS.

The crystal structure of the YNi₂B₂C alloy has been reconfirmed as a modified ThCr₂Si₂ structure. However, this modification occurs not only through a substitution of carbon at the interstitial (0,0,1/2) site, but also involves some substitution at the boron (0,0,z) site with the displaced boron occupying the (0,0,1/2) site. Our neutron diffraction data is the first to show such disorder.

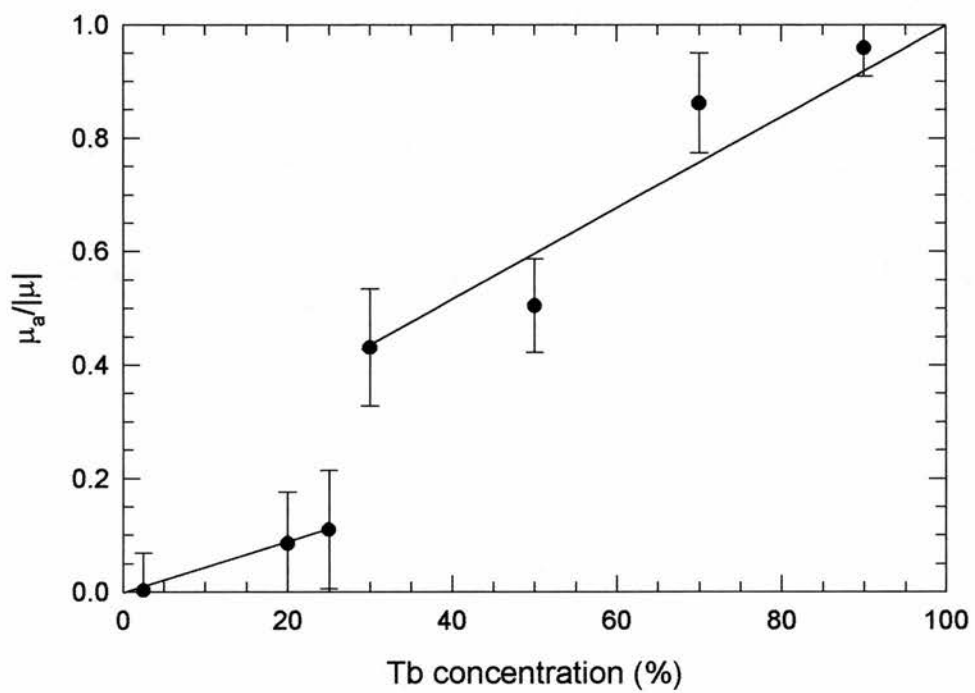


Figure 5.33 The effective moment along the a -axis for $(Er_{1-x}Tb_x)Ni_2B_2C$.

The superconducting ground state has been carefully examined for the $\text{Y}(\text{Ni}_{0.95}\text{Co}_{0.05})_2\text{B}_2\text{C}$, $\text{Y}(\text{Ni}_{0.9}\text{Co}_{0.1})_2\text{B}_2\text{C}$, $\text{LuNi}_2\text{B}_2\text{C}$, $(\text{Y}_{0.95}\text{La}_{0.05})\text{Ni}_2\text{B}_2\text{C}$, $(\text{Y}_{0.8}\text{La}_{0.2})\text{Ni}_2\text{B}_2\text{C}$ and $(\text{Y}_{0.5}\text{La}_{0.5})\text{Ni}_2\text{B}_2\text{C}$ alloys by the use of dc magnetisation and muon spin rotation. A summary of the results can be found in Table 5.7.

Sample	T_c (K)	λ_{mag} (nm)	$\lambda_{\mu\text{SR}}$ (nm)	N at 40mT	ξ_{GL} (nm)	κ
$\text{Y}(\text{Ni}_{0.95}\text{Co}_{0.05})_2\text{B}_2\text{C}$	10.3	113	130	3.1	13.3	8.6
$\text{Y}(\text{Ni}_{0.9}\text{Co}_{0.1})_2\text{B}_2\text{C}$	5.4	206	205	2.1	18.8	11.0
$\text{LuNi}_2\text{B}_2\text{C}$	17.0	80*	224	4.7	7.5	9.1
$(\text{Y}_{0.95}\text{La}_{0.05})\text{Ni}_2\text{B}_2\text{C}$	14.0	143	125	4.6	12.2	11.7
$(\text{Y}_{0.8}\text{La}_{0.2})\text{Ni}_2\text{B}_2\text{C}$	13.0	177	232	4.6	12.7	13.9
$(\text{Y}_{0.5}\text{La}_{0.5})\text{Ni}_2\text{B}_2\text{C}$	6.2	-	460	1.8	-	-

Table 5.7 A summary of the results obtained by dc magnetisation and muon spin rotation.

* This value of λ was obtained from reference 35.

These results show that μSR and dc magnetisation can be used as complementary techniques in determining the fundamental superconducting parameters. The determination of λ for $\text{Y}(\text{NiCo})_2\text{B}_2\text{C}$ and $(\text{YLa})\text{Ni}_2\text{B}_2\text{C}$ are in reasonable agreement. However, for $\text{LuNi}_2\text{B}_2\text{C}$ λ_{mag} is considerable shorter than $\lambda_{\mu\text{SR}}$. This difference can be explained quite simply. Determination of H_{c1} is difficult using DC magnetisation, especially when dealing with a polycrystalline powder. The powder grain size and orientation are unlikely to be uniform and regular, leading to a range of demagnetising factors and hence internal fields. If the demagnetisation factor at one grain is much larger than at another then the applied field will penetrate the grain with the larger demagnetisation factor first and hence provide a low value of H_{c1} . However, with μSR the demagnetisation problem still exists but occurs in a slightly different way. μSR probes the internal fields directly and the sample is in a magnetic equilibrium state. The demagnetisation effect causing a broadening of the sharp features of the flux lattice since the measured distribution is a superposition of signals arising from many grains, each having a different mean internal field. However, in fields well above H_{c1} there is little effect on the second moment of the field distribution, which is related only to the magnetic penetration depth.

The determination of H_{c2} does not suffer from the same demagnetisation problem. H_{c2} for $\text{LuNi}_2\text{B}_2\text{C}$ and $(\text{YLa})\text{Ni}_2\text{B}_2\text{C}$ exhibit a positive curvature for temperatures close to T_c . This curvature is suggestive of local pairing mechanisms being responsible for the superconductivity within these alloys.

Relationships between the magnetic and superconducting phases have also been established. The superconducting transition temperature, T_c , for $(\text{Er}_{1-x}\text{Tb}_x)\text{Ni}_2\text{B}_2\text{C}$ exhibits linear de Gennes scaling with a predicted suppression of T_c at approximately 35% Tb. The Neel temperature, however, does not scale with the de Gennes factor. T_N remains constant for $x=0$ to 0.5 and then scales for $x=0.5$ to 1 reaching a maximum at $x=1$, $\text{TbNi}_2\text{B}_2\text{C}$, of 15K. The neutron diffraction measurements have shown a linear increase in the a lattice parameter whereas the c lattice parameter shows a linear decrease. The overall unit cell volume has shown an increase in size. However, this is a non-linear increase with concentration showing a marked increase in the rate of volume expansion with respect to terbium concentration at 25%Tb. The magnetic neutron refinements have a discontinuity at 25%Tb. For concentrations greater than 25%Tb the magnetic moment suddenly rotates more rapidly away from the propagation vector axis. All these anomalies coincide with the loss of superconductivity. This implies a complex interplay between the superconductivity and magnetic structure in $(\text{Er}_{1-x}\text{Tb}_x)\text{Ni}_2\text{B}_2\text{C}$. The neutron diffraction data has provided no evidence of the reported ferromagnetic component in terbium rich alloys although such a component may be present in the magnetisation data.

5.9 REFERENCES

- ¹ R. Chevrel, M. Sergent, J. Prigent. *J. Solid State Chemistry*, **3**, 515 (1971).
- ² J.G. Bednorz, K.A. Muller, *Z.Phys. B*, **64**, 189 (1986).
- ³ C. Mazumdar, R. Nagarjan, C. Godart, L.C. Gupta, M. Latroche, S.K. Dhar, C. Levy-Clement, B.D. Padalia, R. Vijayaraghaven. *Solid State Communications*, **87**, 413 (1993).
- ⁴ R.J. Cava, H. Takagi, B. B. Batlogg, H.W. Zandbergen, J.J. Krajewski, W.F. Peck Jr, R.B. Vandover, R.J. Felder, T. Siegrist, K. Mizuhashi, J.O. Lee, H. Eisaki, S.A. Carter, S. Uchida. *Nature (London)*, **367**, 252, (1994).
- ⁵ T. Segrist, H.W. Zandbergen, R.J. Cava, J.J. Krajewski, W.F. Peck Jr. *Nature (London)*, **367**, 254 (1994).
- ⁶ J.I. Lee et al *Phys. Rev. B*. **50**, 4030, (1994).
- ⁷ A.K. Gangopadhyay, A.J. Scheutz, J.S. Schilling, *Physica C*, **246**, 317, (1995)
- ⁸ C.C. Hoellwarth, P. Klavins, R.N. Shelton, *Phys. Rev. B*, **53**, 2579, (1996).
- ⁹ R. Cywinski, Z.P. Han, R. Bewley, R. Cubitt, M.T. Wylie, E.M. Forgan, S.L. Lee, M. Warden, S.H. Kilcoyne, *Physica C*, **233**, 273, (1994).
- ¹⁰ Y. Uemura. *Physica C*. **185-189**, 733 (1991).
- ¹¹ B.K. Cho, P.C. Canfield, D.C. Johnson. *Phys. Rev. B*. **53**, 8499, (1996).
- ¹² P. Dervenagas, J. Zarestky, C. Stassis, A.I. Goldman, P.C. Canfield, B.K. Cho. *Phys. Rev. B*. **53**, 8506, (1996).
- ¹³ D.R. Sanchez, H. Micklitz, M.B. Fontes, E Baggio-Saitovitch. *J. Phys. C*. **9**, L229, (1997).
- ¹⁴ C. Detlefs, A.I. Goldman, C. Stassis, P.C. Canfield, B.K. Cho, J.P. Hill, D. Gibbs. *Phys. Rev. B*. **53**, 6355, (1996).
- ¹⁵ M. Massalami, B. Giordanengo, J. Mondragon, E.M. Baggio-Saitovitch, A. Takeuchi, J. Voiron, A. Sulpice. *J. Phys. C*. **7**, 10015, (1995).
- ¹⁶ P. Dervenagas, J. Zarestky, C. Stassis, A.I. Goldman, P.C. Canfield, B.K. Cho. *Physica B*, **212**, 1, (1994).
- ¹⁷ C.V. Tomy, G. Balakrishan, D. McK.Paul. *Physica C*, **248**, 349 (1995).
- ¹⁸ C. V. Tomy, M.R. Lees, L. Afalfiz, G. Balakrishan, D. McK.Paul. *Physical Review B*, **52**, 9186 (1995).
- ¹⁹ J.W. Lynn, Q. Huang, S.K. Sinha, Z. Hossain, L.C. Gupta, R. Nagarajan, C. Godart. *J. Applied Physics*. **79**, 5857, (1996).
- ²⁰ H. Schmidt, M. Weber, H.F. Braun. *Physica C*. **246**, 177 (1995).
- ²¹ A.I. Goldman, C. Stassis, P.C. Canfield, J. Zarestky, P. Dervenagas, B.K. Cho, D.C. Johnston *Phys. Rev. B*. **50**, 9668, (1994).
- ²² Q. Huang, A. Santoro, T.E. Grigereit, J.W. Lynn, R.J. Cava, J.J. Krajewski, W.F. Peck Jr., *Phys. Rev. B*. **51**, 3701, (1995).

-
- ²³ T. Vogt, C. Stassis, A. Goldman, P. Canfield, B. Cho, *Physica B*, **215**, 159, (1995).
- ²⁴ C.V. Tomy, I.J. Chang, D. Mck. Paul, N.H. Andersen, M. Yethiraj, *Physica B*, **213**, 139, (1995).
- ²⁵ C. Godart, L.C. Gupta, R. Nagarajan, S.K. Dhar, H. Noel, M. Potel, C. Mazumdar, Z. Hossain, C. Levyclement. *Physical Review B*. **51**,489, (1995).
- ²⁶ J. Zarestky, C. Stassis, A.I. Goldman, P.C. Canfield, P. Dervenagas, B.K. Cho, D.C. Johnson. *Phys. Rev. B*. **51**, 678, (1995).
- ²⁷ S.K. Sinha, J.W. Lynn, T.E. Grigereit, Z. Hossain, L.C. Gupta, R. Nagarajan, C. Godart. . *Phys. Rev. B*. **51**, 681, (1995).
- ²⁸ R. J. Cava, H. Takagi, B. Batlogg, H.W. Zandbergen, J.J. Krajewski, W.F. Peck, Jr., R.B. van Dover, R.J. Felder, T. Siegrist, K. Mizuhashi, J.O. Lee, H. Easaki, S.A. Carter, S. Uchida, *Nature (London)*, **367**, 146, (1994).
- ²⁹ H. Easaki, H. Takagi, R.J. Cava, K. Mizuhashi, J.O. Lee, B. Batlogg, J.J. Krajewski, W.F. Peck, Jr., S. Uchida, *Phys. Rev. B*. **50**, 647 (1994).
- ³⁰ B.K. Cho, P.C. Canfield, D.C. Johnson, *Phys. Rev. B*. **52**, R3844, (1995).
- ³¹ B.K. Cho, P.C. Canfield, D.C. Johnson, *Phys. Rev. Lett.* **77** 163 (1996).
- ³² F. Canepa, P. Manfrinetti, A. Palenzona, V. Calzona, C. Ferdeghini, D. Marre. *Solid State Communications*. **93**. 21 (1995).
- ³³ Cambridge Crystallography Subroutine Library, ISIS.
- ³⁴ Chakoumakos *et al*, *Physica C*. **227**, 143 (1994).
- ³⁵ H. Takagi, R.J. Cava, H. Eisaki, J.O. Lee, K. Mizuhashashi, B. Batlogg, S. Uchida, J.J. Krajewski, W.F. Peck Jr. *Physica C* **228**, 389, (1994).
- ³⁶ R. Micnas, J. Ranninger, S. Robaszkiewicz, *Reviews of Modern Physic*. **62**, 113 (1990).
- ³⁷ E.H. Brandt. *Reports of progress in Physics*. **58**, 1465 (1995).
- ³⁸ Lecture notes from training school in pulse μ SR techniques. S.H. Kilcoyne (ed.) RAL report: RALTR 96007 (1996).
- ³⁹ Y. De Wilde, M. Iavarone, U. Welp, V. Metlushko, A.E. Koshelev, I. Aranson, G.W. Crabtree, P.C. Canfield. *Phys. Rev. Lett.* **78**, 4273 (1997).
- ⁴⁰ E.H. Brandt. *Physical Review B*. **37**. 2349 (1988).
- ⁴¹ Z. Zeng, D Guenzburger, D.E. Ellis, E. M Baggio-Saitovitch, *Physica C* **271**, 23 (1996).
- ⁴² B.K. Cho, P.C. Canfield, D.C. Johnson, *Phys. Rev. B*. **53**, 8499 (1996).
- ⁴³ J. Rodriguez-Carvajal. FULLPROF refinement program, LLB.

6. Yttrium Hexaboride.

6.1 INTRODUCTION.

The RB_6 compounds (R=rare earth or yttrium) crystallise with the $Pm3m$ space group. The rare earth atoms form a simple cubic sublattice with a boron octahedral cage in the centre (see figure 6.1). There are some structural similarities between the RB_6 compounds and the RNi_2B_2C compounds, for example both have a boron-carbon cage (see figure 6.2 and figure 5.1), and in both cases, the cage surrounds a R atom. The superconducting phase for most borocarbides has been determined to be RT_2B_2C (T=transition metal). However, for Th-Pd-B-C, the superconducting phase has been identified as two products of the sample preparation: $ThPd_2B_2C$ and $ThPd_{0.65}B_{4.7}$ which have superconducting transitions of $14.5K^{1,2}$ and $21K^3$ respectively. Crystallographic studies of $ThPd_{0.65}B_{4.7}$ have shown this 21K superconductor to be a simple derivative of the hexaborides⁴ (see figure 6.3). The Pd atom replaces two boron atoms and is displaced site from the $(1/2, 1/2, x)$ to the $(1/2, 1/2, 0)$ site (see figure 6.3).

The hexaboride family has a variety of magnetic ground states. On changing the R element the ground state can be changed from a semiconducting ferromagnet to a metallic antiferromagnet to a superconductor. EuB_6 is a semiconducting ferromagnet with a transition temperature of $8K^{5,6}$. YbB_6 is also a semiconductor. Ho^7 , Dy^7 , Tb^7 , Gd^8 , Nd^9 and Pr^{10} hexaborides are metallic antiferromagnets with ordering temperatures of 9K, 21.5K, 23K, 17.6K, 8.6K and 7K respectively. Neutron powder diffraction measurements on PrB_6^{11} and NdB_6^{12} have determined the magnetic structure. For PrB_6 at 6.9K an incommensurate magnetic phase with $Q=(0.23, 0.23, 0.5)2\pi/a_0$ is observed. At 4.2K a commensurate magnetic phase was seen, with a $Q=(1/4, 1/4, 1/4)2\pi/a_0$, coexisting with the incommensurate phase. On cooling, still further, to 1.9K only the commensurate phase is observed. However, NdB_6 has a simple commensurate antiferromagnetic structure. No such diffraction measurements exist for the other hexaborides.

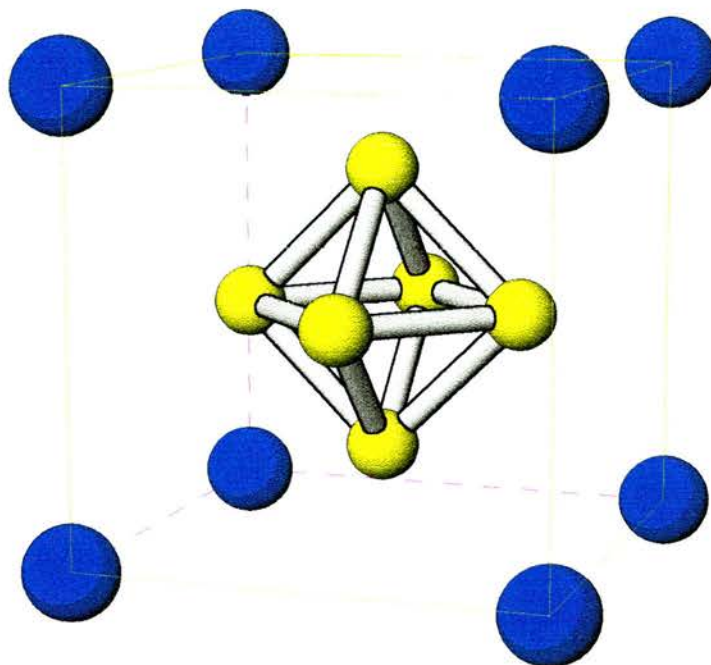


Figure 6.1 The crystal structure of YB₆. The large blue spheres represent the yttrium atoms whereas the small yellow spheres represent the boron atoms.

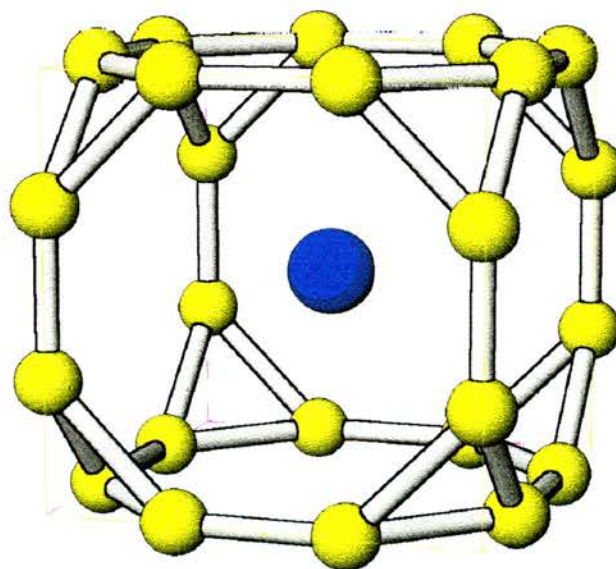


Figure 6.2 The YB₆ crystal structure. The blue and yellow spheres represent the rare earth or yttrium and boron atoms respectively. This shows the boron cage surrounding the rare earth or yttrium atom

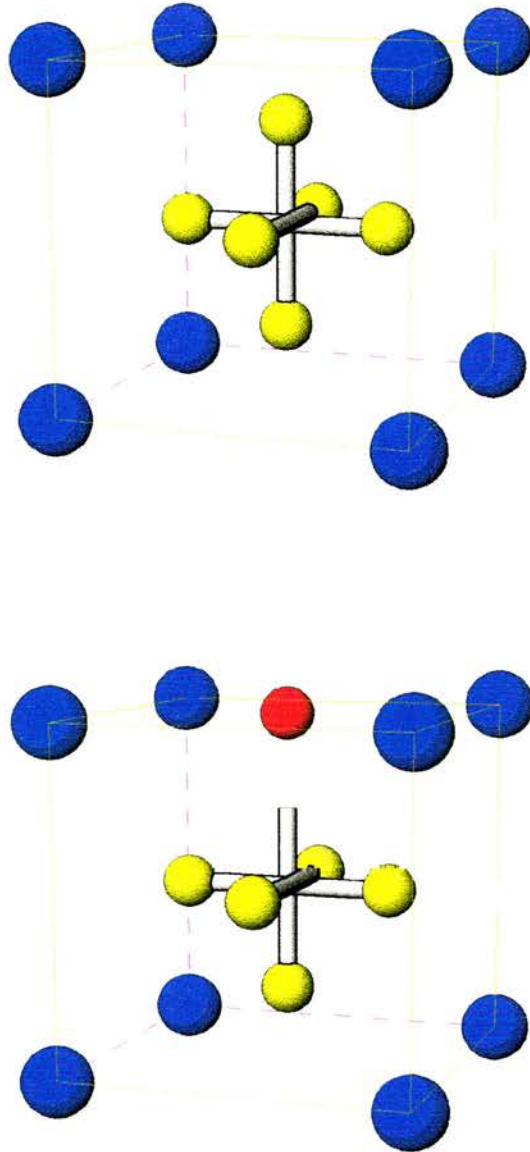


Figure 6.3 The crystal structures of ThB₆ (top) and ThPd_{0.65}B_{4.7} (bottom). This shows the crystallographic relationship between the 21K superconductor ThPd_{0.65}B_{4.7} and ThB₆. The lower picture shows the palladium atom (Red sphere) replacing two boron atoms (yellow spheres). The Thulium is represented by the large blue spheres.

CeB₆ is also an antiferromagnet and a dense Kondo system^{13,14,15}. At 3.2K CeB₆ exhibits antiferro-quadrupolar ordering and below 2.3K antiferromagnetic order is observed. The magnetic structure of CeB₆ below 2.3K has been determined by neutron diffraction^{16,17,18}. A magnetic structure similar to the incommensurate magnetic phase of PrB₆ was observed. The moments are in the x-y plane with $Q=(1/4,1/4,1/2)2\pi/a_0$. However, the magnetic ground state is not fully understood. Muon spin rotation measurements have shown the magnetic structure determined by neutron diffraction can not be possible due to the high internal fields^{19,20}.

The trivalent RB₆ compounds have one conduction electron per formula unit because the boron octahedron bonding orbits are filled with two electrons²¹. Both EuB₆ and YbB₆ are semiconductors because the rare earth ion is divalent. It is remarkable that changing the rare earth element can give rise to such a rich and varied magnetic properties as found in this family of compounds (see Table 6.1).

Sample	T _{Neel} (K)	T _{Curie} (K)	T _c (K)
EuB ₆	-	8 ^{5,6}	-
HoB ₆	9 ⁷	-	-
DyB ₆	21.5 ⁷	-	-
TbB ₆	23 ⁷	-	-
GdB ₆	17.6 ⁸	-	-
NdB ₆	8.6 ⁹	-	-
PrB ₆	7 ¹⁰	-	-
CeB ₆	2.3 ^{13,14,15}	-	-
YB ₆	-	-	7.1 ²²

Table 6.1 A table of the ordering temperatures for RB₆.

However, replacing the rare earth element with yttrium, thus forming YB₆, leads to superconductivity below T_c=7.1K²². It is suggested that YB₆ is a conventional BCS superconductor with a relatively high superconducting transition. This high transition is believed to be a result of strong coupling of the electrons to the Einstein-like modes of the Y

ion situated in the B_6 cage^{23,24}. Considering the structural similarities of the RB_6 and the RNi_2B_2C compounds, and noting that the RB_6 compounds are a simple derivative of the borocarbides, it could be suggested that YB_6 belongs to the same family of superconductors as the RNi_2B_2C compounds. In order to determine the nature of the relationship between YB_6 and RNi_2B_2C , it is clearly necessary to determine the fundamental superconducting parameters of YB_6 .

6.2 INITIAL CHARACTERISATION.

6.2.1 Sample preparation.

The Y-B binary phase diagram²⁵ shows that YB_6 can not be formed directly from the melt since at the YB_6 composition there is no eutectic (see figure 6.4). On examination of the phase diagram, clearly YB_4 , YB_6 and YB_{12} may be formed whilst cooling through the liquidus.

Initial attempts to produce single phase YB_6 by argon arc melting failed. All samples showed a substantial contamination by YB_4 and YB_{12} . We therefore resorted to buying YB_6 directly, as a spectrographically pure powder from Aldrich Chemical Company. The x-ray diffraction spectra were collected using a STOE Stadi P x-ray diffractometer in transmission geometry (see §3.3) with Cu $K_{\alpha 1}$ radiation ($\lambda=0.147\text{nm}$). The resulting spectrum shows that the purchased ' YB_6 ' sample contains two structural phases (see figure 6.5).

Using FULLPROF²⁶ Reitveld refinement program, the spectrum was found to be consistent with two crystallographic phases. The two phases were identified as YB_6 and YB_4 , occurring in the proportion of 70% and 30% respectively. The structural refinement confirmed that the YB_6 phase has a cubic $D2_1$ ($Pm3m$) CaB_6 type structure and a lattice parameter of 0.410nm, while the YB_4 phase has a $D1_c$ ($P4/m3m$) UB_4 type structure with the yttrium again forming a simple cubic lattice and being surrounded with a boron octahedron. However, these boron octahedrons are link together with boron-boron bonds. The lattice parameters of YB_4 were

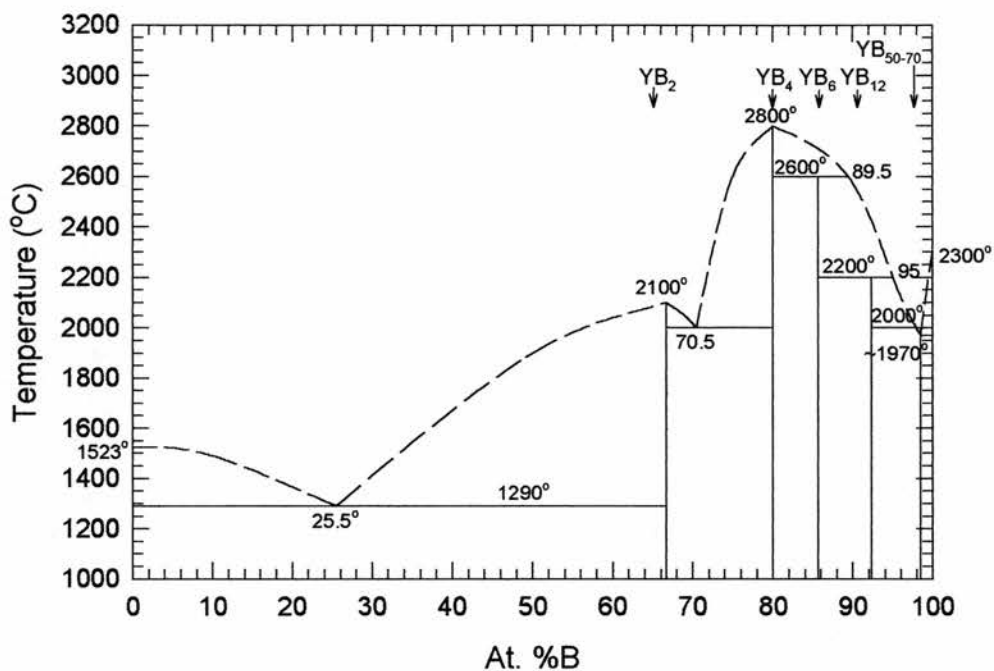


Figure 6.4 The eutectic phase diagram of Y-B alloys²⁵.

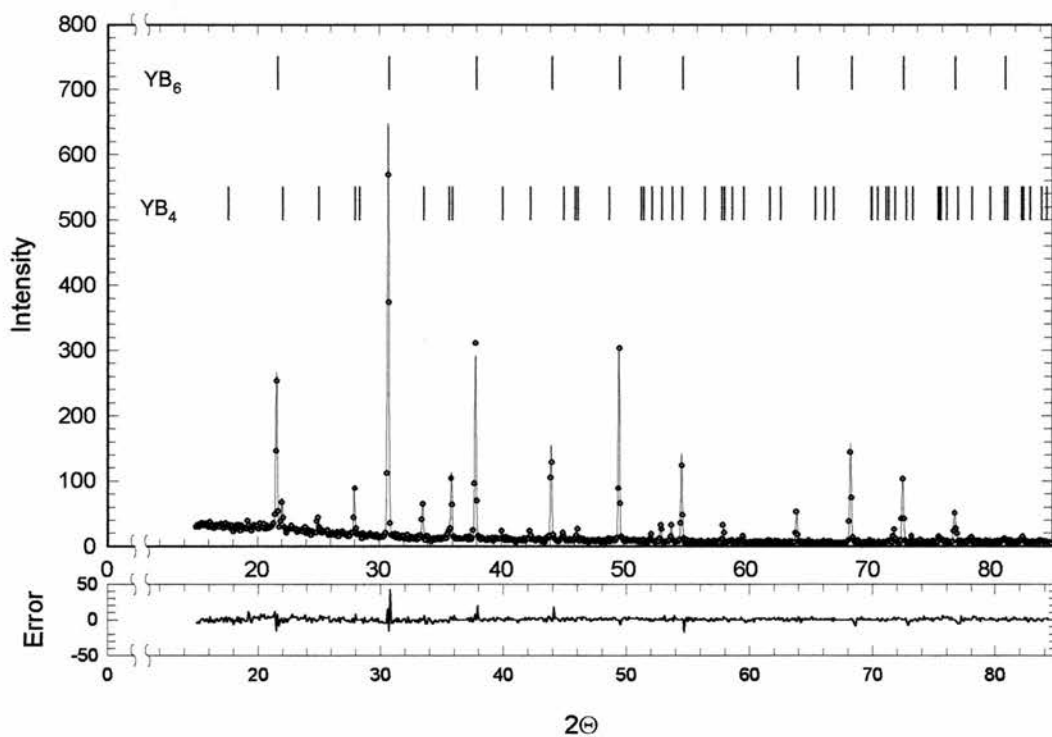


Figure 6.5 The x-ray diffraction pattern and Reitveld refinement of the YB₆ sample. The tick marks represent the diffraction peaks for the YB₆ and YB₄ phases.

found to be 0.710nm and 0.402nm for a and c respectively. However, since YB₄ is non magnetic and non superconducting²⁷ then it is not expected to affect the μ SR studies of the superconducting properties of YB₆.

6.2.2 Magnetic Characterisation.

DC magnetisation measurements were used to determine the superconducting transition temperature and lower and upper critical fields of the ‘YB₆’ sample. The superconducting transition was obtained by zero field cooling the sample to below the reported superconducting transition temperature and subsequently measuring the magnetisation, on warming, in an applied dc field of 6mT. The superconducting transition temperature is found to be 6.8K (see figure 6.6) consistent with reported values of the superconducting transition.

The lower critical field, H_{c1} , of the ‘YB₆’ sample was determined by applying a slowly increasing field (0.5mT/s) after first zero field cooling the sample below the superconducting temperature. The lower critical field is defined as the field at which the magnetic flux first penetrates the sample, and the initial susceptibility first shows a deviation from linearity. This definition must be used with caution; a random orientation of the grains within the sample may lead to a distribution of demagnetisation factors and hence may lead to the formation of an intermediate state in some grains below H_{c1} ²⁸.

The two-fluid model²⁹ has been fitted the lower critical field data (see figure 6.7),

$$H_c(T) = H_c \left(1 - \left(\frac{T}{T_c}\right)^2\right). \quad 6.1$$

At T=0K, $H_{c1}(0)$ is 2.7(1)mT. Because data could be collected only over a limited temperature range the 2-fluid model fit to the data should be treated with caution. Only a limited number of lower critical fields close to the transition were measured and a substantial extrapolation to zero temperature is necessary. The upper critical field, H_{c2} , has also been measured as a function of temperature (see figure 6.8) in this case $H_{c2}(T)$ was defined as the field at which the magnetic hysteresis loop first closes. For the hysteresis measurements the applied field was swept at a rate of 5mT/s in order to reduce

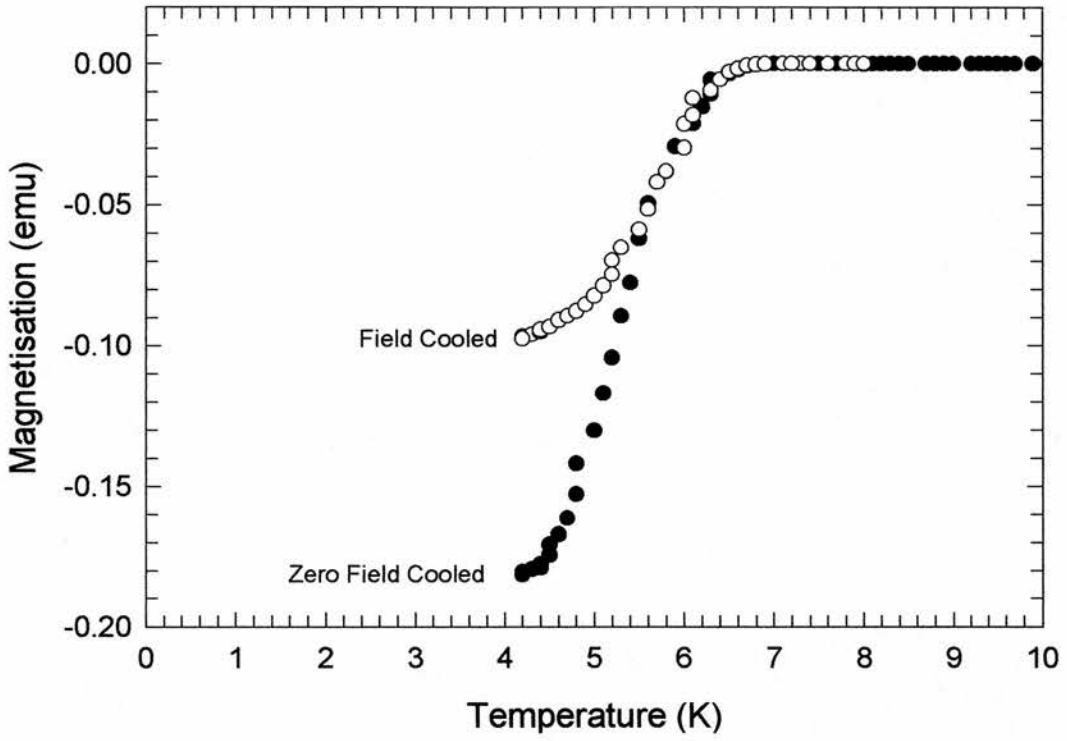


Figure 6.6 The temperature dependence of the magnetisation for YB_6 in an applied field of $6mT$.

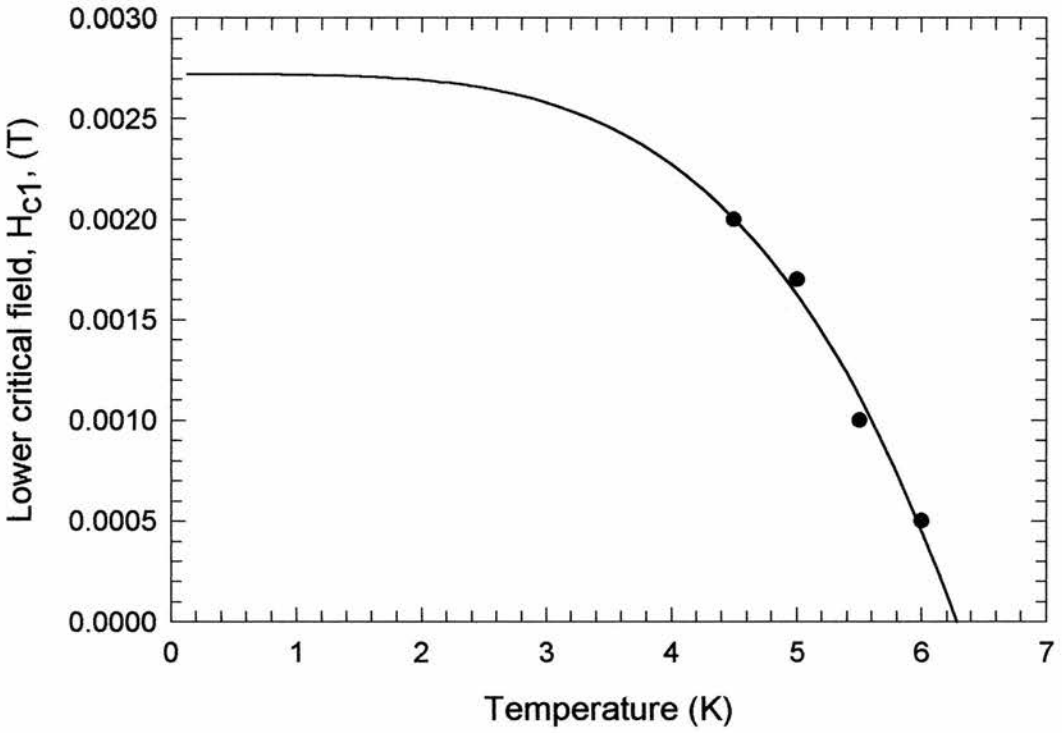


Figure 6.7 The temperature dependence of the lower critical field for YB_6 . The line is a fit to the data using the two fluid model.

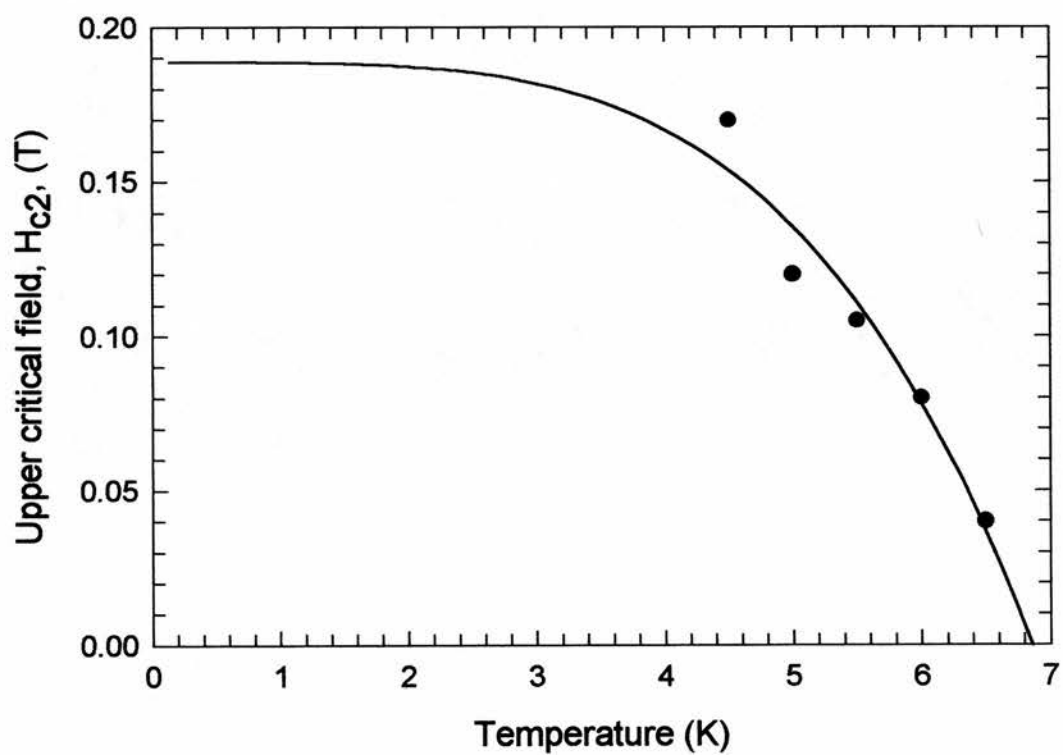


Figure 6.8 The temperature dependence of H_{c2} for YB_6 . The line is the fit to the data using the two fluid model.

the error of the ramp rate dependence of the width of the hysteresis loop. The fit of the two-fluid model to the H_{c2} data leads to the extrapolated value of $H_{c2}(0) = 0.188(3)\text{T}$.

Using equations 5.2 and 5.3 together with our critical field measurements, the magnetic penetration depth, λ , and Ginzburg Landau coherence length, ξ_{GL} , of YB_6 are determined to be 398nm and 42nm respectively.

Using the Bean model³⁰ the width of the hysteresis is often used to provide information on the critical currents and flux pinning strength. The critical current, J_c , is related to the difference in magnetisation, ΔM , by

$$J_c = \frac{16}{3\pi\mu_0\Delta M d} \quad 6.2$$

where d is the diameter and flux pinning is given by

$$F_p = BJ_c. \quad 6.3$$

The difference of the magnetisation in the hysteresis loop of YB_6 is small (see figure 6.9) indicating extremely weak flux pinning and very low critical currents. This result is very surprising considering the presence of the YB_4 impurity phase. The presence of such a large impurity phase usually introduces pinning centres and consequently increases the flux pinning strength. Clearly, the YB_4 phase and YB_6 phase within the sample are discrete, i.e. there are regions of phase pure YB_6 and of YB_4 .

6.3 MUON SPIN ROTATION

The finely powdered ' YB_6 ' sample was mounted onto an aluminum sample holder with GE varnish in such a way as to cover the whole of the incident muon beam. The mounted ' YB_6 ' sample was then inserted into an orange cryostat which can give a temperature range of 1.5K to 310K. Using the MuSR instrument at ISIS, Oxford, UK, the transverse field μSR spectra were collected, on warming, after field cooling the sample below the superconducting transition. The field dependence measurements were collected at 1.5K and the phases were

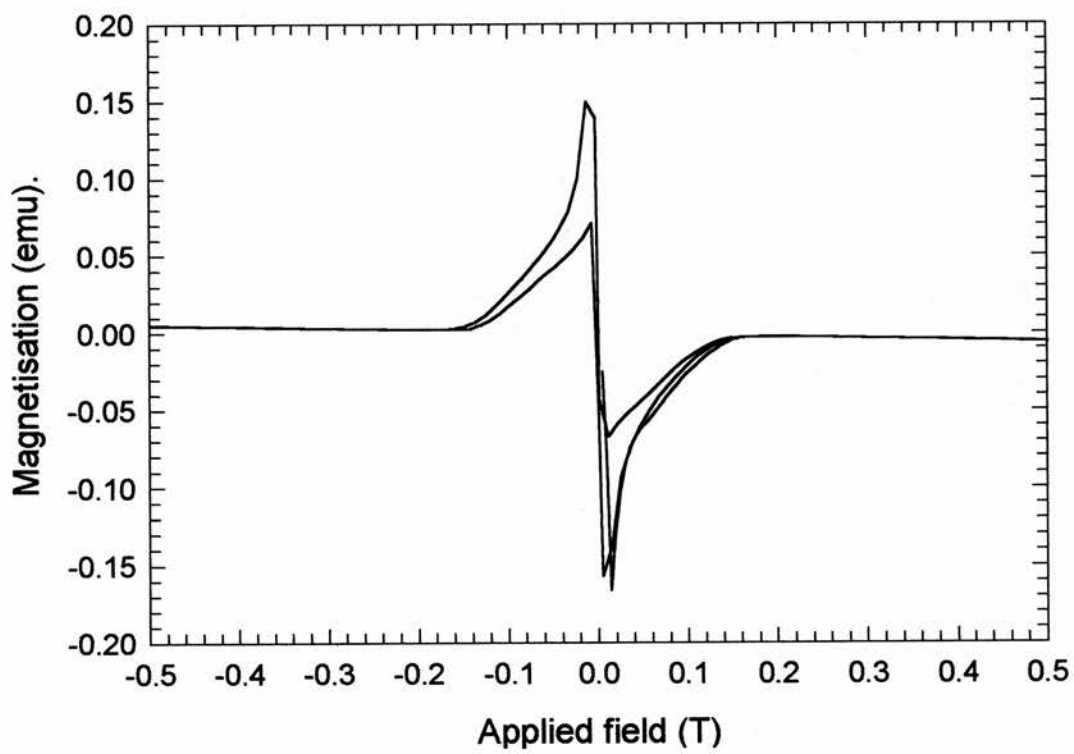


Figure 6.9 A magnetic hysteresis loop at 4.5K.

set using the muon spectra collected at 10K, well above the 7.1K superconducting transition temperature.

Above the superconducting transition, the μ SR depolarisation spectra are well described by (see figure 6.10)

$$G_z(t) = A_o \exp(-\sigma^2 t^2) \cos(\omega t + \phi), \quad 6.4$$

where A_o is the initial asymmetry, σ is the muon depolarisation rate, ω is the muon precession frequency and ϕ is the phase. The depolarisation of the muon spectra above the superconducting transition is due to the dipole fields resulting from the nuclear magnetic moments of yttrium and boron. However, below the superconducting transition temperature the spectra are best represented by (see figure 6.10)

$$G(t) = A_{os} \exp(-\sigma_s^2 t^2) \cos(\omega_s t + \phi) + A_{on} \exp(-\sigma_n^2 t^2) \cos(\omega_n t + \phi) \quad 6.5$$

The first term in relation 6.8 represents the YB_6 component of the sample that is superconducting and in the mixed state. The second term is associated with the non-superconducting YB_4 phase. The ratio of the initial asymmetry of the two Gaussians at 1.5K, i.e. $A_{on}/A_{os}=33/67$, is in excellent agreement with the ratio of the proportions of the two phases obtained from x-ray diffraction measurements on the same sample.

The distribution of internal fields was generated by a maximum entropy Fourier transform of the time domain muon spectra. Two Gaussians have been fitted to the resulting field domain spectra, the first representing the superconducting phase, and the second, centred at the applied field value, representing the non superconducting phase. The Gaussian profile in the superconducting phase is as expected for a polycrystalline powder sample³¹. As can be seen this gives a very good description of the maximum entropy output.

The temperature dependence of the muon depolarisation rate was found to be BCS-like and it was possible to model $\sigma(T)$ using the N-fluid model (see figure 6.12),

$$\sigma(T) = \sigma(0) \left(1 - \left(\frac{T}{T_c}\right)^N\right). \quad 6.6$$

The value of N was found to be 4.0(1) and 2.5(1) for applied fields of 0.015T and 0.04T respectively, indicating the pair binding strength which decreases with increasing field, as

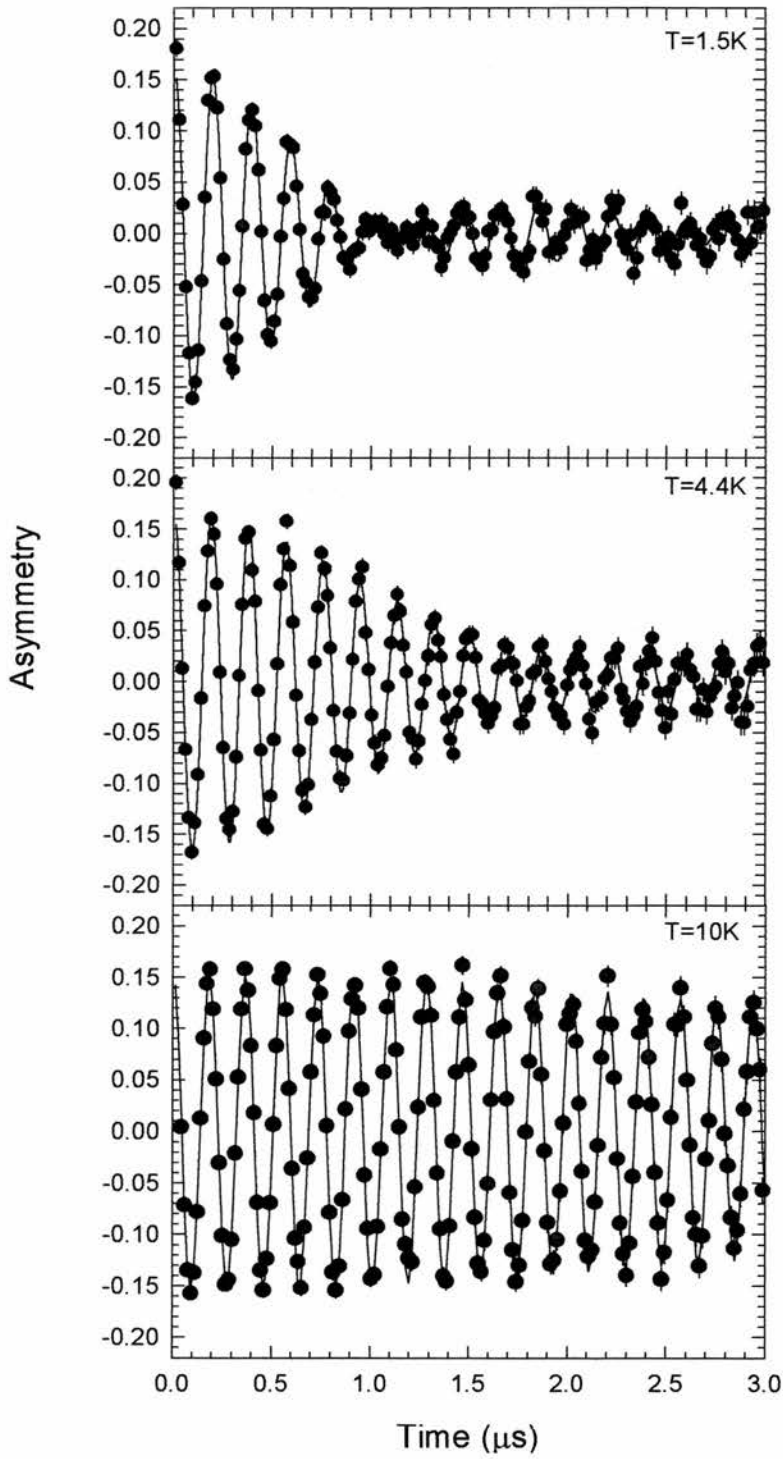


Figure 6.10 The muon depolarisation spectra for YB_6 . The line is the fit to the data.

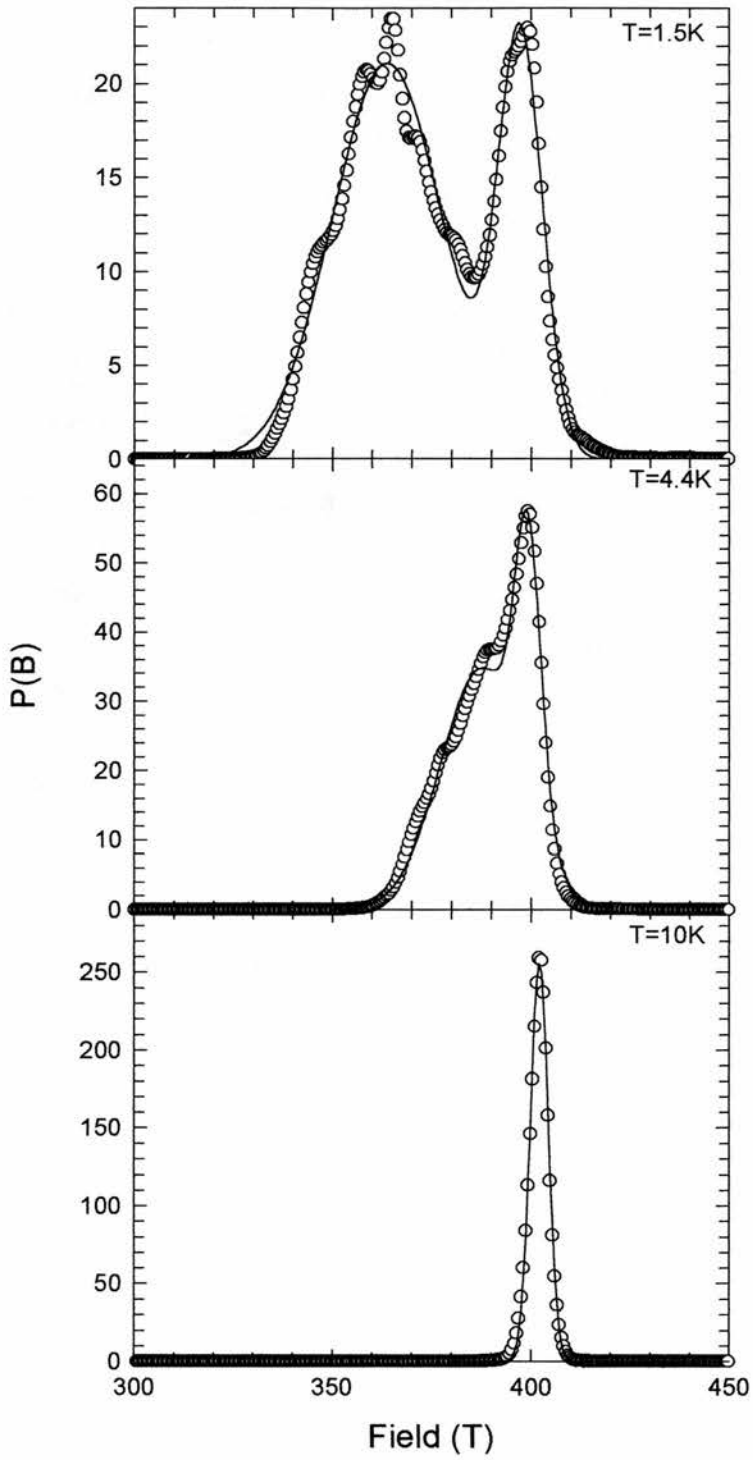


Figure 6.11 The field distribution inside the YB_6 sample. The line is a Gaussian fit to the data.

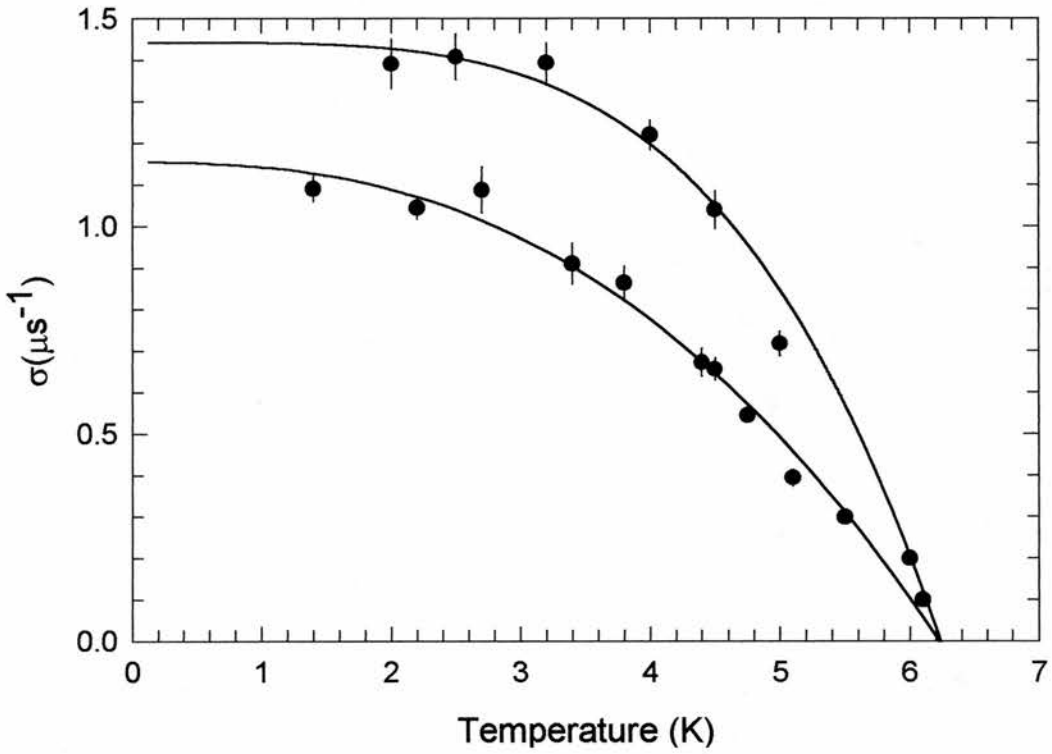


Figure 6.12 The temperature dependence of the muon depolarisation rate for YB_6 . The line is the fit to the data.

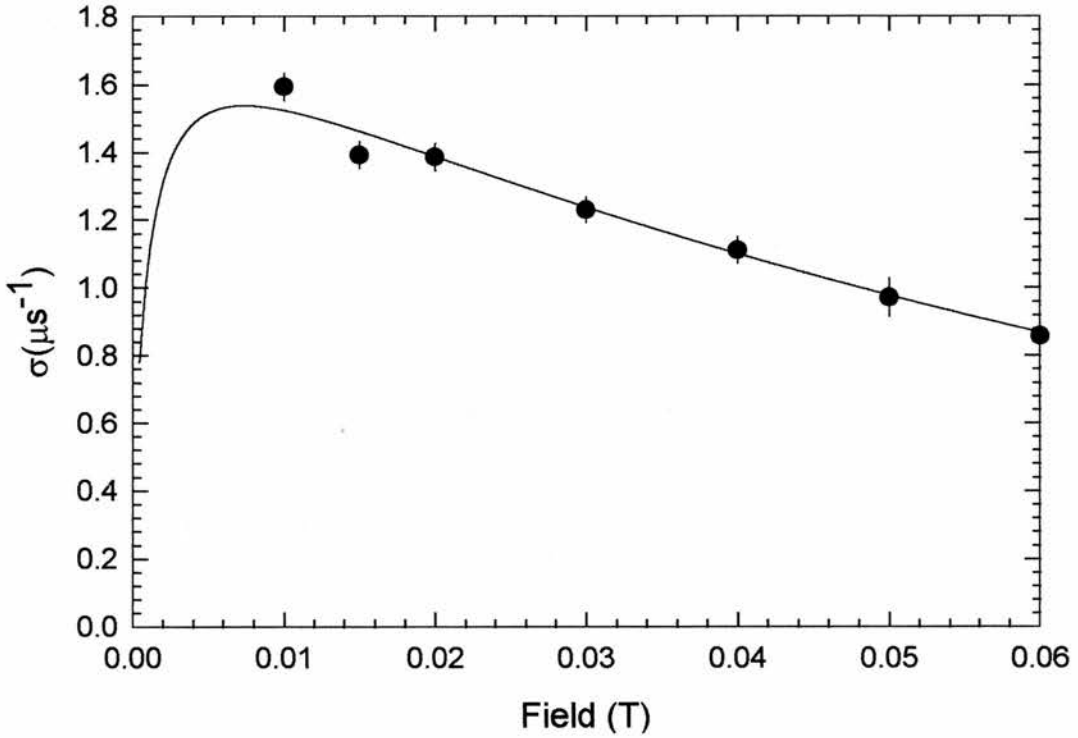


Figure 6.13 The field dependence of the muon depolarisation rate for YB_6 . The line is the fit to the data using the modified London model.

expected. At the lowest measured temperatures (1.5K) the muon depolarisation rate can be approximated to the value at absolute zero. Since the upper critical field of YB₆ is small (less than 0.5T) and hence implying a long coherence length, then the muon depolarisation rate cannot be simply related to the magnetic penetration depth. Instead it is necessary to determine the field dependence of the muon depolarisation rate. The modified London model³²,

$$\sqrt{\overline{\Delta B^2}} = B_0 \sqrt{\sum_{h,k} \frac{\exp(-\xi^2 q_{h,k}^2)}{(1 + q_{h,k}^2 \lambda^2 / (1-b))^2}}, \quad 6.7$$

$$(q_{h,k} \neq 0),$$

where

$$\overline{\Delta B^2} = \frac{2\sigma^2}{\gamma_\mu^2}, \quad 6.8$$

and

$$b = \frac{B_0}{B_{c2}}, \quad 6.9$$

was fitted to the resulting $\sigma(B)$ data with λ and ξ_{GL} as free parameters (see figure 6.13). The fit to the data provides the magnetic penetration, λ , of 192nm and a Ginzburg Landau coherence length, ξ_{GL} , of 33nm.

6.4 CONCLUSIONS

Each experimental technique has given a different magnetic penetration depth on the same 'YB₆' sample. The magnetisation data has given a magnetic penetration depth of 398nm, whereas the μ SR measurements gave 192nm. The difference in the results can be explained quite simply. Determination of H_{c1} is difficult using DC magnetisation, especially when dealing with a polycrystalline powder. This error in the determination of H_{c1} is primarily a result of demagnetisation effects (see §3.4). However, with μ SR the demagnetisation problem still exists but as discussed earlier occurs in a slightly different way. However, the determination of the coherence length using dc magnetisation and μ SR is within reasonable agreement. ξ_{GL} is 33nm and 42nm for μ SR and DC magnetisation respectively.

6.5 REFERENCES

- ¹ J.L. Sarrao, M.C. de Andrade, J. Hermann, S.H. Han, Z. Fisk, M.B. Maple, R.J. Cava. *Physica C*. **229**. 65 (1994).
- ² H.W. Zandbergen, J.L. Sarrao, M.C. de Andrade, J. Hermann, S.H. Han, Z. Fisk, M.B. Maple, R.J. Cava. *Physica C*. **229**. 29 (1994).
- ³ H.W. Zandbergen, T.J. Gortenmulder, J.L. Sarrao, J.C. Harrison, M.C. de Andrade, J. Hermann, S.H. Han, Z. Fisk, M.B. Maple, R.J. Cava. *Physica C*. **232**. 328 (1994).
- ⁴ H.W. Zandbergen, E.J. van Zwet, J. Jansen, J.L. Sarrao, M. B. Maples, Z. Fisk, R.J. Cava. *Philosophical Magazine Letters*. **71**. 131 (1995).
- ⁵ J. Etourneau, P. Hagenmuller. *Philosophical Magazine B* **52**. 589 (1985).
- ⁶ I. Bat'ko, M. Bat'kova, K. Flachbart, D. Macko, E.S. Konovalova, Yu.B. Paderno. *Journal of Magnetism and Magnetic Materials*. **140-144**. 1177 (1995).
- ⁷ K. Seqawa, A. Tomita, K. Iwashita, M. Kasaya, T. Suzuki, S. Kunii. *Journal of Magnetism and Magnetic Materials*. **104-107**. 1233 (1992).
- ⁸ R.M. Galera, P. Morin, S. Kunii, T. Kasuya. *Journal of Magnetism and Magnetic Materials*. **104-107**, 1336 (1992).
- ⁹ H. Hacker, M.S. Lin. *Solid State Communications*. **6**. 379. (1968).
- ¹⁰ H. Hacker, Y. Shimada, K.S. Chung. *Physica Status Solidi A*. **4**. 459. (1971).
- ¹¹ C.M. McCarthy, C.W. Thompson. *Journal of Physical Chemical Solids*. **41**. 1319 (1980).
- ¹² C.M. McCarthy, C.W. Thompson, R.J. Graves, H.W. White, Z. Fisk, H.R. Ott. *Solid State Communications*. **36**. 861 (1980).
- ¹³ M. Kawakami, S. Kunii, T. Komatsubara, T. Kasuya. *Solid State Communications*. **36**. 435 (1980).
- ¹⁴ A. Takase, K. Kojima, T. Komatsubara, T. Kasuya. *Solid State Communications*. **36**. 461 (1980).
- ¹⁵ T. Komatsubara, N. Sato, S. Kunii, I. Oguro, Y. Furukawa, Y. Onuki, T. Kasuya. **31-34**. 368 (1983).
- ¹⁶ S. Horn, F. Steglich, M. Loewenhaupt, H. Scheuer, W. Felsch, K. Winzer. *Z. Phys. B*. **42**. 125. (1981).
- ¹⁷ J.M. Effantin, J. Rossatmignod, P. Burlet, H. Bartholin, S. Kunii, T. Kasuya. *Journal of Magnetism and Magnetic Materials*. **47-8**. 145. (1985)
- ¹⁸ L.P. Regnault, W.A.C. Erkelens, J. Rossatmignod, J. Flouquet, E. Walker, D. Jaccard, A. Amato, B. Hennion. *Journal of Magnetism and Magnetic Materials*. **63-64**. 289. (1987).
- ¹⁹ R. Feyerherm, A. Amato, F.N. Gyax, A. Schenck, Y. Onuki, N. Sato. *Physica B*. **194**. 357. (1994)
- ²⁰ R. Feyerherm, A. Amato, F.N. Gyax, A. Schenck, Y. Onuki, N. Sato. *Journal of Magnetism and Magnetic Materials*. **140-144**. 1175. (1995).
- ²¹ Valance Instabilities. J.M. Effantin, P. Burlet, J. Rosset-Mignod, S. Kunii, T. Kasuya. Eds P. Wachter and H. Boppart. 359. North Holland, Amsterdam. (1982).

- ²² B.T. Matthias, T.H. Geballe, K. Andres, E. Corenzwit, G.W. Hull, J.P. Maita. *Science*. **159**. 530 (1968).
- ²³ G. Schell, H. Winter, H. Rietschel, F. Gomf. *Physical Review B*. **25**. 1589 (1982).
- ²⁴ S. Kunii, T. Kasuya, K. Kadowaki, M. Date, S.B. Woods. *Solid State Communications*. **52**. 659 (1984).
- ²⁵ *Metal's Reference book*. C.J. Smithells and E.A. Brandes. 5th Edition. Butterworth, London (1976).
- ²⁶ J. Rodriguez-Carvajal. FULLPROF refinement program, LLB.
- ²⁷ H.W. Zandbergen, W.G. Sloof, R.J. Cava, J.J. Krajewski, W.F. Peck. *Physica C*. **226**, p365 (1994).
- ²⁸ *Introduction to Superconductivity*. Tickham. McGraw Hill Kogakusha Ltd. Tokyo.
- ²⁹ *Introduction to Superconductivity*. A.C. Rose-Innes and E.H. Rhoderick. Second Edition. Pergamon Press Ltd. Oxford.
- ³⁰ C.P. Bean. *Phys. Rev. Lett.* **8**. 250. (1962).
- ³¹ E.H. Brandt. *Reports of Progress in Physics*. **58**. 1465. (1995).
- ³² E.H. Brandt. *Physical Review B*. **37**. 2349 (1988).

7. The Zr₂TM alloys.

7.1 INTRODUCTION.

The intermetallic alloys Zr₂TM (TM= Fe, Ni, Co and Rh) crystallise with the C16 type structure (see figure 7.1). They have been intensively studied both theoretically and experimentally^{1,2} because of their superconducting properties, close proximity to magnetic order and hydrogen affinity. The Zr₂TM intermetallic alloys can be considered to be unusual since they are superconducting and contain 33% of an elemental ferromagnet (Fe, Co and Ni). The superconducting transition temperature, T_c, varies from 0.18K for Zr₂Fe³ to a maximum of 11.2K for Zr₂Rh⁴.

Sample	T _c (K)	Ref.
Zr ₂ Rh	11.2	4
Zr ₂ Co	5.5	5
Zr ₂ Ni	2	5
Zr ₂ Fe	0.18	3

Table 7.1 A table of the superconducting transition temperatures for Zr₂TM.

Earlier attempts to provide an explanation for superconductivity in these compounds suggested that the structural chains of TM-atoms connecting the Zr planes (see figure 7.1) were responsible for the lattice instabilities^{6,7}, which in turn led to phonon mode softening as in the A15 compounds⁸. No such modes have ever been observed. Later studies concentrated on the electronic properties of these compounds. Superconductivity has been shown to follow the Matthias rule of band filling with increasing electron-to-atom ratios⁵. Detailed self consistent electronic structure calculations have shown the change in T_c is attributable to a shift in the Fermi energy from a peak to a trough in the density of states⁵. This has also been suggested by susceptibility measurements, χ , where the correlation between T_c and χ also provide evidence for a decrease in the density of states at the Fermi energy⁹.

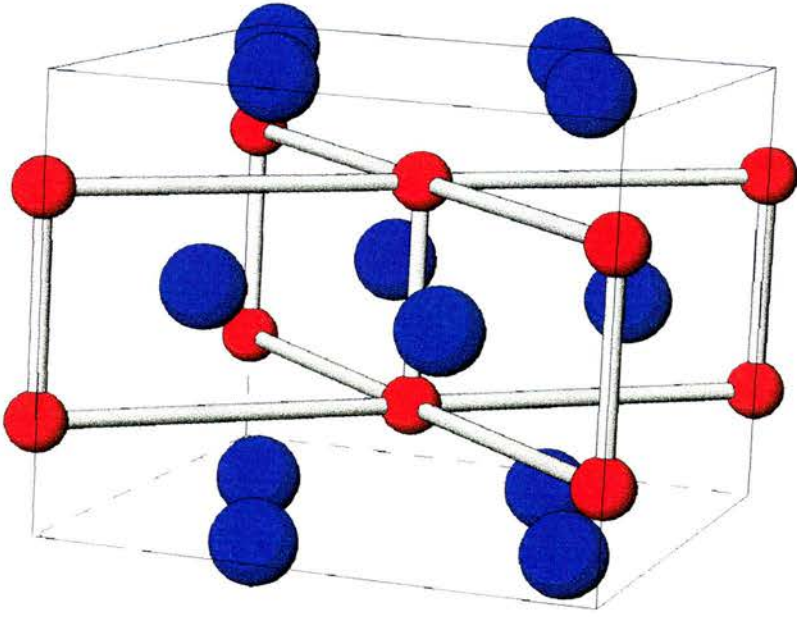


Figure 7.1 The crystal structure of Zr_2TM . The large blue spheres represent the Zr atoms and the smaller red spheres represent the transition metal atoms.

Zirconium based alloys generally absorb large quantities of hydrogen. The hydrogen occupies an interstitial site formed by the zirconium atoms. This leads to a reduction in the density of states at the Fermi level^{10,11,12}. For example¹³: $Zr_2RhH_{4.25}$ shows metallic behaviour but does not superconduct. The susceptibility is half the magnitude of the pure parent compound, Zr_2Rh . Also, the Debye temperature of $Zr_2RhH_{4.25}$ is almost double the Debye temperature for Zr_2Rh thus indicating an increase in the strength of the bonding between constituent elements offering again some support for the suggestion that lattice instabilities might contribute to superconductivity in the Zr_2TM alloys.

An enhanced coefficient of the electronic specific heat has also been noted⁵ in Zr_2TM , suggesting a similar enhancement of the electron effective mass to that observed in the borocarbides^{14,15,16}.

7.2 INITIAL CHARACTERISATION.

7.2.1 Sample preparation and x-ray diffraction.

The samples were prepared by melting stoichiometric amounts of the constituent elements in an argon-arc furnace (see §3.2). The Zr_2TM alloys were checked for phase purity by using x-ray diffraction. The x-ray diffraction patterns were collected on a STOE Stadi P diffractometer in transmission geometry (see §3.3.1) The diffraction patterns have been refined using the FULLPROF¹⁷ Rietveld refinement program. The results of these refinements have concluded that the samples are single phase and have confirmed that Zr_2TM crystallises with the C16 (I4/mcm) type structure directly from the melt (see figure 7.2).

The lattice parameters and atomic positions obtained from the refinement of the x-ray diffraction agree with the literature⁵. Extra Bragg peaks are observed at angles 21.5° and 23.5° and are from a crystalline component in the Vaseline used to mount the sample onto the slide. The curvature of the background is a result of fluorescence from the sample.

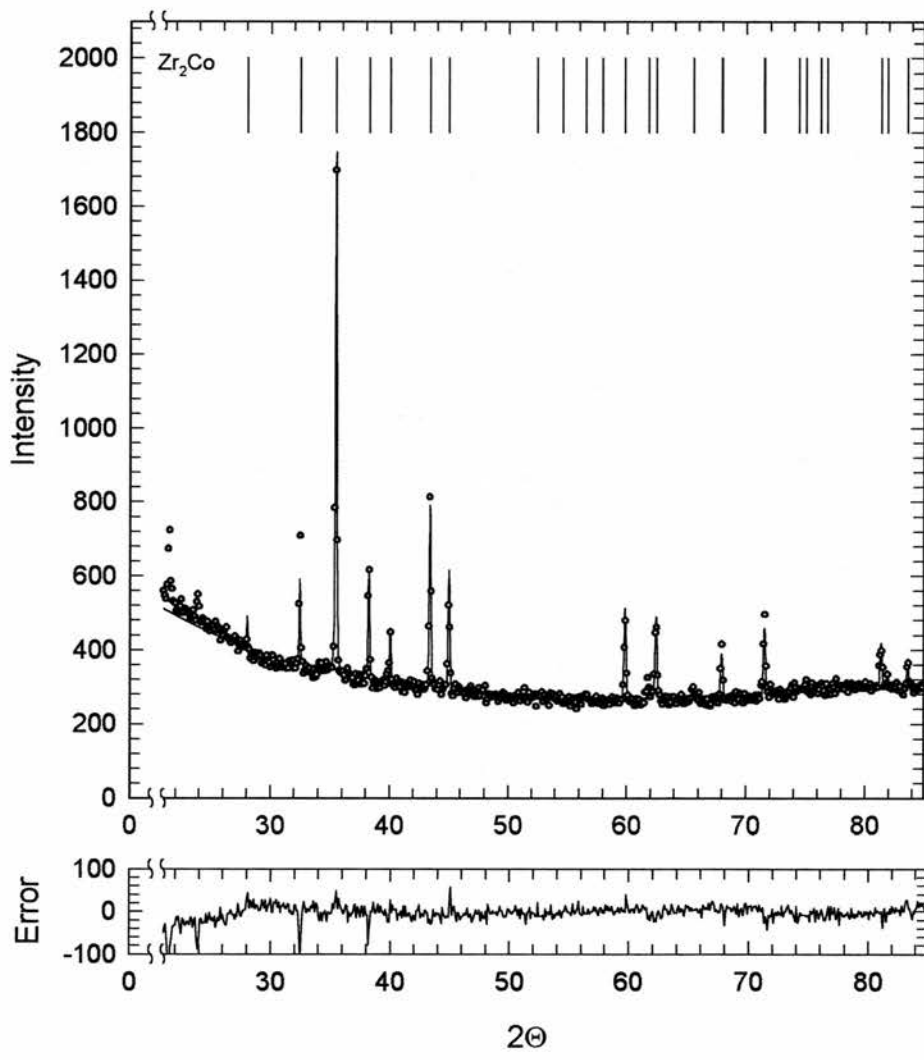


Figure 7.2 The X-ray diffraction pattern for Zr_2Co . The line is the Rietveld refinement fit to the data.

7.2.2 DC magnetisation.

7.2.2.1 The superconducting properties of Zr_2TM ($TM= Rh$ and Co).

The DC magnetisation measurements were collected using a 12T VSM (see §3.4). Since the temperature range available for our VSM is 3.8K to 300K, only Zr_2Rh and Zr_2Co could be examined magnetically. A solid polycrystalline sphere was used for all the VSM measurements. Determination of the superconducting transition temperature was obtained by measuring the magnetisation, on warming, after zero field cooling below the reported superconducting transition and applying a small dc field of 6mT. The magnetisation data has given superconducting transitions of 5.5K and 11.2K for Zr_2Co and Zr_2Rh respectively (see figure 7.3). These results agree with the literature^{4,5}.

Magnetisation as a function of applied field, at a constant temperature, has also been measured. Using these hysteresis loops, the upper and lower critical fields have been determined as a function of temperature. Using dc magnetisation to determine H_{c1} and H_{c2} can introduce a number of systematic errors, as discussed in §3.5. For a range of temperatures H_{c1} and H_{c2} have been determined and the two-fluid model,

$$H_c(T) = H_c(0) \left(1 - \left(\frac{T}{T_c} \right)^2 \right), \quad 7.1$$

has been fitted to these results (see figure 7.4). A summary of the critical fields extrapolated to 0K can be found in Table 7.2.

	$H_{c1}(0)$ (mT)	$H_{c2}(0)$ (T)
Zr_2Rh	36(5)	6.0(1)
Zr_2Co	61(5)	1.1(1)

Table 7.2 A summary of the critical fields for Zr_2Rh and Zr_2Co .

The values of $H_{c1}(0)$ and $H_{c2}(0)$ for Zr_2Co should be taken with caution since the available temperature range is limited and is close to the superconducting transition temperature.

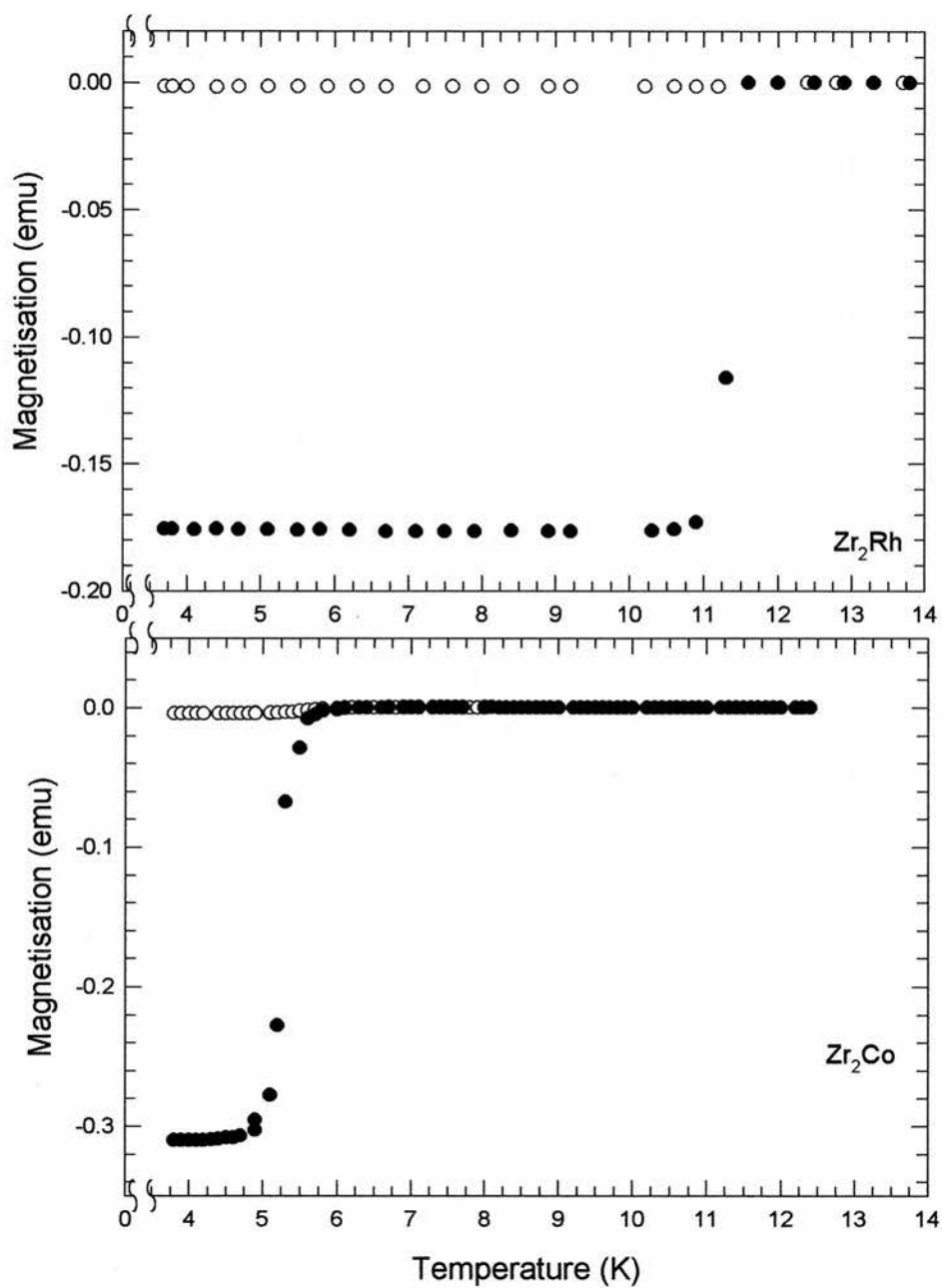


Figure 7.3 The magnetisation curves for Zr_2Rh (top) and Zr_2Co (bottom) with an applied field of 6mT. The ● and ○ represent the zero field cooled and field cooled respectively.

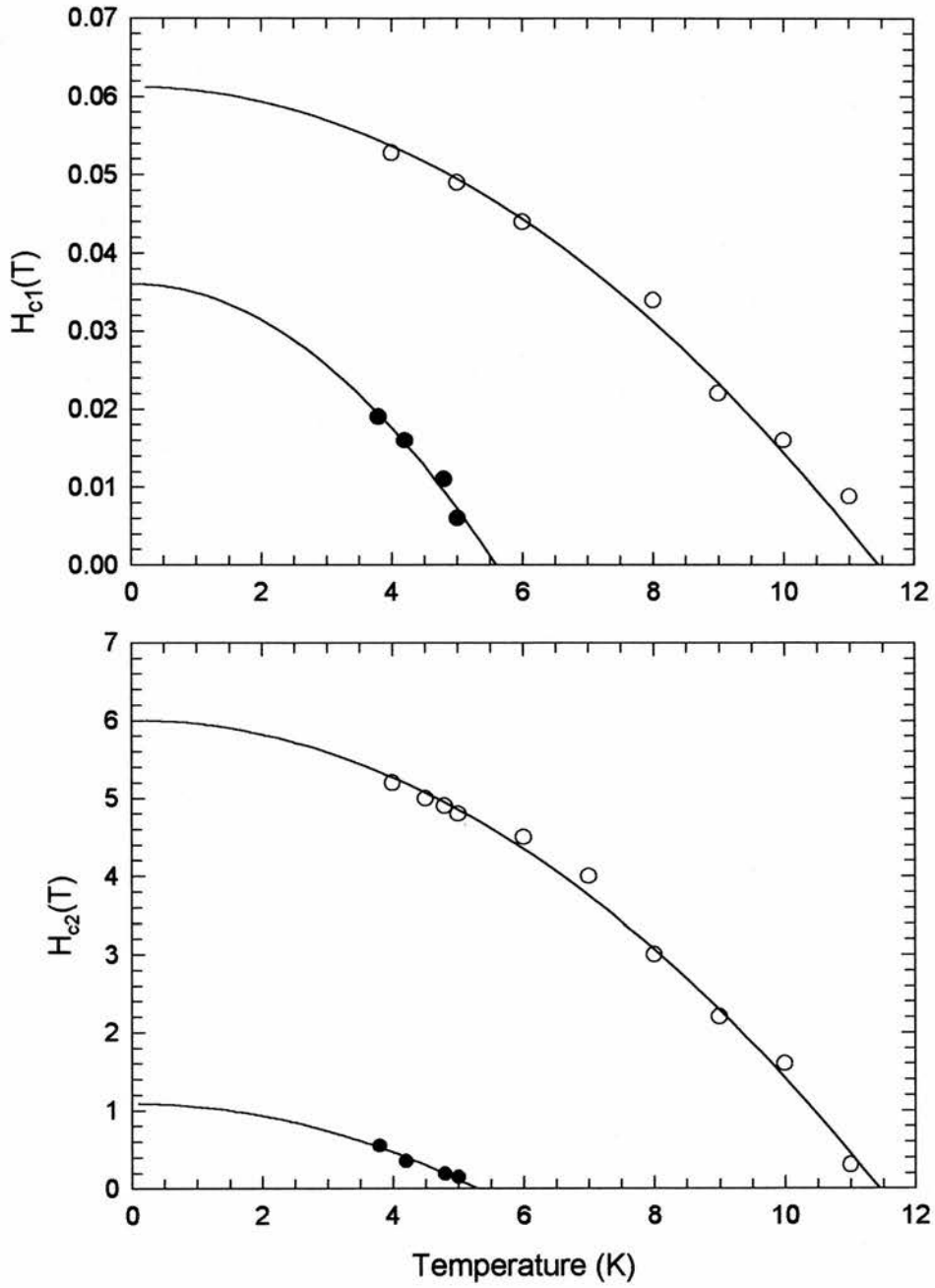


Figure 7.4 The temperature dependence lower critical fields, H_{c1} , (top) and upper critical fields, H_{c2} , (bottom) for Zr_2Co (\bullet) and Zr_2Rh (O). The lines are a fit to the data using the 2-fluid model.

Using the values obtained from the dc magnetisation measurements, λ and ξ_{GL} have been determined using equation 5.2 and 5.3. For Zr_2Co , $\lambda(0)=108nm$ and $\xi_{GL}(0)=17nm$ and for Zr_2Rh , $\lambda(0)=74nm$ and $\xi_{GL}(0)=7.5nm$.

7.2.2.2 Magnetic hysteresis and flux jumps in Zr_2Rh .

The magnetic susceptibility of Zr_2Rh has been determined as a function of temperature by measuring the gradient of the magnetisation curve, above H_{c2} , between 7 Tesla and 12 Tesla in order to ensure that Zr_2Rh was non-superconducting at temperatures below 11K. The susceptibility indicates that Zr_2Rh is an enhanced Pauli paramagnet, with a susceptibility similar in magnitude to that of palladium¹⁸ and in character to YCo_2 ¹⁹ (figure 7.5).

The upper critical field for Zr_2Rh was determined using a field ramp rate of 5mT/s in order to reduce flux pinning errors in the measurement of H_{c2} . However, when the ramp rate of the applied field was increased an unusual phenomenon was observed (see figure 7.6) in which the magnetisation of the Zr_2Rh sample collapses to almost zero. I believe that flux jumping could be responsible for these breakdowns.

The dynamic phenomenon of flux jumping is generally associated with hard superconductors. When the applied field exceeds the internal field by some critical value the shielding currents become unstable and magnetic flux surges into the sample.

The number of flux jumps in the Zr_2Rh hysteresis loop decreases on increasing temperature. For temperatures greater than 5K no jumps are observed. The field at which the initial flux jump occurs is ramp rate dependent (see figure 7.7), while for high values of dB/dt, the initial breakdown field is constant (adiabatic limit). For an intermediate dB/dt, the initial breakdown field is strongly dependent on dB/dt. An increase in dB/dt decreases the initial breakdown field and at low dB/dt no flux jumps occur. All of these stages are shown in figure 7.7.

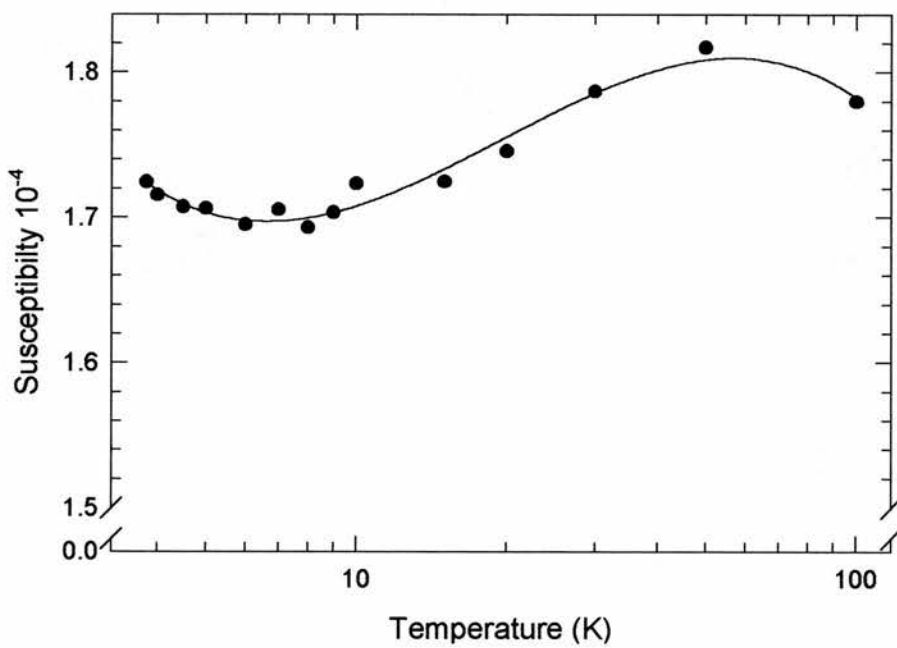


Figure 7.5 The temperature dependence of the susceptibility for Zr₂Rh. The line is a guide to the eye.

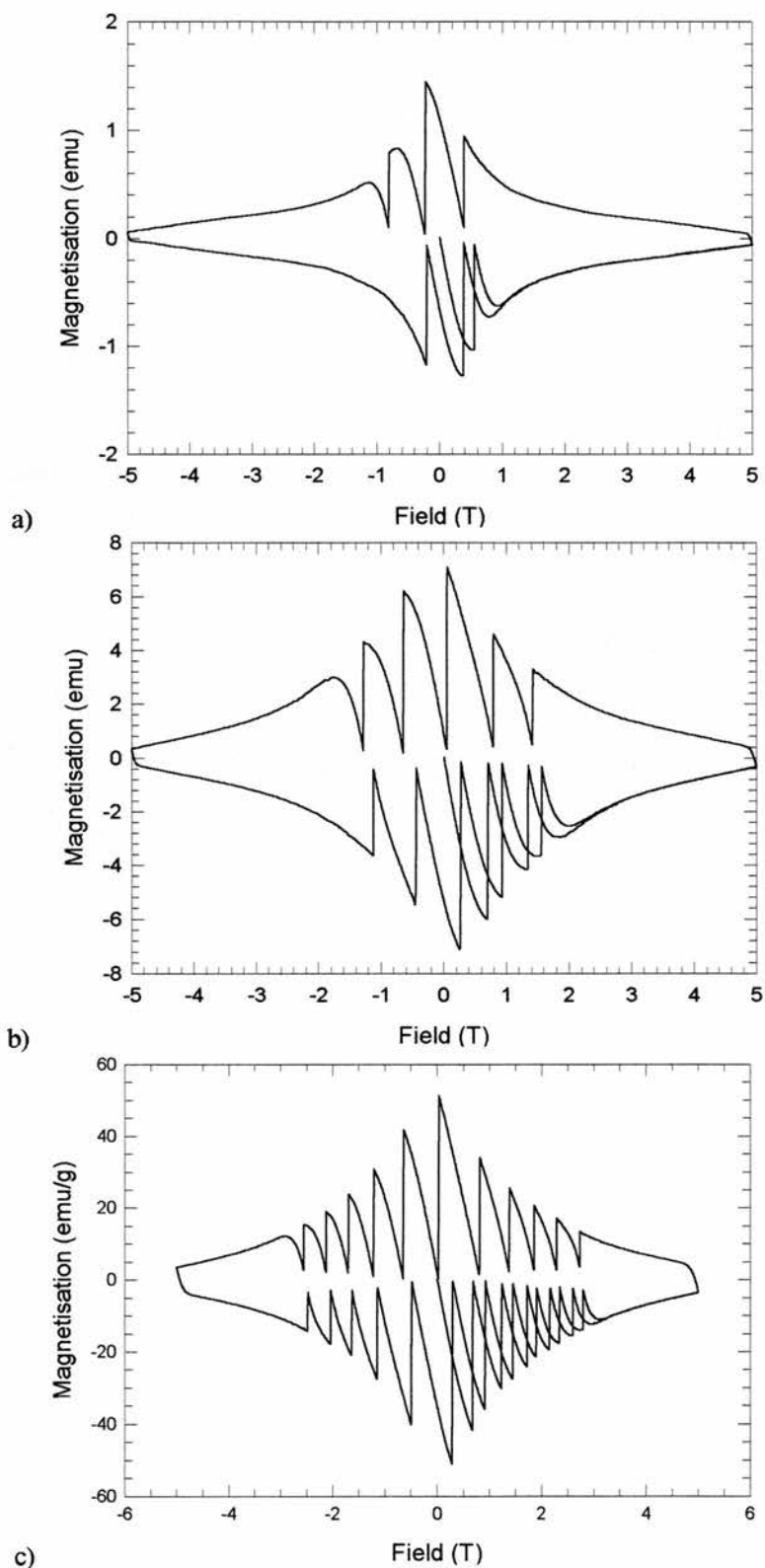


Figure 7.6 The 'Sydney opera house' magnetic hysteresis loop for Zr_2Rh . All the measurements were taken at 4K and the applied field ramp rate was 10mT/s. The only difference between these three measurements are the diameter of the Zr_2Rh samples. Samples a, b and c have diameters 1.58mm, 2.76mm and 5.16mm respectively.

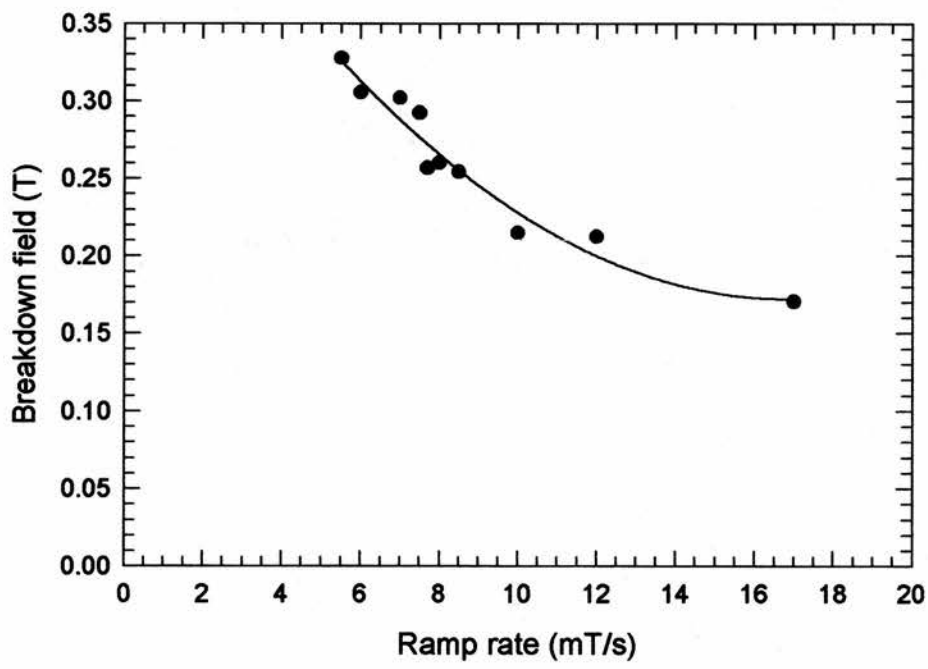


Figure 7.7 The ramp rate dependence of the initial breakdown field for the Zr_2Rh sample with a radius of 0.6mm.

The field at which the flux jumps occurs are also sample size dependent (see figure 7.8). No flux jumps are found below a critical sample thickness. This stability criterion is given by²⁰

$$d^2 < \frac{3c^2C}{\pi J_c} \left| \frac{dJ_c}{dT} \right|^{-1} \quad 7.2$$

where C is the heat capacity, J_c is the critical current density and c is the velocity of light. Using the reported value of C^5 together with J_c obtained by our magnetisation measurements we obtain a minimum diameter of 1mm. It is worth noting that, in agreement with this calculation, the envelope of the plot of breakdown field against sphere diameter (see figure 7.8) converges at a sphere diameter of 1mm. Above this value multiple breakdowns are observed, while below this value only a single breakdown is seen.

Using the magnetic hysteresis loops, the flux pinning density has been determined for a range of sweep rates using the Kramer method (§2.6.2). The initial flux jump is found to occur precisely at the peak of the pinning curve irrespective of sweep rate (see figure 7.9). I believe that this is the first time that such a relationship has been observed.

In summary, flux jumps generally occur in strongly pinned superconductors. Each jump lasts of the order of a millisecond and will locally increase the temperature of the sample. Zr_2Rh is a relatively hard superconductor and has a critical current density of the order of 10^8 - $10^9 A/m^2$, using the Bean model. This indicates that the flux pinning strengths are high. The origins of the high flux pinning strength in this crystallographically perfect sample are not yet known. However, it is tempting to suggest that enhanced Pauli paramagnetism might somehow be involved. Similar effects were not seen in the Zr_2Co sample since the equivalent temperature scales are much reduced.

7.3 MUON SPIN ROTATION.

For transverse field muon spin rotation experiments the Zr_2Rh and Zr_2Co samples were powdered and mounted onto an aluminium plate using GE varnish. The Zr_2Ni sample

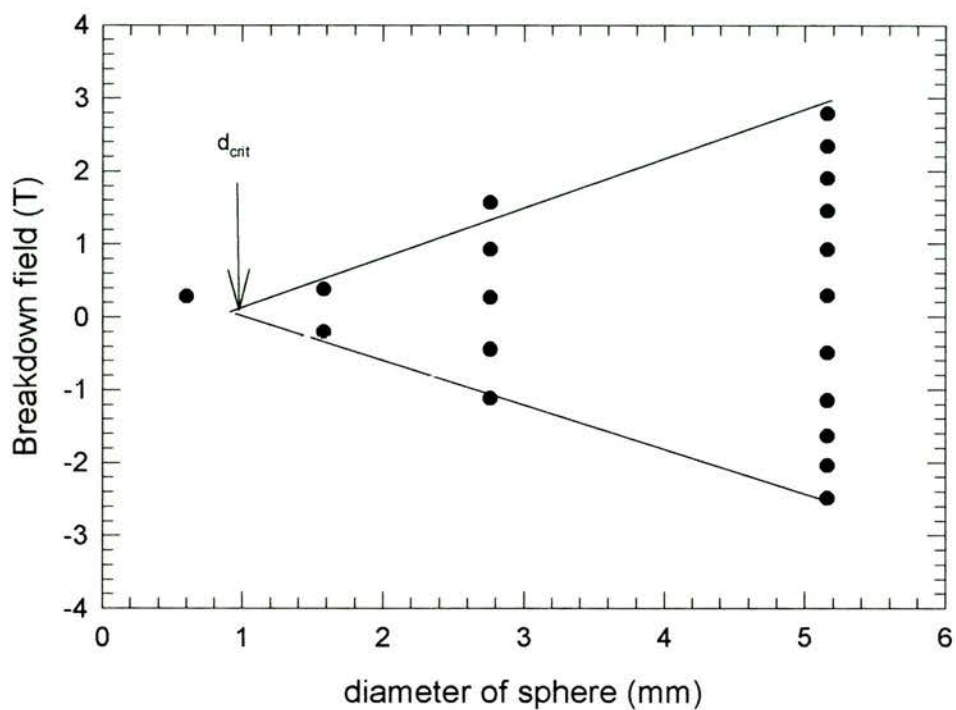


Figure 7.8 The size dependence of the breakdown fields with a field sweep rate of 10mT/s at 4K.

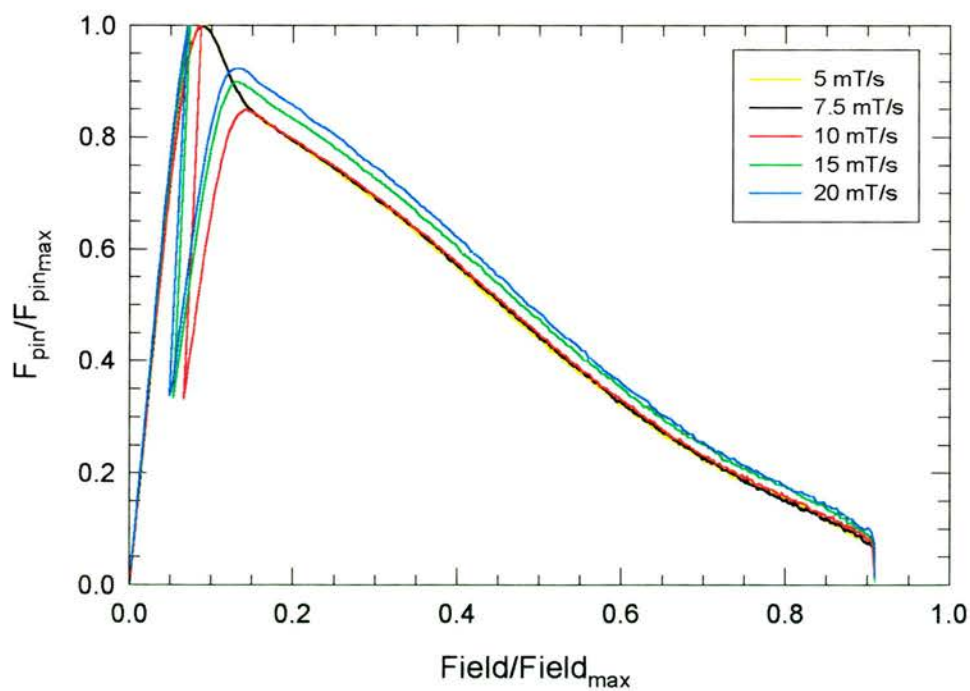


Figure 7.9 The pinning density curve for Zr_2Rh for several field sweep rates. The sample diameter was 0.6mm.

was cut to form a 2cm diameter disk and was attached to a silver plate. However, the Zr_2Fe sample was too brittle to slice and was therefore powdered and mounted onto a silver sample holder. Using the MuSR instrument at ISIS, Oxford UK, the muon spectra were collected on warming the samples after first field cooling below their respective superconducting transitions. The applied field used were 40mT, 20mT, 20mT and 2mT for Zr_2Rh , Zr_2Co , Zr_2Ni and Zr_2Fe respectively. For Zr_2Rh and Zr_2Co , the applied field used in the μ SR measurements is significantly less than the previously determined lower critical field, H_{c1} , value (see §7.2). However, the determination of H_{c1} by magnetisation is difficult since it can be affected by demagnetisation and strong surface pinning whereas μ SR experiment does not suffer with these problems.

The μ SR spectra were fitted assuming a Gaussian distribution of internal fields (see figure 7.10)²¹. This assumption can be justified by examination of the field distribution directly using the maximum entropy technique²² (see figure 7.11). As can be seen in figure 7.11 a Gaussian distribution of internal fields provides a very good description of the data. Above the superconducting transition temperature, the μ SR depolarisation spectra are well described by

$$G_z(t) = A_o \exp(-\sigma^2 t^2) \cos(\omega t + \phi) \quad 7.3$$

where A_o is the initial asymmetry, σ is the muon depolarisation rate, ω is the muon precession frequency and ϕ is the phase. The depolarisation of the muon spectra above the superconducting transition is due to dipole fields resulting from the nuclear magnetic moments of zirconium and the transition metal. However, below the superconducting transition the μ SR spectra were best described by

$$G_z(t) = A_{os} \exp(-\sigma_s^2 t^2) \cos(\omega_s t + \phi) + A_{ob} \exp(-\sigma_b^2 t^2) \cos(\omega_b t + \phi) \quad 7.4$$

where

$$\sigma^2 = \frac{\gamma^2 \langle \Delta B^2 \rangle}{2}. \quad 7.5$$

The equation used to fit the data consists of two components. The first term (with subscript s) is the superconducting fraction term and the second (with subscript b) is the background contribution and/or part of the sample in the normal state.

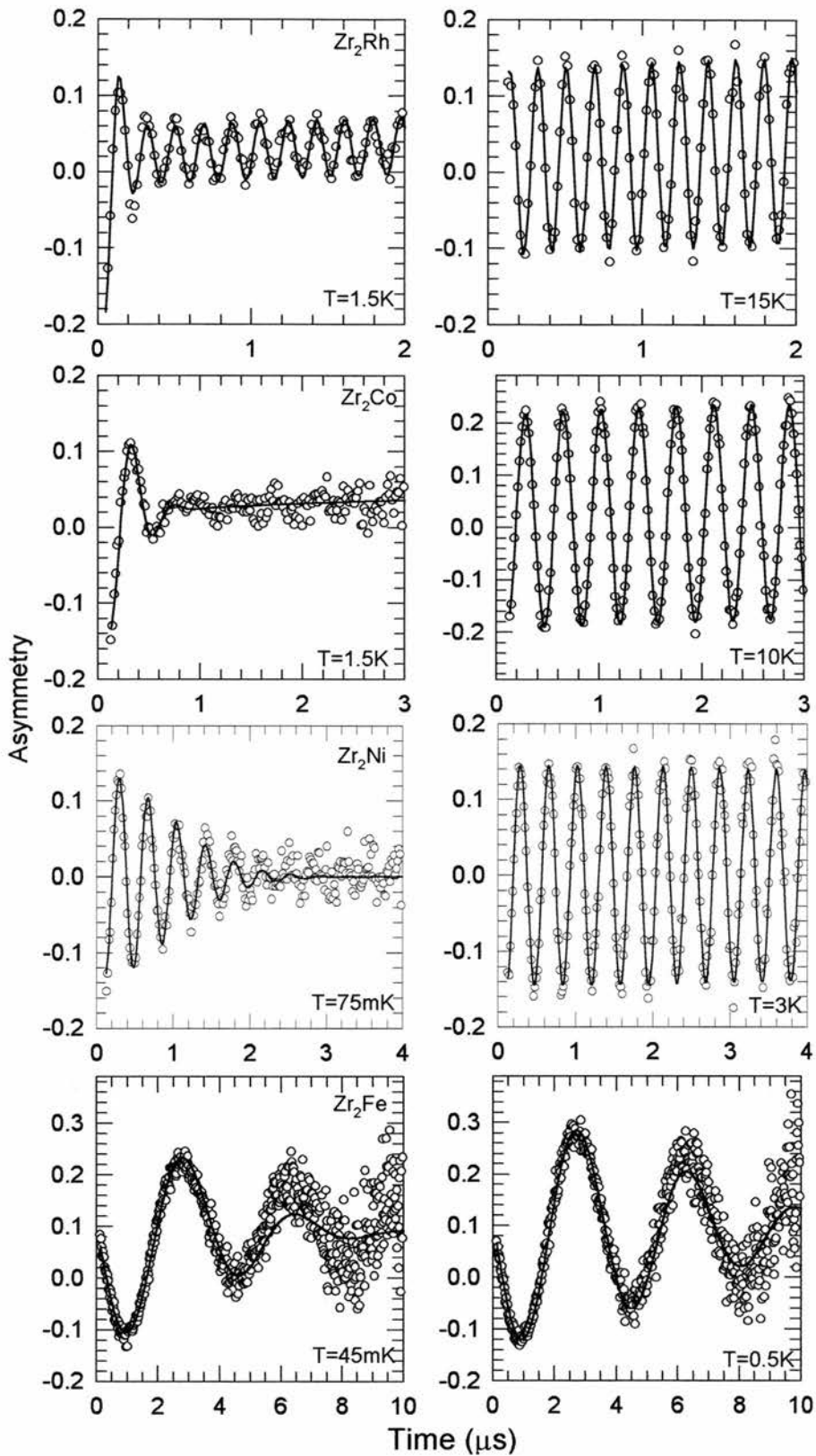


Figure 7.10 The muon depolarisation spectra. The line is a fit to the data. The spectra on the left were obtained whilst the sample was in the superconducting state, whilst the spectra on the right were collected whilst the sample was in the normal state.

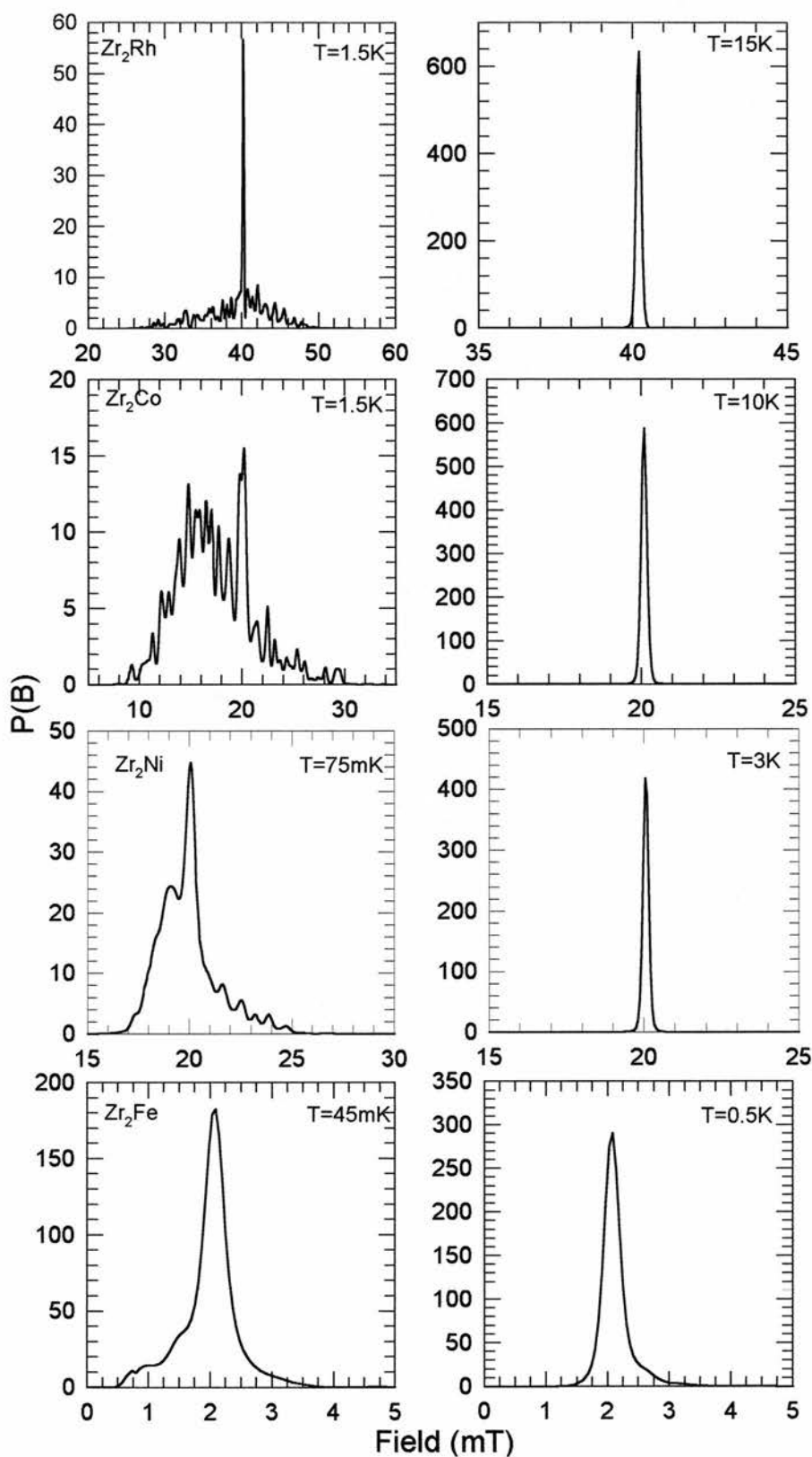


Figure 7.11 The field distribution of the Zr_2TM alloys. The field profile on the left were obtained whilst the sample was in the superconducting state, whilst the field profile on the right were collected whilst the sample was in the normal state.

The temperature dependence of the depolarisation rate for all the samples is characteristic of a BCS superconductor (see figure 7.12) and the N-fluid model,

$$\sigma(T) = \sigma(0)\left(1 - \left(\frac{T}{T_c}\right)^N\right), \quad 7.6$$

was fitted to the muon depolarisation rate for each sample. Using the results from the fit, the determined values of T_c for Zr_2Fe , Zr_2Ni , Zr_2Co and Zr_2Rh are 0.18K, 1.5K, 5.2K and 10.7K respectively. The observed slight suppression of T_c is a consequence of cooling the sample in a field greater than H_{c1} . The value for the exponent N was found to be 2.3, 2.66, 3.8 and 3.5 respectively.

Long coherence lengths can cause overlapping of the flux field lines and hence the muon cannot probe the full field distribution associated with an individual flux line. This leads to a low value of the muon depolarisation rate being observed, as the limits of the field profile are being truncated²³. Simulations using the modified London model²³ show that the Ginzburg Landau coherence length obtained by dc magnetisation measurements in the Zr_2Co and Zr_2Rh samples does not significantly affect the muon depolarisation rate over the field range accessible by MuSR (0-60mT) (see figure 7.13). Therefore, the muon depolarisation rate is directly related to the magnetic penetration depth by the relation

$$\lambda^2 = \frac{0.0609\gamma_\mu\Phi_0}{\sigma}, \quad 7.7$$

for a triangular flux lattice. The resulting magnetic penetration depths, λ , for Zr_2Co and Zr_2Rh are found to be 190nm and 140nm. However, for Zr_2Fe and Zr_2Ni the Ginzburg Landau coherence length, ξ_{GL} , is sufficiently long to affect the muon depolarisation rate, so it was necessary to also measure the field dependence of the muon depolarisation rate. For these samples the muon depolarisation rate at the lowest measured temperature approximates to the value extrapolated to 0K. The measurements of the field dependence were conducted at 45mK and 75mK for Zr_2Fe and Zr_2Ni respectively. For each field measurement, the Zr_2TM alloy was heated to a temperature well above the superconducting transition and then field cooled to the lowest available temperature. The modified London model (see equation 6.7) was fitted to the observed field dependence

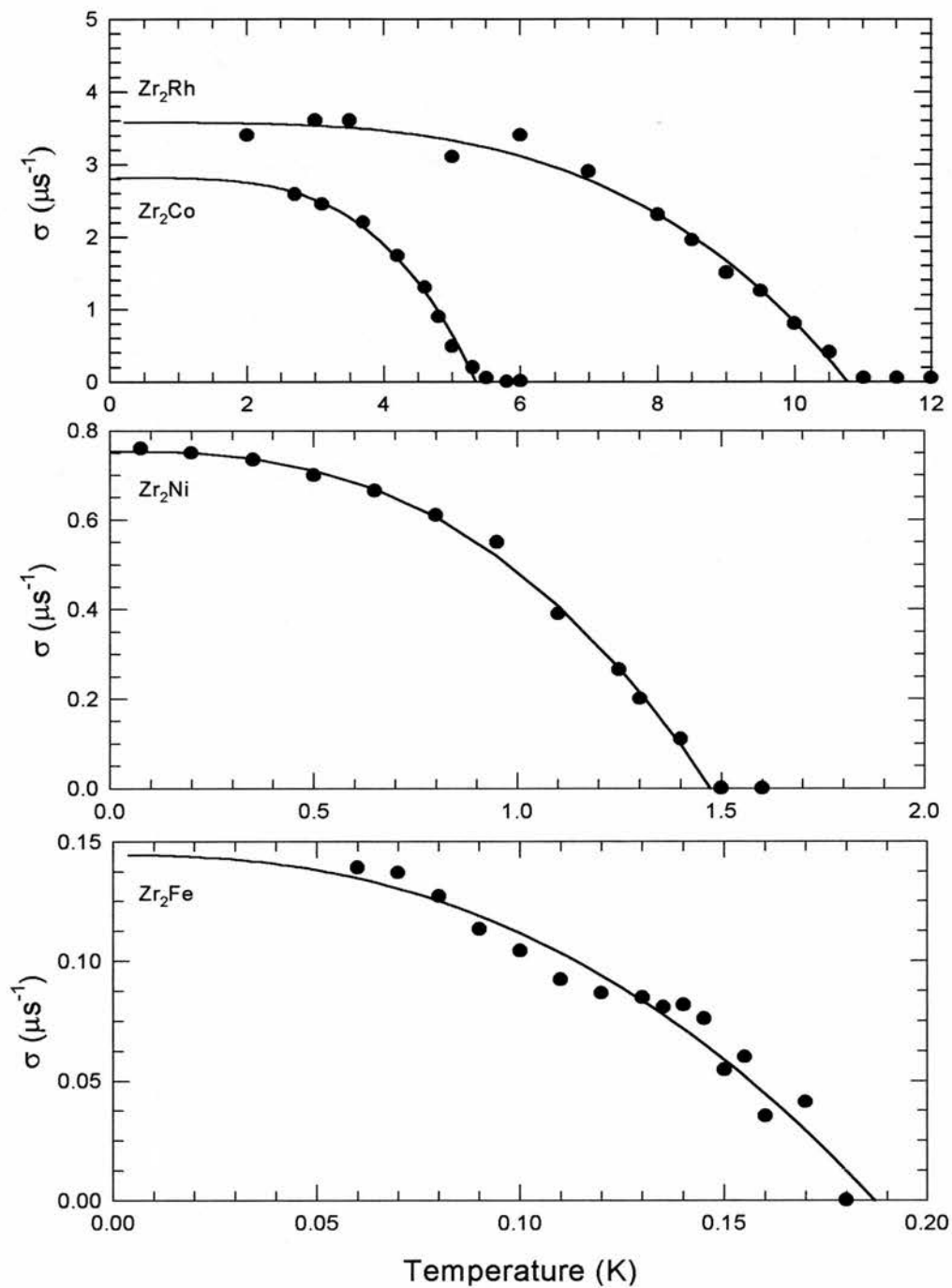


Figure 7.12 The temperature dependence of the muon depolarisation rate for Zr₂Rh (top), Zr₂Co (top), Zr₂Ni (middle) and Zr₂Fe (bottom). The line is the fit to the data using the N-fluid model where $N=3.5$, 3.8, 2.7 and 2.3 for Zr₂Rh, Zr₂Co, Zr₂Ni and Zr₂Fe respectively.

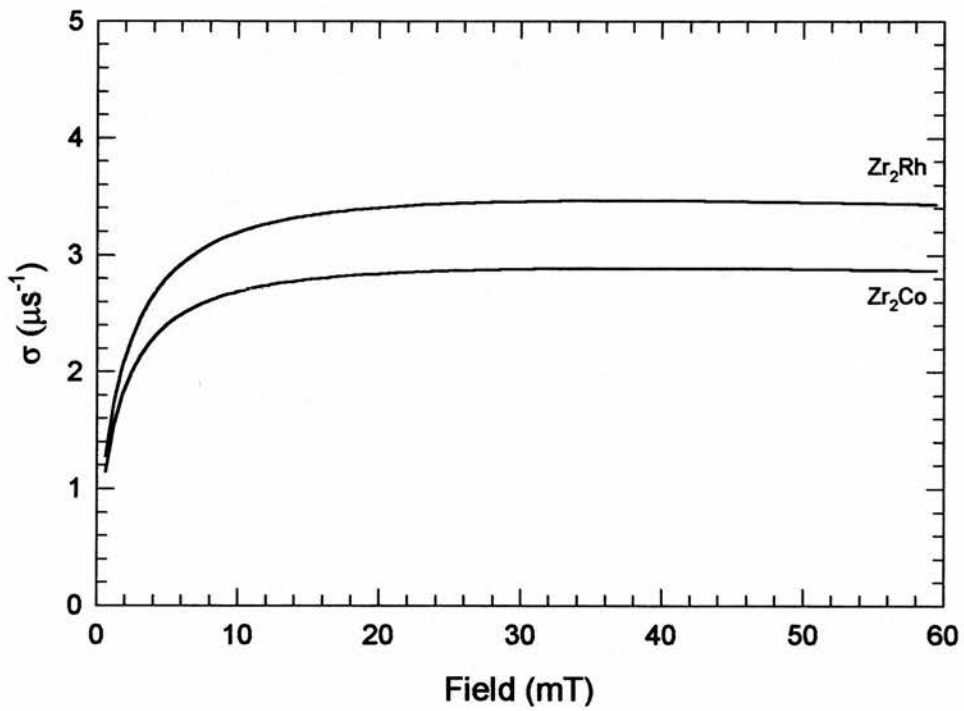


Figure 7.13 Simulations of the muon depolarisation rate as a function of field using the modified London model²⁵.

of the muon depolarisation rate (see figure 7.14). The parameters obtained from the fitted data have given $\lambda=275\text{nm}$ and $\xi_{\text{GL}}=26\text{nm}$ for Zr_2Ni and for Zr_2Fe $\lambda=520\text{nm}$ and $\xi_{\text{GL}}=148\text{nm}$. A summary of these results can be found in Table 7.3.

Sample	T_c (K)	λ (nm)	ξ_{GL} (nm)	ξ_{GL} (nm)
		μSR	μSR	mag
Zr_2Rh	11.2	140	-	7.5
Zr_2Co	5.2	190	-	17
Zr_2Ni	2	275	26	-
Zr_2Fe	0.18	520	148	-

Table 7.3 A summary of the results obtained from the transverse field muon spin rotation measurements.

7.4 CONCLUSIONS

In this chapter I have presented the results of a detailed magnetisation and muon spin rotation study of the superconducting ground state of the Zr_2TM compounds with $\text{TM}=\text{Rh, Co, Ni}$ and Fe . The principal results of this study are the observation of

- remarkable flux jump behaviour in Zr_2Rh which I associate with extremely high pinning in this hard superconductor, and the association of the first flux jump with the peak in the pinning force.
- rather long magnetic penetration depths ($140\text{nm} < \lambda < 520\text{nm}$) as TM progresses from Rh , through Co and Ni , to Fe . The importance of the penetration depth measurements in context of the Uemura classification scheme will be discussed in chapter 9.

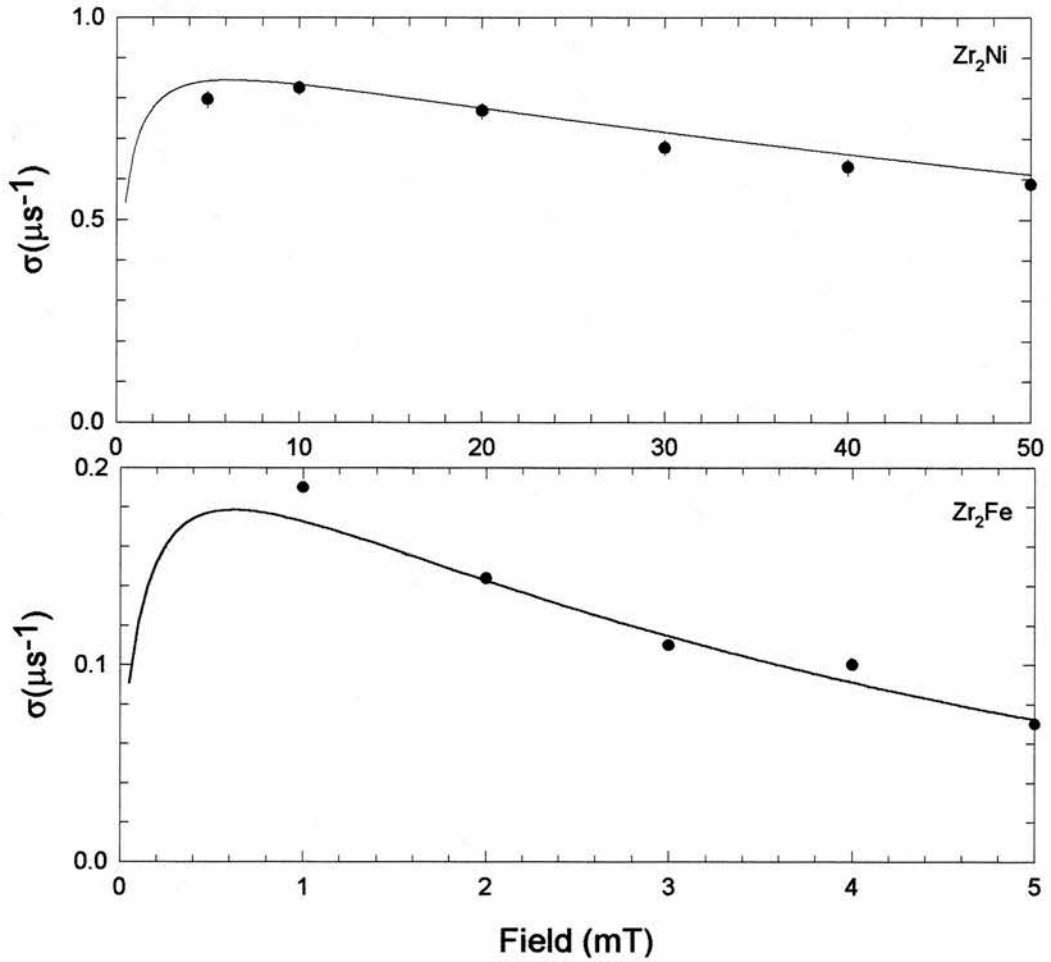


Figure 7.14 The field dependence of the muon depolarisation rate for Zr_2Ni (top) and Zr_2Fe (bottom). The line is the fit to the data using the modified London model (see equation 7.8).

7.5 REFERENCES

- ¹ P. Boyer, A. Baudry. *J. Alloys and compounds*. **129**, 213 (1987).
- ² A. Chikdene, A. Baudry, P. Boyer, S. Miraglia, D. Fruchart, J.L. Soubeyroux. *Z. Phys. Chem.* **163**, 219, (1989).
- ³ E.E. Havinga et al. *Journal of Less-Common Metals*. **27.**, 281 (1972).
- ⁴ R. Kuentzler and R.M Waterstrat. *Solid State Communications*. **54**. 517 (1985).
- ⁵ H. G. Salunke, G.P. Das, P. Raj, V. C. Sahni, S. K. Dhar. *Physica C*. **226**. 385 (1994).
- ⁶ Z. Fisk, R. Viswanathan, G.W. Webb. *Solid State Communications*. **15**. 1797 (1974).
- ⁷ S.K. Sinha, B. Harmon. *Phys. Rev. Lett.* **35**, 1515 (1976).
- ⁸ L. P. Gor'kov and O.N. Dorokhov. *Solid State Communications*. **19**. 1107 (1976).
- ⁹ R. Visnov, F. Ducastelle, G. Treglia, *J. Phys. F*. **12**, 441 (1982).
- ¹⁰ A.F. Anderson, A.J. Maeland. *J. Less-Common Metals*, **129**, 115 (1987).
- ¹¹ A. Chikdene, A. Baudry, P. Boyer, S. Miraglia, D. Fruchart, J.L. Soubeyroux, *Z. Phys. Chem*, **163**, 219 (1989).
- ¹² P. Raj, P. Suryanarayana, A. Sathyamoorthy, K. Shashikala, R.M. Iyer. *J. Alloys and Compounds*. **178**, 393 (1992).
- ¹³ P. Raj, P. Suryanarayana, A. Sathyamoorthy, K. Shashikala, R.M. Iyer, S.K. Dhar, L.C. Gupta, V.C. Sahni, R.J. Begum. *J. Alloys and Compounds*. **206**, 47 (1994).
- ¹⁴ N.M. Hong, H. Michor, M. Vybornov, T. Holubar, P. Hudegger, W. Perthold, G. Hilscher, P. Rogl. *Physica C*. **227**. 85 (1994).
- ¹⁵ J.S. Kim, W.W. Kim, G.R. Stewart. *Physical Review B*. **50**. 3485 (1994).
- ¹⁶ R. Cywinski, Z.P. Han, R. Bewley, R. Cubitt, M.T. Wylie, E.M. Forgan, S. L. Lee, M. Warden, S.H. Kilcoyne, *Physica C*, **233**, 273, (1994).
- ¹⁷ J. Rodriguez-Carvajal. FULLPROF refinement program, LLB.
- ¹⁸ *Introduction to Solid State Physics*. C. Kittel. Sixth edition. J. Wiley and sons, Inc. Chichester.
- ¹⁹ R. Lemaire, J. Schweizer, *Phys. Lett.* **21**, 366 (1966); W. Steiner, H. Ortbauer, *Phys. Status Solidi* **26a**, 451 (1974).
- ²⁰ P.S. Swartz, C.P. Bean, *J. Appl. Phys.*, **39**, 4991, (1968).
- ²¹ E.H. Brandt. *Reports of progress in physics*. **58**. 1465. (1995).
- ²² *Lecture Notes from training School in Pulse μ SR techniques*. S.H. Kilcoyne (ed). RAL report: RALTR 96007 (1996).
- ²³ E.H. Brandt. *Physical Review B*. **37**. 2349 (1988).

8. $ZrV_{2-x}TM_x$.

8.1 INTRODUCTION.

The discovery of ZrV_2 aroused interest in the C15 Laves phase superconductors since at the time of their discovery they had the highest superconducting transition temperature for a Laves phase of $8.2K^1$ and an extremely large upper critical field, H_{c2} . Using resistive techniques, H_{c2} was estimated to be approximately 11 Tesla². These compounds also provoked interest as anomalies were observed in the internal strain and magnetic susceptibility at $123K^3$. As x-ray diffraction indicated no change in the crystallographic structure for temperatures down to $80K^3$ these anomalies were thought to arise from antiferromagnetic ordering or lattice instabilities. However, neutron diffraction measurements conducted by Moncton⁴ have shown that ZrV_2 does in fact undergo a cubic-rhombohedral martensitic transformation at $116.7K$ (see figure 8.1 and figure 8.2). No magnetic order was observed down to $5K$. The isostructural HfV_2 also undergoes a structural transition at approximately $120K^5$ and is also a superconductor at $9.6K^6$. The structural change for HfV_2 is a cubic-orthorhombic transformation. Similar lattice instabilities have been found in numerous other superconductors and are often believed to be a precursor to superconductivity^{7,8,9,10,11}.

The effect of replacing vanadium by iron reduces and eventually removes the lattice transformation but has a very small effect on the superconducting transition temperature¹². As little as 2-3% iron makes the transition diffuse and 10% completely removes the high temperature structural transition. If 50% vanadium is replaced with iron then a C14 crystal structure is formed and the superconductivity is lost. The superconductivity shows a linear decrease in T_c with iron doping and completely disappears at $ZrV_{1.4}Fe_{0.6}$. Further substitution of iron results in a ferromagnetic transition which increases linearly from $0K$ for $ZrV_{0.9}Fe_{1.1}$ to $633K$ for $ZrFe_2$ ¹³. Also for iron concentrations greater than $ZrV_{0.3}Fe_{1.7}$ the structure returns to the original cubic C15 as in ZrV_2 . This indicates that the $ZrV_{2-x}Fe_x$, for $x < 0.6$ is on the verge of magnetic order

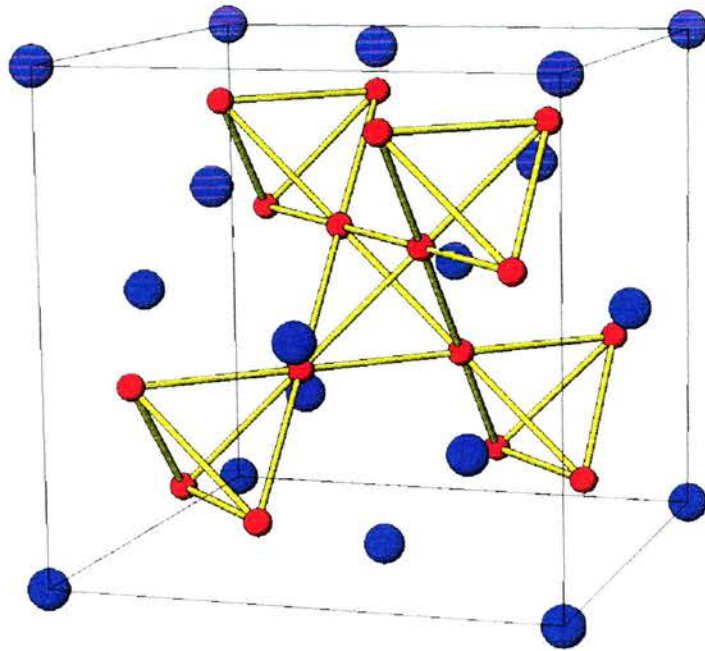


Figure 8.1 The crystal structure of cubic C15 Laves phase superconductor ZrV_2 .

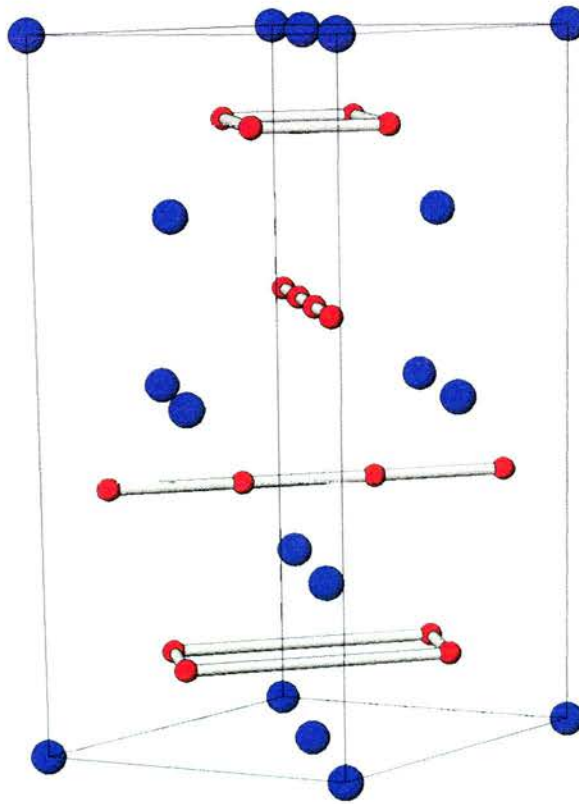


Figure 8.2 The crystal structure of ZrV_2 below the structural transformation temperature.

whilst also supporting a superconducting ground state. Substituting for V with 10% Cr, Mn and Co is also found to remove the structural transformation yet the superconducting transition temperatures remain comparable to that of ZrV_2 (see Table 8.1)¹⁴.

Sample	Tc (K)
ZrV_2	8.2
$ZrV_{1.8}Cr_{0.2}$	8.6
$ZrV_{1.8}Mn_{0.2}$	8.3
$ZrV_{1.8}Fe_{0.2}$	6.8
$ZrV_{1.8}Co_{0.2}$	6

Table 8.1 The superconducting transition temperatures for pure and doped ZrV_2 taken from ref. 14.

This suggests that the lattice instabilities are not necessarily a prerequisite or precursor to superconductivity in these Laves phase superconductors. A measure of the fundamental superconducting parameters will elucidate the effects of the added magnetic impurity and possibly indicate whether spin fluctuations influence the superconducting ground state.

8.2 INITIAL CHARACTERISATION.

8.2.1 Sample preparation.

The $Zr(V_{0.9}TM_{0.1})_2$ (where TM= Co, Fe, Mn, Cr and V) samples were prepared by arc melting together the appropriate amounts of the constituent elements, turning the ingots several times and remelting to ensure sample homogeneity. On cooling through the liquidus, the alloy forms three different phases, as can be seen from the Zr-V binary phase diagram¹⁵ (see figure 8.3). The majority phase is ZrV_2 and the other phases are unwanted Zr and V. To remove the presence of Zr and V the samples were annealed for 1 week at 950°C. Metallographic studies reported by Roy¹⁴ have shown that this procedure reduces the impurity phase to less than 5%. The annealing process was undertaken in a sealed quartz tube with 1/3 of an atmosphere of argon.

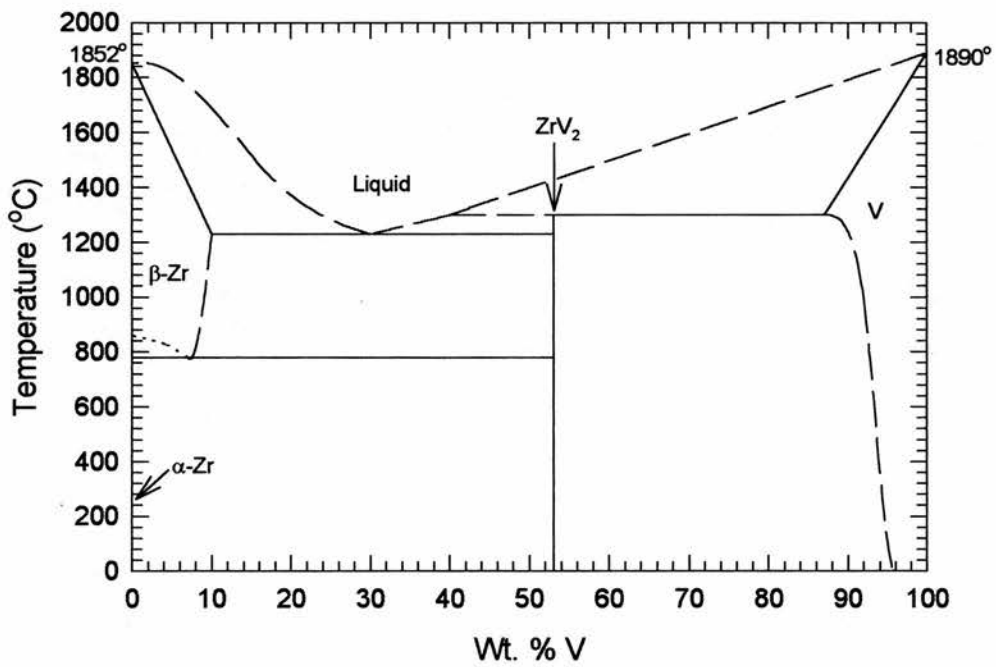


Figure 8.3 The eutectic phase diagram for Zr-V alloys¹⁵.

The quartz tube, when heated, can release oxygen that will oxidise the sample. In order to eliminate this effect the sample is wrapped in Tantalum foil. This foil will oxidise in preference to the sample and hence protect it. After annealing the samples were pulverised into a fine powder.

8.2.2 Magnetic characterisation.

The VSM sample consisted of a known mass of powder mixed with an epoxy resin. This was moulded into a spherical shape. The sample and epoxy resin were cooled below the superconducting transition temperature in zero field. At the lowest available temperature, 3.8K, a small dc field was applied (7mT) and the temperature dependence of the magnetisation was measured. Using this magnetisation data the superconducting transition temperatures have been determined (see figure 8.4) to be 8.2K, 8.5K, 8.3K, 6.8K and 6K for ZrV_2 , $Zr(V_{0.9}Cr_{0.1})_2$, $Zr(V_{0.9}Mn_{0.1})_2$, $Zr(V_{0.9}Fe_{0.1})_2$ and $Zr(V_{0.9}Co_{0.1})_2$ respectively. These transition temperatures agree with the published results^{12,14}.

The problem associated with a range of demagnetising factors in a powder sample in determining H_{c1} can be clearly seen in figure 8.5. In figure 8.5 the magnetisation curve is not linear even at the lowest fields. All the H_{c1} measurements of $ZrV_{1.8}TM_{0.2}$ have suffered from this problem and no reliable estimate of the value of H_{c1} can be made. However, the upper critical field, H_{c2} , does not suffer, to the same extent, from the demagnetisation problem. H_{c2} has been determined from the closing of the magnetic hysteresis loop at a constant temperature (see figure 8.6).

The temperature dependence of H_{c2} has been found, for each sample, and the two-fluid model,

$$H_{c2}(T) = H_{c2}(0) \left[1 - \left(\frac{T}{T_c} \right)^2 \right], \quad 8.1$$

has been fitted to the resulting data (see figure 8.7). Using this fit, the H_{c2} value was extrapolated back to 0K. These extrapolated values are related to the coherence length, ξ_{GL} , by equation 5.3. The $H_{c2}(0)$ and calculated values of ξ_{GL} can be found in Table 8.2.

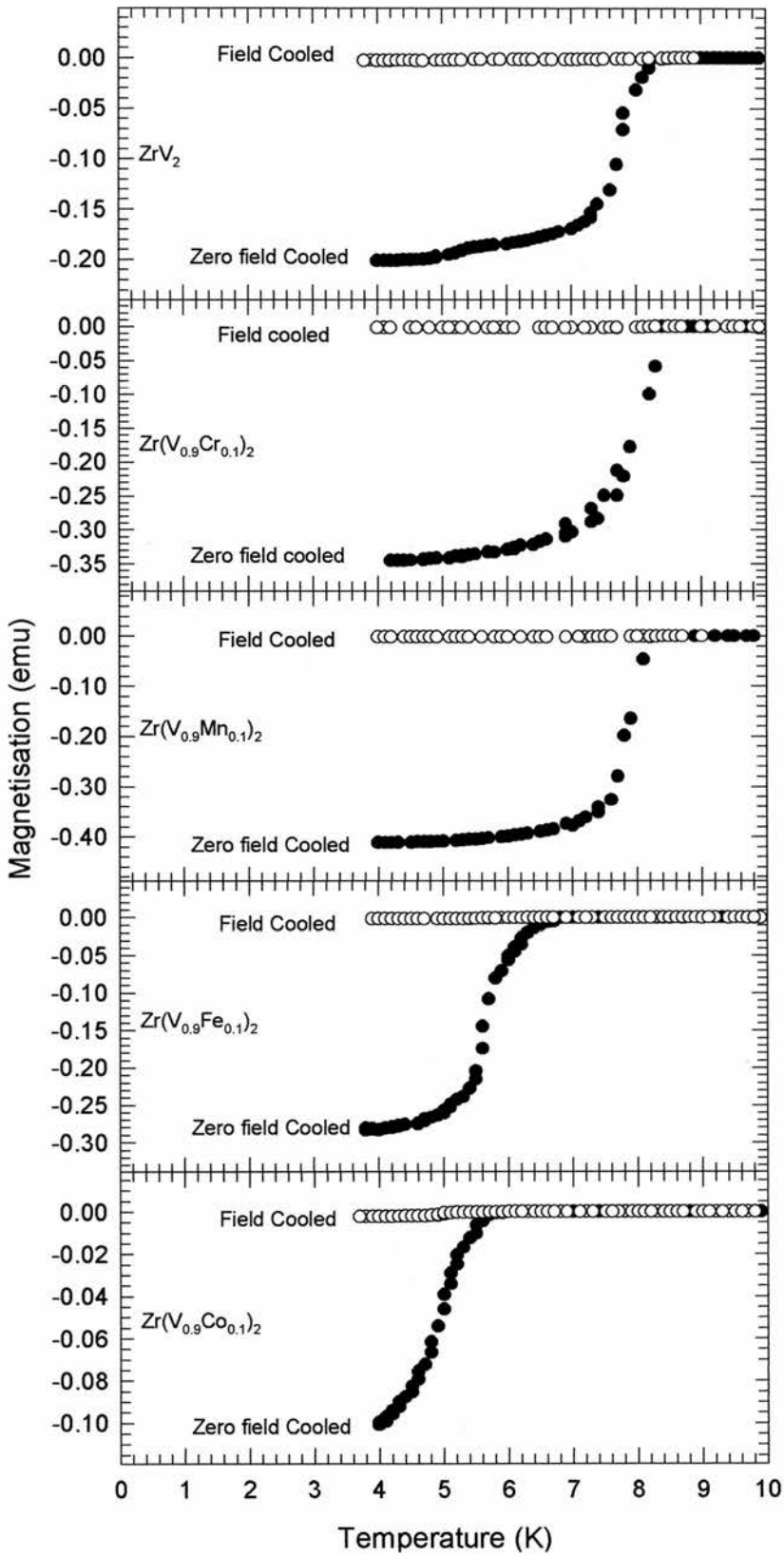


Figure 8.4 The temperature dependence of the magnetisation for $ZrV_{1.8}TM_{0.2}$.

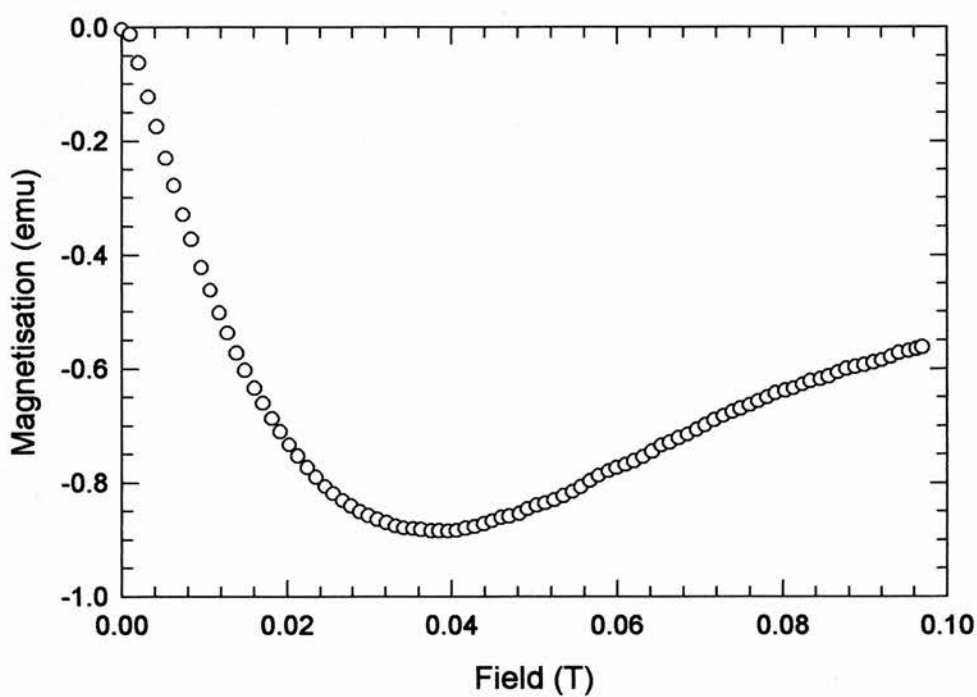


Figure 8.5 The field dependence of the magnetisation after zero field cooling $ZrV_{1.8}Cr_{0.2}$ at 4K. This result shows the difficulty in determining the lower critical field with a powder sample.

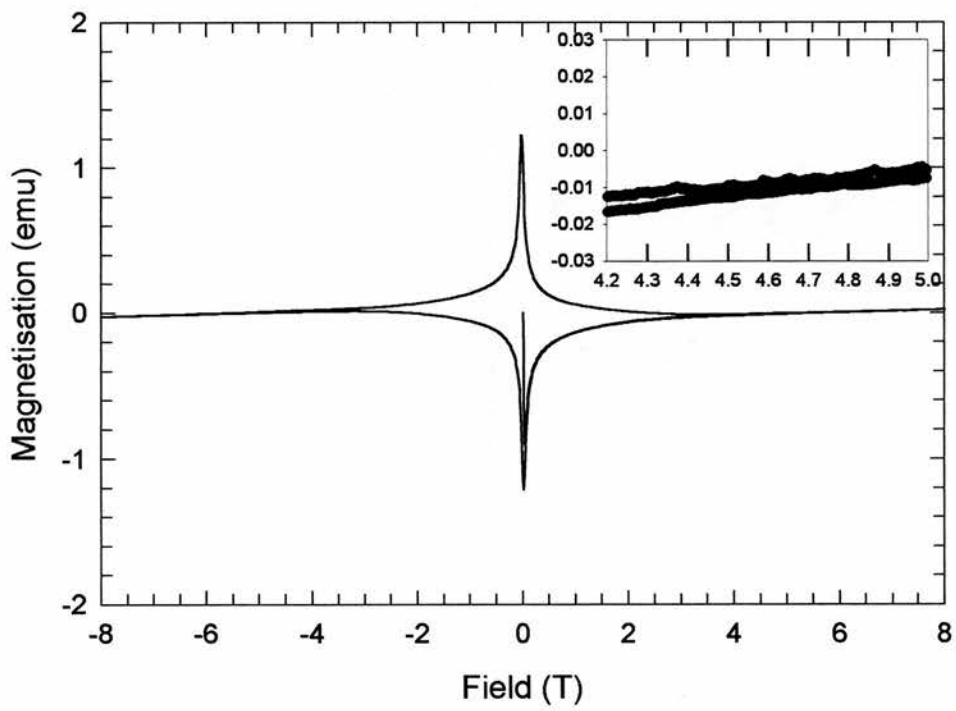


Figure 8.6 The full field dependence $ZrV_{1.8}Cr_{0.2}$ at 4K. The upper critical field, H_{c2} , has been determined as 4.5Tesla using this data.

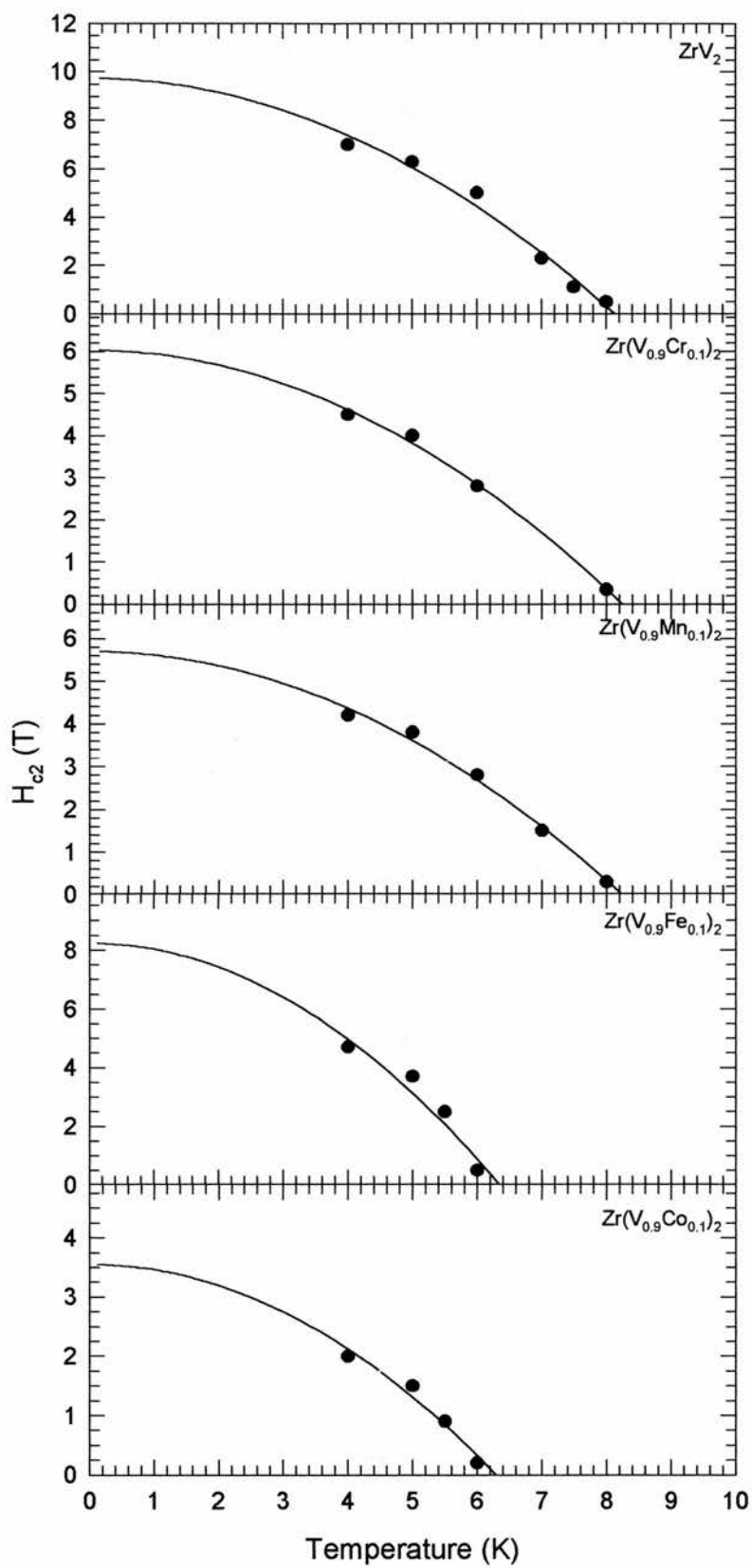


Figure 8.7 The determined values of the upper critical field for $ZrV_{1.8}TM_{0.2}$. The line is the 2 fluid model fit to the data.

Sample	T _c (K)	H _{c2} (0), Tesla	ξ _{GL} , nm
ZrV ₂	8.2(1)	9.7(4)	5.8(2)
Zr(V _{0.9} Cr _{0.1}) ₂	8.5(1)	6.1(2)	7.3(2)
Zr(V _{0.9} Mn _{0.1}) ₂	8.3(1)	5.7(2)	7.6(2)
Zr(V _{0.9} Fe _{0.1}) ₂	6.8(1)	8.3(5)	6.3(3)
Zr(V _{0.9} Co _{0.1}) ₂	6.0(1)	3.6(4)	9.6(9)

Table 8.2 A table of the parameters determined from the magnetisation measurements

8.3 MUON SPIN ROTATION

The finely powdered sample was mounted onto an aluminium sample holder using GE varnish. Using the MuSR instrument at ISIS, Oxford, UK, the muon spin rotation spectra were collected, on warming, after field cooling the sample below their respective superconducting transition temperatures. The phases of each detector were determined from the muon spectra obtained at 10K, well above any superconducting transition temperature. All the muon spin rotation spectra are well described by

$$G_z(t) = A_0 \exp(-\sigma^2 t^2) \cos(\omega t + \phi) \quad 8.2$$

where A_0 is the initial asymmetry, σ is the muon depolarisation rate, ω is the muon precession frequency and ϕ is the phase (see figure 8.8). The absence of a second term in equation 8.2 implies that the samples are phase pure and the background term has been eliminated.

Using the maximum entropy Fourier transform technique, the field profile inside the superconductor can be determined¹⁶. It has been shown that the field profile inside a powdered polycrystalline superconductor in the mixed state approximates a Gaussian profile¹⁷. As can be seen, the field profiles are closely Gaussian in form (see figure 8.9).

The muon depolarisation rate was corrected for the nuclear component of the muon depolarisation rate using the relation

$$\sigma_{\text{corr}} = \sqrt{\sigma_s^2 - \sigma_n^2}. \quad 8.3$$

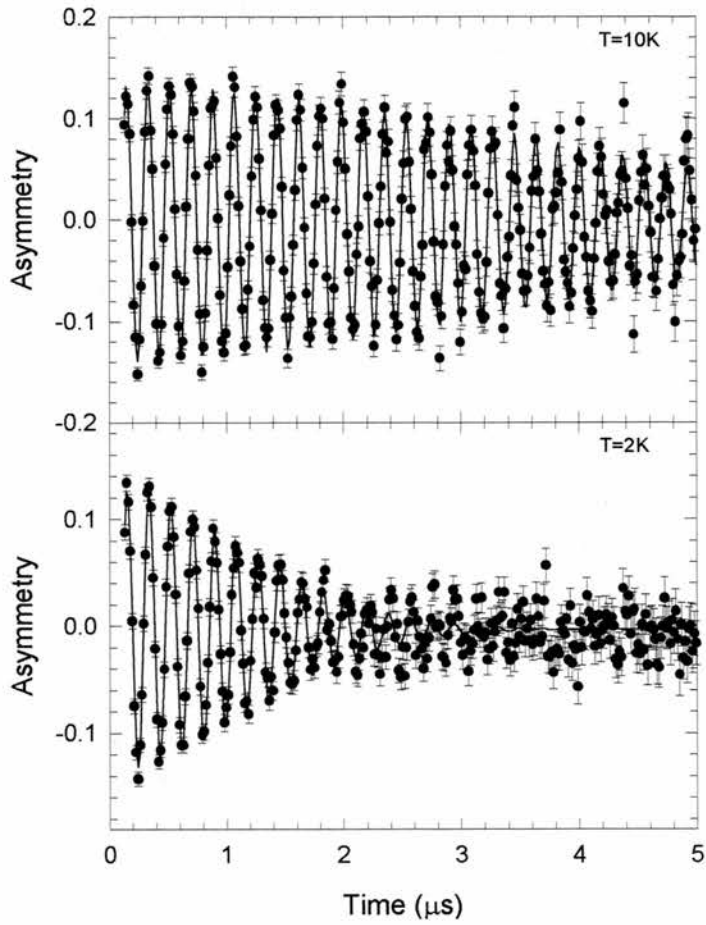


Figure 8.8 The μSR spectra for $\text{ZrV}_{1.8}\text{Fe}_{0.2}$ at 10K and 2K. The line is a least squares fit to the data assuming a Gaussian distribution of internal fields.

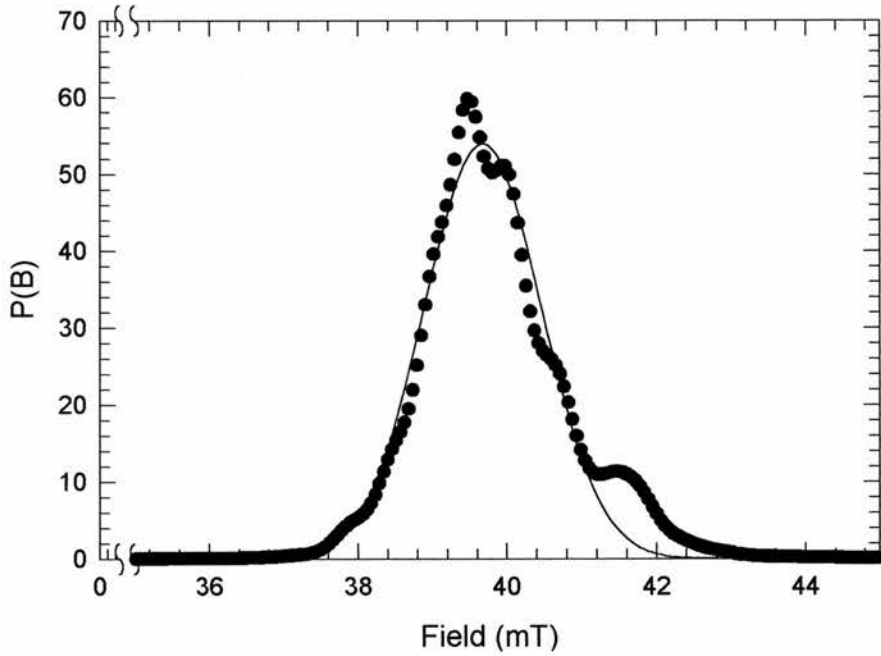


Figure 8.9 The maximum entropy field distribution inside $\text{ZrV}_{1.8}\text{Fe}_{0.2}$ at 2K with an applied field of 40mT. The line is a Gaussian fit to the data.

The temperature dependence of the corrected muon depolarisation rate, σ_{corr} , is BCS-like and the N-Fluid model,

$$\sigma(T) = \sigma(0) \left[1 - \left(\frac{T}{T_c} \right)^N \right], \quad 8.4$$

has been fitted to the data (see figure 8.10). The superconducting transition temperatures obtained are 8.0(1)K, 8.2(1)K, 5.7(1)K, 5.8(1)K and 5.6(1)K for ZrV_2 , $\text{ZrV}_{1.8}\text{Cr}_{0.2}$, $\text{ZrV}_{1.8}\text{Mn}_{0.2}$, $\text{ZrV}_{1.8}\text{Fe}_{0.2}$ and $\text{ZrV}_{1.8}\text{Co}_{0.2}$ respectively. The slight suppression of T_c is a direct result of applying a field greater than H_{c1} .

The determined values of N are 1.5(2), 6.0(1), 5.7(1), 3.6(1) and 4.0(1) for ZrV_2 , $\text{ZrV}_{1.8}\text{Cr}_{0.2}$, $\text{ZrV}_{1.8}\text{Mn}_{0.2}$, $\text{ZrV}_{1.8}\text{Fe}_{0.2}$ and $\text{ZrV}_{1.8}\text{Co}_{0.2}$. A summary of these results can be found in Table 8.2. If we consider the doped $\text{ZrV}_{1.8}\text{TM}_{0.2}$ samples then the N scales with T_c (see figure 8.11).

It should be noted that for these compounds the muon depolarisation rate, $\sigma_{\text{corr}}(0)$, is directly related to the magnetic penetration depth, λ ,

$$\lambda^2 = \frac{0.0609\gamma_\mu \Phi_0}{\sigma}, \quad 8.5$$

since the coherence length is short. Simulations using the modified London model¹⁸ show that the Ginzburg-Landau coherence length of approximately 10nm does not affect the muon depolarisation rate, σ , over a field range accessible by the MuSR instrument (0-6mT) (see figure 8.12).

The addition of a transition metal impurity on the V site has a drastic effect on λ . Although λ seems to be independent of magnetic impurity (see figure 8.11), each doped ZrV_2 sample has an increased penetration depth of $\lambda \approx 340(10)\text{nm}$. The μSR results are summarised in Table 8.3.

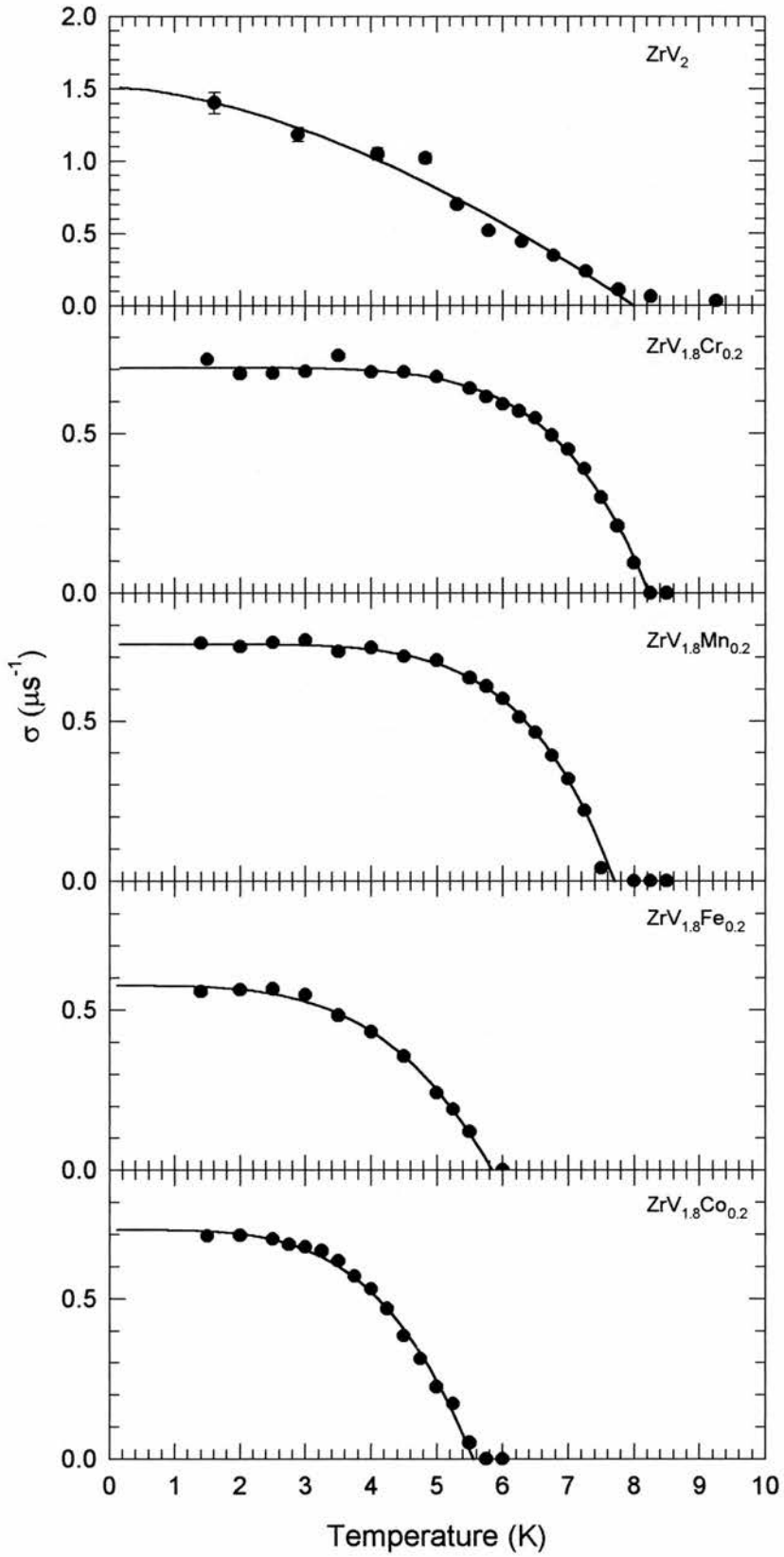


Figure 8.10 The temperature dependence of the muon depolarisation rate for $\text{ZrV}_{1.8}\text{TM}_{0.2}$ (where $\text{TM}=\text{V}, \text{Cr}, \text{Mn}, \text{Fe}$ and Co). The line is the N-Fluid model fit to the data.

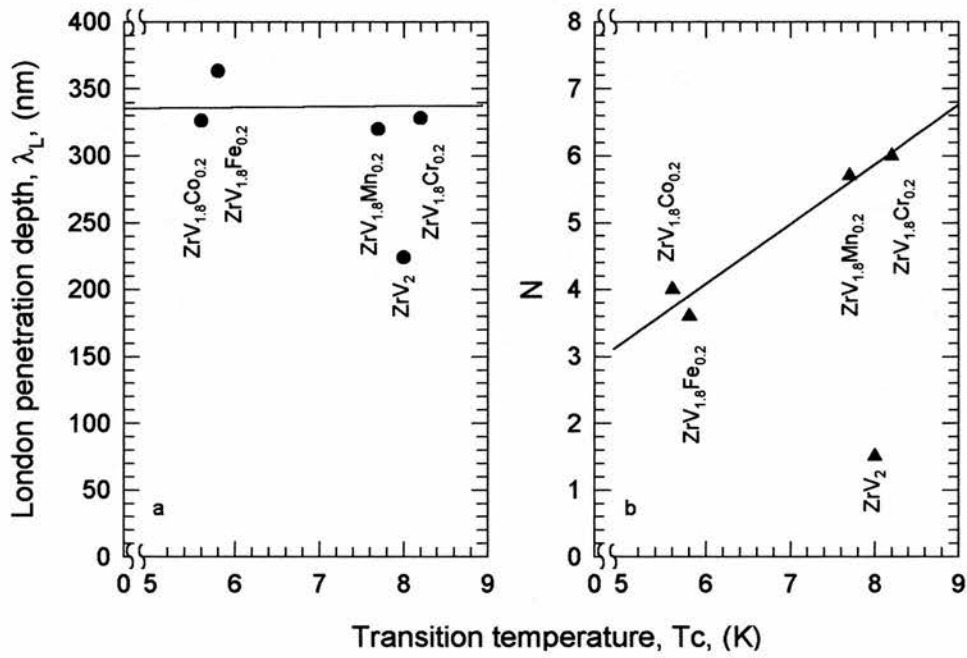


Figure 8.11 The scaling of λ_L (a) and N (b) with T_c for $ZrV_{1.8}TM_{0.2}$ (where $TM = V, Cr, Mn, Fe, Co$).

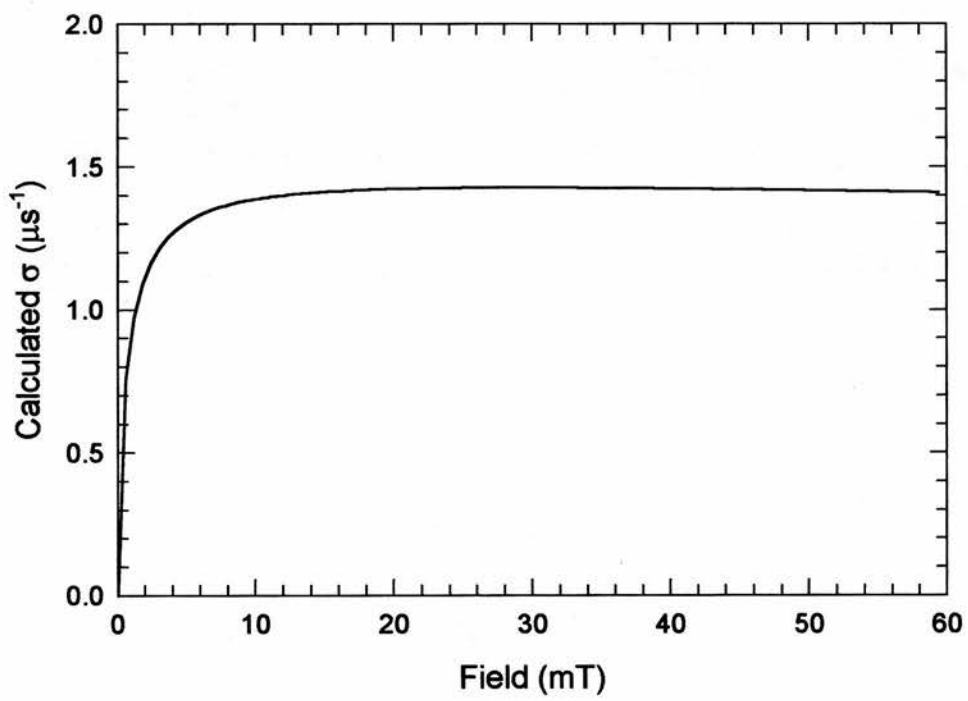


Figure 8.12 A simulation of the muon depolarisation rate as a function of field for ZrV_2 over the field range accessible by MuSR.

Sample	T_c (K)	λ_L (nm)	N
ZrV ₂	8.0(1)	224(6)	1.5(2)
ZrV _{1.8} Cr _{0.2}	8.2(1)	328(5)	6.0(1)
ZrV _{1.8} Mn _{0.2}	7.7(1)	320(7)	5.7(1)
ZrV _{1.8} Fe _{0.2}	5.8(1)	363(6)	3.6(1)
ZrV _{1.8} Co _{0.2}	5.6(1)	326(9)	4.0(1)

Table 8.3 A summary of all the transverse field μ SR results.

8.4 CONCLUSIONS.

The fundamental superconducting parameters, λ and ξ_{GL} , have been measured using muon spin rotation and dc magnetisation as complementary techniques. The upper critical field, $H_{c2}(0)$, for ZrV₂ is 9.7(4)T. This value of $H_{c2}(0)$ is high for a binary intermetallic superconductor. Even with 10% doping of Cr, Mn, Fe or Co for V has very little effect on the $H_{c2}(0)$ and hence very little effect on ξ_{GL} . However, the effect on λ_L is much more dramatic. λ_L is 50% larger for the doped ZrV_{1.8}TM_{0.2} than for ZrV₂. It is interesting that the change in magnetic penetration depth is almost independent of dopant. A summary of all these results can be found in Table 8.4.

Finally it should be noted that from the values of κ it can be concluded that all members of the Zr(VTM)₂ family are extreme type II superconductor.

Sample	$T_{c\text{ mag}}$ (K) ^a	$T_{c\text{ } \mu\text{SR}}$ (K) ^b	λ_L (nm) ^b	ξ_{GL} (nm) ^b	κ	N ^b
ZrV ₂	8.2(1)	8.0(1)	224(6)	5.8(2)	39	1.5(2)
ZrV _{1.8} Cr _{0.2}	8.5(1)	8.2(1)	328(5)	7.3(2)	45	6.0(1)
ZrV _{1.8} Mn _{0.2}	8.3(1)	7.7(1)	320(7)	7.6(2)	42	5.7(1)
ZrV _{1.8} Fe _{0.2}	6.8(1)	5.8(1)	363(6)	6.3(3)	57	3.6(1)
ZrV _{1.8} Co _{0.2}	6.0(1)	5.6(1)	326(9)	9.6(9)	34	4.0(1)

Table 8.4 A summary of all the results obtained by dc magnetisation^a and μ SR^b.

8.5 REFERENCES

- ¹ B.T. Matthias, V.B. Compton, E. Corenzwit. *J. Phys. Chem. Solids*. **19**. 130. (1961).
- ² K. Yasoshama, N. Usut. *Japan. J. Applied. Phys.* **7**. 1128. (1968).
- ³ J.E. Doherty, D.F. Gibbons. *Phys. Stat. Sol (b)*. **44**. K5. (1971).
- ⁴ D.E. Moncton. *Solid State Communications*. **13**. 1779. (1973).
- ⁵ A.C. Lawson. W.H. Zachariasen. *Phys. Lett* **38A**. 1. (1972).
- ⁶ V. Sadagopan, E. Pollard, H.C. Gatos, *Solid State Communications*. **3**. 97. (1965).
- ⁷ J.C. Phillips. *Phys. Rev. Lett.* **26**. 543. (1971).
- ⁸ E.W. Collings, J.C. Ho, R.I. Jaffee. *Phys. Rev. B*. **5**. 4435. (1972).
- ⁹ L.R. Testardi. *Phys. Rev. B*. **5**. 4342. (1972).
- ¹⁰ A.C. Lawson. *Mat. Res. Bull.* **7**. 773. (1972).
- ¹¹ C.W. Chu, E. Bucher, A.S. Cooper, J.P. Maita. *Phys. Rev. B*. **4**, 320. (1970).
- ¹² P. Duffer, S.G. Sankar, V.U.S. Rao, R.L. Bergner, R. Obermyer. *Phys. Stat. Sol. (A)*. **31**. 655 (1975).
- ¹³ S.A. Marei, R.S. Craig, W.E. Wallace, T. Tsuchida, *J. Less-common metals*, **13**. 391. (1967).
- ¹⁴ S.B. Roy. *Phil. Mag. B*. **65**. 1435. (1992).
- ¹⁵ *Metals Reference book*. C.J. Smithells and E.A. Brandes. 5th Edition. Butterworth, London (1976).
- ¹⁶ *Lecture Notes from training School in Pulse μ SR techniques*. S.H. Kilcoyne (ed). RAL report: RALTR 96007 (1996).
- ¹⁷ E.H. Brandt. *Reports of Progress in Physics*. **58**. 1465. (1995).
- ¹⁸ E.H. Brandt. *Physical Review B*. **37**. 2349 (1988).

9. Discussion and conclusions.

9.1 CLASSIFICATION OF SUPERCONDUCTORS WITHIN THE UEMURA SCHEME.

In the introduction to this thesis the Uemura classification scheme¹ for classifying ‘unconventional’ or ‘exotic’ superconductors was discussed in some detail. In essence this scheme proposes that for such superconductors a linear relationship between T_c and the effective Fermi temperature, T_F , is observed and moreover that the ratio of T_c/T_F is close to that expected for Bose-Einstein or local pairing superconductivity.

In many respects all the superconductors discussed in this thesis could be considered as ‘unconventional’ or ‘exotic’. Most are based on the elements which form ferromagnetic elemental metals, such as Ni, Fe and Co or contain transition metals which are close to moment localisation. Some, i.e. the nickel borocarbides, exhibit the coexistence of magnetic order and superconductivity in a similar fashion to that observed in the ‘exotic’ Chevrel phases. The positive curvature of H_{c2} close to T_c (e.g. $\text{LuNi}_2\text{B}_2\text{C}$ and $\text{Y}_{1-x}\text{La}_x\text{Ni}_2\text{B}_2\text{C}$) is also characteristic of unconventional or local pairing superconductors.

It is therefore instructive to examine the fundamental physical parameters of the superconducting ground state of the superconductors studied in this thesis with a view to placing those superconductors within the Uemura scheme. To perform their classification we require not only the penetration depth measurements, as provided by my μSR measurements, but also the coefficient of specific heat. In this way the following equations:-

$$\lambda(0) = \left[\frac{m^*/m_e}{4\pi n_s r_c} \left(1 + \frac{\xi}{\ell_c} \right) \right]^{1/2} \quad 9.1$$

$$\gamma_s = \left(\frac{\pi}{3} \right)^{2/3} \frac{k_B^2 m^* n_e^{2/3}}{\hbar^2} \quad 9.2$$

can be used to extract m^* and n_s independently, from which T_F may be calculated (see equation 1.5). It is also possible to separate m^* and n_s using the Pauli susceptibility,

$$\chi = \frac{\mu_0 \mu^2 V m^*}{\pi^2 \hbar^2} (3\pi^2 n_s)^{1/3} \quad 9.3$$

Unfortunately for the compounds discussed here this is not always possible because of the effects of localised magnetic moments and/or impurity effects, both of which mask the intrinsic Pauli susceptibility of the matrix. It should also be noted that to extract m^* and n_s from equations 9.1 and 9.2, we also require an estimate of the mean free path of the electron in order to assess the dirty limit correction. The mean free path, ℓ_e , has been calculated using the expression

$$\ell_e = \frac{0.18\pi^2 k_B \hbar}{\rho \gamma_s e^2 \xi_0 T_c} \quad 9.4$$

where possible values for ρ have been taken from the literature.

I have extracted m^* , n_s and ℓ_e and hence estimated T_F for most of the samples studied in this thesis. The results are tabulated in table 9.1, together with the value of T_c/T_F .

Using these values I have been able to place the superconductors I have studied on the Uemura plot. The resulting plots for the nickel borocarbides, YB_6 , Zr_2TM phase and the Laves phase samples can be seen in figures 9.1, 9.2, 9.3.

Sample	T_c (K)	λ_L (nm)	ξ (nm)	γ mJmol^{-1} K^{-2}	m^*/m_e	n_s $\times 10^{23}$ (cm^{-3})	ℓ_e (nm)	T_F (K)	T_c/T_F
$\text{LuNi}_2\text{B}_2\text{C}$	17	224	7.5	11.0^2	9.5	0.65	26^3	1540	1/92
$\text{YNi}_2\text{B}_2\text{C}^4$	15	103	8.1	18.0^5	9.4	2.8	7^6	4200	1/280
$\text{Y}(\text{Ni}_{0.95}\text{Co}_{0.05})_2\text{B}_2\text{C}^7$	8.6	130	13. 3	15.2^8	11.3	1.4	7^6	2180	1/250
$\text{Y}(\text{Ni}_{0.9}\text{Co}_{0.1})_2\text{B}_2\text{C}^7$	6.2	205	18. 8	12.0^8	10.8	0.6	7^6	1238	1/200
YB_6^7	7.1	192	33	2.8^9	3.1	0.24	$0^{10,11}$	2433	1/343
Zr_2Rh	11	140	7.5	68.0^{12}	39	5	n/a	1517	1/138
Zr_2Co	5.2	190	17	20.1^{12}	21	2	n/a	1294	1/249
Zr_2Ni	2	275	26	23.7^{12}	23	0.8	n/a	770	1/385
Zr_2Fe	0.17	520	148	16.5^{12}	26	0.3	n/a	330	1/1941
ZrV_2	8	224	5.8	12.0^{13}	7.9	0.58	25^{13}	1713	1/214

Table 9.1 A summary of the all the results obtained from our μSR measurements.

To summarise these results:

a) the nickel borocarbides and YB_6 .

The associated values for T_c/T_F are 1/280, 1/250 and 1/200 for $\text{Y}(\text{Ni}_{1.0}\text{Co}_{0.0})_2\text{B}_2\text{C}$, $\text{Y}(\text{Ni}_{0.95}\text{Co}_{0.05})_2\text{B}_2\text{C}$ and $\text{Y}(\text{Ni}_{0.90}\text{Co}_{0.10})_2\text{B}_2\text{C}$ respectively. While, at first sight, these values appear to preclude $\text{Y}(\text{Ni}_{1-x}\text{Co}_x)_2\text{B}_2\text{C}$ from the unified class of exotic superconductors, the compounds cannot readily be classed as conventional superconductors. T_c/T_F is still rather high, and the almost linear relationship between T_c and T_F as Co concentration is varied may be an indication of an underlying exotic pairing mechanism, such as the proposed antiferromagnetic spin fluctuations¹⁴, which leads to BE-like condensation. Within the Uemura classification scheme YB_6 , like $\text{YNi}_2\text{B}_2\text{C}$, therefore lies extremely close to the boundary separating exotic from conventional

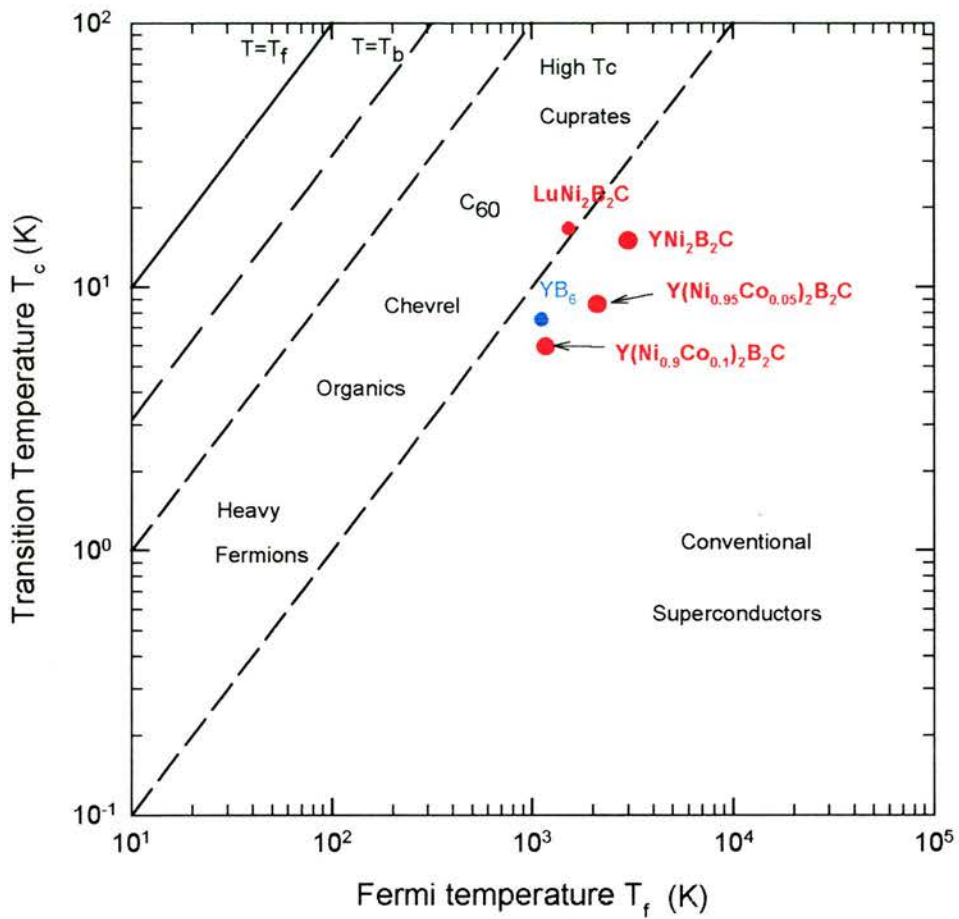


Figure 9.1 The Uemura classification of the nickel borocarbides and YB_6 using our muon spin rotation measurements.

superconducting systems. This perhaps provides the first indication that superconductivity in YB_6 may not be entirely conventional

b) Zr_2TM

The changing of the transition metal was expected to simply change the superconducting electron density. However, this is clearly not the case (see table 9.1 and figure 9.2). It is tempting to conclude that the transition metal moments are localising as the Zr_2Fe compound is approached and it is this localisation process that is decreasing T_c . In other words, the moments are acting as magnetic pair breakers.

c) ZrV_2

Again, the ZrV_2 alloy is tantalisingly close to the boundary of the exotic superconductors. This close proximity to the boundary of the exotic superconductors suggests that the superconductivity in these compounds may not be entirely conventional. However, with additional information from specific heat capacity measurements any other conclusions about the superconducting mechanisms are unable to be made.

9.2 THE ROLE OF SPIN FLUCTUATIONS.

It is apparent from the Uemura plot that the superconductors I have studied in this thesis cannot be considered as entirely 'exotic'. However on the Uemura plot they fall at or extremely close to the rather diffuse boundary separating conventional and unconventional superconductors. In this respect they may interpolate between conventional phonon mediated BCS processes and the more exotic Bose-Einstein like local pairing.

It is therefore relevant to consider whether there might be a common origin for superconductivity in these compounds that is not entirely BCS like. Moreover such a mechanism should be consistent with local pairing superconductivity.

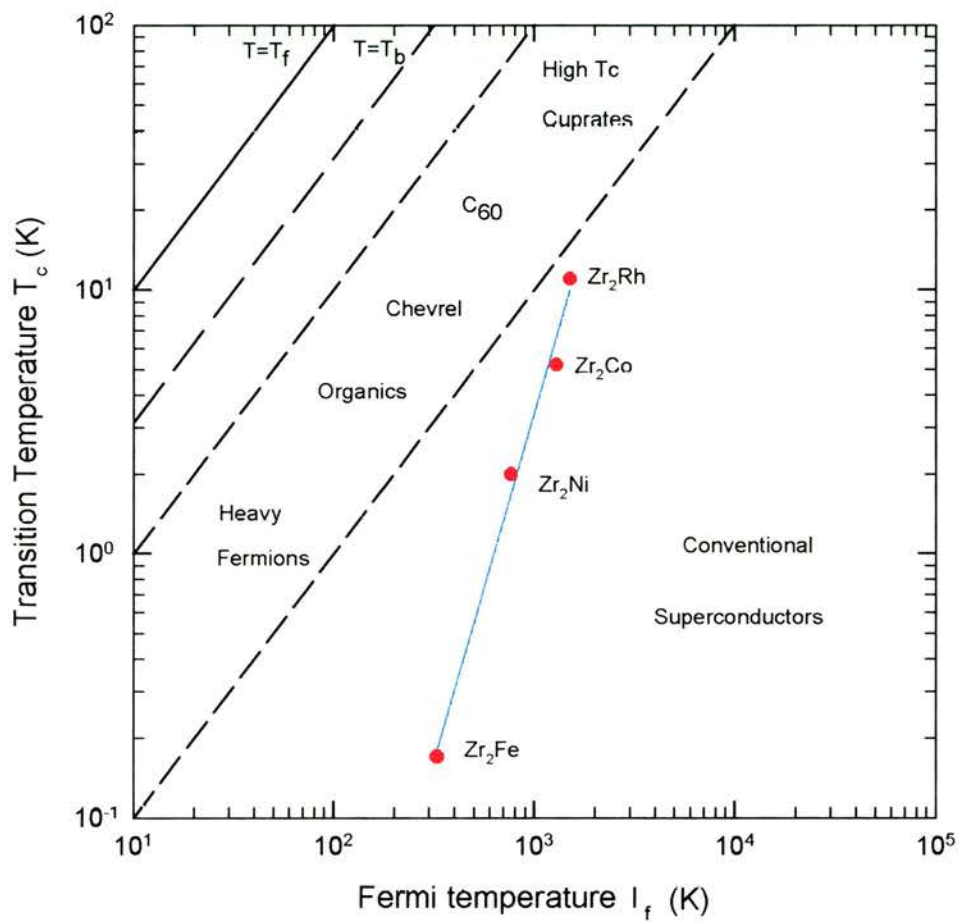


Figure 9.2 The Uemura classification of Zr_2TM ($TM = Rh, Co, Ni$ and Fe) using our muon spin rotation measurements.

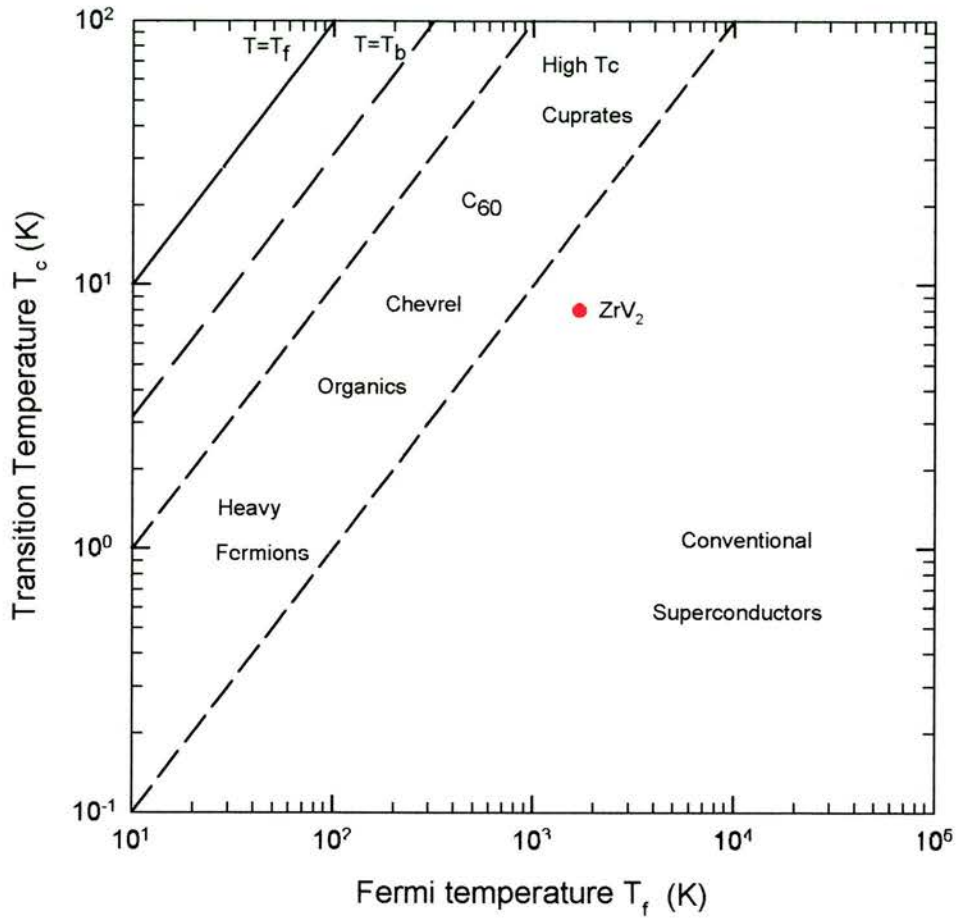


Figure 9.3 The Uemura classification of ZrV_2 using our muon spin rotation measurements.

Interestingly, Nakamura, Moriya and Ueda¹⁴ have recently formulated a theory of unconventional superconductivity based on magnetic spin fluctuations. On the basis of these observations it is tempting to suggest that the condensation mechanism in the various exotic superconductors may share a common origin. Indeed, recent calculations within the self consistent renormalisation (SCR) theory of spin fluctuations have suggested that the same antiferromagnetic spin fluctuation mechanism may be responsible for superconductivity in the high T_C cuprates, heavy fermion systems and 2d organic superconductors. Within the SCR theory the energy scale of the pairing mechanism is determined predominantly by the energy width of the dynamic spin fluctuations, T_0 . Moreover a linear dependence of T_C upon T_0 is derived (see figure 9.4). Interestingly, the ratio T_C/T_0 is of the same order as the ratio T_C/T_B obtained from the Uemura plot, suggesting that energetically T_0 and the Bose-Einstein temperature, T_B , are closely similar. The real space local pairing of superconducting carriers necessary for a BE-like condensation could therefore be mediated by such spin fluctuations.

There are numerous methods in which to determine T_0 , for example, high energy neutron scattering, NMR and heat capacity measurements. Following the formulation given by Nakamura, Moriya and Ueda it is possible to estimate the spin fluctuation temperature, T_0 , from heat capacity measurements

$$T_0 \approx \frac{12500}{\gamma [\text{mJ/mol K}^2]} \quad 9.5$$

Whilst this formulation was specifically developed for heavy fermion behaviour, and extended for high T_c system, there is no reason why it should not be equally applicable to these systems. Indeed, Nakamura, Moriya and Ueda have used this expression to calculate the spin fluctuation temperature of $\text{LuNi}_2\text{B}_2\text{C}$. We therefore place our superconducting systems on the Nakamura, Moriya and Ueda plot, as can be seen in figure 9.4.

Remarkably most of the systems fall on or close to the linear relationship predicted by Nakamura, Moriya and Ueda. It is strongly tempting to conclude that spin fluctuations could well be important in stabilising the superconducting ground state in the systems studied.

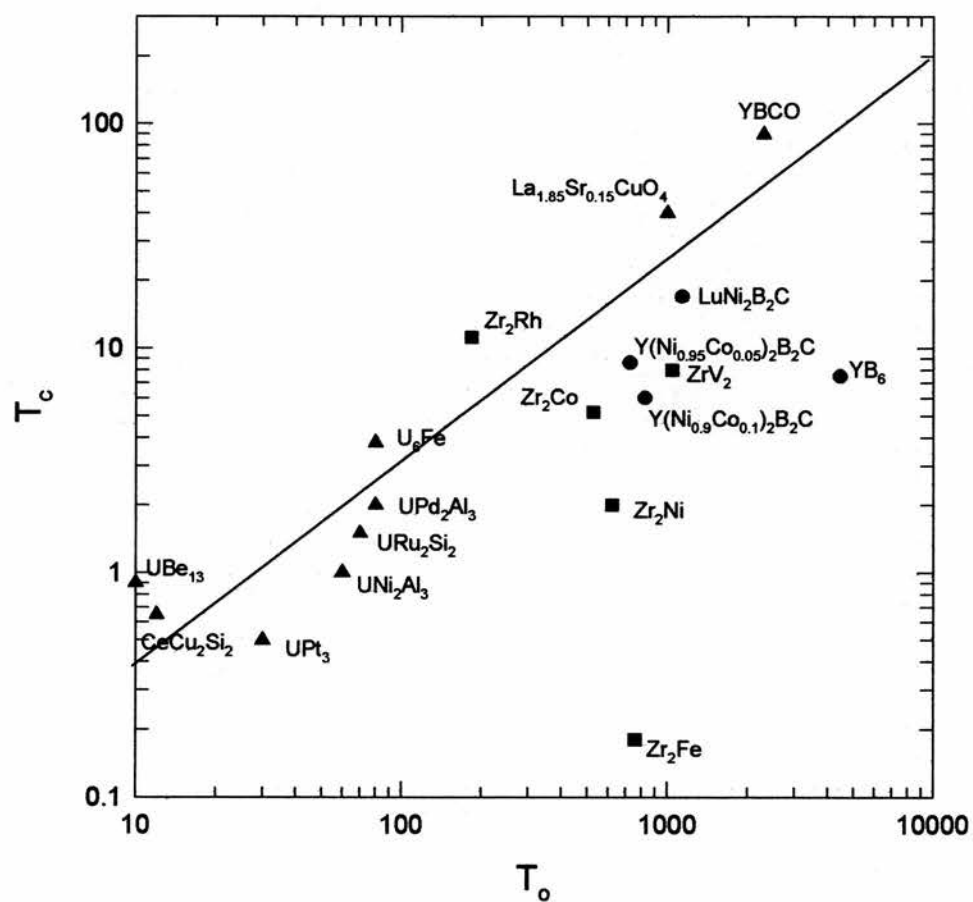


Figure 9.4 The superconducting transition temperature, T_c , versus the spin fluctuation energy width, T_0 , showing the close proximity to superconductivity being mediated by spin fluctuations in the samples examined in this thesis.

9.3 FUTURE WORK.

It is clear that I have examined only a small subset of superconducting systems which could be considered as 'exotic'. Work is currently underway to investigate using μ SR, other systems such as amorphous ZrTM, YC_2 , La_3TM and $Zr_2(RhFe)$. Although the measurements presented have shown a remarkable level of consistency, within the Uemura scheme, the results we shall obtain from these new systems may lead to support the supposition that these systems are exotic. It is also important that we confirm the role of spin fluctuation in establishing superconductivity in these systems, particularly in light of the prediction of Nakamura, Moriya and Ueda. In order to detect the spin fluctuations in these compounds a series of muon spin relaxation and high energy inelastic neutron scattering experiments are planned.

9.4 REFERENCES.

- ¹ Y. Uemura, *Physica C*, **185-189**, 733 (1991).
- ² J.S. Kim, W.W. Kim, G.R. Stewart, *Physical Review B*, **50**, 3485 (1994).
- ³ K.D.D. Rathnayaka, A.K. Bhatnagar, A. Parasisiris, D.G. Naugle, P.C. Canfield, B.K. Cho, *Phys. Rev. B*, **55**, 8506 (1997).
- ⁴ R. Cywinski, Z.P. Han, R. Bewley, R. Cubitt, M.T. Wylie, E.M. Forgan, S.L. Lee, M. Warden, S.H. Kilcoyne, *Physica C*, **233**, 273, (1994).
- ⁵ N.M. Hong, H. Michor, M. Vybornov, T. Holubar, P. Hudegger, W. Perthold, G. Hilscher, P. Royl, *Physica C*, **227**, 85 (1994).
- ⁶ R.J. Cava, H. Takagi, H.W. Zandbergen, J.J. Krajewski, W.F. Peck Jr., T. Siegrist, B. Batlogg, R.B. van Dover, R.J. Felder, K. Mizuhashi, J.O. Lee, E. Eisaki, S. Uchida, *Nature (London)*, **367**, 252 (1994).
- ⁷ A.D. Hillier and R. Cywinski, *Applied Magnetic Resonance*, **13**, 95 (1997)
- ⁸ C C Hoellwarth, P Klavins and R N Shelton, *Phys Rev B*, **53**, 2579 (1996)
- ⁹ B.T. Matthias, T.H. Geballe, K. Andres, E. Corenzwit, G.W. Hull, J.P. Maita, *Science*, **159**, 530 (1968).
- ¹⁰ S Kunii, Y Kasuya, K Kadowaki, M Date and S B Woods, *Solid State Communications*, **52**, 659 (1984).
- ¹¹ T Tanaka, T Akahane, E Bannai, S Kawai, N Tsuda and Y Ishizawa, *J Phys C: Solid State Physics*, **9**, 1235 (1976).
- ¹² H.G. Salunke, G.P. Das, P. Raj, V. C. Sahni, S.K. Dhar, *Physica C*, **226**, 385 (1994).
- ¹³ S. B. Roy, *Philosophical Magazine B* **65**, 1435 (1992).
- ¹⁴ S. Nakamura, T. Moriya, K. Ueda, *J Phys Soc Japan* **65**, 4026 (1996).